ANALYSIS OF SLENDER PIEZOELECTRIC WING CONFIGURATIONS FOR ENERGY HARVESTING: AEROELASTIC MODELING AND EXPERIMENTAL COMPARISONS

POLITECNICO DI TORINO

PhD in Aerospace Engineering

Cycle XXVIII

ANALYSIS OF SLENDER PIEZOELECTRIC WING CONFIGURATIONS FOR ENERGY HARVESTING: AEROELASTIC MODELING AND EXPERIMENTAL COMPARISONS

Doctoral Dissertation of:

Claudia Bruni

Tutors:

Prof. Giacomo Frulla

Prof. Enrico Cestino

External Supervisor :

Prof. Pier Marzocca

April 2016

ACKNOWLEDGEMENTS

The PhD was a professional and personal challenge, embraced after two years working for an renowned aeronautical company, and undertook for the sake of experiencing the academic reality and to enlarge the technical knowledge. It was a very variegated path, made of good and bad moments, as usual, but definitely all of them were necessary to acquire a certain level of awareness.

During these three years I had the great opportunity to be part of the A2-Net team, a research exchange project, under the Marie-Curie fellowship, which involved several Europeans and a North American universities. As a researcher, belonging to the just mentioned program, I spent six months at Clarkson University (USA), where I had the honor to work with Professor Marzocca. Working with professor Marzocca was an enriching experience not only because of his incredible academic background but also because of his truthful passion and dedication for his work and his unique human touch in dealing with people. During the experience in the States I also had the chance to work with Professor Gibert, who I really thank for his kindness and for his huge commitment to our collaboration.

I thank my tutors, Professor Frulla and Professor Cestino, who accompanied me in this experience from the beginning and who gave me the chance to learn many things about this beautiful subject, named Aeroelasticity, and to experience a splendid international research context.

I also would like to express my gratitude to Nicola D'Onghia, ex-student at Politecnico di Torino, for sharing his experimental results and so promoting the achievements of some of the outcomes presented in this thesis.

Least but not last I really thank my husband who constantly supported me in the good but especially in the bad moments of this experience, with his patience and dedication.

Contents

List of Figure

List of Tables

1 Introduction

1.1 Research motivation, outcomes and gaps

The doctoral research activity carried out during three years, mainly at the Politecnico di Torino and for a six months period at Clarkson University, is summarized in the present manuscript. The study of the aeroelastic response of slender piezoelectric wings gains its importance in the design of High Altitude and Long Endurance (HALE) unmanned aircrafts and in the concept of energy independent systems. The exploitation of new energy sources, which do not imply any direct penalization of the flight performances and of the original design concept, has a big potential application on HALE unmanned air vehicles (UAVs). The main characteristic of HALE UAVs is to perform very long missions at high altitudes and therefore they are mostly used for ground surveillance and communication purposes. Long range missions entail several design requirements such as high aspect ratio wing and low zero fuel weight, both with the common objective of reducing the energy consumption. However, albeit the structural design challenges afforded during the last years to increase as much as possible the mission duration of HALE aircrafts [1], satellite systems still remain the most effective solution for ground surveillance purposes. The opportunity to have additional energy form alternative sources, such as from structural vibrations, has to be interpreted as an extremely innovative application for this class of aircraft. It is one of the main outcomes of the doctoral research activity: extract energy from the aeroelastic and gust response of slender wings, by the structural coupling between the wing main structure and a pair of piezoelectric patches bonded on it. De Marqui et al. [37] performed a study in frequency domain,

showing the effect over the flutter response of a piezoelectric plate. They introduced into the model two type of electric circuits: a resistive circuit and a resistive-inductive circuit. The resistive-inductive circuit showed better performances both in the sense of flutter postponement than in that of power extraction. Bryant et al. [38] investigated the flutter response of a piezoelectric wing and the amount of energy harvested from post-flutter LCOs, due to the introduction into the model of nonlinearities, coming from the dynamic stall model. The extraction of energy from turbulence induced oscillation was the object of attention of many researchers. Akaydin et al. [39] proposed a piezoelectric beam which is able to generate electric energy from the vibrations induced by a turbulent flow at high Reynolds number. Abdelkefi et al. [40] investigated the possibility to harvest energy from transverse galloping oscillations in frequency domain and for different cross-section geometries of the chosen bluff-body. Mehmood et al. [41] evaluated the amount of energy harvested from vortex-induced vibrations of a circular cylinder. De Marqui Jr. et al. [42] modeled a piezoelectric wing generator with continuous and segmented electrodes for the purpose of energy harvesting from a discrete gust. In the work of Bryant et al. [43] come out an interesting design for power generation from aeroelastic vibrations which consist in a simple wing pin connected to the tips of a pair of bimorph piezoelectric beams. They proposed a switching energy harvesting on and off, according to the vibration amplitude, in order expand the range of speeds at which the system is able to extract energy. The number of publications available in literature which can be added to those just mentioned is vast since the demands of extra-energy at low implementation costs lead many researchers during the years to focus their activities on the possibility of energy harvesting from vibrations. The results proposed in this thesis document contributes to the subject of energy harvesting from aeroelastic

vibrations with the application of the piezo-patches on a wing structure, modeled in a more accurate way, providing the means to study also the sub-critical aeroelastic instabilities at which a slender wing, or a slender aerodynamic surface more in general, is likely to incur. A preparatory scrupulous study on the response of slender wing is necessary not only to have a better comprehension of the phenomena that should be reproduced but also to estimate the correct amount of harvestable energy through the integration of the piezoelectric patches in the main structure. A detailed description of the piezoelectric wing model and the numerical and experimental results obtained from the study of multiple aeroelastic instabilities is presented in the next chapters. The study of the aeroelastic instabilities for energy harvesting is oriented to the development of an engineering solution, such as additional aerodynamic surfaces, which exploit self-sustained oscillations, but not only, to produce electric energy.

Chapter 2 provides an extensive treatment on the derivation of the 3-D nonlinear equations of motion of a slender wing, according to the Euler-Bernoulli assumptions and the Wagner model for representation of the unsteady aerodynamic loads. The derivation of the equations of motion follows a variational approach which leads to a set of partial differential equations (PDE) expressed as a function of space and time variables. The nonlinear terms are retained into the equations up to the third order of nonlinearity, and a subsequent proper reduction is proposed in Paragraph 2.3 in order to simplify the nonlinear equations without losing the sensitivity towards the order of nonlinearity. The so obtained set of nonlinear equations is then compared, in Paragraph 2.2, to other existing derivations, in order to highlight differences and similarities with respect to them. The approximate representation of the nonlinear equations of motion is reported in section 2.5, where according to the Galerkin method the

PDEs are transformed into a set of ordinary differential equations (ODEs), suitable for the study of the wing dynamical response in time domain. The main aeroelastic phenomena which a slender wing with high probability might get into are illustrated in Chapter 3, where the characteristics of each of the analyzed aeroelastic instability is treated in detail, providing theoretical and numerical explanations. High aspect ratio wings are particularly affected by such aeroelastic problems, because of their high flexibility, strong nonlinear behavior and high static deflections, to which they are subjected during the flight. Several are the works available in literature on the aeroelastic response of high aspect ratio wings which requires the nonlinear terms to be included into the aeroelastic equations of motion to correctly capture its behavior. Cesnik and Brown [4], studied the opportunity for the HALE-class of aircraft to substitute the discrete wing control surfaces with embedded anisotropic piezo-composite actuators for primary wing control. Tang and Dowell [5], Patil and al. [6],[7] investigated the effects of geometrical, structural and aerodynamic nonlinearities on the aeroelastic response of high aspect ratio wings. In particular, aerodynamic nonlinearities are mainly responsible for post flutter LCO (limit cycle oscillations), while geometrical may cause LCO behind the critical flutter speed. Chapter 4 proposes a detailed study on the effect of geometrical nonlinearities over the dynamic and aeroelastic response of a slender wing. When the wing is subjected to a notable static deformation a stable self-sustained harmonic motion may appear at speed lower than the critical flutter speed. It is mainly due to the fact that if the nonlinear terms are retained and the wing is subjected to a static deformation, the modal response in frequency domain changes with respect to the zero static deformation condition. HALE aircrafts, more than any other type of aircrafts, suffer from pre-flutter LCOs because of the high wing static deformations during the flight. The work carried out at

Politecnico di Torino on the design of HELIPLAT [24], [26], [27], [30], [31], a solar-powered HALE aircraft, gave evidence of all these aeroelastic phenomena [25], [28], [29], [32], [33], [34], [35]. For the specific wing analyzed in Chapter 4, the modal response shows a reduction of the initial lag frequency, the first lag frequency at zero static deflection, and an increase of the original first torsional frequency. The change of the frequency spectrum affects the aeroelastic response with the rise of a sub-critical LCO at speeds quite behind the critical flutter speed, and besides dependent of the order of nonlinearity assumed into the numerical model and of the number of modes used to represent the approximated solution. If the numerical model retains nonlinear terms up to the third order the speed at which the LCO first appears is higher than that obtained with a nonlinear model truncated at the second order. The third order nonlinear terms introduce a stiffening effect that was lost with as second order nonlinear model. Furthermore a special attention was paid to the influence of some specific nonlinear third order terms over the oscillation amplitude when the trim loads generate simultaneously plunge and pitch static deformations. The numerical results were compared with the data collected during experimental test and a good match was highlighted, taking into account all the possible uncertainties which derive from the experimental test and the approximations made in the numerical model. Most of the numerical solutions available in literature stops to the second order of nonlinearities in the numerical implementation of the equations of motion. It is the case of the solution proposed by Tang and Dowell [8], where a nonlinear second order model is sufficient to describe the aeroelastic response of the wing. However, the results of Chapter 4 show that a nonlinear model truncated to the second order might be ineffective when the static deformation is high, therefore a priori analysis is necessary to establish the order of nonlinearity has to be retained into the equations of motion. The core of the doctoral

research activity, which provides the most innovative outcomes, is presented in Chapters 5 and 6. These chapters present the nonlinear model of a piezoelectric wing, which connected to a purely resistive electric circuit is able to extract kinetic energy from the wing with the double purpose of damping the dynamic response and of harvesting electric energy. The amount of harvestable energy depends of the structural and geometrical characteristics of the wing, of the properties of the piezoelectric material, of the position of the piezoelectric elements with respect to the hosting structure and of how they the piezo-elements are loaded. All the vibrations sources which the wing undergo are eligible for energy harvesting and although flutter represents a critical circumstances for the aircraft safety it is the suitable condition, together with LCOs, for energy harvesting, because of their typical self sustained simple harmonic motion, characterized by a well defined oscillation frequency. By knowing that the outcomes of the study might be used for the design of an additional aerodynamic surface which exploit self-induced oscillation to generate electric energy. The analysis performed with regards to energy harvesting from the critical flutter condition and presented in Chapter 5 are preparatory for the studies on the energy harvesting from LCOs. The contribution, available in literature, on the energy extraction from aeroelastic vibrations and specifically from flutter is tremendous. Eturk et al. [9] propose a bimorph cantilever beam for energy harvesting from flutter. Sodano et al. [10] studied the amount of harvestable energy from a sinusoidal excitation of cantilever bimorph beam. Results on the amount of energy extracted from flutter are also available in the works of De Marqui et al. [11] and of Eturk et al. [12]. The contribution to the subject goes much further, however the critical flutter condition has to be treated carefully in terms of energy harvesting due to its intrinsic linear nature, which make the theoretical means unable to establish the real oscillation

amplitude. For these reasons most of the results, such as those of Chapter 5, are presented as the amount of harvestable power per unitary plunge displacement. Another important outcome of the linear analysis, included in Chapter 5, is the postponement of the flutter speed, aeroelastic tailoring, as a direct effect of the energy extraction from the system. Albeit this last result may appear poor, the state of the art in the direction of flutter postponement, or suppression in some cases, shows how the improvements may be consistent by properly designing the overall structure, in terms of structural characteristics, piezo-patches placing and active control [13], [14], [15],[16], [17], [18]. Flutter is a typical aeroelastic instability which has to be kept out of the operational flight envelope because it may lead to catastrophic failures, however in many cases the experimental test showed a discrepancy between the theoretical results and the reality. The oscillation amplitude is restrained into a stable region when the aircraft speed exceed the flutter speed and often at considerable lower speed, if high static displacements occur, which may be conceive not negligible fatigue problems, when the oscillation amplitude is important, but without immediate catastrophic effects. The theoretical and numerical solution to LCOs is obtained by the introduction of nonlinearities into the wing model. Chapter 5 afford the LCO solution, in terms of time domain response and harvestable energy, by including only geometrical nonlinearities into the model. The aerodynamic nonlinearities are not considered since the wing pitch response is always behind the dynamic stall angle. The numerical results highlighted a peak in the power response versus the resistive load which not necessarily correspond to the maximum reduction of the plunge oscillation amplitude. The effects of the piezo length over the extracted energy are also investigated. As previously mentioned, the aeroelastic instabilities characterized by a self-sustained harmonic motion are suitable for energy harvesting, however they might be

deleterious for the structure integrity and avoided whenever it possible. This lead to think also to new vibration sources to exploit, if the piezos are placed directly over the wing, for piezoelectric energy harvesting purpose. A good candidate is the turbulence or the discrete gust, which generate a prorogated state of excitation beneficial for the electric energy generation. Nevertheless the previous results which showed a subcritical bifurcation due to low speed LCOs cannot be separated from the study of the gust response because as shown by Tang and Dowell [19] the combination of high static deformation and high gust perturbation may trigger LCOs. The results presented on Chapter 5 about the gust response are based on a linear wing model, therefore do not account for any possible LCOs induced by the gust disturbances. The objective is to show the wing response, with zero static deformation, to two different gust profiles: squared gust,that's to say two sharp edge gust opposite in sign, and 1-Cosine gust. The characteristic parameters for the 1-Cosine gust profile are chosen according to the FARs prescriptions and then adapted to the other gust profiles, which are not available from the rules, with the objective of harmonizing the comparisons among all of them. The analytical gust model is based on the Kuessner function and therefore it takes into account the fact that an abrupt change in the pitch angle do not instantaneously affect the aerodynamic loads. Chapter 5 shows how the choice of the aerodynamic model influences the result in terms of instantaneous electrical power generated by a discrete gust disturbance. It also shows which is the most effective gust profile for energy harvesting in terms of the gust penetration gradient parameter. Evaluating the amount of energy harvesting during and after the gust action for different gust profiles and through the indicial function approach for the representation of the aerodynamic loads is an innovative contribution to the state of the art. The last Chapter, the sixth, propose the design of a piezoelectric harvester based on the experimental text

campaign, carried out at Clarkson University and in the frame of the same research project, on a piezoelectric wing prototype. An initial parametric study, based also on the uncertainties of the experimental results, is performed in order to set the numerical model in such a way that it may respond in a similar manner to the experimental prototype. The reference parameters to be used into the Matlab ® code, which reproduce the dynamic behavior of a nonlinear piezoelectric wing, are obtained from a FEM wing model, created by respecting geometry and the material properties of the test wing. The first test campaign concerns to the modal testing, where a shaker, properly set, excited the wing piezoelectric modes. The comparison between the experimental results and the numerical results is quite satisfactory both in terms of response amplitude than of power extracted. Furthermore, the modal testing, emphasized the opportunity to study the dependency of the amount of energy harvested from the position of the piezo patches along the wing longitudinal axis. When the wing is excited with a frequency close to that belonging to the second bending mode, the configuration with the piezo patches placed in the immediate proximity of the wing root it's proved not being the best solution. In fact, by moving the piezo to the tip direction the amount of harvestable energy increase. The experimental test campaign ended with the wind tunnel test where the piezoelectric wing was brought to speed higher than the critical flutter in order to experience post flutter LCOs. The numerical results keep a good agreement with the experimental results also for the wind tunnel tests.

The whole study presented throughout the chapters of this manuscript provides a detailed representation of the equations of motion of slender piezoelectric wing suitable for the study of aeroelastic problems. The limits and the potentialities of the analytical model and of the results applicability

are highlighted in each dedicated section of the thesis. The model gives the opportunity to study the dynamic response of the wing in many conditions and not simply in the flutter one. Therefore, the response extends to post flutter LCOs, pre-flutter LCOs, induced by large static deformations, and discrete gust. The study of the wing LCOs and of the energy harvested from such dynamic conditions it is possible because of the introduction into the mathematical model of the geometric nonlinearities. What is still miss in the current numerical representation, although a brief analytical insight is provided in Chapter 2, is the dynamic stall model. The numerical simulations were restricted into a field where the stall model was not necessary, however for wider application of the model it is recommended to insert it in future applications. The objective of the study was to investigate the possibility to harvest energy from aeroelastic phenomena by the means of shunted piezoelectric elements. The energy is extracted from the system through a purely resistive electric circuit connected to the piezo-electrodes and voltage measured across the electric resistance allow to estimate the value of electrical power. The results provides an instantaneous value of the electric power which in the most favorable condition is of the order of $10\,mW$. It represent a satisfactory results if we think to the energy consumption of the new generation of micromechanical systems (MEMS) [20]. Despite the encouraging results it is important to highlight the limitations which may derive from the purely resistive electric circuit. When the piezoelectric circuit do not work at its resonant frequency, which is very hard to accomplish unless the wing is designed for this purpose, the amount of energy extracted from the vibrations is reduced and change with the loading condition, therefore it cannot guarantee a constant behavior. To improve the efficiency of the piezoelectric harvester the electric circuit has to be thought in a more sophisticated way. Several are the solutions available in the literature. Niederberg [44] in his work

offers an exhaustive overview on all the applicable shunting techniques. Some of them represents a good opportunity to improve the amount of energy extracted from the systems, such as the switching shunting solution, while others have a very limited range of effectiveness. These are proposed in detail in Chapter 5.

The comparison with the experimental tests, in Chapter 6, brought out an important issue which represent a gap into the state o the art of bimorph piezoelectric cantilevered energy harvester. It deal with the problem of long piezo-patches which may not be treated linearly, as in the approximation of very short piezo-patches. The literature offers many results regarding energy harvesting from flutter by using linear models, only few study nonlinear response for the purpose of energy harvesting and most often truncate the equations to the second order of nonlinearities [21]. The results of Chapter 6 extend to the third order and show the importance of such extension to the correct representation of the solution. The next evolution of the nonlinear model is the introduction of the nonlinearities also to the piezoelectric parameters which up to now are assumed linear.

References

[1] Nickol, C. L., Guynn, M. D., Kohout, L. L., & Ozoroski, T. A. (2007). High altitude long endurance air vehicle analysis of alternatives and technology requirements development. *AIAA Paper*, *1050*, 2007.

[2] Goraj, Z., Frydrychewicz, A., Świtkiewicz, R., Hernik, B., Gadomski, J., Goetzendorf-Grabowski, T., ... & Chajec, W. (2004). High altitude long endurance unmanned aerial vehicle of a new generation–a design challenge for a low cost, reliable and high performance aircraft. *TECHNICAL SCIENCES*,*52*(3).

[3] Patil, M. J., Hodges, D. H., & S. Cesnik, C. E. (2001). Nonlinear aeroelasticity and flight dynamics of high-altitude long-endurance aircraft. *Journal of Aircraft*,*38*(1), 88-94.

[4] Cesnik, C. E., & Brown, E. L. (2002, April). Modeling of high aspect ratio active flexible wings for roll control. In Proceedings of the 43rd AIAA/ASME/ASCE/AHS Structures, Structural Dynamics, and Materials Conferences, Denver, Colorado (pp. 2002-1719).

[5] Tang, D., & Dowell, E. H. (2001). Experimental and theoretical study on aeroelastic response of high-aspect-ratio wings. *AIAA journal*, *39*(8), 1430-1441.

[6] Patil, M. J., Hodges, D. H., & Cesnik, C. E. (1999, June). Characterizing the effects of geometrical nonlinearities on aeroelastic behavior of high-aspect ratio wings. In *NASA Conference Publication* (pp. 501-510). NASA.

[7] Patil, M. J., & Hodges, D. H. (2004). On the importance of aerodynamic and structural geometrical nonlinearities in aeroelastic behavior of high-aspect-ratio wings. *Journal of Fluids and Structures*, *19*(7), 905-915.

[8] Tang, D., & Dowell, E. H. (2001). Experimental and theoretical study on aeroelastic response of high-aspect-ratio wings. *AIAA journal*, *39*(8), 1430-1441.

[9] Erturk, A., & Inman, D. J. (2009). An experimentally validated bimorph cantilever model for piezoelectric energy harvesting from base excitations.Smart Materials and Structures, 18(2), 025009.

[10] Sodano, H. A., Park, G., & Inman, D. J. (2004). Estimation of electric charge output for piezoelectric energy harvesting. Strain, 40(2), 49-58.

[11] De Marqui Jr, C., Erturk, A., & Inman, D. J. (2009). Piezoaeroelastically Coupled Modeling and Analysis of Electrical Power Generation and Shunt Damping for a Cantilever Plate. In Proceedings of the 17th International Conference on Composite Materials, Edinburgh, UK, Jul (pp. 27-31).

[12] Erturk, A., Vieira, W. G. R., De Marqui Jr, C., & Inman, D. J. (2010). On the energy harvesting potential of piezoaeroelastic systems. Applied Physics Letters, 96(18), 184103.

[13] Wang, Q., & Quek, S. T. (2002). Enhancing flutter and buckling capacity of column by piezoelectric layers. International Journal of Solids and Structures,39(16), 4167-4180.

[14] Heeg, J. (1993). Analytical and experimental investigation of flutter suppression by piezoelectric actuation.

[15] Suleman, A., Costa, P. A., & Moniz, P. A. (1999, July). Experimental flutter and buffeting suppression using piezoelectric actuators and sensors. In 1999 Symposium on Smart Structures and Materials (pp. 72-81). International Society for Optics and Photonics.

[16] Ardelean, E. V., McEver, M. A., Cole, D. G., & Clark, R. L. (2003, April). Flutter suppression using V-stack piezoelectric actuator. In Proceedings of the 44th AIAA/ASME/ASCE/ASC Structures, Structural Dynamics, and Materials Conference.

[17]Gao, L., Lu, Q., Fei, F., Liu, L., Liu, Y., & Leng, J. (2013). Active vibration control based on piezoelectric smart composite. Smart Materials and Structures, 22(12), 125032.

[18] Bruni, C., Cestino, E., Frulla, G. "Parametric analysis of a fluttering piezoelectric wing", Aircraft Engineering and Aerospace Technology, 2016, 10.1108/AEAT-02-2014-0024.R2.

[19] Tang, D., & Dowell, E. H. (2002). Experimental and theoretical study of gust response for high-aspect-ratio wing. AIAA journal, 40(3), 419-429.

[20] Warneke, B. A., & Pister, K. S. (2002). MEMS for distributed wireless sensor networks. In Electronics, Circuits and Systems, 2002. 9th International Conference on (Vol. 1, pp. 291-294). IEEE.

[21] Abdelkefi, A., Nayfeh, A. H., & Hajj, M. R. (2012). Effects of nonlinear piezoelectric coupling on energy harvesters under direct excitation. Nonlinear Dynamics, 67(2), 1221-1232.

[22] Romeo G.; Frulla G. (2000) HELIPLAT:High Altitude very-long endurance Solar Powered UAV for telecommunication Applications. FEM analysis manufacturing and testing of 21m long CFRP wing box. In: Applied vehicle Technology - Panel symposium on unmanned vehicles for aerial, ground and naval military operations. RTO Meeting, Ankara - Turkey, October 2000.

[23] Romeo G.; Frulla G; Fattore L (2000) HELIPLAT: A Solar Powered HAVE-UAV for Telecommunication Applications. Design & Parametric Results. Analysis,

Manufacturing & Testing of Advanced Composite Structures. In: INTERNATIONAL TECHNICAL CONFERENCE on "UNINHABITED AERIAL VEHICLES. UAV 2000, Paris, France, 14 – 16, June 2000.

[24] Frulla G. (2002) HELIPLAT: Structural Analysis of High Altitude very-long endurance Solar Powered platform for Telecommunication and earth observation Applications. In: ICAS - 2002 Conference (Toronto), 8-13 September. pp. 1-10

[25] Frulla G. (2004) Aeroelastic behavior of solar powered high altitude very long endurance unmanned air vehicle slender wing. In: PROCEEDINGS OF THE INSTITUTION OF MECHANICAL ENGINEERS. PART G, JOURNAL OF AEROSPACE ENGINEERING, vol. 218 Part G NoG3, pp. 179-188. - ISSN 0954-4100

[26] Romeo G.; Frulla G; Cestino E; Corsino G (2004) HeliPlat: Design, Aerodynamic Structural Analysis of Long-Endurance Solar-Powered Stratospheric Platform. In: JOURNAL OF AIRCRAFT, vol. 41 n. 6, pp. 1505-1520. - ISSN 0021-8669

[27] Tuzcu I; Marzocca P; Cestino E; Romeo G; Frulla G. (2007) Stability and Control of a High-Altitude-Long-Endurance UAV. In: JOURNAL OF GUIDANCE CONTROL AND DYNAMICS, vol. 30, pp. 713-721. - ISSN 0731-5090

[28] Frulla G.; Cestino E (2007) Eccentricity Effect on the Critical Aeroelastic Condition of Slender Wings. In: INTERNATIONAL JOURNAL OF MECHANICS AND CONTROL, vol. 8 N.1, pp. 9-17. - ISSN 1590-8844

[29] Romeo G., Frulla G., Cestino E. (2007) Design of high-altitude long-endurance solar-powered unmanned air vehicle for multi-payload and operations. In: PROCEEDINGS OF THE INSTITUTION OF MECHANICAL ENGINEERS. PART G, JOURNAL OF AEROSPACE ENGINEERING, vol. 221, pp. 199-216. - ISSN 0954-4100

[30] Frulla G.; Romeo G (2008) Numerical/experimental structural characterization of composite advanced joints for HALE-UAV platforms. In: COMPOSITES. PART B, ENGINEERING, vol. 39, pp. 656-664. - ISSN 1359-8368

[31] Frulla G.; Cestino E (2008) Design, manufacturing and testing of a HALE-UAV structural demonstrator. In: COMPOSITE STRUCTURES, vol. 83, pp. 143-153. - ISSN 0263-8223

[32] Frulla G; Cestino E.; Marzocca P (2010) Critical Behaviour of Slender Wing Configurations. In: PROCEEDINGS OF THE INSTITUTION OF MECHANICAL ENGINEERS. PART G, JOURNAL OF AEROSPACE ENGINEERING, vol. 224, pp. 587-600. - ISSN 0954-4100

[33] Cestino E., Frulla G., Marzocca P. (2013) A Reduced Order Model for the Aeroelastic Analysis of Flexible Wings. In: SAE INTERNATIONAL JOURNAL OF AEROSPACE, vol. 6 n. 2. - ISSN 1946-3855 [34]

[34] Cestino E., Frulla G., Perotto E., Marzocca P. (2011) Theoretical and Experimental Flutter Predictions in High Aspect Ratio Composite Wings. In: SAE INTERNATIONAL JOURNAL OF AEROSPACE, vol. 4 n. 2, pp. 1365-1372. - ISSN 1946-3855

[35] Cestino E., Frulla G.,Perotto E.,Marzocca P. (2014) Experimental Slender Wing Model Design by the Application of Aeroelastic Scaling Laws. In: JOURNAL OF AEROSPACE ENGINEERING, vol. 27 n. 1, pp. 112-120. - ISSN 0893-1321

[36] CESTINO E. (2006). "Design of solar high altitude long endurance aircraft for multi payload & operations". AEROSPACE SCIENCE AND TECHNOLOGY, vol. 10 n. 6, pp. 541-550; ISSN 1270-9638; DOI:10.1016/j.ast.2006.06.001

[37] De Marqui, C., Vieira, W. G., Erturk, A., & Inman, D. J. (2011). Modeling and analysis of piezoelectric energy harvesting from aeroelastic vibrations using the doublet-lattice method. *Journal of Vibration and Acoustics*, *133*(1), 011003.

[38] Bryant, M., & Garcia, E. (2011). Modeling and testing of a novel aeroelastic flutter energy harvester. *Journal of vibration and acoustics*, *133*(1), 011010.

[39] Akaydin, H. D., Elvin, N., & Andreopoulos, Y. (2010). Energy harvesting from highly unsteady fluid flows using piezoelectric materials. *Journal of Intelligent Material Systems and Structures*, *21*(13), 1263-1278.

[40] Abdelkefi, A., Hajj, M. R., & Nayfeh, A. H. (2012). Piezoelectric energy harvesting from transverse galloping of bluff bodies. *Smart Materials and Structures*, *22*(1), 015014.

[41] Mehmood, A., Abdelkefi, A., Hajj, M. R., Nayfeh, A. H., Akhtar, I., & Nuhait, A. O. (2013). Piezoelectric energy harvesting from vortex-induced vibrations of circular cylinder. *Journal of Sound and Vibration*, *332*(19), 4656-4667.

[42] Júnior, C. D. M., & Maria, M. J. EFFECT OF PIEZOELECTRIC ENERGY HARVESTING ON THE RESPONSE OF A GENERATOR WING TO A TURBULENCE GUST.

[43] Bryant, M., & Garcia, E. (2009, March). Development of an aeroelastic vibration power harvester. In *SPIE Smart Structures and Materials+ Nondestructive Evaluation and Health Monitoring* (pp. 728812-728812). International Society for Optics and Photonics.

[44] Niederberg, D., Smart Damping Materials using Shunt Control, Dissertation thesis submitted to the Swiss Federal Institute of Technology (ETH), Zurich, 2005.

2 Slender wing model

Slender wings, characterized by the high aspect ratio, find significant applications in HALE (high altitude long endurance) UAV (unmanned aerial vehicle). The main advantages of high aspect ratio wings are reduced induced drag and lower fuel consumption for increased range and endurance, which however comes at the price of the reduced maneuverability. These highly flexible wings experience large deflection during their typical flight operating conditions, much more than what is exhibited by low aspect ratio wings for an equivalent load distribution. The higher the deflection is and more important the nonlinear behavior becomes. This primarily implies that for a proper representation of its flight dynamics and aeroelastic behavior the equations of motion of slender wings should properly account for nonlinearities. There is a wide literature available on the importance of the nonlinearities to detect some pre-flutter aeroelastic instabilities when the static deformation of the wing is non-zero. Patil et al [23] show how the geometrical nonlinearities drive the dynamical response when the steady-state curvature is non-zero. This combination of geometrical nonlinearities and high structural static deformation may induce LCO to appear in the pre-flutter domain, with the risk of affecting the flight envelope. A reduction from 40% to 60% of the "flutter speed", depending on the static load or on the static deformation assumed, is shown in [23], [24], [25] and [26]. The nonlinear response of a slender wing statically deformed by the aerodynamic loads and the importance of the nonlinear terms over the unsteady response is presented by a series of numerical analysis in Chapter 4. The following sections, instead, lead to the mathematical derivation of the equations of motion implemented numerically in the subsequent paragraphs.

2.1 Derivation of the equations of motion

In order to derive the nonlinear equations of motion of a slender wing two reference frames are identified: a fixed frame XYZ and a local frame $\xi\eta\zeta$, which follows the wing cross section [1].

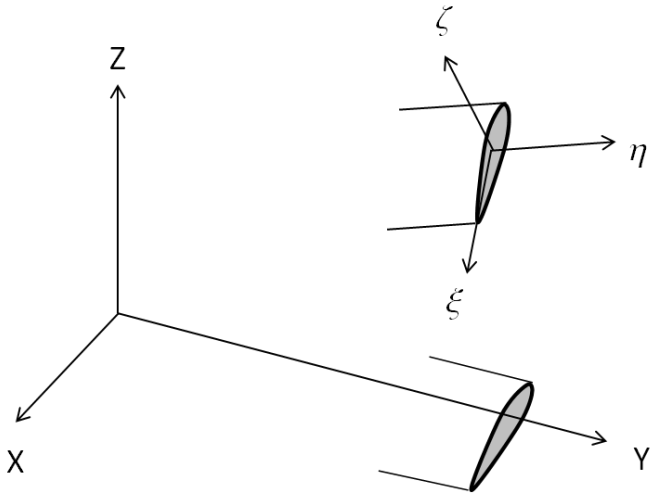

Figure 1 Wing reference frames [26]

The displacements along X,Y,Z are respectively: $u[y,t], v[y,t], w[y,t]$. The superscript $^{(l,m)}$, which often appears into the following equations, represents the order of derivative with respect to the two independent variables, y and t, respectively. Therefore, $^{(1,1)}$ indicates the first derivative with respect both variables, y and t. The two frames XYZ and $\xi\eta\zeta$ are linked through the transformation matrix $[T]$. Therefore, by knowing the coordinate of a point over the wing in the inertial frame, it is possible to have the same information with respect to the moving frame by applying the transformation matrix to the original data set. All the elements of the transformation matrix are derived from a sequences of rotations, *1-3-2* from Figure 2, performed to go from XYZ to $\xi\eta\zeta$. The angles of rotation are called Euler angles and are respectively ϕ, ψ, θ.

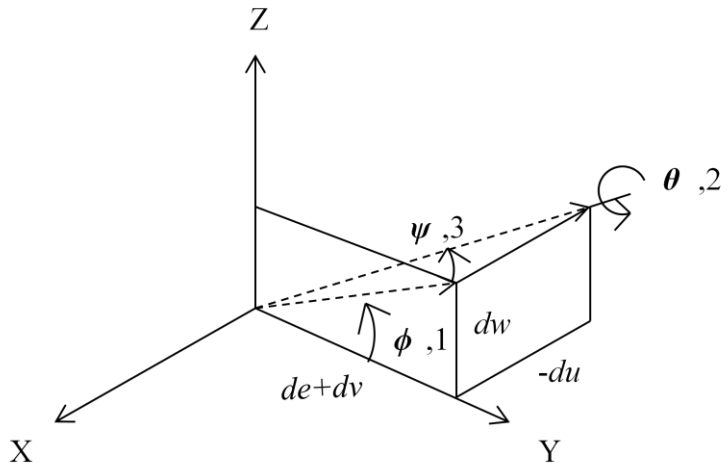

Figure 2 Euler angles and derivative displacements

$$[T] =$$

$$\begin{bmatrix} cos\,\theta\,cos\,\psi & cos\,\theta\,sin\,\psi\,cos\,\phi + sin\,\theta\,sin\,\phi & cos\,\theta\,sin\,\psi\,sin\,\phi - sin\,\theta\,cos\,\phi \\ -sin\,\psi & cos\,\psi\,cos\,\phi & cos\,\psi\,sin\,\phi \\ sin\,\theta\,cos\,\psi & sin\,\theta\,sin\,\psi\,cos\,\phi - cos\,\theta\,sin\,\phi & sin\,\theta\,sin\,\psi\,sin\,\phi + cos\,\theta\,cos\,\phi \end{bmatrix}$$

2.1

$$cos\,\phi = \frac{1+v[y,t]^{(1,0)}}{\sqrt{\left(1+v[y,t]^{(1,0)}\right)^2+w[y,t]^{(1,0)^2}}} \quad 2.2$$

$$sin\,\phi = \frac{w[y,t]^{(1,0)}}{\sqrt{\left(1+v[y,t]^{(1,0)}\right)^2+w[y,t]^{(1,0)^2}}} \quad 2.3$$

$$cos\,\psi = \frac{\sqrt{\left(1+v[y,t]^{(1,0)}\right)^2+w[y,t]^{(1,0)^2}}}{\sqrt{\left(1+v[y,t]^{(1,0)}\right)^2+u[y,t]^{(1,0)^2}+w[y,t]^{(1,0)^2}}} \quad 2.4$$

$$sin\,\psi = \frac{-u[y,t]^{(1,0)}}{\sqrt{\left(1+v[y,t]^{(1,0)}\right)^2+u[y,t]^{(1,0)^2}+w[y,t]^{(1,0)^2}}} \quad 2.5$$

$$\phi = tan^{-1}\frac{w[y,t]^{(1,0)}}{1+v[y,t]^{(1,0)}} \quad 2.6$$

$$\psi = tan^{-1}\frac{-u[y,t]^{(1,0)}}{\sqrt{\left(1+v[y,t]^{(1,0)}\right)^2+w[y,t]^{(1,0)^2}}} \quad 2.7$$

Applying a Taylor expansion up to the third order to Equations 2.1 through 2.7, yields:

$$cos\,\phi = 1 - \frac{1}{2} w[y,t]^{(1,0)^2} + w[y,t]^{(1,0)^2} v[y,t]^{(1,0)} \quad 2.8$$

$$sin\,\phi = w[y,t]^{(1,0)} - w[y,t]^{(1,0)} v[y,t]^{(1,0)} + w[y,t]^{(1,0)} v[y,t]^{(1,0)^2} - \frac{1}{2} w[y,t]^{(1,0)^3} \quad 2.9$$

$$cos\,\psi = 1 - \frac{1}{2} u[y,t]^{(1,0)^2} + u[y,t]^{(1,0)^2} v[y,t]^{(1,0)} \quad 2.10$$

$$sin\,\psi = -u[y,t]^{(1,0)} + u[y,t]^{(1,0)} v[y,t]^{(1,0)} - u[y,t]^{(1,0)} v[y,t]^{(1,0)^2} + \frac{1}{2} u[y,t]^{(1,0)} w[y,t]^{(1,0)^2} + \frac{1}{2} u[y,t]^{(1,0)^3} \quad 2.11$$

$$cos\,\theta = 1 - \frac{1}{2} \theta[y,t]^2 \quad 2.12$$

$$sin\,\theta = \theta[y,t] - \frac{1}{6} \theta[y,t]^3 \quad 2.13$$

$$\phi = w[y,t]^{(1,0)} + \frac{1}{2} w[y,t]^{(1,0)} u[y,t]^{(1,0)^2} + \frac{1}{6} w[y,t]^{(1,0)^3} \quad 2.14$$

$$\psi = -u[y,t]^{(1,0)} - \frac{1}{6} u[y,t]^{(1,0)^3} \quad 2.15$$

By assuming all structural elements to be inextensional, $e = 0$, the displacement along the longitudinal axis, $v[y,t]$, and its variation with respect to the axial coordinate, $\delta_y v[y,t]$, can be written as:

$$v[y,t] = -1/2 \int_0^y ((\delta_y u[y,t])^2 + (\delta_y w[y,t])^2)\, dy \quad 2.16$$

$$\delta_y v[y,t] = -1/2\, ((\delta_y u[y,t])^2 + (\delta_y w[y,t])^2) \quad 2.17$$

Substituting Equation 2.16 into the previous equations, the transformation matrix $[T]$ become:

$$[T] = \begin{bmatrix} T_{11} & T_{12} & T_{13} \\ T_{21} & T_{22} & T_{23} \\ T_{31} & T_{32} & T_{33} \end{bmatrix} \quad 2.18$$

$$T_{11} = 1 - \frac{1}{2}\theta[y,t]^2 - \frac{1}{2}u^{(1,0)}[y,t]^2 \quad 2.19$$

$$\mathrm{T_{12}} = -\mathrm{u}^{(1,0)}[\mathrm{y,t}] + \frac{1}{2}\theta[\mathrm{y,t}]^2\mathrm{u}^{(1,0)}[\mathrm{y,t}] + \theta[\mathrm{y,t}]\mathrm{w}^{(1,0)}[\mathrm{y,t}] + \frac{1}{2}\mathrm{u}^{(1,0)}[\mathrm{y,t}]\mathrm{w}^{(1,0)}[\mathrm{y,t}]^2 \quad 2.20$$

$$T_{13} = -\theta[y,t] + \frac{1}{6}\theta[y,t]^3 - u^{(1,0)}[y,t]w^{(1,0)}[y,t] + \frac{1}{2}\theta[y,t]w^{(1,0)}[y,t]^2 \quad 2.21$$

$$T_{21} = u^{(1,0)}[y,t] \quad 2.22$$

$$T_{22} = 1 - \frac{1}{2}u^{(1,0)}[y,t]^2 - \frac{1}{2}w^{(1,0)}[y,t]^2 \quad 2.23$$

$$T_{23} = w^{(1,0)}[y,t] \quad 2.24$$

$$T_{31} = \theta[y,t] - \frac{1}{6}\theta[y,t]^3 - \frac{1}{2}\theta[y,t]u^{(1,0)}[y,t]^2 \quad 2.25$$

$$T_{32} = -\theta[y,t]u^{(1,0)}[y,t] - w^{(1,0)}[y,t] + \frac{1}{2}\theta[y,t]^2w^{(1,0)}[y,t] - \frac{1}{2}u^{(1,0)}[y,t]^2w^{(1,0)}[y,t] \quad 2.26$$

$$T_{33} = 1 - \frac{1}{2}\theta[y,t]^2 - \theta[y,t]u^{(1,0)}[y,t]w^{(1,0)}[y,t] - \frac{1}{2}w^{(1,0)}[y,t]^2 \quad 2.27$$

The curvatures and the angular speed along the wing are defined as:

$$\rho_1 = \phi^{(1,0)}\, cos\, \theta\, cos\, \psi - \psi^{(1,0)}\, sin\, \theta \quad 2.28$$

$$\rho_2 = -\phi^{(1,0)}\, sin\, \psi + \theta^{(1,0)} \quad 2.29$$

$$\rho_3 = \phi^{(1,0)}\, sin\, \theta\, cos\, \psi + \psi^{(1,0)}\, cos\, \theta \quad 2.30$$

$$\omega_1 = \phi^{(0,1)}\, cos\, \theta\, cos\, \psi - \psi^{(0,1)}\, sin\, \theta \quad 2.31$$

$$\omega_2 = -\phi^{(0,1)}\, sin\, \psi + \theta^{(0,1)} \quad 2.32$$

$$\omega_3 = \phi^{(0,1)}\, sin\, \theta\, cos\, \psi + \psi^{(0,1)}\, cos\, \theta \quad 2.33$$

Substituting Equations from 2.12 to 2.15 into Equations from 2.28 to 2.33, the wing curvatures and the angular speeds become:

$$\rho_1 = w^{(2,0)}[y,t] + \theta[y,t]u^{(2,0)}[y,t] + u^{(1,0)}[y,t]w^{(1,0)}[y,t]u^{(2,0)}[y,t] - \frac{1}{2}\theta[y,t]^2 w^{(2,0)}[y,t] + \frac{1}{2}w^{(1,0)}[y,t]^2 w^{(2,0)}[y,t] \quad 2.34$$

$$\rho_2 = \theta^{(1,0)}[y,t] + u^{(1,0)}[y,t]w^{(2,0)}[y,t] \quad 2.35$$

$$\rho_3 = -u^{(2,0)}[y,t] + \frac{1}{2}\theta[y,t]^2 u^{(2,0)}[y,t] - \frac{1}{2}u^{(1,0)}[y,t]^2 u^{(2,0)}[y,t] + \theta[y,t]w^{(2,0)}[y,t] \quad 2.36$$

$$\omega_1 = w^{(1,1)}[y,t] + \theta[y,t]u^{(1,1)}[y,t] + u^{(1,0)}[y,t]w^{(1,0)}[y,t]u^{(1,1)}[y,t] - \frac{1}{2}\theta[y,t]^2 w^{(1,1)}[y,t] + \frac{1}{2}w^{(1,0)}[y,t]^2 w^{(1,1)}[y,t] \quad 2.37$$

$$\omega_2 = \theta^{(0,1)}[y,t] + u^{(1,0)}[y,t]w^{(1,1)}[y,t] \quad 2.38$$

$$\omega_3 = -u^{(1,1)}[y,t] + \frac{1}{2}\theta[y,t]^2 u^{(1,1)}[y,t] - \frac{1}{2}u^{(1,0)}[y,t]^2 u^{(1,1)}[y,t] + \theta[y,t]w^{(1,1)}[y,t] \quad 2.39$$

$$\omega = \begin{bmatrix} 0 & \omega_1 & -\omega_2 \\ -\omega_3 & 0 & \omega_1 \\ \omega_2 & -\omega_1 & 0 \end{bmatrix} \quad 2.40$$

The equations of motions are derived by applying the extended Hamilton principle. It consists in the time integration of the variation of the total energy:

$$\int_{t_1}^{t_2} (\delta T - \delta \Pi + \delta W_{nc}) dt = 0 \quad 2.41$$

δT is the kinetic energy, δΠ the elastic energy and δW_{nc} the work done by the non-conservative forces.

$$\delta T = -\int_0^{l_w} \iint_{A_w} \rho_w R_w^{(0,2)} \delta R_w dA_w dy \qquad 2.42$$

$$\delta R = \{i_x \quad i_y \quad i_z\} \begin{Bmatrix} \delta u[y,t] \\ \delta v[y,t] \\ \delta w[y,t] \end{Bmatrix} + \{i_1 \quad i_2 \quad i_3\}[r] \begin{Bmatrix} \delta\theta_1 \\ \delta\theta_2 \\ \delta\theta_3 \end{Bmatrix} \qquad 2.43$$

where $\delta\theta_1, \delta\theta_2$ and $\delta\theta_3$ are the virtual rotation.

$$R^{(0,2)} =$$

$$\{u^{(0,2)} \quad v^{(0,2)} \quad w^{(0,2)}\} \begin{Bmatrix} i_x \\ i_y \\ i_z \end{Bmatrix} + \{{\omega_1}^{(0,1)} \quad {\omega_2}^{(0,1)} \quad {\omega_3}^{(0,1)}\}[r]^T \begin{Bmatrix} i_1 \\ i_2 \\ i_3 \end{Bmatrix} -$$

$$\{\omega_1 \quad \omega_2 \quad \omega_3\}[r] \begin{Bmatrix} i_1 \\ i_2 \\ i_3 \end{Bmatrix} \qquad 2.44$$

$$[r] = \begin{bmatrix} 0 & z & 0 \\ -z & 0 & x \\ 0 & -x & 0 \end{bmatrix} \qquad 2.45$$

If the gravity center is unbalanced with respect to the shear center along the x coordinate only, the $[r]$ matrix become:

$$[r] = \begin{bmatrix} 0 & 0 & 0 \\ 0 & 0 & x_\alpha \\ 0 & -x_\alpha & 0 \end{bmatrix} \qquad 2.46$$

Consequently one can express

$$\delta T =$$

$$-\int_0^{l_w} \left\{ \left[m_w \begin{Bmatrix} u^{(0,2)}[y,t] \\ v^{(0,2)}[y,t] \\ w^{(0,2)}[y,t] \end{Bmatrix} + [T]^T [J1_w] \begin{Bmatrix} \omega_1^{(0,1)} \\ \omega_2^{(0,1)} \\ \omega_3^{(0,1)} \end{Bmatrix} \right. -$$

$$[T]^T[\omega][J1_w]\begin{Bmatrix}\omega_1\\ \omega_2\\ \omega_3\end{Bmatrix}\Bigg]\begin{Bmatrix}\delta u[y,t]\\ \delta v[y,t]\\ \delta w[y,t]\end{Bmatrix}+\Bigg[[J2_w]\begin{Bmatrix}\omega_1^{(0,1)}\\ \omega_2^{(0,1)}\\ \omega_3^{(0,1)}\end{Bmatrix}-[\omega][J2_w]\begin{Bmatrix}\omega_1\\ \omega_2\\ \omega_3\end{Bmatrix}-$$

$$[J1_w][T]\begin{Bmatrix}u^{(0,2)}[y,t]\\ v^{(0,2)}[y,t]\\ w^{(0,2)}[y,t]\end{Bmatrix}\Bigg]\begin{Bmatrix}\delta\theta_1\\ \delta\theta_2\\ \delta\theta_3\end{Bmatrix}\Bigg\} \qquad 2.47$$

$$m_w=\iint_{A_w}\rho_w\,dA_w\,,\ J1_w=\iint_{A_w}\rho_w[r]\,dA_w\ ,\ J2_w=\iint_{A_w}\rho_w[r]^T[r]\,dA_w$$

2.48

while the elastic energy is cast as:

$$\delta\Pi=\int_0^{l_w}\iint_{A_w}[\sigma_{22}(\delta e-z\,\delta\rho_1+x\,\delta\rho_3)+\sigma_{21}\,z\,\delta\rho_2-\sigma_{23}\,x\,\delta\rho_2]dy\,dA_w$$

2.49

$$F2=\iint_{A_w}\sigma_{22}\,dA_w,\ \begin{Bmatrix}M_1\\ M_2\\ M_3\end{Bmatrix}=\iint_{A_w}\begin{Bmatrix}-\sigma_{22}\,z\\ \sigma_{21}\,z-\sigma_{23}\,x\\ \sigma_{22}\,x\end{Bmatrix}dA_w \qquad 2.50$$

$$\delta\Pi=\int_0^{l_w}\left(F_{2_w}\delta e+M_{1_w}\delta\rho_1+M_{2_w}\delta\rho_2+M_{3_w}\delta\rho_3\right)dy \qquad 2.51$$

and where for initially straight beam $\delta e=T_{21}\delta u[y,t]^{(1,0)}+T_{22}\delta v+T_{23}\delta w[y,t]^{(1,0)}$. The constitutive matrix of the wing cross section relates the moments with the curvatures:

$$\begin{Bmatrix}M_{1_w}\\ M_{2_w}\\ M_{3_w}\end{Bmatrix}=\begin{bmatrix}D_{11}&D_{12}&D_{13}\\ D_{21}&D_{22}&D_{23}\\ D_{31}&D_{32}&D_{33}\end{bmatrix}\begin{Bmatrix}\rho_1\\ \rho_2\\ \rho_3\end{Bmatrix} \qquad 2.52$$

and in the case of isotropic material, the constitutive matrix becomes:

$$\begin{Bmatrix} M1_w \\ M2_w \\ M3_w \end{Bmatrix} = \begin{bmatrix} D_{11} & 0 & 0 \\ 0 & D_{22} & 0 \\ 0 & 0 & D_{33} \end{bmatrix} \begin{Bmatrix} \rho_1 \\ \rho_2 \\ \rho_3 \end{Bmatrix} \quad 2.53$$

The non-conservatives terms are included in the expression of $\delta \mathrm{Wnc_w}$ as:

$$\delta Wnc_w = \int_0^{l_w} \left(-c_1\, u^{(0,1)}[y,t]\delta u - c_2 v^{(0,1)}[y,t]\delta v - c_3 w^{(0,1)}[y,t]\delta w - c_5 \theta^{(0,1)}[y,t]\delta\theta 2 + q_1\delta u + q_2\delta v + q_3\delta w + q_5\delta\theta\right) dy \quad 2.54$$

where c_1, c_2, c_3, c_5 are the structural damping coefficients, while q_1, q_2, q_3, q_5 are the external loads acting on the wing. Substituting all the energy terms into the Hamilton expression, collecting all the coefficients of each variation δ, and equating to zero each variations coefficient the following three equations of motion are obtained.

In-plane bending:

$$\frac{\partial}{\partial y}\left(\lambda_{1_w} T_{11} + F_{2_w} T_{21} + \lambda_{3_w} T_{31}\right) - \left(A_{u_w} + c_1 u^{(0,1)}[y,t] - q_1\right) = 0 \quad 2.55$$

Out-of-plane bending:

$$\frac{\partial}{\partial y}\left(\lambda_{1_w} T_{13} + F_{2_w} T_{23} + \lambda_{3_w} T_{33}\right) - \left(A_{w_w} + c_3 w^{(0,1)}[y,t] - q_3\right) = 0 \quad 2.56$$

Torsion:

$$M_{2_w}{}^{(1,0)} - M_{3_w}\rho_1 + M_{1_w}\rho_3 - A_{\theta_{2_w}} - c_5\theta^{(0,1)}[y,t] + q_5 = 0 \quad 2.57$$

Implying the dependency from [y, t] of the concerned variable, the explicit forms of the bending-bending-torsion equations are:

In-plane Bending:

$$c_1 u^{(0,1)} + x_a m_W \theta^{(0,1)^2} - m_W u^{(0,2)} + x_a m_W \theta\theta^{(0,2)} - \frac{1}{2}\left(\int_0^y \left(2u^{(1,1)^2} + 2w^{(1,1)^2} + 2u^{(1,0)}u^{(1,2)} + 2w^{(1,0)}w^{(1,2)}\right) dy\right) m_W u^{(1,0)} +$$

$$x_a m_W \theta^{(0,2)} u^{(1,0)} w^{(1,0)} + 2I_x \theta^{(0,1)} \theta^{(1,0)} u^{(1,1)} - 2I_z \theta^{(0,1)} \theta^{(1,0)} u^{(1,1)} +$$
$$2x_a m_W {u^{(1,1)}}^2 + 2x_a m_W \theta^{(0,1)} u^{(1,0)} w^{(1,1)} + x_a m_W {w^{(1,1)}}^2 +$$
$$2I_x \theta u^{(1,1)} \theta^{(1,1)} - 2I_z \theta u^{(1,1)} \theta^{(1,1)} + I_x w^{(1,1)} \theta^{(1,1)} - I_y w^{(1,1)} \theta^{(1,1)} -$$
$$I_z w^{(1,1)} \theta^{(1,1)} + 2I_x \theta \theta^{(1,0)} u^{(1,2)} - 2I_z \theta \theta^{(1,0)} u^{(1,2)} +$$
$$x_a m_W \theta u^{(1,0)} w^{(1,2)} + I_x \theta^{(1,0)} w^{(1,2)} - I_z \theta^{(1,0)} w^{(1,2)} +$$
$$\left(\int_{l_w}^{y} (-\frac{1}{2} (\int_0^y \left(2{u^{(1,1)}}^2 + 2{w^{(1,1)}}^2 + 2u^{(1,0)} u^{(1,2)} + \right. \right.$$
$$\left. \left. 2w^{(1,0)} w^{(1,2)} \right) dy \right) m_W + x_a m_W {\theta^{(0,1)}}^2 u^{(1,0)} + x_a m_W \theta \theta^{(0,2)} u^{(1,0)} +$$
$$x_a m_W \theta^{(0,2)} w^{(1,0)} + 2x_a m_W \theta \theta^{(0,1)} u^{(1,1)} + 2x_a m_W \theta^{(0,1)} w^{(1,1)} +$$
$$2x_a m_W w^{(1,0)} u^{(1,1)} w^{(1,1)} + x_a m_W u^{(1,0)} {w^{(1,1)}}^2 - x_a m_W u^{(1,2)} +$$
$$\frac{1}{2} x_a m_W \theta^2 u^{(1,2)} + \frac{1}{2} x_a m_W {w^{(1,0)}}^2 u^{(1,2)} + x_a m_W \theta w^{(1,2)} +$$
$$x_a m_W u^{(1,0)} w^{(1,0)} w^{(1,2)}) \, dy) u^{(2,0)} - x_a m_W u^{(0,2)} u^{(2,0)} -$$
$$2D_{11} {\theta^{(1,0)}}^2 u^{(2,0)} + 2D_{33} {\theta^{(1,0)}}^2 u^{(2,0)} + I_z {u^{(1,1)}}^2 u^{(2,0)} + I_x {w^{(1,1)}}^2 u^{(2,0)} -$$
$$I_y {w^{(1,1)}}^2 u^{(2,0)} + 2I_z u^{(1,0)} u^{(1,2)} u^{(2,0)} + I_x w^{(1,0)} w^{(1,2)} u^{(2,0)} - D_{33} {u^{(2,0)}}^3 -$$
$$x_a m_W w^{(0,2)} w^{(2,0)} + I_x u^{(1,0)} w^{(1,2)} w^{(2,0)} - D_{11} u^{(2,0)} {w^{(2,0)}}^2 +$$
$$D_{22} u^{(2,0)} {w^{(2,0)}}^2 - 2D_{11} \theta u^{(2,0)} \theta^{(2,0)} + 2D_{33} \theta u^{(2,0)} \theta^{(2,0)} -$$
$$D_{11} w^{(2,0)} \theta^{(2,0)} + D_{22} w^{(2,0)} \theta^{(2,0)} + D_{33} w^{(2,0)} \theta^{(2,0)} + 2I_x \theta \theta^{(0,1)} u^{(2,1)} -$$
$$2I_z \theta \theta^{(0,1)} u^{(2,1)} + 2I_z u^{(1,0)} u^{(1,1)} u^{(2,1)} + I_x \theta^{(0,1)} w^{(2,1)} - I_y \theta^{(0,1)} w^{(2,1)} -$$
$$I_z \theta^{(0,1)} w^{(2,1)} + 2I_x u^{(1,0)} w^{(1,1)} w^{(2,1)} - 2I_y u^{(1,0)} w^{(1,1)} w^{(2,1)} + I_z u^{(2,2)} +$$
$$I_x \theta^2 u^{(2,2)} - I_z \theta^2 u^{(2,2)} + I_z {u^{(1,0)}}^2 u^{(2,2)} + I_x \theta w^{(2,2)} - I_z \theta w^{(2,2)} +$$
$$I_x u^{(1,0)} w^{(1,0)} w^{(2,2)} - 4D_{11} \theta \theta^{(1,0)} u^{(3,0)} + 4D_{33} \theta \theta^{(1,0)} u^{(3,0)} -$$
$$4D_{33} u^{(1,0)} u^{(2,0)} u^{(3,0)} - 2D_{11} \theta^{(1,0)} w^{(3,0)} + D_{22} \theta^{(1,0)} w^{(3,0)} +$$
$$2D_{33} \theta^{(1,0)} w^{(3,0)} - D_{11} w^{(1,0)} u^{(2,0)} w^{(3,0)} - 3D_{11} u^{(1,0)} w^{(2,0)} w^{(3,0)} +$$
$$2D_{22} u^{(1,0)} w^{(2,0)} w^{(3,0)} - D33 u^{(4,0)} - D_{11} \theta^2 u^{(4,0)} + D_{33} \theta^2 u^{(4,0)} -$$

$$D_{33}u^{(1,0)^2}u^{(4,0)} - D_{11}\theta w^{(4,0)} + D_{33}\theta w^{(4,0)} - D_{11}u^{(1,0)}w^{(1,0)}w^{(4,0)} = -q_1 \quad 2.58$$

Torsion:

$$-c_5\theta^{(0,1)} + x_a m_W \theta u^{(0,2)} + x_a m_W w^{(0,2)} - \frac{1}{2}x_a m_W \theta^2 w^{(0,2)} - I_y\theta^{(0,2)} + \frac{1}{2}x_a\left(\int_0^y \left(2u^{(1,1)^2} + 2w^{(1,1)^2} + 2u^{(1,0)}u^{(1,2)} + 2w^{(1,0)}w^{(1,2)}\right)dy\right)m_W w^{(1,0)} - \frac{1}{2}x_a m_W w^{(0,2)}w^{(1,0)^2} + I_x\theta u^{(1,1)^2} - I_z\theta u^{(1,1)^2} + I_x u^{(1,1)}w^{(1,1)} - I_y u^{(1,1)}w^{(1,1)} - I_z u^{(1,1)}w^{(1,1)} - I_x\theta w^{(1,1)^2} + I_z\theta w^{(1,1)^2} - I_y u^{(1,0)}w^{(1,2)} - D_{11}\theta u^{(2,0)^2} + D_{33}\theta u^{(2,0)^2} - D_{11}u^{(2,0)}w^{(2,0)} + D_{22}u^{(2,0)}w^{(2,0)} + D_{33}u^{(2,0)}w^{(2,0)} + D_{11}\theta w^{(2,0)^2} - D_{33}\theta w^{(2,0)^2} + D_{22}\theta^{(2,0)} + D_{22}u^{(1,0)}w^{(3,0)} = -q_5$$

2.59

Out of plane bending:

$$-c_3 w^{(0,1)}x_a m_W \theta\theta^{(0,1)^2} - m_W w^{(0,2)} + x_a m_W \theta^{(0,2)} - \frac{1}{2}x_a m_W \theta^2\theta^{(0,2)} - \frac{1}{2}\left(\int_0^y \left(2u^{(1,1)^2} + 2w^{(1,1)^2} + 2u^{(1,0)}u^{(1,2)} + 2w^{(1,0)}w^{(1,2)}\right)dy\right)m_W w^{(1,0)} + \frac{1}{2}x_a m_W \theta^{(0,2)}w^{(1,0)^2} - \frac{1}{2}x_a\left(\int_0^y \left(2u^{(1,1)^2} + 2w^{(1,1)^2} + 2u^{(1,0)}u^{(1,2)} + 2w^{(1,0)}w^{(1,2)}\right)dy\right)m_W\theta^{(1,0)} + x_a m_W u^{(0,2)}u^{(1,0)}\theta^{(1,0)} + x_a m_W w^{(0,2)}w^{(1,0)}\theta^{(1,0)} - x_a m_W \theta u^{(1,1)^2} - 2I_x\theta^{(0,1)}\theta^{(1,0)}w^{(1,1)} + 2I_z\theta^{(0,1)}\theta^{(1,0)}w^{(1,1)} + 2x_a m_W u^{(1,1)}w^{(1,1)} - 2x_a m_W \theta w^{(1,1)^2} +$$

$$I_x u^{(1,1)}\theta^{(1,1)} + I_y u^{(1,1)}\theta^{(1,1)} - I_z u^{(1,1)}\theta^{(1,1)} - 2I_x\theta w^{(1,1)}\theta^{(1,1)} +$$
$$2I_z\theta w^{(1,1)}\theta^{(1,1)} + I_x\theta^{(1,0)}u^{(1,2)} - I_z\theta^{(1,0)}u^{(1,2)} + x_a m_W u^{(1,0)}w^{(1,2)} -$$
$$2I_x\theta\theta^{(1,0)}w^{(1,2)} + 2I_z\theta\theta^{(1,0)}w^{(1,2)} + x_a m_W\theta u^{(0,2)}u^{(2,0)} +$$
$$I_x u^{(1,1)}w^{(1,1)}u^{(2,0)} + I_y u^{(1,1)}w^{(1,1)}u^{(2,0)} - I_z u^{(1,1)}w^{(1,1)}u^{(2,0)} +$$
$$I_x w^{(1,0)}u^{(1,2)}u^{(2,0)} +$$
$$\left(\int_{l_w}^{y}\left(-\frac{1}{2}\left(\int_0^y\left(2u^{(1,1)^2} + 2w^{(1,1)^2} + 2u^{(1,0)}u^{(1,2)} +\right.\right.\right.\right.$$
$$\left.\left.\left.\left.2w^{(1,0)}w^{(1,2)}\right)dy\right)m_W + x_a m_W\theta^{(0,1)^2}u^{(1,0)} + x_a m_W\theta\theta^{(0,2)}u^{(1,0)} +\right.\right.$$
$$x_a m_W\theta^{(0,2)}w^{(1,0)} + 2x_a m_W\theta\theta^{(0,1)}u^{(1,1)} + 2x_a m_W\theta^{(0,1)}w^{(1,1)} +$$
$$2x_a m_W w^{(1,0)}u^{(1,1)}w^{(1,1)} + x_a m_W u^{(1,0)}w^{(1,1)^2} - x_a m_W u^{(1,2)} +$$
$$\left.\frac{1}{2}x_a m_W\theta^2 u^{(1,2)} + \frac{1}{2}x_a m_W w^{(1,0)^2}u^{(1,2)} + x_a m_W\theta w^{(1,2)} +\right.$$
$$\left.x_a m_W u^{(1,0)}w^{(1,0)}w^{(1,2)}\right)dy\Bigg)w^{(2,0)} + x_a m_W\theta w^{(0,2)}w^{(2,0)} +$$
$$2D_{11}\theta^{(1,0)^2}w^{(2,0)} - 2D_{33}\theta^{(1,0)^2}w^{(2,0)} + I_x u^{(1,1)^2}w^{(2,0)} +$$
$$I_x w^{(1,1)^2}w^{(2,0)} + I_x u^{(1,0)}u^{(1,2)}w^{(2,0)} + 2I_x w^{(1,0)}w^{(1,2)}w^{(2,0)} -$$
$$2D_{11}u^{(2,0)^2}w^{(2,0)} - D_{22}u^{(2,0)^2}w^{(2,0)} + D_{33}u^{(2,0)^2}w^{(2,0)} - D_{11}w^{(2,0)^3} -$$
$$D_{11}u^{(2,0)}\theta^{(2,0)} - D_{22}u^{(2,0)}\theta^{(2,0)} + D_{33}u^{(2,0)}\theta^{(2,0)} + 2D_{11}\theta w^{(2,0)}\theta^{(2,0)} -$$
$$2D_{33}\theta w^{(2,0)}\theta^{(2,0)} + I_x x\theta^{(0,1)}u^{(2,1)} + I_y\theta^{(0,1)}u^{(2,1)} - I_z\theta^{(0,1)}u^{(2,1)} +$$
$$2I_x w^{(1,0)}u^{(1,1)}u^{(2,1)} + I_x u^{(1,0)}w^{(1,1)}u^{(2,1)} + I_y u^{(1,0)}w^{(1,1)}u^{(2,1)} -$$
$$I_z u^{(1,0)}w^{(1,1)}u^{(2,1)} - 2I_x\theta\theta^{(0,1)}w^{(2,1)} + 2I_z\theta\theta^{(0,1)}w^{(2,1)} +$$
$$I_x u^{(1,0)}u^{(1,1)}w^{(2,1)} + I_y u^{(1,0)}u^{(1,1)}w^{(2,1)} - I_z u^{(1,0)}u^{(1,1)}w^{(2,1)} +$$
$$2I_x w^{(1,0)}w^{(1,1)}w^{(2,1)} + I_x\theta u^{(2,2)} - I_z\theta u^{(2,2)} + I_x u^{(1,0)}w^{(1,0)}u^{(2,2)} +$$
$$I_x w^{(2,2)} - I_x\theta^2 w^{(2,2)} + I_z\theta^2 w^{(2,2)} + I_x w^{(1,0)^2}w^{(2,2)} - 2D_{11}\theta^{(1,0)}u^{(3,0)} -$$
$$D_{22}\theta^{(1,0)}u^{(3,0)} + 2D_{33}\theta^{(1,0)}u^{(3,0)} - 3D_{11}w^{(1,0)}u^{(2,0)}u^{(3,0)} -$$

$$2D_{11}u^{(1,0)}w^{(2,0)}u^{(3,0)} - D_{22}u^{(1,0)}w^{(2,0)}u^{(3,0)} + D_{33}u^{(1,0)}w^{(2,0)}u^{(3,0)} + 4D_{11}\theta\theta^{(1,0)}w^{(3,0)} - 4D_{33}\theta\theta^{(1,0)}w^{(3,0)} - D_{11}u^{(1,0)}u^{(2,0)}w^{(3,0)} - D_{22}u^{(1,0)}u^{(2,0)}w^{(3,0)} + D_{33}u^{(1,0)}u^{(2,0)}w^{(3,0)} - 4D_{11}w^{(1,0)}w^{(2,0)}w^{(3,0)} - D_{11}\theta u^{(4,0)} + D_{33}\theta u^{(4,0)} - D_{11}u^{(1,0)}w^{(1,0)}u^{(4,0)} - D_{11}w^{(4,0)} + D_{11}\theta^2 w^{(4,0)} - D_{33}\theta^2 w^{(4,0)} - D_{11}{w^{(1,0)}}^2 w^{(4,0)} = -q_3 \quad 2.60$$

Equations 2.58, 2.59 and 2.60 represent the nonlinear equations of motion of the elastic wing which consider geometric nonlinearities up to the third order. For sake of simplicity the structural damping is assumed to be linear. The external loads acting on the wing, q_1, q_3 and q_5, can be an imposed load, which do not depend of the deformation of wing, such as the one transferred during a shaker test, or a load which depend of the generalized coordinates of the wing that changes with the wing deformation, such as the aerodynamic loads, or both, such as in the case of a wing undergoing forced oscillations by a discrete gust. The aerodynamic model will be treated more in detail into the next sections.

Some further considerations on the way of writing the equations of motion might be done by reflecting on the type of problems which are going to be analyzed. Pai explains in [4] that several derivations are possible, depending on the specific behavior we are interested in representing. To treat beam-like structures that undergo rigid-elastic deformations in *ZY* plane, Figure 2, the variation of the virtual angle $\delta\theta_2$, in Eqs. 2.47 and 2.54, may be written with respect to the variation of the Euler angle $\delta\theta[y,t]$ as:

$$\delta\theta_2 = \delta\theta[y,t] + u^{(1,0)}[y,t]\delta w^{(1,0)}[y,t] \quad 2.61$$

substituting Equation 2.61 into Equations 2.47 a number of additional terms are obtained and should be added to the out of plane bending equation. These are:

$$x_a m_W u^{(0,2)} u^{(1,0)} \theta^{(1,0)} + \frac{1}{2} x_a \left(\int_0^y (2u^{(1,1)^2} + 2w^{(1,1)^2} + 2u^{(1,0)} u^{(1,2)} + 2w^{(1,0)} w^{(1,2)}) \, dy \right) m_W u^{(1,0)^2} \theta^{(1,0)} - c_5 u^{(1,0)} \theta^{(1,1)} + x_a m_W \theta u^{(1,0)} u^{(1,2)} + x_a m_W u^{(1,0)} w^{(1,2)} - I_y u^{(1,0)} \theta^{(1,2)} + q_5 u^{(2,0)} - c_5 \theta^{(0,1)} u^{(2,0)} + x_a m_W \theta u^{(0,2)} u^{(2,0)} + x_a m_W w^{(0,2)} u^{(2,0)} - I_y \theta^{(0,2)} u^{(2,0)} + x_a \left(\int_0^y (2u^{(1,1)^2} + 2w^{(1,1)^2} + 2u^{(1,0)} u^{(1,2)} + 2w^{(1,0)} w^{(1,2)}) \, dy \right) m_W \theta u^{(1,0)} u^{(2,0)} + \frac{1}{2} xa \left(\int_0^y (2u^{(1,1)^2} + 2w^{(1,1)^2} + 2u^{(1,0)} u^{(1,2)} + 2w^{(1,0)} w^{(1,2)}) \, dy \right) m_W w^{(1,0)} u^{(2,0)} + I_x u^{(1,1)} w^{(1,1)} u^{(2,0)} - I_y u^{(1,1)} w^{(1,1)} u^{(2,0)} - I_z u^{(1,1)} w^{(1,1)} u^{(2,0)} - 2I_y u^{(1,0)} w^{(1,2)} u^{(2,0)} + \frac{1}{2} x_a \left(\int_0^y (2u^{(1,1)^2} + 2w^{(1,1)^2} + 2u^{(1,0)} u^{(1,2)} + 2w^{(1,0)} w^{(1,2)}) \, dy \right) m_W u^{(1,0)} w^{(2,0)} - D_{11} u^{(2,0)^2} w^{(2,0)} + D_{22} u^{(2,0)^2} w^{(2,0)} + D_{33} u^{(2,0)^2} w^{(2,0)} + D_{22} u^{(2,0)} \theta^{(2,0)} + I_x u^{(1,0)} w^{(1,1)} u^{(2,1)} - I_y u^{(1,0)} w^{(1,1)} u^{(2,1)} - I_z u^{(1,0)} w^{(1,1)} u^{(2,1)} + I_x u^{(1,0)} u^{(1,1)} w^{(2,1)} - I_y u^{(1,0)} u^{(1,1)} w^{(2,1)} - I_z u^{(1,0)} u^{(1,1)} w^{(2,1)} - I_y u^{(1,0)^2} w^{(2,2)} - D_{11} u^{(1,0)} w^{(2,0)} u^{(3,0)} + D_{22} u^{(1,0)} w^{(2,0)} u^{(3,0)} + D_{33} u^{(1,0)} w^{(2,0)} u^{(3,0)} - D_{11} u^{(1,0)} u^{(2,0)} w^{(3,0)} + 3D_{22} u^{(1,0)} u^{(2,0)} w^{(3,0)} + D_{33} u^{(1,0)} u^{(2,0)} w^{(3,0)} + D_{22} u^{(1,0)} \theta^{(3,0)} + D_{22} u^{(1,0)^2} w^{(4,0)}$$

2.62

These terms included into Equation 2.62 are added to Equation 2.60 for the numerical representation of the wing dynamical problems. The choice of writing the variation of the virtual angle as a function of the variation of the Euler angle is simply a matter of style, the representations are both

corrects, what changes is the interpretation of the angle. The equations of motion reported in this paragraph have been derived using Mathematica®.

2.2 Comparison with other mathematical models

The equations of motion, 2.58, 2.59 and 2.60, agree with those proposed by Pai [1], Crespo Da Silva [2] and Kim [3]. They are assumed as the reference models for this work, however there are some differences which deserve to be highlighted for sake of correctness and to better appreciate the effort made in the derivation *ex novo* of these equations. The equations of motion derived in Chapter 2 are based on the nonlinear 3-D Euler-Bernoulli beam theory [1]. 3-D because they include not only the in-plane and out of plane bending motions but also the torsional motion. The 3-D Euler-Bernoulli beam model, which assumes: the beam cross section infinitely rigid in its own plane, plane cross section after deformation and normal to the deformed axis of the beam, the rate of twist uniform along the beam, it is justified when dealing with structure which have one dimension much larger than the other two; such as slender wing. Experimental observations show that these assumptions are reasonable for slender structures made of isotropic materials with solid cross sections subjected to extension, bending and torsional deformations. When one or more of these conditions are not met, the classical beam model derived based on these assumptions may be inaccurate. For the purposes of our investigations and for the study cases analyzed the 3-D Euler-Bernoulli beam model represents a good compromise between the reliability of the results and the complexity of the model. Furthermore Eqs. 2.58, 2.59 and 2.60 refer to an initially straight beam. The current approach to treat slender wings undergoing aeroelastic disturbances is not a novel solution, many are the works available in literature based on it, [11] ,[12], [13], [14], [15], [16]. All these works, on the dynamical response of slender wings,

refer to a set of equations of motion perfectly comparable to those proposed by Pai [1] or in Crespo Da Silva [2] for an initially straight nonlinear beam. Kim [3] propose a model which considers the gravity center of the beam not coincident with the shear center, while Pai [1] and Crespo Da Silva [2] assume these to be coincident. The final representation of the equation of motion is not unique as it can be appreciated by a direct comparison of each terms in the equation of motions from [1], [2], [3] with Eqs. 2.58, 2.59 and 2.60. Pai [1] assumes the inertial moments of order 2 therefore his equations contain only the inertial terms which depend of the degree of freedom at the first order. All the higher order inertial terms are discarded. Crespo Da Silva [2], instead, includes these terms but compared to those of Equations 2.58, 2.59 and 2.60 a few are still missing. As an example in Equation 2.59, the in plane bending equation, Crespo includes all terms with the exceptions of those which represent the mismatch between the gravity center and the shear center and other inertial terms which are listed hereafter:

$$2I_z u^{(1,0)}[y,t]u^{(1,2)}[y,t]u^{(2,0)}[y,t] + I_x w^{(1,0)}[y,t]w^{(1,2)}[y,t]u^{(2,0)}[y,t] + I_x u^{(1,0)}[y,t]w^{(1,2)}[y,t]w^{(2,0)}[y,t] + I_z u^{(1,0)}[y,t]^2 u^{(2,2)}[y,t] + I_x u^{(1,0)}[y,t]w^{(1,0)}[y,t]w^{(2,2)}[y,t] \quad 2.63$$

The stiffness terms are all included. On the reason why these inertial terms are not included into the in-plane equation of motion by Crespo Da Silva it is very difficult to speculate therefore the only worthy thing to do is to highlight the differences between the two mathematical models. The same conclusion may be done on the out of plane bending equation which is not reported here for the sake of brevity. The torsion equation instead presented by Crespo Da Silva is equivalent to Equation 2.59 except for the terms which include the mismatch between shear center and gravity center, which in Crespo Da Silva have not been accounted for. A more refined version of

the equations of motion, based on the asymptotic reduction procedure is presented in Paragraph 2.3. This last set of equations, obtained through a proper reduction procedure, are those numerically implemented in Matlab®, after the being reduced according to Paragraph 2.3, and used for the numerical simulations of Chapters 3, 4 and 5.

2.3 Numerically derived asymptotic form of the equations of motion.

The equations of motion such as they are presented in Paragraphs 2.1 and 2.2 are very long and not all the terms are really useful for the problems analysis. However what is very important to understand is that the relevance of one term with to respect to the others, in the equations of motion, strictly depends on the characteristics of the model that has to be analyzed. As shown in Table 1 all the wings that have been studied for the PhD research activity have similar parameters, therefore the reduction procedure, which depends on the weight of each term, is the same. This means that it is possible to extract a unique set of equations of motion valid to treat all these wing configurations. If the parameters reported in Table 1 change, the reduced set of equations have to be reviewed.

Table 1 Reduced wing parameters and order of magnitude.

Wing parameters	Wing data of Chapters 3 and 4	Wing data of Chapter 5	Wing data of Chapter 6	Order of smallness
c/l	0.225	0.088123	0.257143	$\varepsilon^{0.5}$
$\frac{c}{r}=\frac{c}{\sqrt{I/m_w}}$	1.652	2.740144	4.126982	ε^{0}
x_a/l	0	0	0.015057	ε^{1}
D_{11}/D_{33}	0.023	0.010333	0.001	ε^{1}
D_{22}/D_{11}	0.008	1.016129	1.931915	ε^{0}
D_{22}/D_{33}	0.0002	0.0105	0.001932	ε^{1}
$\frac{1}{k}=\frac{2U}{\omega c}$	10.07	2.96764	5.551094	$\varepsilon^{-0.5}$
$\frac{\rho c^2}{m_w}$	0.045	0.117823	0.133845	$\varepsilon^{0.5}$

The reduction procedure is based on previous works [5], [6], [20], [21] and extended to beam wise structures [22], to which the author remand for a more exhaustive explanation of the procedure. The key point is to assume the maximum strain developed in classical materials as the reference infinitesimal parameter. All other variables and coefficients are scaled accordingly. The variables are assumed of a certain order of smallness, ε^{α}, and the final order of each term in the equation is compared to the others. The loading configuration drives the reduction, which means that in order to guarantee a balance into the equations it will be the term related to aerodynamic load what gives the main order of magnitude. The variation of the variable along the longitudinal direction is assumed of order 0, therefore the derivatives are of order of the variable itself (in certain cases there might be an influence of the order of derivative which is not considered in this work). The variation of the solution inside the system is not considered or it is assumed of order zero. In order to understand which terms are fundamental and so which to retain into the equations of motions, these last have to be rewritten in a non dimensional form. It will lead to a easier identification of the driving terms. The nonlinear inertial terms, including so the rotational inertia, can be discarded a priori from the equations because they are higher order terms and in the cases of small perturbations do not influence the response of the wing. The same assumption was made by Pai [1], Crespo Da Silva [2] and Kim [3]. The aerodynamic loads are assumed linear because in none of the studied conditions the pitch angle reached values which could justify the introduction of the dynamic stall model into the equations of motion. The non dimensional equations of motion are obtained and by substituting the following geometric parameters into Eqs.2.59, 2.60, 2.61, 2.62, simplified by the assumption made over the inertial terms: $\zeta = \frac{x}{l}$, $\bar{w} = \frac{w}{l}$, $\bar{u} = \frac{u}{l}$,

$\frac{dz}{dx} = \frac{1}{l}\frac{dz}{d\zeta}$, $\bar{u} = \bar{u}(\zeta)\, sin\, \omega t$, $\bar{w} = \bar{w}(\zeta) \sin \omega t$, $\bar{\theta} = \bar{\theta}(\zeta)\, sin\, \omega t$, and by dividing all the terms of the in-plane and out of plane equations by $\omega^2 * m_W * l$ and the torsion equation by $\omega^2 * I_y * l^2$:

In-plane Bending

$$-\frac{c_1}{\omega * m_W}\bar{u}^{(0,1)} + \frac{x_a}{l}\theta^{(0,1)^2} + \underline{\bar{u}} - \frac{x_a}{l}\theta^2 + 2\frac{x_a}{l}\bar{u}^{(1,1)^2} + \frac{x_a}{l}\bar{w}^{(1,1)^2} + \frac{x_a}{l}\bar{u}\bar{u}^{(2,0)} + \frac{2\,D_{33}}{\omega^2 * m_W * l^4}\left(1 - \frac{D_{11}}{D_{33}}\right)\theta^{(1,0)^2}\bar{u}^{(2,0)} - \frac{D_{33}}{\omega^2 * m_W * l^4}\bar{u}^{(2,0)^3} + \frac{x_a}{l}\bar{w}\bar{w}^{(2,0)} + \frac{D_{11}}{\omega^2 * m_W * l^4}\left(\frac{D_{22}}{D_{11}} - 1\right)\bar{u}^{(2,0)}\bar{w}^{(2,0)^2} + \frac{2\,D_{33}}{\omega^2 * m_W * l^4}\left(1 - \frac{D_{11}}{D_{33}}\right)\theta\bar{u}^{(2,0)}\theta^{(2,0)} + \frac{D_{33}}{\omega^2 * m_W * l^4}\left(-\frac{D_{11}}{D_{33}} + \frac{D_{22}}{D_{33}} + \underline{1}\right)\bar{w}^{(2,0)}\theta^{(2,0)} - \frac{I_z}{m_W * l^2}\bar{u}^{(2,0)} + \frac{4\,D_{33}}{\omega^2 * m_W * l^4}\left(1 - \frac{D_{11}}{D_{33}}\right)\theta\theta^{(1,0)}\bar{u}^{(3,0)} - \frac{4D_{33}}{\omega^2 * m_W * l^4}\bar{u}^{(1,0)}\bar{u}^{(2,0)}\bar{u}^{(3,0)} + \frac{D_{33}}{\omega^2 * m_W * l^4}\left(\underline{2} - 2\frac{D_{11}}{D_{33}} + \frac{D_{22}}{D_{33}}\right)\theta^{(1,0)}\bar{w}^{(3,0)} + \frac{4D_{11}}{\omega^2 * m_W * l^4}\left(\frac{D_{22}}{2D_{11}} - 1\right)\bar{w}^{(1,0)}\bar{u}^{(2,0)}\bar{w}^{(3,0)} - \underline{\underline{\frac{D_{33}}{\omega^2 * m_W * l^4}}}\bar{u}^{(4,0)} + \frac{D_{33}}{\omega^2 * m_W * l^4}\left(1 - \frac{D_{11}}{D_{33}}\right)\theta^2\bar{u}^{(4,0)} - \frac{D_{33}}{\omega^2 * m_W * l^4}\bar{u}^{(1,0)^2}\bar{u}^{(4,0)} + \frac{D_{33}}{\omega^2 * m_W * l^4}\left(\underline{1} - \frac{D_{11}}{D_{33}}\right)\theta\bar{w}^{(4,0)} - \frac{D_{11}}{\omega^2 * m_W * l^4}u^{(1,0)}\bar{w}^{(1,0)}\bar{w}^{(4,0)} = \underline{\underline{-\frac{q_1}{\omega^2 * m_W * l}}} \qquad 2.64$$

Bending out-of-plane

$$-\frac{c_3}{\omega * m_W}\bar{w}^{(0,1)} + \underline{\bar{w}} - \frac{x_a}{l}\theta + \frac{2D_{11}}{\omega^2 * m_W * l^4}\left(1 - \frac{D_{33}}{\underline{D_{11}}}\right)\theta^{(1,0)^2}\bar{w}^{(2,0)} + \frac{D_{11}}{\omega^2 * m_W * l^4}\left(-2 - \frac{D_{22}}{D_{11}} + \frac{D_{33}}{D_{11}}\right)\bar{u}^{(2,0)^2}\bar{w}^{(2,0)} - \frac{D_{11}}{\omega^2 * m_W * l^4}\bar{w}^{(2,0)^3} + \frac{D_{11}}{\omega^2 * m_W * l^4}\left(-1 - \frac{D_{22}}{D_{11}} + \frac{D_{33}}{\underline{D_{11}}}\right)\bar{u}^{(2,0)}\theta^{(2,0)} + \frac{2D_{11}}{\omega^2 * m_W * l^4}\left(1 - \frac{D_{33}}{\underline{D_{11}}}\right)\theta\bar{w}^{(2,0)}\theta^{(2,0)} - \frac{Ix}{m_W * l^2}\bar{w}^{(2,0)} + \frac{D_{11}}{\omega^2 * m_W * l^4}\left(-2 - \frac{D_{22}}{D_{11}} +\right.$$

$$2\frac{D_{33}}{D_{11}}\Big)\theta^{(1,0)}\bar{u}^{(3,0)} - \frac{3D_{11}}{\omega^2*m_W*l^4}\bar{w}^{(1,0)}\bar{u}^{(2,0)}\bar{u}^{(3,0)} + \frac{D_{11}}{\omega^2*m_W*l^4}\Big(-2 - \frac{D_{22}}{D_{11}} +$$

$$\frac{D_{33}}{D_{11}}\Big)\bar{u}^{(1,0)}\bar{w}^{(2,0)}\bar{u}^{(3,0)} + \frac{4D_{11}}{\omega^2*m_W*l^4}\left(1 - \frac{D_{33}}{D_{11}}\right)\theta\theta^{(1,0)}\bar{w}^{(3,0)} +$$

$$\frac{D_{11}}{\omega^2*m_W*l^4}\Big(-1 - \frac{D_{22}}{D_{11}} + \frac{D_{33}}{D_{11}}\Big)\bar{u}^{(1,0)}\bar{u}^{(2,0)}\bar{w}^{(3,0)} -$$

$$\frac{4D_{11}}{\omega^2*m_W*l^4}\bar{w}^{(1,0)}\bar{w}^{(2,0)}\bar{w}^{(3,0)} + \frac{D_{11}}{\omega^2*m_W*l^4}\left(-1 + \frac{D_{33}}{D_{11}}\right)\theta\bar{u}^{(4,0)} -$$

$$\frac{D_{11}}{\omega^2*m_W*l^4}\bar{u}^{(1,0)}\bar{w}^{(1,0)}\bar{u}^{(4,0)} - \frac{D_{11}}{\omega^2*m_W*l^4}\bar{w}^{(4,0)} + \frac{D_{11}}{\omega^2*m_W*l^4}\Big(1 -$$

$$\frac{D_{33}}{D_{11}}\Big)\theta^2\bar{w}^{(4,0)} - \frac{D_{11}}{\omega^2*m_W*l^4}\bar{w}^{(1,0)^2}\bar{w}^{(4,0)} - \frac{x_a}{l}\bar{u}^{(1,0)}\bar{w}^{(1,0)} - \frac{x_a}{l}\bar{w}\bar{u}^{(2,0)} +$$

$$\frac{D_{11}}{\omega^2*m_W*l^4}\Big(-1 + \frac{D_{22}}{D_{11}} + \frac{D_{33}}{D_{11}}\Big)\bar{u}^{(2,0)^2}\bar{w}^{(2,0)} + \frac{D_{22}}{\omega^2*m_W*l^4}\bar{u}^{(2,0)}\theta^{(2,0)} +$$

$$\frac{D_{11}}{\omega^2*m_W*l^4}\Big(-1 + \frac{D_{22}}{D_{11}} + \frac{D_{33}}{D_{11}}\Big)\bar{u}^{(1,0)}\bar{w}^{(2,0)}\bar{u}^{(3,0)} + \frac{D_{11}}{\omega^2*m_W*l^4}\Big(-1 + 3\frac{D_{22}}{D_{11}} +$$

$$\frac{D_{33}}{D_{11}}\Big)\bar{u}^{(1,0)}\bar{u}^{(2,0)}\bar{w}^{(3,0)} + \frac{D_{22}}{\omega^2*m_W*l^4}\bar{u}^{(1,0)}\theta^{(3,0)} + \frac{D_{22}}{\omega^2*m_W*l^4}\bar{u}^{(1,0)^2}\bar{w}^{(4,0)} =$$

$$-\frac{q_3}{\omega^2*m_W*l} \qquad 2.65$$

Torsion

$$-\frac{c_5}{\omega*I_y*l^2}\theta^{(0,1)} - \frac{x_a m_W}{I_y*l}\theta\bar{u} - \frac{x_a m_W}{I_y*l}\bar{w} + \underline{\underline{\theta}} +$$

$$\frac{D_{22}}{\omega^2*I_y*l^4}\Big(-\frac{D_{11}}{D_{22}} + \frac{D_{33}}{D_{22}}\Big)\theta\bar{u}^{(2,0)^2} + \frac{D_{22}}{\omega^2*I_y*l^4}\left(-\frac{D_{11}}{D_{22}} + 1 + \frac{D_{33}}{D_{22}}\right)\bar{u}^{(2,0)}\bar{w}^{(2,0)} +$$

$$\frac{D_{22}}{\omega^2*I_y*l^4}\left(\frac{D_{11}}{D_{22}} - \frac{D_{33}}{D_{22}}\right)\theta\bar{w}^{(2,0)^2} + \frac{D_{22}}{\omega^2*I_y*l^4}\theta^{(2,0)} + \frac{D_{22}}{\omega^2*I_y*l^4}\bar{u}^{(1,0)}\bar{w}^{(3,0)} =$$

$$-\frac{q_5}{\omega^2*I_y*l^2} \qquad 2.66$$

Defining the following structural parameters: ${\omega_F}^2 = \frac{D_{11}}{m_w * l^4}$, ${\omega_L}^2 = \frac{D_{33}}{m_w * l^4}$, ${\omega_T}^2 = \frac{D_{22}}{I_y * l^2}$, $\mathrm{r}^2 = \frac{\mathrm{I}}{\mathrm{m_w}}$, where the subscripts indicate respectively the proper flap, lag and torsion frequencies, and the order of smallness of some ratios, such as $\frac{{\omega_{F,L,T}}^2}{\omega^2} = \varepsilon^0$, $\frac{c_i}{\omega * m_w} = \varepsilon^{1.5}$, $\frac{c_i}{\omega * I_y * l^2} = \varepsilon^1$, together with those reported in Table 1, it is possible to identify the main terms into the equations. However in order to do that, as previously mentioned, the order of smallness of the aerodynamic loads has to be defined. It depends of the loading condition, in fact it is straightforwardly understandable that when the load is applied at the shear center the pitch moment will be lower and consequently the pitch deformation. Considering two loading conditions: 1) the vertical load applied at the shear center, and 2) the vertical load applied at the aerodynamic center. When the load is applied at the aerodynamic center there will be and additional pitch moment due to the lift per the distance between aerodynamic center and shear center. Therefore, if the load is applied at the shear center (SC) $\frac{q_1}{\omega^2 * m_W * l} = \varepsilon^{0.5}$, $\frac{q_1}{\omega^2 * m_W * l} = \varepsilon^{1.5}$, $\frac{q_5}{\omega^2 * I_y * l^2} = \varepsilon^1$, while if the load is applied at the aerodynamic center (AC) $\frac{q_1}{\omega^2 * m_W * l} = \varepsilon^{0.5}$, $\frac{q_1}{\omega^2 * m_W * l} = \varepsilon^{1.5}$, $\frac{q_5}{\omega^2 * I_y * l^2} = \varepsilon^{0.5}$. The fact of having a different order of smallness for the pitch moment, influences the order of smallness of the pitch variable and so of all the terms which include the pitch variable in it. Therefore, if the load is applied at the shear center: $\theta = \varepsilon^1$, $\bar{u} = \varepsilon^{1.5}$, $\bar{w} = \varepsilon^{0.5}$, while if it is applied to the aerodynamic center: $\theta = \varepsilon^{0.5}$, $\bar{u} = \varepsilon^1$, $\bar{w} = \varepsilon^{0.5}$. The main terms for both loading conditions are identified directly into equations 2.64, 2.65 and 2.66, by a double line under the terms when they are important for both conditions and a single line when they are relevant only for the case of the load applied at the aerodynamic center. What comes out from Eqs. 2.64, 2.65

and 2.66 is that in-plane and torsion equations of motion are not influenced by the load application point while the out of plane equation yes. The fundamental terms are those underlined, which doesn't mean that if also the others are included it is an error. What is important is that, for wing configurations comparables to those here analyzed, the underlined terms are not discarded. The effect of neglecting some of the main nonlinear terms into the equations is showed by numerical results in Chapter 4. What follow are the equations of motion such as they are used for the numerical simulation presented in the next chapters.

In-plane Bending

$$-m_W u^{(0,2)} - D_{11} w^{(2,0)} \theta^{(2,0)} + D_{22} w^{(2,0)} \theta^{(2,0)} + D_{33} w^{(2,0)} \theta^{(2,0)} + I_z u^{(2,2)} - 2D_{11} \theta^{(1,0)} w^{(3,0)} + D_{22} \theta^{(1,0)} w^{(3,0)} + 2D_{33} \theta^{(1,0)} w^{(3,0)} - D_{33} u^{(4,0)} - D_{11} \theta w^{(4,0)} + D_{33} \theta w^{(4,0)} = -q_1 \quad 2.67$$

Bending out-of-plane

$$-m_W w^{(0,2)} + x_a m_W \theta^{(0,2)} - D_{11} u^{(2,0)} \theta^{(2,0)} - D_{22} u^{(2,0)} \theta^{(2,0)} + D_{33} u^{(2,0)} \theta^{(2,0)} + I_x w^{(2,2)} - 2D_{11} \theta^{(1,0)} u^{(3,0)} - D_{22} \theta^{(1,0)} u^{(3,0)} + 2D_{33} \theta^{(1,0)} u^{(3,0)} + 4D_{11} \theta \theta^{(1,0)} w^{(3,0)} - 4D_{33} \theta \theta^{(1,0)} w^{(3,0)} - 4D_{11} w^{(1,0)} w^{(2,0)} w^{(3,0)} - D_{11} \theta u^{(4,0)} + D_{33} \theta u^{(4,0)} - D_{11} w^{(4,0)} + D_{11} \theta^2 w^{(4,0)} - D_{33} \theta^2 w^{(4,0)} + D_{22} u^{(2,0)} \theta^{(2,0)} + 2D_{11} \theta w^{(2,0)} \theta^{(2,0)} - 2D_{33} \theta w^{(2,0)} \theta^{(2,0)} + 2D_{11} {\theta^{(1,0)}}^2 w^{(2,0)} - 2D_{33} {\theta^{(1,0)}}^2 w^{(2,0)} = -q_3 \quad 2.68$$

Torsion

$$x_a m_W w^{(0,2)} - I_y \theta^{(0,2)} - D_{11} \theta {u^{(2,0)}}^2 + D_{33} \theta {u^{(2,0)}}^2 - D_{11} u^{(2,0)} w^{(2,0)} + D_{22} u^{(2,0)} w^{(2,0)} + D_{33} u^{(2,0)} w^{(2,0)} + D_{11} \theta {w^{(2,0)}}^2 - D_{33} \theta {w^{(2,0)}}^2 + D_{22} \theta^{(2,0)} + D_{22} u^{(1,0)} w^{(3,0)} = -q_5 \quad 2.69$$

Eqs. 2.67, 2.68 and 2.69 have to be kept as references for the analysis that follow.

2.4 Aerodynamic model

To study the aeroelastic response of slender wings, for several wing configurations, a proper aerodynamic model, able to work in and off the critical flutter condition, has to be identified and combined with the structural model into Eqs. 2.67, 2.68 and 2.69, in order to obtain the final aeroelastic model. The aerodynamic forces are written as a function of the wing's degree of freedom and change coherently with the wing elastic deformation. Dealing with high aspect ratio wings, the effect of the finite wing length, known as free vortices, may be neglected, such as the effect of the air compressibility because of the low speed range experienced in the current study. Based on this assumptions the unsteady aerodynamic forces are calculated according to thin airfoil theory, therefore the unsteady flow is composed of a non circulatory part, expressed trough sources and sinks, and a circulatory part related to the flat vorticity surface which extends from the trailing edge to infinity. The first limitation of this theory is caused by the wing stall, since the magnitude of the circulation cannot be predicted theoretically when the angle of attack exceeds a certain limit, because the flow separate from the surfaces. In order to account for the stall effect a proper stall model needs to be introduced into the equations of motion. A mathematical representation of the stall model is presented at the end of this paragraph. The first to derive the unsteady aerodynamic forces, based on the thin airfoil theory, due to small perturbations, which implies a flat wake behind the airfoil extending to infinity, was Theodorsen [17]. The airfoil motion was restricted to be harmonic. This assumption allowed the vortex sheet extending from the trailing edge to infinity to be integrated, leading to a solution in the form of Bessel functions. Through this solution, Theodorsen, showed that the lift due to circulation was a function of the reduced frequency. Theodorsen’s function is useful in

describing the effect of the wake on the airloads as a function of reduced frequency. Garrick extended Theodorsen theory to develop the thrust force generated by a flat plate in unsteady flow [18], while Wagner solved the problem of an airfoil that is initially at rest and started abruptly, by introducing the concept of theoretical aerodynamic indicial functions [8]. In this approach, the variations with time of the angle of attack and angular velocity are replaced by a large number of small instantaneous steps changes. The transient aerodynamic reactions to a large number of small instantaneous step changes are termed "indicial functions" [7]. This formulation is suitable to treat dynamical problems in time domain, which is very useful when looking at nonlinear aeroelasticity. Therefore the main advantages of the Wagner formulation, or of other more complex time domain formulations, is that it allows to study the system response even when it is not the purely simple harmonic one.

An approximate expression for the Wagner's function [9] is given by:

$$\Theta(t) = 1 - \psi_1 e^{-\varepsilon_1 \frac{Ut}{b}} - \psi_2 e^{-\varepsilon_2 \frac{Ut}{b}} \qquad 2.70$$

where $\psi_1 = 0.165,\ \psi_2 = 0.335,\ \varepsilon_1 = 0.0455,\ \varepsilon_2 = 0.3.$ The time variation of the lift coefficient, expressed in terms of the Wagner function, is as follows:

$$c_l(t) = 2\pi\alpha\Theta(t) \qquad 2.71$$

The corresponding lift force variation becomes:

$$L(t) = \rho\pi U^2 c\alpha\Theta(t) = \pi\rho U c U_{DW}\Theta(t) \qquad 2.72$$

where $U_{DW} = U\alpha$ denotes the downwash velocity. The Wagner's function predicts the lift after a sudden step-change in the airfoil angle of attack, as shown in Figure 3.

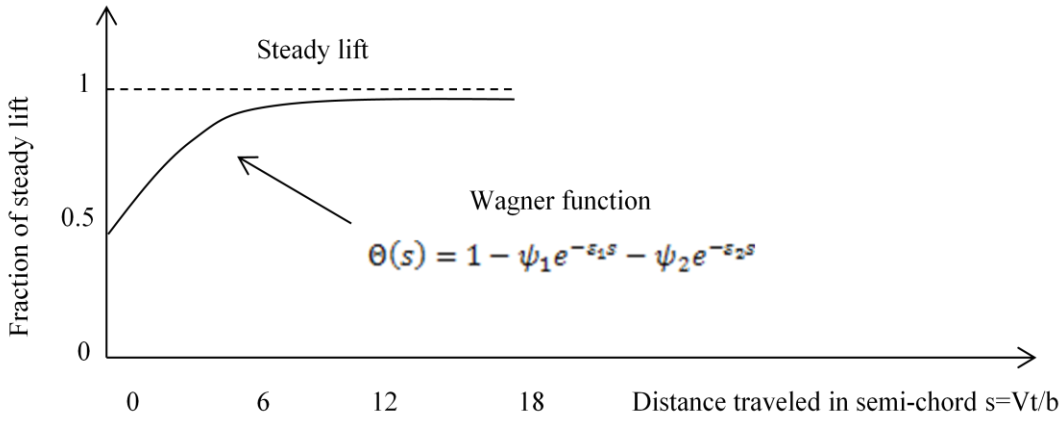

Figure 3 Wagner function evolution

Assuming the unsteady motion as a superposition of many small impulsive changes in angle of attack, the lift variation at all time due to a small change in pitch angle at time t_0 is:

$$L_C(t) = \rho\pi Uc \int_{-\infty}^{t} \Theta(t - t_0) \frac{dU_{DW}(t_0)}{dt_0} dt_0 \qquad 2.73$$

For a motion starting at $t = 0$ the lift generated at negative times is:

$$L_C(t)|_{t_0<0} = \rho\pi Uc \int_{-\infty}^{0} \Theta(t - t_0) \frac{dU_{DW}(t_0)}{dt_0} dt_0 = \pi\rho Uc\Theta(t)U_{DW}(0) \qquad 2.74$$

Therefore the lift at all time, after integration by parts, is:

$$L_C(t) = \pi\rho Uc \left(U\theta[y,t] + w[y,t]^{(0,1)} + \left(\frac{3}{4}c - x_f\right)\theta[y,t]^{(0,1)}\right)\Theta(0) - \pi\rho Uc \int_0^t \frac{\partial\Theta(t-t_0)}{\partial t_0}\left(U\theta[y,t_0] + w[y,t_0]^{(0,1)} + \left(\frac{3}{4}c - x_f\right)\theta[y,t_0]^{(0,1)}\right) dt_0 \qquad 2.75$$

Expanding by parts the integral of Equation 2.75 and substituting in it the added aerodynamic states $w_i[y,t]$, defined as:

$$w_1[y,t] = \int_0^t e^{-\varepsilon_1 {}^{U(t-t_0)}/_b} w[y,t_0] dt_0$$

$$w_2[y,t] = \int_0^t e^{-\varepsilon_2 {}^{U(t-t_0)}/_b}\, w[y,t_0]dt_0$$

$$w_3[y,t] = \int_0^t e^{-\varepsilon_1 {}^{U(t-t_0)}/_b}\, \theta[y,t_0]dt_0$$

$$w_4[y,t] = \int_0^t e^{-\varepsilon_1 {}^{U(t-t_0)}/_b}\, \theta[y,t_0]dt_0 \qquad 2.76$$

The circulatory component of the lift takes the form of equation 2.76.

$$L_C(t) = \pi\rho Uc\Theta(0)\left[U\theta[y,t] + \left(\frac{3}{4}c - x_f\right)\theta[y,t]^{(0,1)} - w[y,t]^{(0,1)}\right] + \pi\rho Uc\Theta(0)^{(1)}\left[-\left(\frac{3}{4}c - x_f\right)\theta[y,t] + w[y,t]\right] - 2\pi\rho U^3\left[\psi_1\varepsilon_1\left(-1 - \varepsilon_1\left(\frac{1}{2} - e\right)\right)w_1 + \psi_2\varepsilon_2\left(-1 - \varepsilon_2\left(\frac{1}{2} - e\right)\right)w_2 + \psi_1\frac{{\varepsilon_1}^2}{b}w_3 + \psi_2\frac{{\varepsilon_2}^2}{b}w_4\right] + \pi\rho Uc\Theta(t)^{(1)}\left(-w[y,0] + \left(\frac{3}{4}c - x_f\right)\theta[y,0]\right) \qquad 2.77$$

The aerodynamic moment around the shear center due to the unsteady lift force can be cast as:

$$M_C(t) = ecL_C(t) \qquad 2.78$$

To have a complete representation of the aerodynamic forces the added mass effects must be superimposed, therefore the complete expressions of the unsteady aerodynamic forces are:

$$q_3 = L(t) = \pi\rho b^2\left[-w[y,t]^{(0,2)} - \left(x_f - \frac{c}{2}\right)\theta[y,t]^{(0,2)}\right] + \pi\rho Uc\left[\left(\frac{c}{4} + \Theta(0)\left(\frac{3}{4}c - x_f\right)\right)\theta[y,t]^{(0,1)} - \Theta(0)w[y,t]^{(0,1)}\right] + \pi\rho U^2c\Theta(0)\theta[y,t] + \pi\rho Uc\left[-\left(\frac{3}{4}c - x_f\right)\Theta(0)^{(1)}\theta[y,t] + \Theta(0)^{(1)}w[y,t]\right] - 2\pi\rho U^3\left[\psi_1\varepsilon_1\left(-1 - \varepsilon_1\left(\frac{1}{2} - e\right)\right)w_1 + \psi_2\varepsilon_2\left(-1 - \varepsilon_2\left(\frac{1}{2} - e\right)\right)w_2 + \psi_1\frac{{\varepsilon_1}^2}{b}w_3 + \psi_2\frac{{\varepsilon_2}^2}{b}w_4\right] + \pi\rho Uc\Theta(t)^{(1)}\left(-w[y,0] + \left(\frac{3}{4}c - x_f\right)\theta[y,0]\right)$$

2.79

$$q_5 = M_a(t) = \pi\rho b^2 \left[\left(-\left(x_f - \frac{c}{2}\right)^2 - \frac{b^2}{8}\right)\theta[y,t]^{(0,2)} - \left(x_f - \frac{c}{2}\right)w[y,t]^{(0,2)}\right] +$$

$$\pi\rho Uc\left[\left(-\left(\frac{3}{4}c - x_f\right)\frac{c}{4} + ec\Theta(0)\left(\frac{3}{4}c - x_f\right)\right)\theta[y,t]^{(0,1)} - ec\Theta(0)w[y,t]^{(0,1)}\right] + \pi\rho U^2 c\Theta(0)ec\theta +$$

$$\pi\rho Uc\left[-ec\left(\frac{3}{4}c - x_f\right)\Theta(0)^{(1)}\theta[y,t] + ec\Theta(0)^{(1)}w[y,t]\right] -$$

$$2\pi\rho U^3\left[ec\psi_1\varepsilon_1\left(-1 - \varepsilon_1\left(\frac{1}{2} - e\right)\right)w_1 + ec\psi_2\varepsilon_2\left(-1 - \varepsilon_2\left(\frac{1}{2} - e\right)\right)w_2 + ec\psi_1\frac{{\varepsilon_1}^2}{b}w_3 + ec\psi_2\frac{{\varepsilon_2}^2}{b}w_4\right] + \pi\rho Uc\Theta(t)^{(1)}\left(-ecw[y,0] + ec\left(\frac{3}{4}c - x_f\right)\theta[y,0]\right)$$ 2.80

In order to include the nonlinear dynamic stall and the trailing edge flow separation a modified Beddos-Leishman (B-L) formulation was adopted, as in [19]. Therefore the contribution to the model of the unsteady aerodynamic loads of Eqs. 2.79 and 2.80 is expressed as:

$$L_s(t) = \frac{1}{2}\rho cU^2\left(C_{L,\Theta}(\theta^E - \alpha_0)w_5 + C_L^{FS}\theta^E(1 - w_5) + \pi T_U\partial_t\theta\right) \quad 2.81$$

$$M_s(t) = \frac{1}{2}\rho c^2U^2\left({C_M}^{ST}\theta^E + C_L^{US}(\beta^{ST}w_5 - \beta^{ST}f^{ST}\theta^E) - \frac{\pi}{2}T_U\partial_t\theta\right) \quad 2.82$$

where β^{ST} is the arm of the lift force and it is a function of the separation point distance f^{ST} on the upper wing surface. $T_U = \frac{b}{U}$ is a time constant, θ^E is the effective angle of attack, while

$$C_L^{US} = C_{L,\Theta}(\theta^E - \alpha_0)w_6 + C_L^{FS}(1 - w_6) + \pi T_U\partial\theta \quad 2.83$$

where $C_{L,\Theta}$ is the slope of the lift curve in the linear region of attached flow and C_L^{FS} is the lift coefficient for the fully separated flow. w_5 and w_6 are the two added aerodynamic states coming from the stall model. The contribution of dynamic stall, Eqs. 2.81 and 2.82, to the aerodynamic loads enter into the equations of motion of the slender wing as:

$$\begin{Bmatrix} q_5 \\ q_3 \\ 0 \end{Bmatrix} = \begin{Bmatrix} M_a(t) \\ L(t) \\ 0 \end{Bmatrix} + \begin{Bmatrix} M_s(t) \\ L_s(t) \\ 0 \end{Bmatrix} \tag{2.84}$$

The results presented hereafter, in the next chapters, do not include the stall model since the angle of attack of the wing is always far behind the 11°, critical value for the wing dynamic stall.

2.5 Approximate solution

The equations of motion, 2.67, 2.68 and 2.69, derived in the previous paragraphs are expressed in the form of partial differential equations (PDEs). In order to obtain a time domain solution of equations 2.67, 2.68, 2.69 the dependency from the space coordinate into the equations have to be removed by assuming an approximate solution which lead to a set of ordinary differential equations (ODEs). To achieve the transformation from PDEs to ODEs the modal representation of the displacements field by the Galerkin approach is introduced. The displacements are represented by the product of a time function variable and a set of truncated modes which approximate the solution in space:

$$\begin{Bmatrix} \theta[y,t] \\ w[y,t] \\ u[y,t] \end{Bmatrix} = [\Phi(y)]\{r(t)\} =$$

$$\begin{bmatrix} \phi_{\theta_i} & \cdots & \phi_{\theta_n} & 0 & \cdots & 0 & 0 & \cdots & 0 \\ 0 & \cdots & 0 & \phi_{w_i} & \cdots & \phi_{w_n} & 0 & \cdots & 0 \\ 0 & \cdots & 0 & 0 & \cdots & 0 & \phi_{u_i} & \cdots & \phi_{u_n} \end{bmatrix} \begin{Bmatrix} r_{\theta_i} \\ \vdots \\ r_{\theta_n} \\ r_{w_i} \\ \vdots \\ r_{w_n} \\ r_{u_i} \\ \vdots \\ r_{u_n} \end{Bmatrix} \qquad 2.85$$

The subscript n represents the number of modes used to approximate the solution. The polynomial basis functions $\phi_{\theta_i} \dots \phi_{\theta_n}, \phi_{w_i} \dots \phi_{w_n}, \phi_{u_i} \dots \phi_{u_n}$ chosen to discretize the components of the displacement vector correspond to the decoupled bending-torsion mode shapes of the clamped rigid beam, that is:

$$\phi_{\theta_i} = \sqrt{2}\, sin(\gamma_i y) \qquad 2.86$$

$$\phi_{w_i,u_i} = cosh(\alpha_i y) - cos(\alpha_i y) - \beta_i[sinh(\alpha_i y) - sin(\alpha_i y)] \qquad 2.87$$

with $\gamma_i = \frac{\pi\left(i-\frac{1}{2}\right)}{l}$, α_i and β_i chosen coherently with the assumed number of modes. The equations of motion, 2.67, 2.68 and 2.69, can be rewritten in a matrix form after the substitution into them of the flight loads, 2.79 and 2.80, and the discrete representation of the displacement vector, 2.85:

$$[M_s]\{\ddot{r}\} + [D_s]\{\dot{r}\} + [K_s]\{r\} = [M_a]\{\ddot{r}\} + [D_a]\{\dot{r}\} + [K_a]\{r\} + \{F_e\} \qquad 2.88$$

where $[M_s]$, $[D_s]$, $[K_s]$ are respectively the modal mass, the modal damping and the modal stiffness matrices of the wing structure, while $[M_a]$, $[D_a]$, $[K_a]$ are modal mass, the modal damping and the modal stiffness matrices deriving from the aerodynamic model. $\{F_e\} = \begin{Bmatrix} \pi\rho U^2 e c^2 \alpha_{trim} \\ \pi\rho U^2 c \alpha_{trim} \\ 0 \end{Bmatrix}$ is the vector of the loads due to the trimmed condition. and the dot over the variable indicate the order of the time derivative. Due to the validness of the Wagner approach only in the range of the small perturbations, the vector of the generalized coordinates can be written as the sum of an equilibrium value and of a perturbation:

$$\{r\} = \{r_e\} + \{\tilde{r}\} \qquad 2.89$$

Substituting Eq. 2.89 into Eq. 2.88 and collecting all the terms which depend only on the equilibrium variables in a separate set of equilibrium equations, and then applying the Galerkin approximation, we obtain:

$$\int_0^l \begin{bmatrix} [\Phi]^t & \begin{bmatrix} 0 & \cdots & 0 \\ \vdots & \cdots & \vdots \\ 0 & \cdots & 0 \end{bmatrix} \\ \begin{bmatrix} 0 & \cdots & 0 \\ \vdots & \cdots & \vdots \\ 0 & \cdots & 0 \end{bmatrix} & [\Phi]^t \end{bmatrix} \begin{bmatrix} \begin{bmatrix} M_s + M_{a_{QS}} \end{bmatrix} & \begin{bmatrix} 0 & \cdots & 0 \\ \vdots & \cdots & \vdots \\ 0 & \cdots & 0 \end{bmatrix} \\ \begin{bmatrix} 0 & \cdots & 0 \\ \vdots & \cdots & \vdots \\ 0 & \cdots & 0 \end{bmatrix} & [M_s + M_a] \end{bmatrix} dy \begin{Bmatrix} \ddot{r}_e \\ \ddot{\tilde{r}} \end{Bmatrix} +$$

$$\int_0^l \begin{bmatrix} [\Phi]^t & \begin{bmatrix} 0 & \cdots & 0 \\ \vdots & \cdots & \vdots \\ 0 & \cdots & 0 \end{bmatrix} \\ \begin{bmatrix} 0 & \cdots & 0 \\ \vdots & \cdots & \vdots \\ 0 & \cdots & 0 \end{bmatrix} & [\Phi]^t \end{bmatrix} \begin{bmatrix} \begin{bmatrix} D_s + D_{a_{QS}} \end{bmatrix} & \begin{bmatrix} 0 & \cdots & 0 \\ \vdots & \cdots & \vdots \\ 0 & \cdots & 0 \end{bmatrix} \\ \begin{bmatrix} 0 & \cdots & 0 \\ \vdots & \cdots & \vdots \\ 0 & \cdots & 0 \end{bmatrix} & [D_s + D_a] \end{bmatrix} dy \begin{Bmatrix} \dot{r}_e \\ \dot{\tilde{r}} \end{Bmatrix} +$$

$$\int_0^l \begin{bmatrix} [\Phi]^t & \begin{bmatrix} 0 & \cdots & 0 \\ \vdots & \cdots & \vdots \\ 0 & \cdots & 0 \end{bmatrix} \\ \begin{bmatrix} 0 & \cdots & 0 \\ \vdots & \cdots & \vdots \\ 0 & \cdots & 0 \end{bmatrix} & [\Phi]^t \end{bmatrix} \begin{bmatrix} \begin{bmatrix} K_s + D_{a_{QS}} \end{bmatrix} & \begin{bmatrix} 0 & \cdots & 0 \\ \vdots & \cdots & \vdots \\ 0 & \cdots & 0 \end{bmatrix} \\ \begin{bmatrix} K_{s_{ep}} \end{bmatrix} & [K_s + K_a] \end{bmatrix} dy \begin{Bmatrix} r_e \\ \tilde{r} \end{Bmatrix} +$$

$$\int_0^l \begin{bmatrix} \begin{bmatrix} 0 & \cdots & 0 \\ \vdots & \cdots & \vdots \\ 0 & \cdots & 0 \end{bmatrix} & \begin{bmatrix} 0 & \cdots & 0 \\ \vdots & \cdots & \vdots \\ 0 & \cdots & 0 \end{bmatrix} \\ \begin{bmatrix} 0 & \cdots & 0 \\ \vdots & \cdots & \vdots \\ 0 & \cdots & 0 \end{bmatrix} & [\Phi_w] \end{bmatrix} \begin{bmatrix} \begin{bmatrix} 0 & \cdots & 0 \\ \vdots & \cdots & \vdots \\ 0 & \cdots & 0 \end{bmatrix} & \begin{bmatrix} 0 & \cdots & 0 \\ \vdots & \cdots & \vdots \\ 0 & \cdots & 0 \end{bmatrix} \\ \begin{bmatrix} 0 & \cdots & 0 \\ \vdots & \cdots & \vdots \\ 0 & \cdots & 0 \end{bmatrix} & [W] \end{bmatrix} dy \begin{Bmatrix} 0 \\ \vdots \\ 0 \\ w_1 \\ \vdots \\ w_k \end{Bmatrix} =$$

$$\int_0^l \begin{bmatrix} [\Phi]^t & \begin{bmatrix} 0 & \cdots & 0 \\ \vdots & \cdots & \vdots \\ 0 & \cdots & 0 \end{bmatrix} \\ \begin{bmatrix} 0 & \cdots & 0 \\ \vdots & \cdots & \vdots \\ 0 & \cdots & 0 \end{bmatrix} & [\Phi]^t \end{bmatrix} dy \begin{Bmatrix} M_e \\ L_e \\ 0 \\ 0 \\ \vdots \\ 0 \end{Bmatrix} \qquad 2.90$$

where $[\Phi_w]$ is the matrix of the mode shapes which multiply the added aerodynamic states. Equation 2.90 can be rewritten according to the state-space formulation, which is a very compact and convenient way to reorganize the ordinary differential equations, especially for numerical simulation purpose:

$$\{\dot{z}\} = [S]\{z\} + [N]\{z(0)\} + \{B\} \qquad 2.91$$

$$\{z\} = \begin{matrix} \{\dot{r}_{\theta_{e1}} & \cdots & \dot{r}_{\theta_{en}} & \dot{r}_{w_{e1}} & \cdots & \dot{r}_{w_{en}} & \dot{r}_{u_{e1}} & \cdots & \dot{r}_{u_{en}} \\ \tilde{\dot{r}}_{\theta_1} & \cdots & \tilde{\dot{r}}_{\theta_n} & \tilde{\dot{r}}_{w_1} & \cdots & \tilde{\dot{r}}_{w_n} & \tilde{\dot{r}}_{u_1} & \cdots & \tilde{\dot{r}}_{u_n} \\ r_{\theta_{e1}} & \cdots & r_{\theta_{en}} & r_{w_{e1}} & \cdots & r_{w_{en}} & r_{u_{e1}} & \cdots & r_{u_{en}} \\ \tilde{r}_{\theta_1} & \cdots & \tilde{r}_{\theta_n} & \tilde{r}_{w_1} & \cdots & \tilde{r}_{w_n} & \tilde{r}_{u_1} & \cdots & \tilde{r}_{u_n} \\ & & & & & & w_1 & \cdots & w_k\} \end{matrix}$$

2.92

$$\{B\} = \left\{ \int_0^l \begin{bmatrix} [\Phi]^t & \begin{bmatrix} 0 & \cdots & 0 \\ \vdots & \cdots & \vdots \\ 0 & \cdots & 0 \end{bmatrix} \\ \begin{bmatrix} 0 & \cdots & 0 \\ \vdots & \cdots & \vdots \\ 0 & \cdots & 0 \end{bmatrix} & [\Phi]^t \end{bmatrix} dy \begin{Bmatrix} M_e \\ L_e \\ 0 \\ 0 \\ \vdots \\ 0 \end{Bmatrix} \right\} \quad \begin{matrix} \\ \\ \\ \\ 0 \\ \vdots \\ 0 \end{matrix}$$

2.93

$$[S] = \begin{bmatrix} -\left[M_s + M_{aQS}\right]^{-1}\left[D_s + D_{aQS}\right] & \begin{bmatrix} 0 & \cdots & 0 \\ \vdots & \ddots & \vdots \\ 0 & \cdots & 0 \end{bmatrix} \\ -[M_s + M_a]^{-1}\left[D_{s_{ep}}\right] & -[M_s + M_a]^{-1}[D_s + D_a] \\ \begin{bmatrix} 1 & \cdots & 1 \\ \vdots & \ddots & \vdots \\ 1 & \cdots & 1 \end{bmatrix} & \begin{bmatrix} 0 & \cdots & 0 \\ \vdots & \ddots & \vdots \\ 0 & \cdots & 0 \end{bmatrix} \\ \begin{bmatrix} 0 & \cdots & 0 \\ \vdots & \ddots & \vdots \\ 0 & \cdots & 0 \end{bmatrix} & \begin{bmatrix} 1 & \cdots & 1 \\ \vdots & \ddots & \vdots \\ 1 & \cdots & 1 \end{bmatrix} \\ \begin{bmatrix} 0 & \cdots & 0 \\ \vdots & \ddots & \vdots \\ 0 & \cdots & 0 \end{bmatrix} & \begin{bmatrix} 0 & \cdots & 0 \\ \vdots & \ddots & \vdots \\ 0 & \cdots & 0 \end{bmatrix} \end{bmatrix}$$

$$\begin{bmatrix} -\left[M_s + M_{aQS}\right]^{-1}\left[K_s + K_{aQS}\right] & \begin{bmatrix} 0 & \cdots & 0 \\ \vdots & \ddots & \vdots \\ 0 & \cdots & 0 \end{bmatrix} & \begin{bmatrix} 0 & \cdots & 0 \\ \vdots & \ddots & \vdots \\ 0 & \cdots & 0 \end{bmatrix} \\ -[M_s + M_a]^{-1}\left[K_{s_{ep}}\right] & -[M_s + M_a]^{-1}[K_s + K_a] & -[M_s + M_a]^{-1}[W] \\ \begin{bmatrix} 0 & \cdots & 0 \\ \vdots & \ddots & \vdots \\ 0 & \cdots & 0 \end{bmatrix} & \begin{bmatrix} 0 & \cdots & 0 \\ \vdots & \ddots & \vdots \\ 0 & \cdots & 0 \end{bmatrix} & \begin{bmatrix} 0 & \cdots & 0 \\ \vdots & \ddots & \vdots \\ 0 & \cdots & 0 \end{bmatrix} \\ \begin{bmatrix} 0 & \cdots & 0 \\ \vdots & \ddots & \vdots \\ 0 & \cdots & 0 \end{bmatrix} & \begin{bmatrix} 0 & \cdots & 0 \\ \vdots & \ddots & \vdots \\ 0 & \cdots & 0 \end{bmatrix} & \begin{bmatrix} 0 & \cdots & 0 \\ \vdots & \ddots & \vdots \\ 0 & \cdots & 0 \end{bmatrix} \\ & [W_0] & \end{bmatrix}$$

2.94

$[W]$ and $[W_0]$ are two linear matrix depending on the constant terms of the Wagner function. $[N]$ is a linear matrix containing the first time derivative of the Wagner's function. The solution of equation 2.91 is found by applying the Runge-Kutta method [10]. The nonlinear analytical model of a slender wing defined in the previous sections has been numerically implemented using Matlab® and Simulink®. Several dynamical conditions have been studied in order to highlight the importance of the nonlinear terms and their class of importance. The code was validated through the results available in the literature and some experimental test performed at Clarkson University. Chapter 4 contains all the results just mentioned.

References

[1] Nayfeh, A. H. and Pai, P. F. Linear and non-linear structural mechanics, 2004 (Wiley Interscience, New York).

[2] Crespo Da Silva, M., R. , M., Glynn, C., C., "Nonlinear Flexural-Flexural-Torsional Dynamic of Inextensional Beam", 1986, Journal of structural mechanics, Volume 6 Issue 4.

[3] Kim, K., Nonlinear Aeroelastic Analysis of Aircraft Wing-With-Store Configurations, 2004, Ph.D thesis.

[4] Pai, P., F., "Three Geometrically Exact Beam Theories for Analysis of Highly Flexible 1-D Structures", 2011, 52nd AIAA/ASME/ASCE/AHS/ASC Structures, Structural Dynamics and Materials Conference, 4-7 April 2011, Denver, Colorado.

[5] Antona E., Frulla G. (2001). Some considerations about the concepts of asymptotic approach. ATTI Della ACCADEMIA delle SCIENZE di Torino ,2001,pp. 135-161.

[6] Antona E., Frulla G. (2001). Cicala's asymptotic approach to the linear shell theory. COMPOSITE STRUCTURES , Vol. 52, pp. 13-26.2001.

[7] Murray ,T., " On the use of the indicial function concept in the analysis of unsteady motions of the wings and wing-tail combinations", NASA report 1188.

[8] Wagner, H., " Über die Entstehung des dynamischen Auftriebes von Tragflügeln ", Berlin: VDI-Verl., 1925.

[9] Shams, Sh., Haddadpour, H., Sadr Lahidjani, M. H., Kheiri, M., "An Analytical Method in Computational Aeroelasticity Based on Wagner Function", 2006, 25th International congress of the aeronautical sciences, ICAS 2006.

[10] Sedaghat A., Cooper J.E., Wright J.R., Leung A.Y.T., “Prediction of non-linear aeroelastic instabilities”. ICAS 2000, 27 August - 1 September 2000

[11] Tang, D., Dowell, E. H., "Experimental and Theoretical Study on Aeroelastic Response of High-Aspect-Ratio Wings", AIAA Journal, Vol. 39, No, 8, August 2001.

[12] Shams, Sh., Sadr Lahidjani, M.H., Haddadpour, H., "An efficient method for nonlinear aeroelasticity of slender wings " , Nonlinear Dyn, 2012, Doi 10.1007/s11701-011-0018-2.

[13] Kim, K., Strganac, T.W., "Nonlinear response of a cantilever wing with an external store", 44th AIAA/ASME/ASCE/AHS Structures, Structural Dynamics, and Materials Conference, 7-10 April 2003, Norfolk, Virginia.

[14] Cestino, E., Frulla, G., Perotto, E., Marzocca, P., " Experimental Slender Wing Model Design by the Application of Aeroelastic Scaling Laws", Journal of Aerospace Engineer, January 2014, DOI: 10.1061/(ASCE)AS.1943-5525.0000211.

[15] Abbas, L.K., Chen, Q., Marzocca, P., Milanese, A., “Non-linear aeroelastic investigations of store(s)-induced limit cycle oscillations”, Proc. IMechE Vol. 222 Part G: J. Aerospace Engineering, 2008.

[16] Frulla G., Cestino E., Marzocca P.,(2010b) ,“Critical behaviour of slender wing configurations” Proc. of the institution of mechanical engineers. Part G, Journal of Aerospace Engineering ,Vol.224, pp.527-636.

[17] Theodorsen, T., “General Theory of Aerodynamic Instability and the Mechanism of Flutter,” NACA TR No. 496, May 1934.

[18] Garrick, I. E., “Propulsion of a Flapping and Oscillating Airfoil,” NACA TR No. 567, May 1936. [3] von Karman, T. and Burgers, J. M., General Aerodynamic Theory-Perfect Fluids, Vol. II, Julius Springer, Berlin, 1935.

[19] Cestino E., Frulla G., Marzocca P. (2013). A Reduced Order Model for the Aeroelastic Analysis of Flexible Wings. In: SAE INTERNATIONAL JOURNAL OF AEROSPACE, vol. 6 n. 2. - ISSN 1946-3855.

[20] Cicala P. Teoria delle verghe e delle travi Elastiche . Atti di Scienze Fisiche dell'Accademia delle Scienze di Torino. Vol. 9, 1985.

[21] Cicala P. Linear Shell theory : an Asymptotic approach. Levrotto e Bella Torino. 1978.

[22] Frulla G. Problemi strutturali di un rotore snodato. Final PhD Thesis. Torino . 2000.

[23] Patil, M. J., Hodges, D. H., Cesnik, C. E. S., "Characterizing the Effects of Geometrical Nonlinearities on Aeroelastic Behavior of High-Aspect-Ration Wings", Presented at the International Forum of Aeroelasticity and Structural Dynamics , Willianmsburg, Virginia, USA, June 22-25, 1999.

[24] Tang, D.M. and Dowell, E.H., "Effects of geometric structural nonlinearity on flutter and limit cycle oscilaltions of high-aspect-ratio wings", Journal of Fluids and Structures 19 (2004) 291-306, 2004, doi:10.1016/j.jfluidstructs.2003.10.007.

[25] Frulla, G., Cestino, E. and Marzocca, P., "Critical behavoiur of slender wing configuration", Proc. IMEchE . 224 Part G: J. Aerospace Engineering, 2009, DOI:10.1243/09544100JAERO553.

[26] Bruni, C., Cestino, E., Frulla, G., and Marzocca, P., "Nonlinear Slender Beam-Wise Schemes for Structural Behavior of Flexible UAS Wings," SAE Technical Paper 2015-01-2462, 2015, doi:10.4271/2015-01-2462.

3 Aeroelastic phenomena

The interaction between the structure, the flight control system and the atmosphere is now a largely studied condition and the deriving aeroelastic phenomena a constraint in the aircraft design. If the airplane was assumed perfectly rigid this problem wouldn't exist, therefore it is the aircraft flexibility the responsible for aeroelastic phenomena. The aeroelastic phenomena can be split into two categories: static and dynamic. The first refers to the interaction between the aerodynamic and elastic forces only, while the second include also the inertial forces. How the aeroelastic phenomena are classified based on these three main families of forces which mutually interact is shown in the Collar diagram of Figure 4.

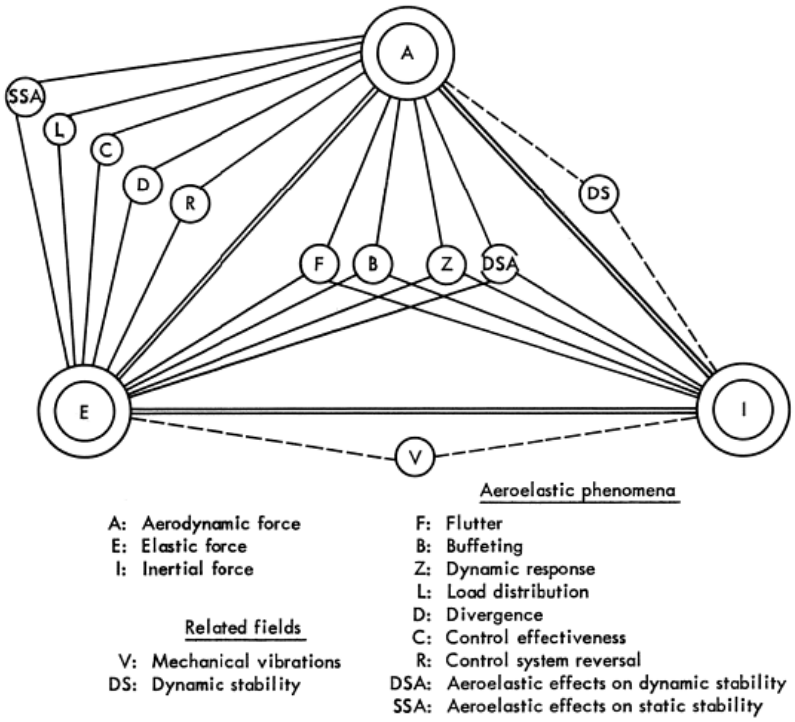

Figure 4 Collar diagram for the aeroelastic phenomena identification [1]

The relevance of the aeroelastic analysis over the aircraft design cannot be overlooked, especially in fatigue structural design. Only a few of all the

existing aeroelastic phenomena are treated in the following sections, that's to say: Flutter, LCO and Gust dynamic response.

3.1 Flutter

With flutter one can identify the self-sustained oscillatory instability which rises from the interaction of the aerodynamic loads and the elastic response of the body. Two types of flutter can be experienced: the stall flutter and the "classical" flutter. The first is related to flow separation due to the aircraft high angle of attack reached during the flight mission while the second do not necessarily involve flow separation, it is rather avoided. The classical flutter, which from here onward we will refer to with the simple name of flutter, involves a minimum of two degree of freedom of the system and for systems with negligible structural damping, as for this study, it is usually attributed to a coalescence of the wing bending and torsion frequencies. When the air speed increases, the aerodynamic damping does the same until a value of the air speed at which the damping rapidly decreases, reaching the zero value. In this condition a small perturbation of the body may establish a self-sustained simple harmonic oscillatory motion. This value of air speed is called critical flutter speed. Each perturbation of the body motion at air speed higher than the critical flutter speed may lead to a catastrophic event, due to the rapid increase of the oscillation amplitude. Flutter is an aeroelastic phenomenon which had to be briefly investigated during the aircraft design in order obtain a final flight envelope free from flutter. Sometimes, and more often for the new generation of flexible aircrafts, it is not an easy task keeping the flutter event out of the flight envelope, several techniques are applied in order to move the flutter speed outside the flight envelope reduce. The most commons techniques are: increasing the structural stiffness, increase the structural damping, mass balancing, act on the flight control surfaces and more recently by extracting energy from the system.

The flutter problem is widely studied because it is easier mathematically to describe the aerodynamic loads due to a simple harmonic motion. Theoretical flutter often consists of assuming in advance that all dependent variables are proportional to $e^{i\omega t}$, and finding combinations of U and ω for which this actually occurs. In the previous chapters it was provided an analytical nonlinear wing model whose dynamical behavior is analyzed in time domain. However for the purpose of identifying the critical flutter condition the model can be assumed linear in a first instance, which means linearizing the nonlinear equations 2.67, 2.68 and 2.69 about the zero steady state condition. Therefore the critical flutter speed is not influenced by the nonlinear terms, and the vector of the generalized coordinates is taken exponential, $r = \bar{r}e^{i\omega t}$, such as

$$[M]\ddot{r} + [K]r = P \qquad 3.1$$

The structural damping in Eq. 3.1 is neglected. Assuming harmonic response at frequency ω, the equations of motion become:

$$-\omega^2[M]\bar{r} + [K]\bar{r} = \pi\rho b^2\omega^2[A(k)]\bar{r} \qquad 3.2$$

where $[A(k)]$ is the aerodynamic matrix, depending on the reduced frequency:

$$[A(k)] = \int_0^l [\Phi]^t \begin{bmatrix} b^2(M_\theta - (0.5+a)(L_\theta + M_w) + (0.5+a)^2 L_w) & b^2(M_w - (0.5+a)L_w) & 0 \\ b(L_\theta - (0.5+a)L_w) & b(L_w) & 0 \\ 0 & 0 & 0 \end{bmatrix} [\Phi] dy \qquad 3.3$$

with:

$$L_w = 1 - \frac{2iC}{k};\ M_w = \frac{1}{2};\ L_\theta = \frac{1}{2} - \frac{i(1+2C)}{k} - \frac{2C}{k^2};\ M_\theta = \frac{3}{8} - \frac{i}{k} \qquad 3.4$$

C is the Theodorsen's function , which is expressed in terms of the Hankel functions$H_n^{(2)} = J_n - iY_n$, where J_n and Y_n are the Bessel functions of the first and second kind respectively, as:

$$C = \frac{H_1^{(2)}(k)}{H_1^{(2)}(k)+i\,H_0^{(2)}(k)} \qquad 3.5$$

$k = \frac{\omega b}{U}$ is called reduced frequency. Dividing the torsion equation of the system by mb^2l and the two bending equations by mbl and introducing an artificial damping g proportional to the stiffness matrix:

$$\left([\bar{M}] + \frac{1}{\mu}[A(k)]\right) r - \frac{(1+ig)}{\omega^2}[\bar{K}]r = 0 \qquad 3.6$$

substituting $\Omega = \frac{(1+ig)}{\omega^2}$:

$$[\bar{K}]^{-1}\left([\bar{M}] + \frac{1}{\mu}[A(k)]\right) r - \Omega\, r = 0 \qquad 3.7$$

the solution becomes a problems of eigenvalues and eigenvectors, from which:

$$\omega_i = \sqrt{\frac{1}{Re(\Omega_i)}};\ U_i = \frac{\omega_i b}{k}\ ;\ g_i = \frac{Im(\Omega_i)}{Re(\Omega_i)} \qquad 3.8$$

These results presented in Chapter 3 refer to the wing data reported in Table 2 and taken from [2]. This wing will be studied also in Chapter 5 where the piezoelectric contribution have been accounted for.

Table 2 Wing data [2]

Name	Value	Definition
l	1.2	Wing length $[m]$
b	0.135	Wing semi-chord $[m]$
a	-0.8	Elastic axis location
ζ_1	0	Gravity center location

h	0.0324	Wing-box thickness $[m]$
m	1.973	Wing mass $[Kg/m]$
EI_1	476.9	Wing out of plane stiffness $[N \cdot m^2]$
EI_3	20980	Wing in plane stiffness $[N \cdot m^2]$
GJ	3.988	Wing torsion stiffness $[N \cdot m^2]$

The solution of equation 3.7 for the wing of Table 1 is reported in Figure 4 and 5, known as V-g plots.

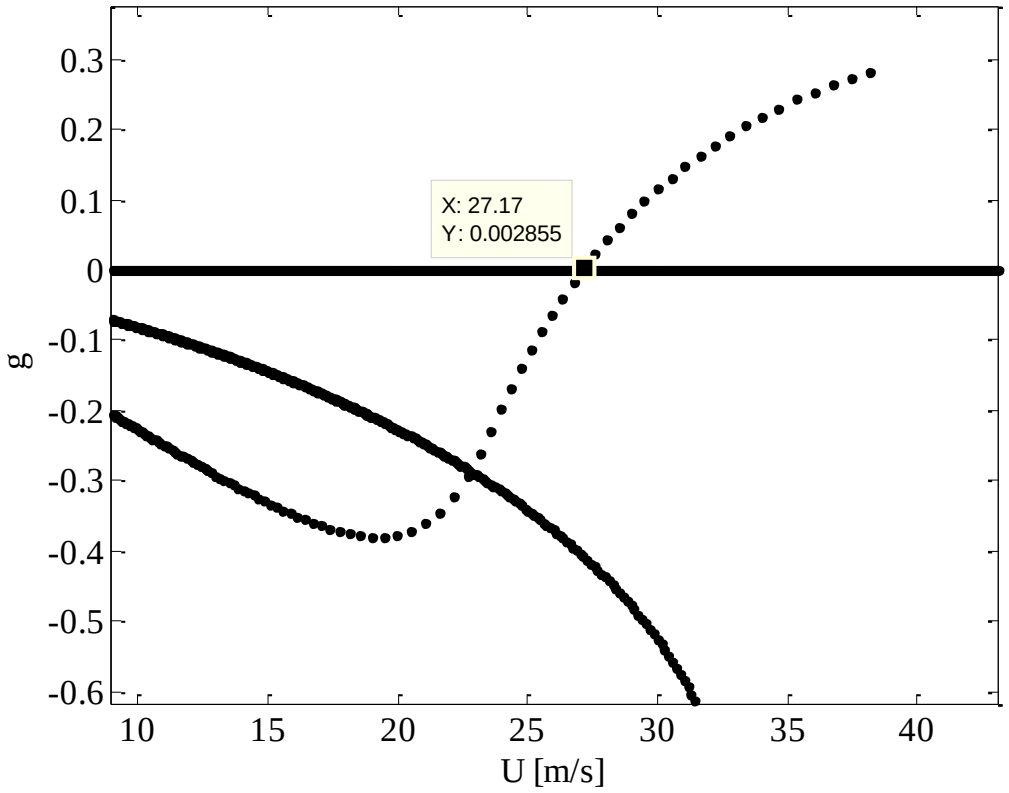

Figure 5 Artificial damping vs. horizontal air speed, referring to the wing data reported in Table 1.

From Figure 5 and 6 it is possible to extract the critical flutter condition. The branch of Figure 5 which after a certain speed value become instable, crosses the $g = 0$ line at a air speed value which correspond with the critical flutter speed, 27.17 m/s. With this value of air speed and knowing

that it is the "torsion" branch" that become instable we can enter into Figure 6 and identify the corresponding value of the flutter frequency, 3.814 Hz.

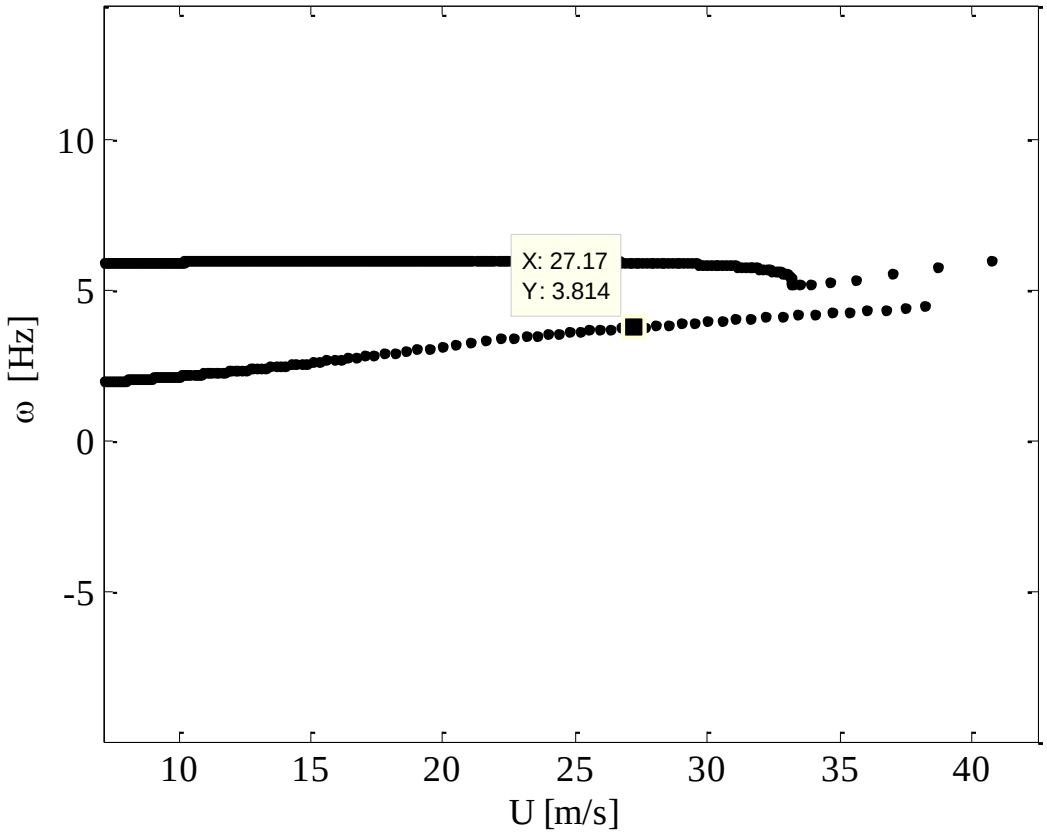

Figure 6 Modes frequencies vs. horizontal air speed, referring to the wing data reported in Table 1.

Both values, the flutter speed and the flutter frequency, are in good agreement with the values shown in [2] . There are several parameters which may influence the flutter condition. For example the elastic axis location a, measured respect to the mid-chord wing profile, and the distance between the shear center and the gravity center, ζ_1, both normalized with respect the wing semi-chord. Figures 7 and 8 show how for the specific wing of Table 2, with aerodynamic center behind the shear center, moving the elastic axis and the gravity center proportionally towards the mid-chord position increases the flutter speed while moving it towards the leading edge reduce the critical flutter speed value. A similar

effect but with lower intensity and opposite direction is obtained by moving the position of the gravity center with respect to the elastic axis, while keeping this last fixed. If the gravity center is moved towards the mid-chord position the critical flutter speed will increase, while moving it towards the trailing edge the flutter speed will decrease. The green curves of Figures 7 and 8 instead reproduce the effect of the variation of the shear center with respect to the mid-cord position when the gravity center is kept to a constant distance, -0.8*b, with respect to the mid-chord profile.

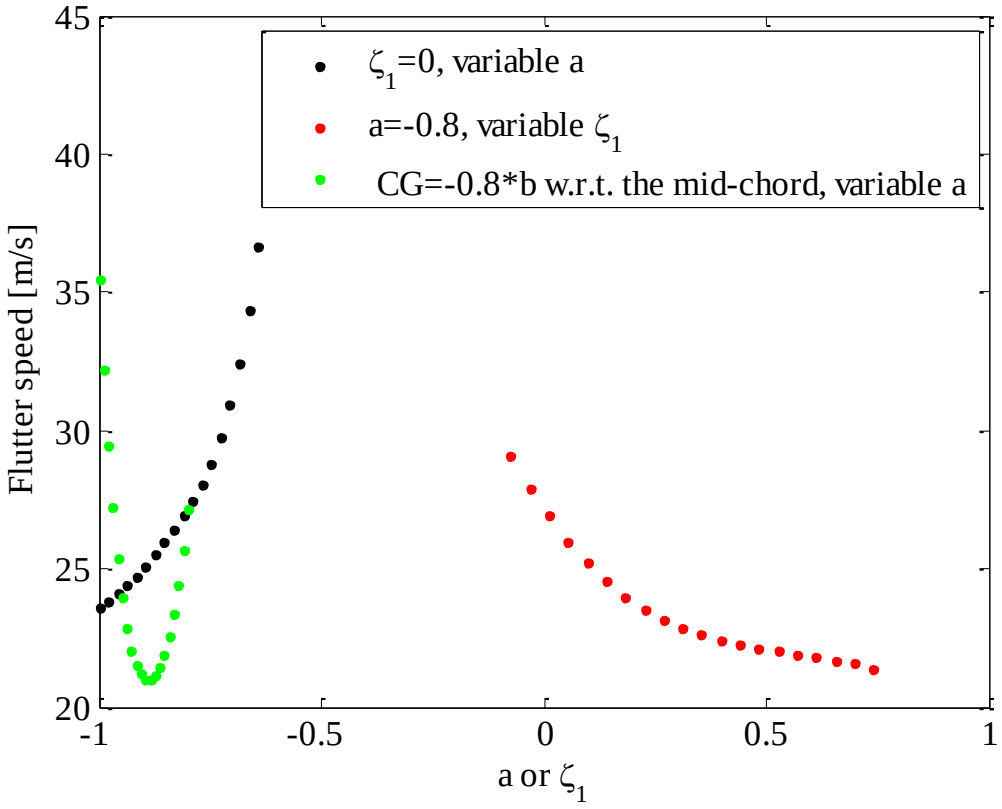

Figure 7 Flutter speed variation with respect to the elastic axis location a and the distance between the wing shear center and the gravity center.

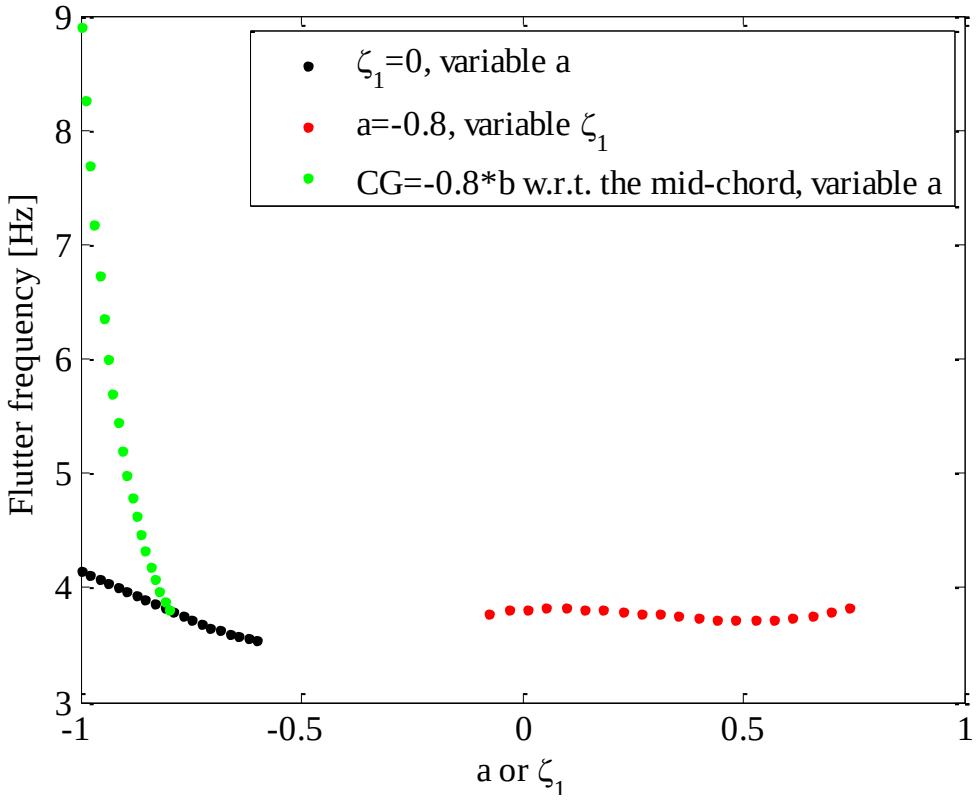

Figure 8 Flutter frequency variation with respect to the elastic axis location a and the distance between the wing shear center and the gravity center.

3.2 LCO

The limit cycle is an isolated closed trajectory, which means that neighbouring trajectories are not closed. If the neighbouring trajectories approach the limit cycle, we say the limit cycle is stable, otherwise. Stable limit cycles model systems exhibit self-sustained oscillations. Limit cycle is inherently nonlinear phenomenon therefore it is not a feature of a linear system and cannot be predicted by linear theory. Of course a linear system can have closed orbits but they won't be isolated, consequently, the amplitude of a linear oscillation is set entirely by initial condition; any slight disturbance of the amplitude will persist forever. In contrast limit cycle oscillations are determined by the structure of the system itself.

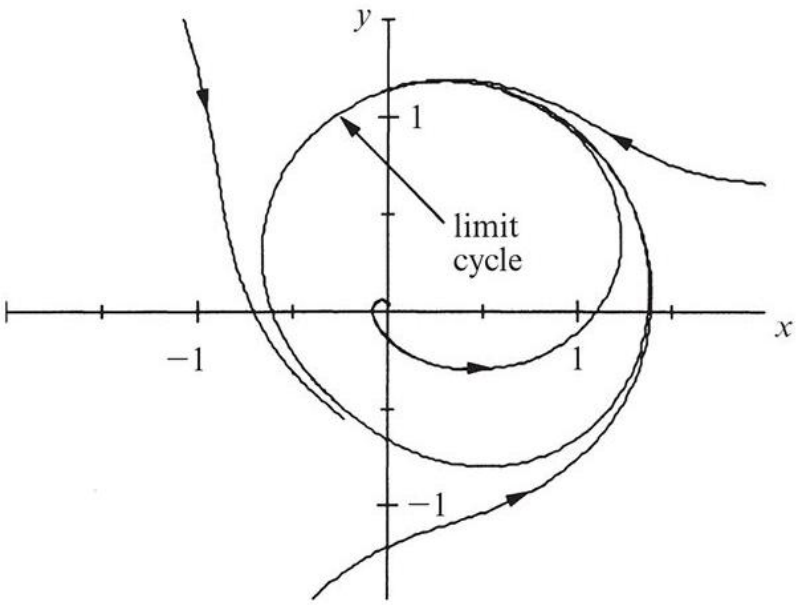

Figure 9 LCO trajectory [3]

This phenomenon is considered to be closely linked to the classical flutter, except that the coupling of the structural response and the unsteady aerodynamic forces are nonlinear in nature, resulting in a limited amplitude oscillatory motion. Figure 10 shows the different response of the system at airspeed slightly higher than the critical flutter speed when geometrical

nonlinearities are introduced into the mathematical model. The time simulations refer to the wing data reported in Table 2 and presented in its piezoelectric version in Chapter 5. The presence of the geometrical nonlinearities into the model induces the oscillation to be self-sustained, periodic but not catastrophically divergent.

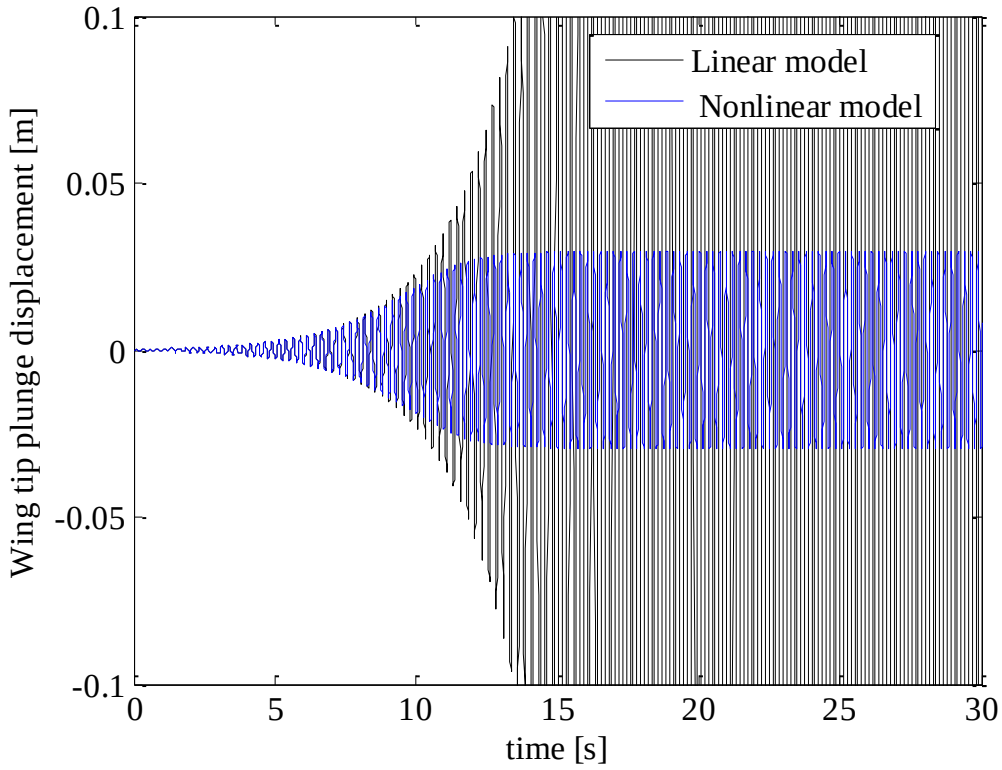

Figure 10 Post flutter Linear and nonlinear response of the wing of Table 1.

LCO is often associated to flutter and in the past terms like limit cycle flutter or limited amplitude flutter were used to identify this phenomenon. There are several reasons to think at LCO as strictly dependent from flutter, although many engineers believe that the genesis of LCO is in the flight control system. Some of these reasons are: the fact that LCO was first experienced during flutter flight testing and using typical flutter flight test procedures, that once the LCO is well established, all part of the aircraft vibrate in a single mode, at a single frequency. Therefore we can use flutter analysis to identify the LCO condition: the frequency at which the

damping goes to zero. Despite the technical aspects, the aircraft manufacturers are not in favor for using the word flutter to describe LCOs because of the idea of catastrophic failure associated with the classical flutter. The typical LCO amplitude is constant in stabilized flight conditions. Once above the LCO onset speed, the acceleration of the aircraft leads to continuous increase of the oscillation amplitude until a new target speed is reached. Although the LCO onset frequency of supercritical hopf-bifurcation might be calculated trough the classical flutter analysis methods, the LCO onset speed and the amplitude of the oscillation require nonlinear analysis to be realistically predicted. The sources of nonlinearities are multiples and singularly assumed in the mathematical model might not be sufficient to reproduce the LCO phenomenon into the numerical simulations. Often the LCOs derive from a combination of different types of nonlinearities, the most common are: geometrical nonlinearities, structural nonlinearities and aerodynamic nonlinearities. Only geometrical nonlinearities have been assumed in this work, which is translated into a structure nonlinear stiffening, or softening, if we retain in the mathematical model only nonlinear terms up to the third order, while inertial ones are considered of being higher order, and will be discard. According to this the total stiffness matrix can be recast as:

$$[K_s] = [K_s]_L + k * [K_s]_{NL} \qquad 3.9$$

The values of k are chosen in a range that goes from 1 to 0, where 1 represents the full contribution of the nonlinear terms up to the third order, while 0 is indicative of the linear case. Figure 11 and 12 indicates that by increasing the contribution of the nonlinear terms the oscillations amplitude in the LCO region decrease.

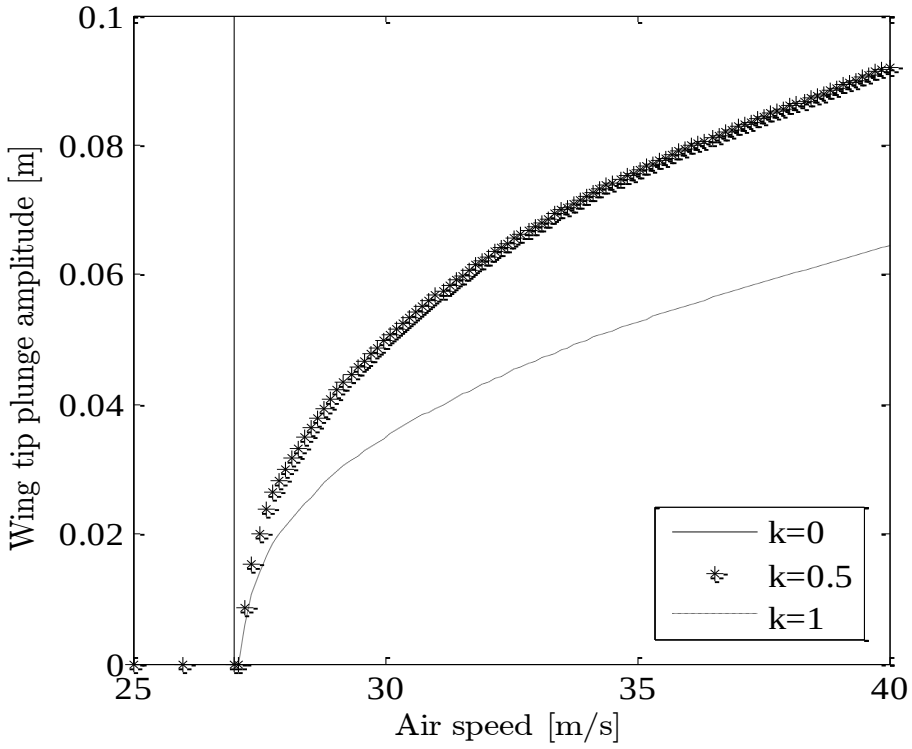

Figure 11 Wing tip plunge amplitude vs. airspeed for different nonlinear stiffness contribution.

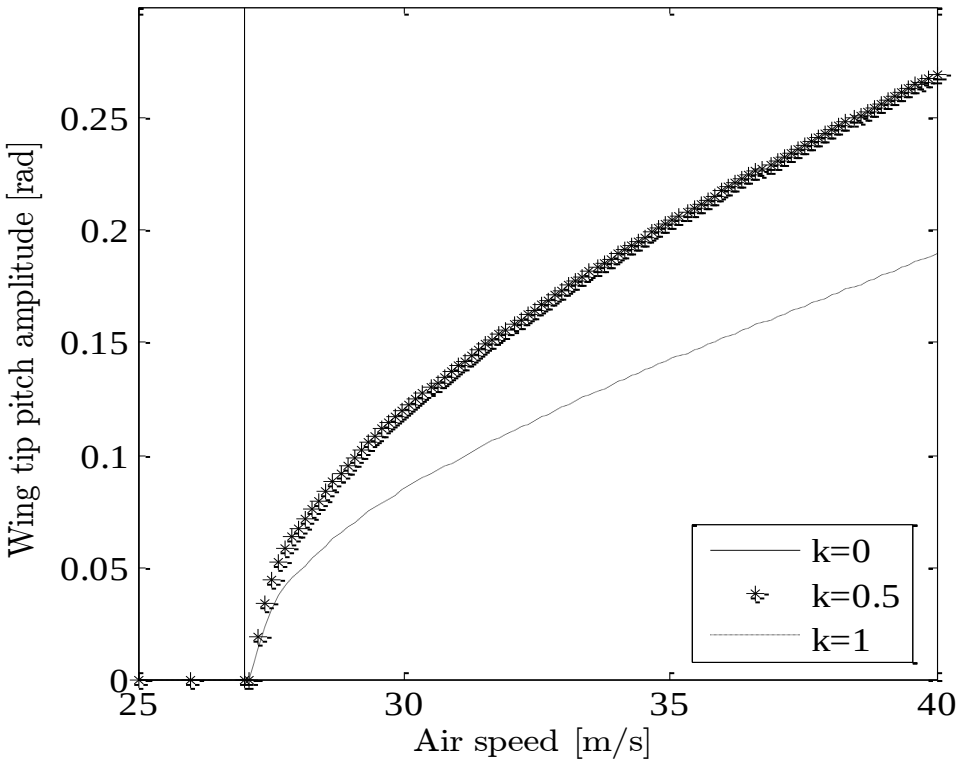

Figure 12 Wing tip pitch amplitude vs. airspeed for different nonlinear stiffness contribution.

Figures from 13 to 16 show the phase diagrams and the pitch and plunge time domain responses for the wing of Table 2. These curves reproduce the wing tip LCO at 29 m/s.

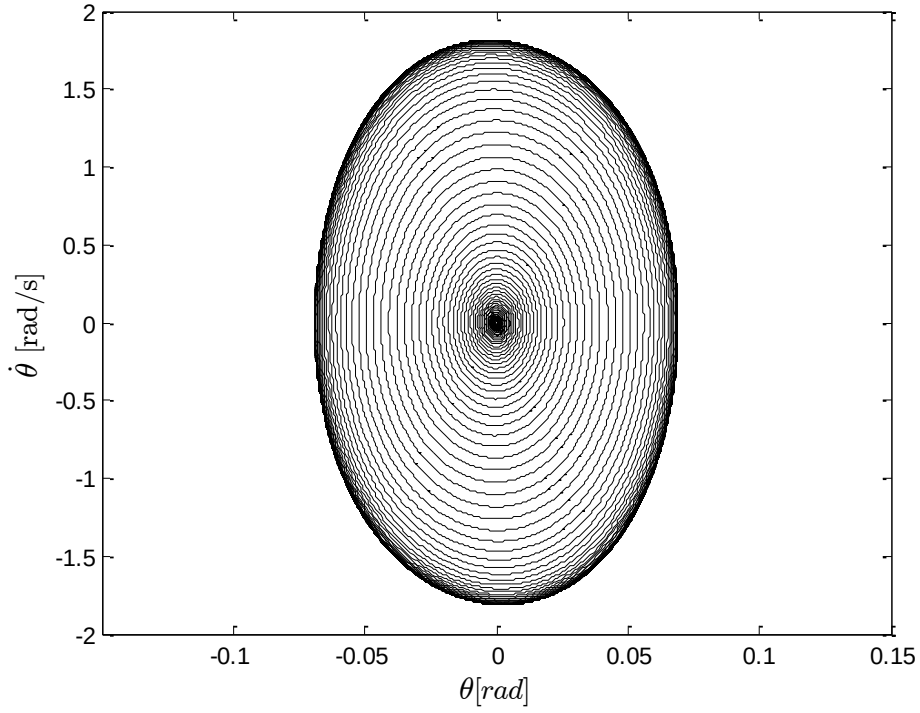

Figure 13 Pitch phase diagram at 29 m/s.

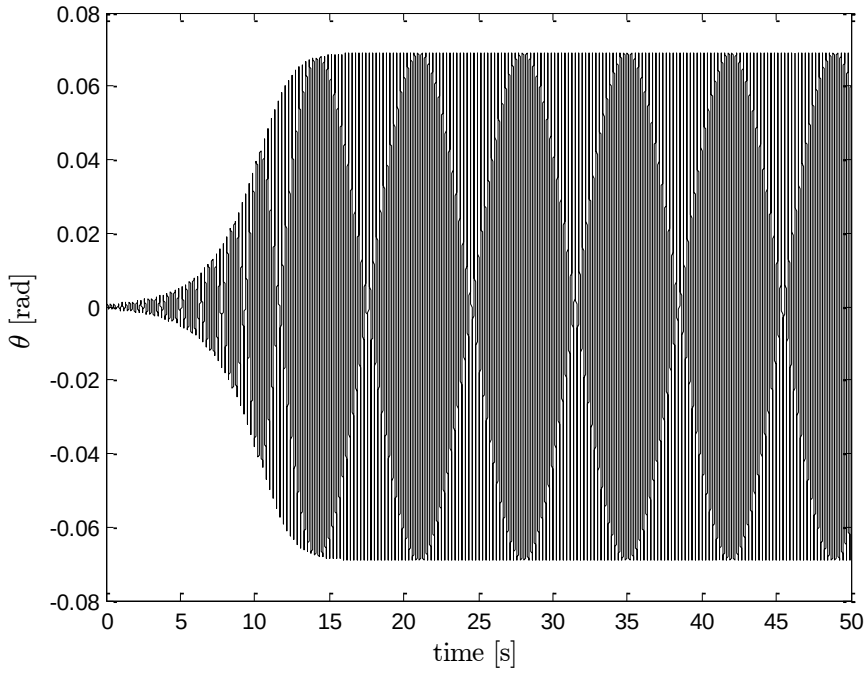

Figure 14 Pitch time history at 29 m/s.

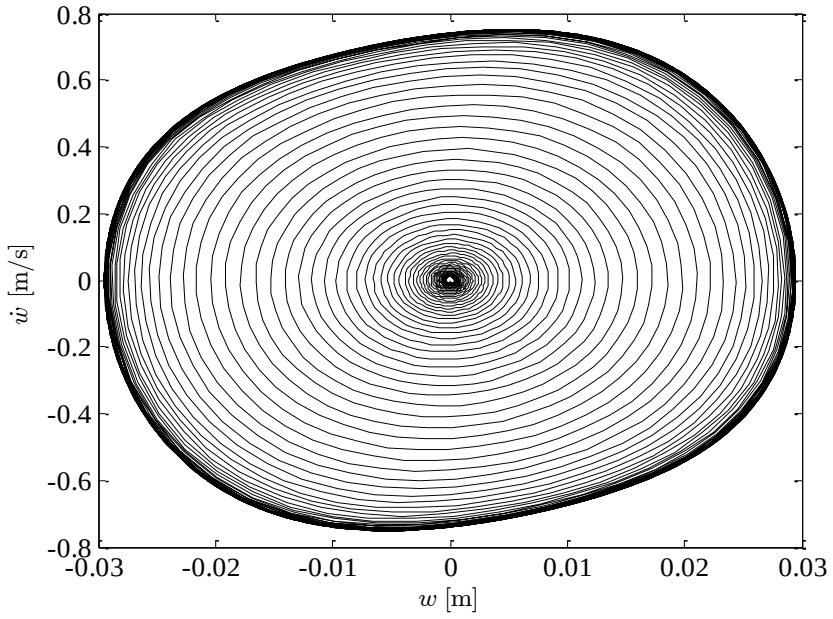

Figure 15 Plunge phase diagram at 29 m/s.

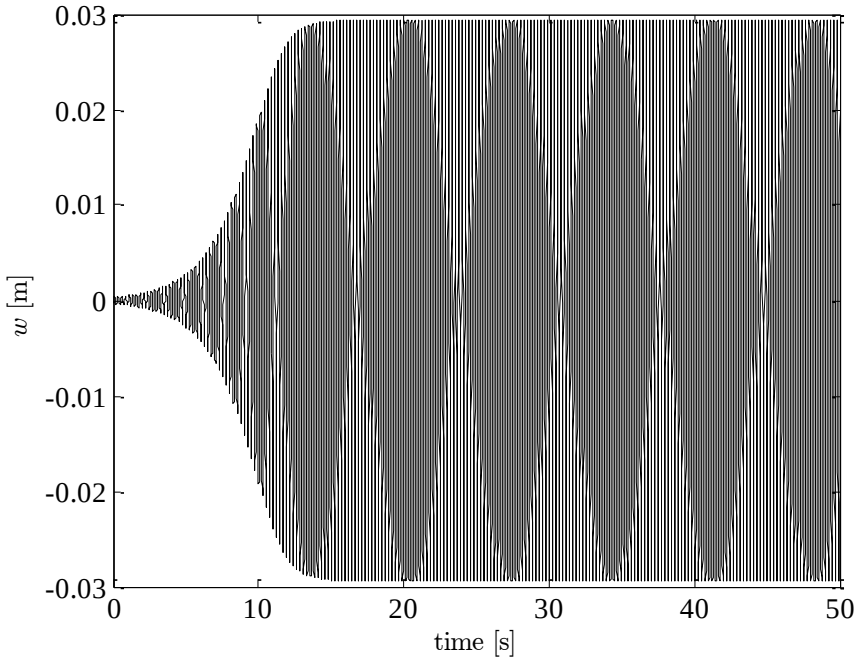

Figure 16 Plunge time history at 29 m/s.

The phase diagrams, Figures 13 and 15, show clearly how after a short amount of time the motion of the wing tip becomes simple harmonic. The amplitude of the steady oscillation depends from the external airspeed as already shown in Figures 11 and 12; by increasing the airspeed from 29 m/s to 40 m/s and maintaining the same value of k we obtain the results of

Figures from 17 to 20. The oscillation amplitude increases with the airspeed increase, coherently whit the results presented in Figures 11 and 12.

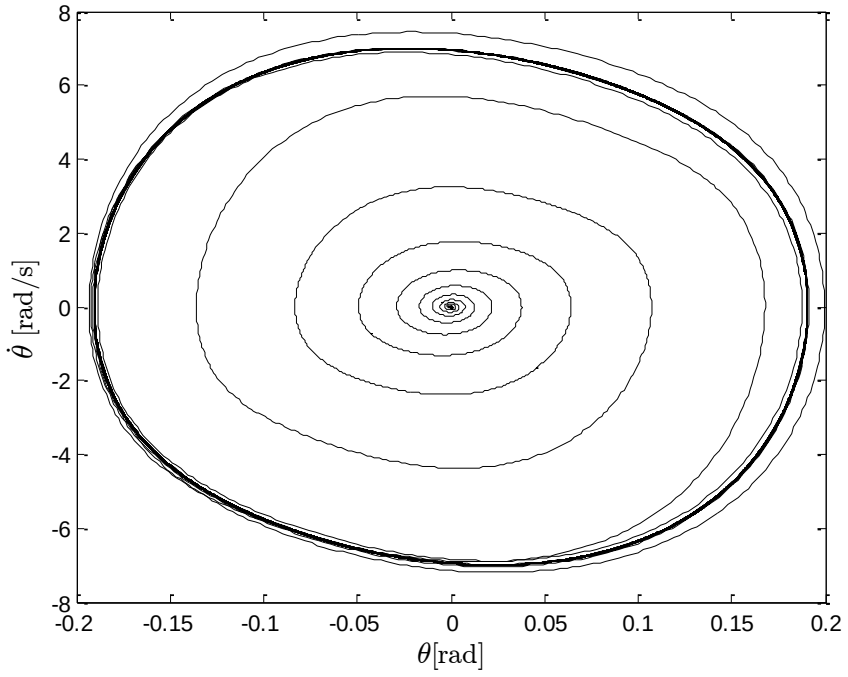

Figure 17 Pitch phase diagram at 40 m/s.

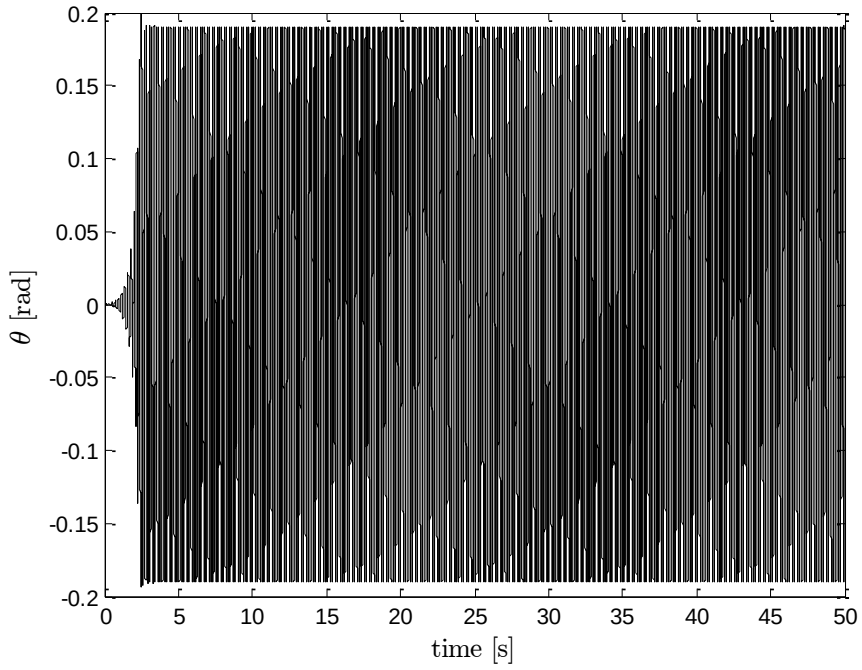

Figure 18 Pitch time history at 40 m/s.

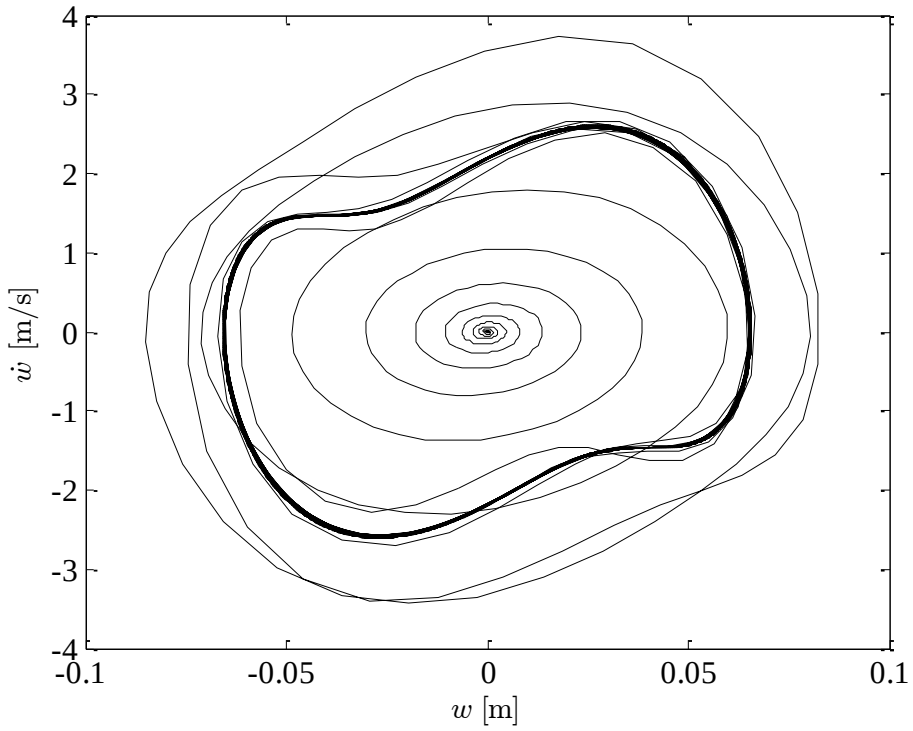

Figure 19 Plunge phase diagram at 40 m/s.

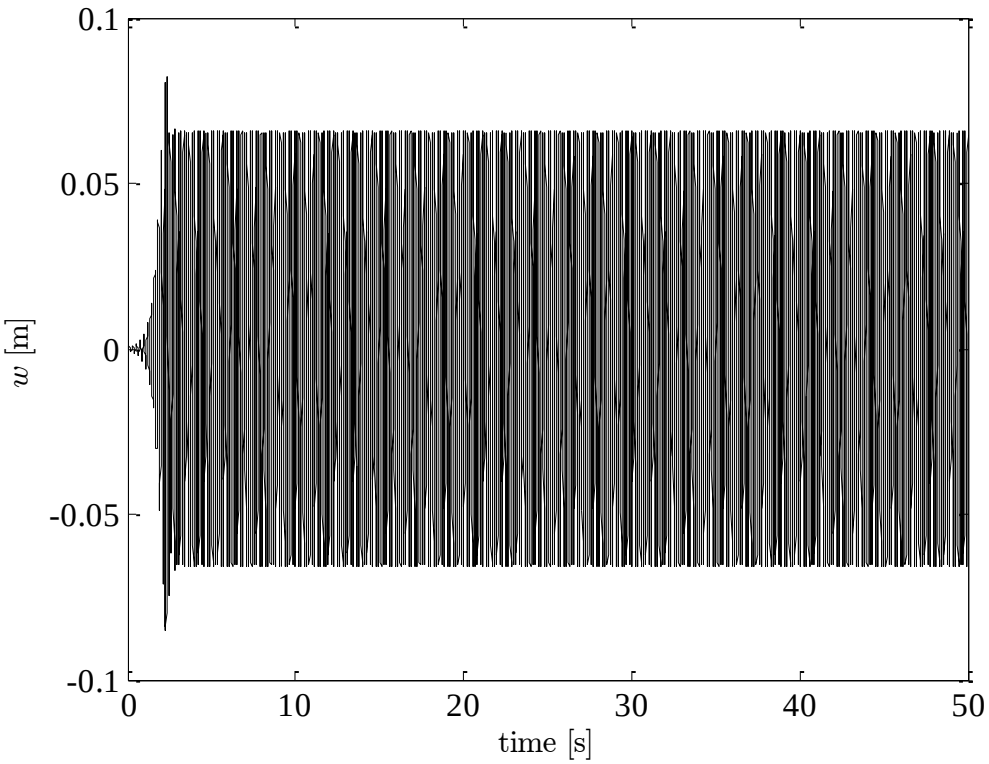

Figure 20 Plunge time history at 40 m/s.

3.3 Gust response

The motion of the air in the atmosphere can be characterized by two primary factors: the duration of the motion and the amount of air involved in it. The short and temporary motion of a small amount of air with respect to its surrounding is called gust. The study of the air motion in the atmosphere is a complex activity since its nature is purely chaotic. However, for the sake of simplicity and thanks to the experimental data collected during the years, this macroscopically chaotic motion can be reduced into a sequence of recognizable structures, Figure 21. The approximation of a turbulent motion with a series of discrete gust profiles is a clear simplification of what happens in reality, moreover the experimental results and the successes in the aircraft design till nowadays are the main evidence of the reliability of this approach [9].

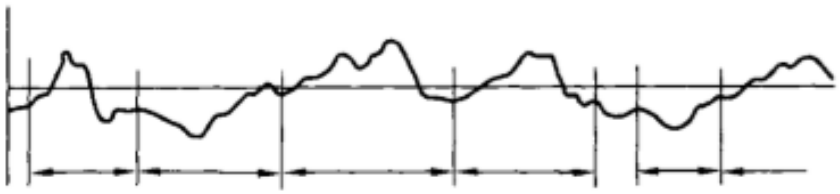

Figure 21 Turbulence profile [9].

The gust can occur with different orientations with respect to the aircraft body frame due to the isotropic nature of atmospheric turbulence, but what mostly affect the aircraft design are the vertical and lateral gusts. This is the reason why a wide literature is available on the impact of the vertical and lateral gusts over the aircraft design rather than of the longitudinal, for example. The sources of turbulence are various, the most common are the storm, the cumulus-cloud and also the clear air. In particular this last, although it represents the less severe type of turbulence, it is gaining a lot of attention in the most recent years due to the tendency for aircrafts to

perform high altitude flights. The atmosphere is characterized by three distinct layers of turbulence: the first, placed from 5500 m to 9000 m, where the gust can be very intense, the second, from 9000 m to 1200m, where the gust is less intense and lose continuously its intensity up to 14500 m, and finally the third, from 14500 m onward, where the intensity grows again. The cruise altitude, at which the aircraft spends most of its flying time, is generally contained in the range between 9000 m and 1200 m, therefore it represents the altitude where we have an higher probability of encountering a gust disturbance. The clear air characterizing the cruise altitude guarantees the presence of less severe gust profiles but at the same time less predictable, therefore not avoidable by the pilot during the flight mission. Three types of deterministic gust profiles, sharp edge gust, graded gust and 1-cosine gust, responsible of the structure elastic vibrations, are commonly studied in the frame of the gust induced loads. Albeit the availability in the literature of the three mentioned gust shapes only the 1-cosine is prescribed by the airworthiness standards of the FAA and EASA as design criterion. The reason why the first two type of gust are important can also be found in the pioneering work of Kussner, von Karman and Sears [9], [10] , where these analytical representations are use to describe the penetration of a 2D airfoil to a gust and description led to important close form solutions that are still used today. This section proposes a study on the dynamical response to gust loads which includes all the three previous mentioned gust profiles. Factually if we imagine a gust which coming from the bottom hits the aircraft, instead of being crossed by the aircraft trajectory, we can assume that the sharp-edge gust represents a satisfactory approximation of the event. Based on this assumption each of the three gust profiles was considered for the purpose of this study. The study of gust event is important not only for the simple induced dynamic

response but also because it can act as trigger for some more critical aeroelastic instabilities.

3.3.1 Sharp-edge gust

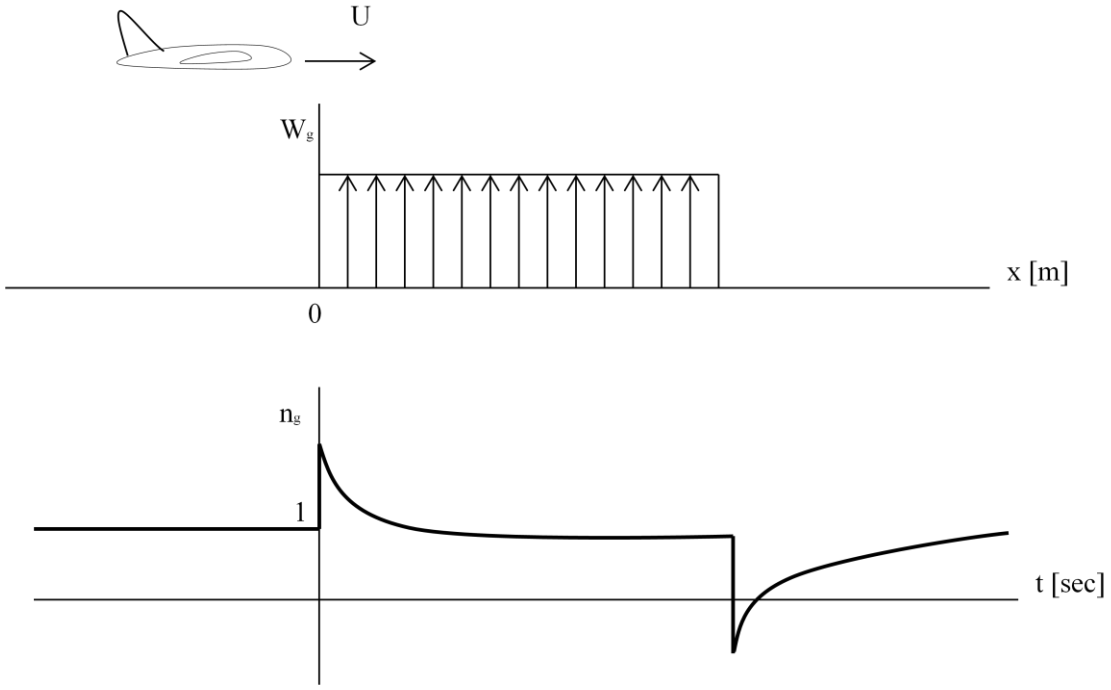

Figure 22 Sharp edge gust profile. Plot based on [11].

The sharp-edge gust profile doesn't show a transition zone, which means that when the aircraft enter into the atmospheric disturbance with U as its horizontal speed this is instantaneously combined with the maximum and constant value of the gust speed intensity. Figure 22 shows in its upper part the sharp-edge gust profile with respect to the space coordinate while the lower plot reproduce the tendency of the load factor due to the sharp-edge gust. The phases which have to be highlighted in the load factor evolution are:

The aircraft horizontal speed U combines with the gust vertical speed W_g creating an abrupt variation of the pitch angle

$$\Delta\alpha_1 \cong \frac{W_g}{U} \qquad 3.9$$

The lift increase, due to the pitch angle variation, produces a vertical acceleration and generate the inertial forces which excite the structure. The aircraft vertical speed will gradually increase, reducing the relative vertical air speed. Due to this new variation of the pitch angle, the acceleration and consequently the inertial forces will decrease.

After a certain time the aircraft vertical speed will reach the same value as the gust vertical speed, therefore the aircraft will move of uniform motion over a linear trajectory with ramp angle equal to:

$$\beta \cong \frac{W_g}{U} \qquad 3.10$$

The mathematical expressions for the sharp-edge gust profiles is:

$$W_g(t) = H(t)\bar{W}_g \qquad 3.11$$

3.3.2 Graded gust

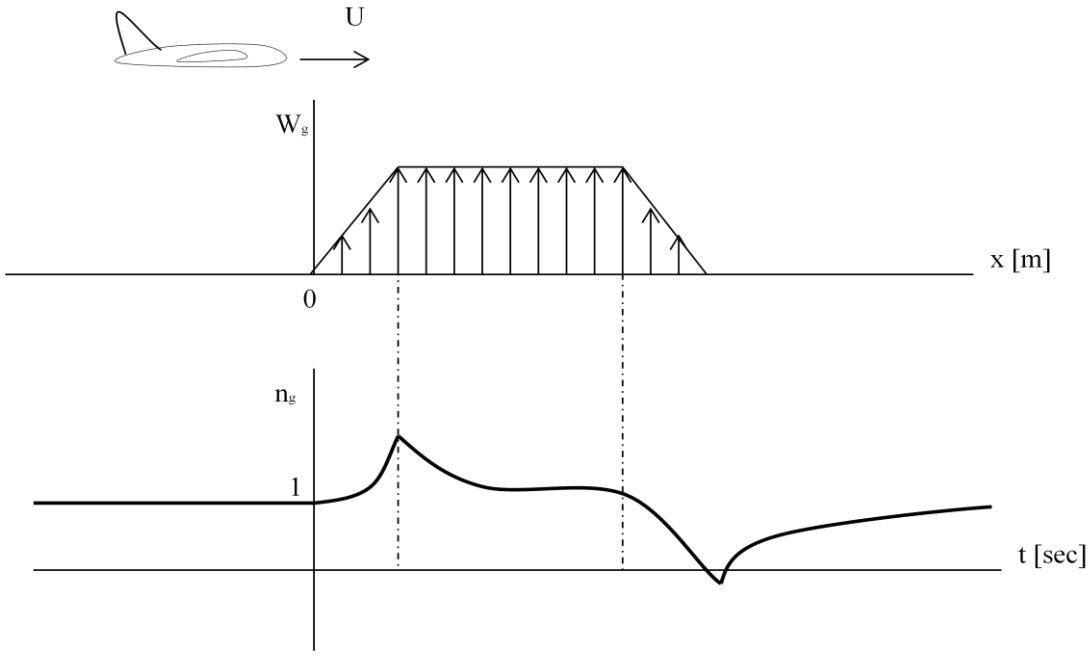

Figure 23 Graded gust profile. Plot based on [11].

The graded gust profile derives from the sharp-edge gust profile with the only difference that we assume that due to the air viscosity the aircraft will more likely experience a gradual increase of the vertical gust speed. The mathematical expression for the graded gust profile is:

$$W_g(t) = H(t)\bar{W}_g(1 - e^{-0.75t}) \qquad 3.12$$

3.3.3 1-Cosine gust

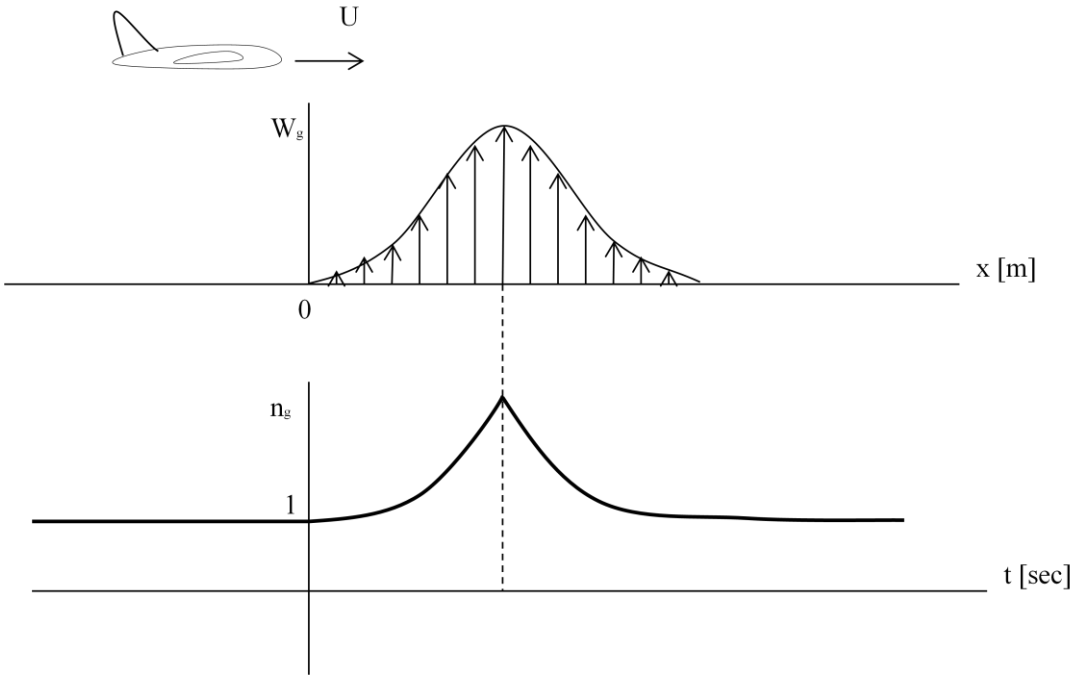

Figure 24 1-Cosine gust profile. Plot based on [11].

As already mentioned the 1-Cosine gust profile is the only discrete gust profile, among those presented in this section, prescribed by the airworthiness regulations as a condition to be checked in order to certify the aircraft. Although new models have been developed during the years to get a more realistic representation of the atmospheric disturbances trough a continuous turbulence representation, the 1-cosine discrete gust still remain a certification criterion.

The mathematical expressions for the 1-Cosine gust profiles is:

$$W_g(t) = H(t)\frac{1}{2}\bar{W}_g\left(1 - cos\frac{\pi t}{t_g}\right) - H(t - 2t_g)\frac{1}{2}\bar{W}_g\left(1 - cos\frac{\pi t}{t_g}\right) \qquad 3.13$$

$H(t)$ is the unitary step function while $\bar{W}_g$ represent the intensity of the maximum vertical speed of the gust. $t_g = \frac{H}{U}$ is the time took by the aircraft to cross a distance equal to the gust gradient H. The numerical value of H is prescribed by the FAARs and the EASA respectively in PART 25.341 and CS 25.3041. The simulations have to cover a range of value for the gust gradient which goes from 9.14 m to 106,68 m. The gust loads, the lift and the aerodynamic moment due to the gust, are evaluated for each specific gust profile according to the formula:

$$L_g = 2\pi\rho bU\left(W_g(0)\,\Psi(t) + \int_0^t \frac{\partial W_g(\sigma)}{\partial\sigma}\Psi(t-\sigma)\,d\sigma\right) \qquad 3.14$$

where σ is a time variable and $\Psi(t)$ the Kuessner function, defined as [1], [8], [9]: Graded gust:

$$W_g(t) = H(t)\bar{W}_g(1 - e^{-0.75t}) \qquad 3.12$$

$$\Psi(t) = 1 - A_3 e^{-b_3\frac{U}{b}t} - A_4 e^{-b_4\frac{U}{b}t} \qquad 3.15$$

The Kuessner function $\Psi(t)$ introduce a delay to the aircraft response when subjected to a gust disturbance. Therefore, the variation of the pitch angle of the aircraft is not instantaneous, it is required a certain time before experiencing the expected pitch angle gradient. By applying integration by parts to 3.14, the lift due to the gust become:

$$L_g = 2\pi\rho bU\int_0^t W_g(\sigma)\,\dot{\Psi}(t-\sigma)\,d\sigma \qquad 3.16$$

References

[1] Bisplinghoff, R., Ashley, H., Halfman, R., Aeroelasticity, Dover 1996.

[2] Abbas, L.K., Chen, Q., Marzocca, P., Milanese, A., “Non-linear aeroelastic investigations of store(s)-induced limit cycle oscillations”, Proc. IMechE Vol. 222 Part G: J. Aerospace Engineering, 2008.

[3] Strogatz, S. H., Nonlinar Dynamic and Chaos, Westview Press 2015.

[4] Strganac, T. W., "Theoretical and Experimental Investigations of Internal Resonances, and Related Behavior, in Nonlinear Aeroelastic Systems", AFOSR GRANT NO. F.49620-00-1-0051, June 2004.

[5] Bunton, R. W., Deenegri Jr., C. M., "Limit Cycle Oscillation Characteristics of Fighter Aircraft".

[6] Patil,M. J., Hodges, D. H., Cesnik, C. E. S., "Limit Cycle Oscillations in High-Aspect-Ratio Wings", Journal of Fluids and Structures, 2001.

[7] Seydel, R., Basic Bifurcation Phenomena, Word of Bifurcation 1999.

[8] Fung, Y. C., An Introduction to the Theory of Aeroelasticity, Dover 1968.

[9] F. Hoblit (1988). Gust Loads on Aircraft: Concepts and Applications. American Institute of Aeronautics & Astronautics.

[10] Di Jan R. Wright,Jonathan E. Cooper, Introduction to Aircraft Aeroelasticity and Loads, ISBN: 978-1-118-48801-0

[11] Lausetti, A., Filippi, F., Elementi diMeccanica del Volo, Libreria Editrice Universitaria Levrotto & Bella, 1984.

4 Dedicated study on the Nonlinear response of a slender wing

The mathematical model presented in the previous chapters has been numerically carried out and solved via a Matlab routine and a Simulink block scheme. To reduce the computation time of the modal matrices in the Matlab domain, these matrices have been implemented in symbolic form and solved for different dataset in the Mathematica workspace. Mathematica and Matlab have been connected in such a way that each time a new condition was analyzed, Matlab was able to take a new set of modal matrices from Mathematica and to solve equation 2.84 by a Runge-Kutta solver for each initial and external conditions set. In order to validate the analytical model, some simulations were run by using the data available in Tang and Dowell [1]. In particular, for reasons of similarity with the loading conditions analyzed in the current work, Case 2 of the work of Tang and Dowell [1] was reproduced and presented in Table 3.

Table 3 Comparison between the results obtained by Tang and Dowell [1] and those obtained by the current model.

	Tang and Dowell [11]- Case 2	**Current work**
Flutter speed	32.5 m/s	33.59 m/s
Flutter frequency	22.8 rad/s	21.18 rad/s
Flutter speed at circa 1.6 m of steady tip displacement	~13 m/s	~13 m/s
Flutter frequency at circa 1.6 m of steady tip displacement	~8 rad/s	~7.67 rad/s

Flutter speed at circa 1 m of steady tip displacement	~27 m/s	~27 m/s
Flutter frequency at circa 1 m of steady tip displacement	~18 rad/s	~17.14 rad/s

The data reported in Table 3 show how the current numerical model provide a set of results in agreement with those available in the literature. That is an initial validation of the model but necessary to analyze the next set of results with an higher level of confidence. The numerical results which follow refer to the wing of Table 4.

Table 4 Wing Model [2] used for numerical simulations

Description of the variable	**Variable name**	**Value**
Wing chord	c	0.046 m
Wing semi-span	l	0.522 m
Wing mass per unitary length	m_w	0.022 kg/m
Polar inertia of the wing w.r.t. the elastic axis	I_y	$6.20 \cdot 10^{-6}\ kg \cdot m$
Elastic axis location in half-chord w.r.t. the mid-chord position	a	0
Mass center location in half-chord w.r.t. the elastic axis position	x_a	0
Torsion stiffness of the wing cross section	D_{22}	$0.315\ N \cdot m^2$
Out of plane bending stiffness of the wing cross section	D_{11}	$0.31\ N \cdot m^2$
In plane bending stiffness of the wing cross section	D_{33}	$30\ N \cdot m^2$

The good agreement with Tang and Dowell [1] results, Table 3, shows how the current numerical model is able to capture the specific pre flutter dynamic response, typical of a certain kind of wings when subjected to a notable out of plane deflection. To verify if a similar behavior characterize also the wing of Table 4, the solutions of the equations of motion 2.64, 2.65 and 2.66 in the frequency and time domains are presented hereafter. In particular, to better understand the procedure which leads to the flutter solution in the frequency domain, please refer to Chapter 3.

The wing model of Table 4 shows a critical flutter speed equal to 32.886 m/s circa and a flutter frequency of about 76.68 Hz. These values are obtained assuming a zero steady state deflection of the wing and they are confirmed by both frequency and time domain procedures. Figures 25 and 26 contain the V-g plots, for the wing of Table 3, from which we can identify the flutter condition when the artificial damping g is equal to zero.

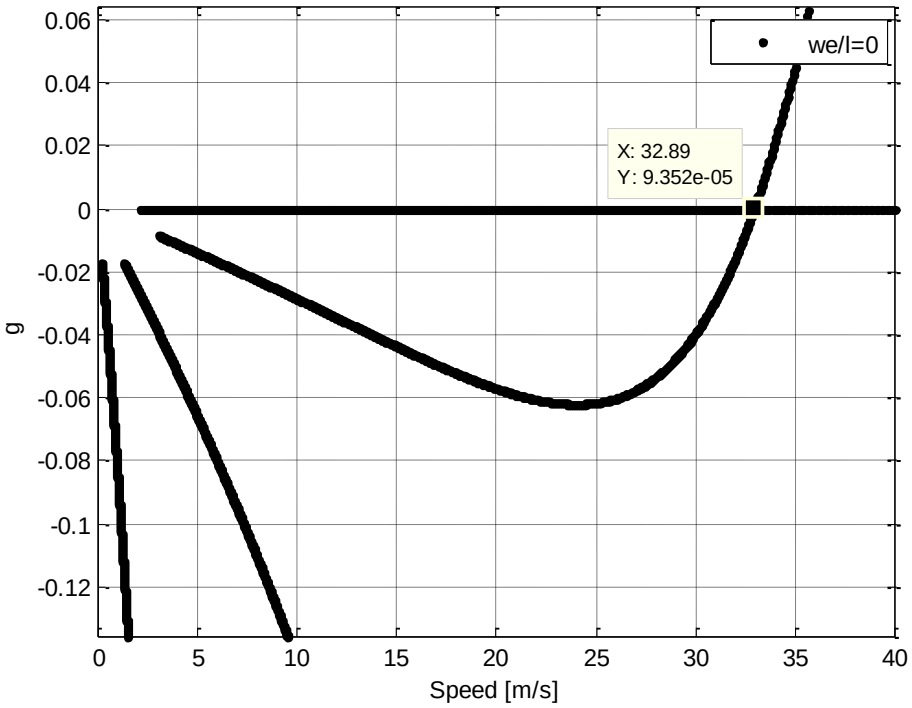

Figure 25 Artificial damping vs. air speed for the non-deflected wing of Table 4

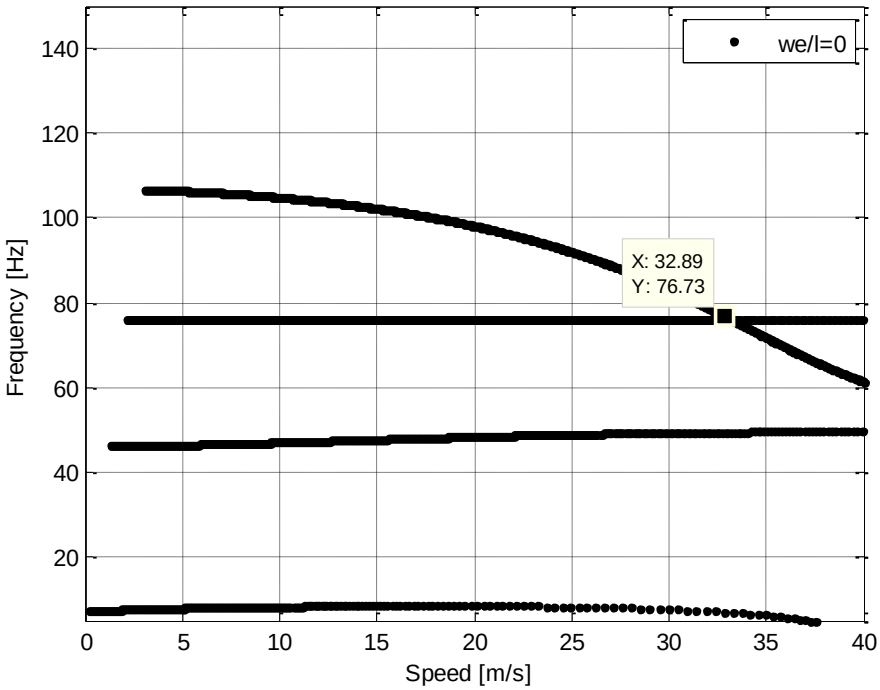

Figure 26 Frequency vs. air speed for the non-deflected wing of Table 4

Figures 27 and 28 show the FFT of the flutter time histories reported in Figures 29 and 30.

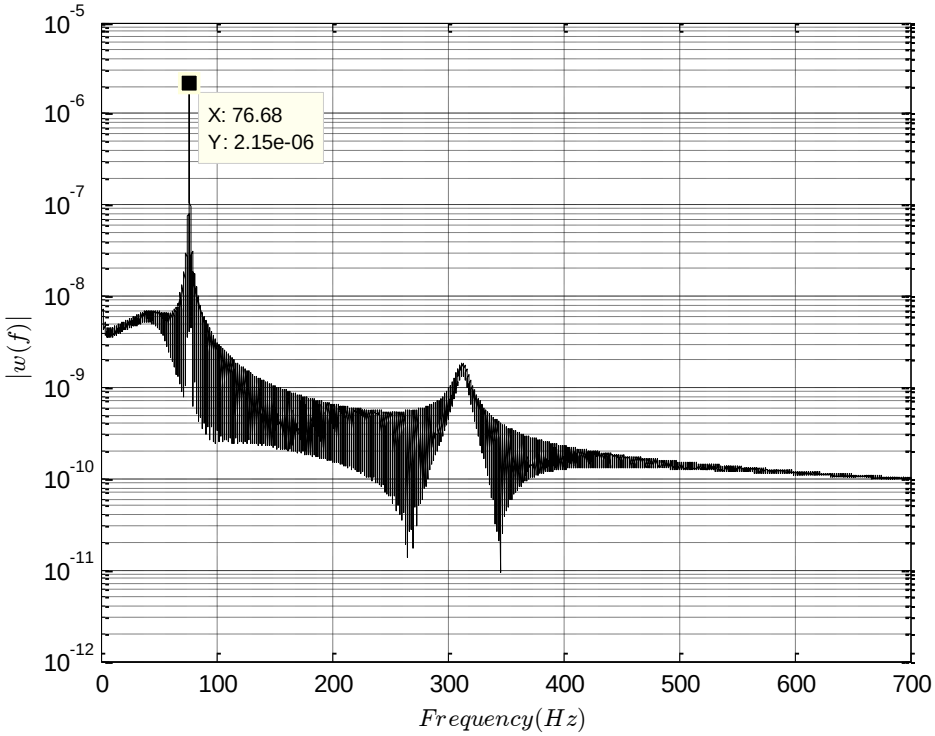

Figure 27 FFT of the plunge response of the wing of Table 4

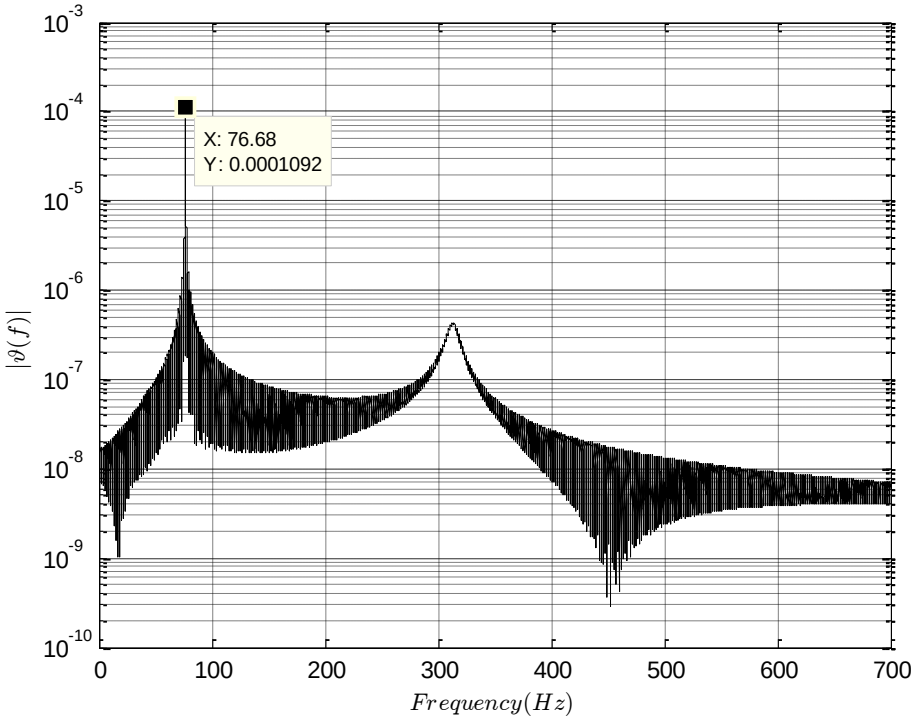

Figure 28 FFT of the pitch response of the wing of Table 4

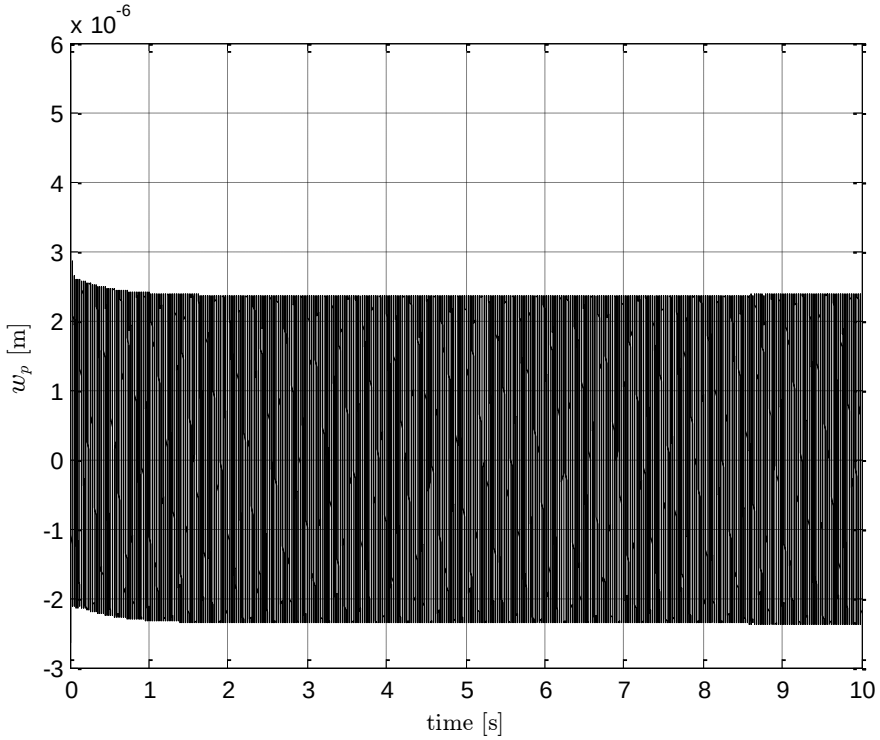

Figure 29 Plunge time history at the critical flutter condition

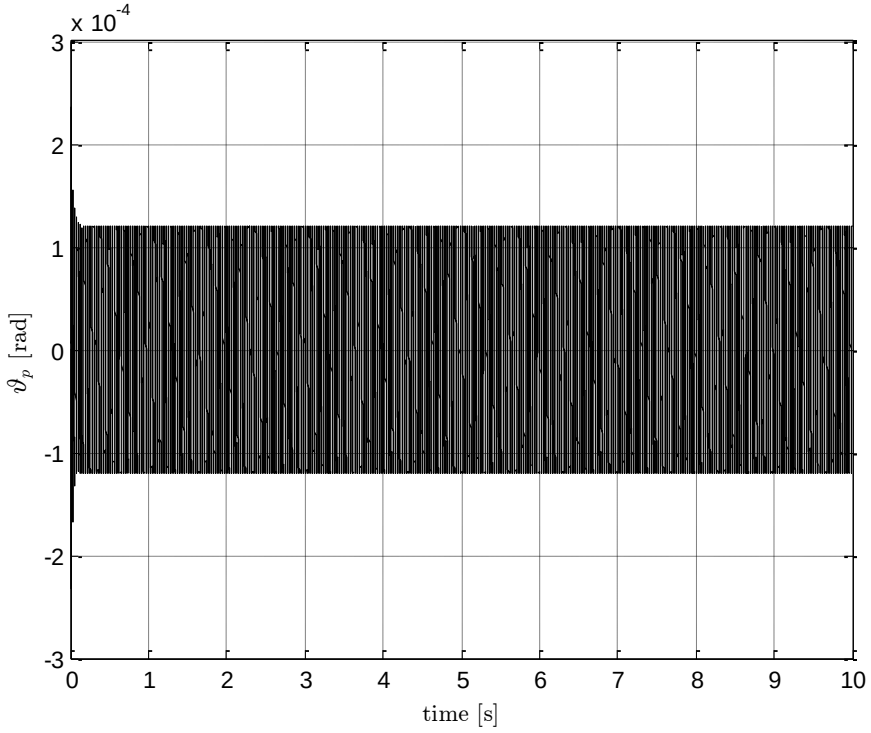

Figure 30 Pitch time history at the critical flutter condition

As for the Tang and Dowell wing of Table 3, also the wing of Table 4, shows an anticipated LCO, which occurs at speed lower than the critical flutter speed, and depending on the wing steady state deflection. In order to highlight the importance of the nonlinear terms order, the results which follow are split according to the order of nonlinearity retained into the solution and the number of modes used for the analysis, therefore the single mode and the multimode solutions are presented in two separate sections. The most direct way to check if the wing shows a pre-flutter LCO is to analyze the solution of the incipient LCO in the frequency domain, trough the methods used for the critical flutter condition in Chapter 3. To account for the effect of the wing steady state deflection in the frequency solution, equation 2.90 have to be linearized in the perturbations terms, while the nonlinear equilibrium terms become a constant when a specific equilibrium solution is assumed. Therefore, the stiffness matrices of equation 2.90, when only the main third order terms are retained, according to the asymptotic reduction procedure, become:

$$K_{s_e} = \begin{bmatrix} [K_{\theta_e}] \\ [K_{w_e}] \\ [K_{u_e}] \end{bmatrix},\ K_{s_p} = \begin{bmatrix} [K_{\theta_p}] \\ [K_{w_p}] \\ [K_{u_p}] \end{bmatrix},\ K_{s_{ep}} = \begin{bmatrix} [K_{\theta_{ep}}] \\ [K_{w_{ep}}] \\ [K_{u_{ep}}] \end{bmatrix} \quad 4.1$$

$$K_{\theta_e} = D_{22}\theta_e'' + (-D_{11} + D_{22} + D_{33})u_e''w_e'' + D_{22}u_e'w_e''' + (-D_{11} + D_{33})\theta_e u_e''^2 + (D_{11} - D_{33})\theta_e w_e''^2 \quad 4.2$$

$$K_{\theta_p} = D_{22}\theta_p'' \quad 4.3$$

$$K_{\theta_{ep}} = (-D_{11} + D_{22} + D_{33})\left(u_e'w_p'' + u_p''w_e''\right) + D_{22}\left(u_e'w_p''' + u_p'w_e'''\right) + (-D_{11} + D_{33})\left(\theta_p u_e''^2 + 2\theta_e u_e''u_p''\right) + (D_{11} - D_{33})\left(\theta_p w_e''^2 + 2\theta_e w_e''w_p''\right) \quad 4.4$$

$$K_{w_e} = -D_{11}w_e'''' + (-D_{11} - 2D_{22} + D_{33})\theta_e''u_e'' + (-2D_{11} - D_{22} + 2D_{33})\theta_e'u_e''' + (-D_{11} + D_{33})\theta_e u_e'''' - D_{22}\theta_e'''u_e' - (D_{33} - D_{11})\theta_e^2 w_e'''' - 4(D_{33} - D_{11})\theta_e\theta_e'w_e'''' + 2(\mathrm{D}_{11} - \mathrm{D}_{33})\theta_e w_e''\theta_e'' + 2(\mathrm{D}_{11} - \mathrm{D}_{33})\theta_e'^2 w_e'' \quad 4.5$$

$$K_{w_p} = -D_{11}w_p'''' \quad 4.6$$

$$K_{w_{ep}} = (-D_{11} - 2D_{22} + D_{33})\left(u_e''\theta_p'' + u_p''\theta_e''\right) + (-2D_{11} - D_{22} + 2D_{33})\left(u_p'''\theta_e' + u_e'''\theta_p'\right) + (-D_{11} + D_{33})\left(\theta_e u_p'''' + \theta_p u_e''''\right) - D_{22}\left(\theta_e'''u_p' + \theta_p'''u_e'\right) - (-D_{11} + D_{33})\left(\theta_e^2 w_p'''' + 2\theta_e\theta_p w_e''''\right) - 4(-D_{11} + D_{33})\left(\theta_e'\theta_p w_e''' + \theta_p'\theta_e w_e''' + \theta_e'\theta_e w_p'''\right) + 2(D_{11} - D_{33})\left(\theta_e w_e''\theta_p'' + \theta_e w_p''\theta_e'' + \theta_e w_p''\theta_p'' + \theta_p w_e''\theta_e'' + \theta_p w_e''\theta_p'' + \theta_p w_p''\theta_e''\right) + 2(D_{11} - D_{33})\left(\theta_e'^2 w_p'' + \theta_p'^2 w_e'' + 2\theta_e'\theta_p' w_e'' + 2\theta_e'\theta_p' w_p''\right) \quad 4.7$$

$$K_{u_e} = -D_{33}u_e'''' + (-D_{11} + D_{22} + D_{33})w_e''\theta_e'' + (-2D_{11} + D_{22} + 2D_{33})w_e'''\theta_e' + (-D_{11} + D_{33})\theta_e w_e'''' \quad 4.8$$

$$K_{u_p} = -D_{33}{u_p}'''' \qquad 4.9$$

$$K_{u_{ep}} = (-D_{11} + D_{22} + D_{33})\left({w_e}''{\theta_p}'' + {w_p}''{\theta_e}''\right) + (-2D_{11} + D_{22} + 2D_{33})\left({w_p}'''{\theta_e}' + {w_e}'''{\theta_p}'\right) + (-D_{11} + D_{33})\left(\theta_e {w_p}'''' + \theta_p {w_e}''''\right) \qquad 4.10$$

Equations from 4.1 to 4.10 show how the equilibrium matrices become constants when the equilibrium or better the steady state solution is assigned previously. This procedure allows a linear analysis which accounts for the nonlinear contribution of the equilibrium terms and for the effect of the wing deformation over the frequency analysis. As previously mentioned, the V-g method, which is a typical method to identify the flutter condition, can be also used for the identification of the pre-flutter LCO, if any exists. The V-g method, as deeply explained in Chapter 3, is based on the linear equations of motion which are written in the frequency domain and solved as an eigenvalues problem. The pre-flutter LCO is investigated for the wing of Table 4 which behaves as by equation 2.84, where the stiffness matrices are those from equation 4.2 to 4.10 and the steady state generalized coordinates as in Table 5.

Table 5 Steady state value of the wing generalized coordinates

w_e/l	$r_{\theta_{e1}}$	$r_{\theta_{e2}}$	$r_{w_{e1}}$	$r_{w_{e2}}$	$r_{u_{e1}}$	$r_{u_{e2}}$	**Plot color**
0	0	0	0	0	0	0	black
0,06705	0	0	0,018	2,5436*10^-4	0	0	red
0,136015	0	0	0,036	5,0872*10^-4	0	0	magenta
0,175954	0	0	0,0465	6,5624*10^-4	0	0	green

Table 5 contains four steady state deformation conditions of the wing, w_e/l, and the corresponding value of the generalized coordinates which have

been estimated through a time domain solution of the steady state response of the wing when subjected to a vertical load applied at the wing shear center. The column of Table 5 called " **Plot color**" refers to the colors of the curves in Figures from 31 to 34. The point highlighted in Figure 31, which correspond to an air speed value of 21.69 m/s and about zero artificial damping, is the incipient LCO condition of the wing of Table 4 when its steady state displacement is the 13% circa of the semi wing span. The value obtained is substantially in line with the experimental values reported in [2]. What Figures from 31 to 34 highlight is that by increasing the wing steady deformation, the LCO solution moves towards lower air speed values. The main difference between Figures 31-32 and Figures 33-34 is that the first two, that's to say Figures 31 and 32, are obtained by retaining only the second order nonlinear equilibrium terms of equations from 4.2 to 4.10, while the second two, Figures 33 and 34, retain also the main nonlinear terms up to the third order.

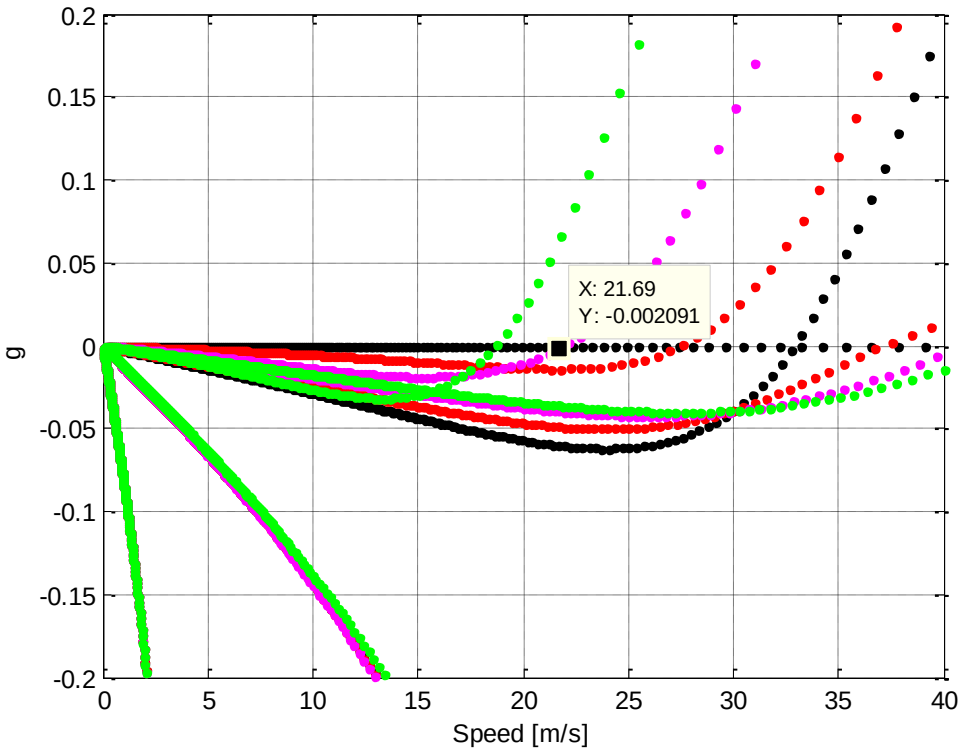

Figure 31 Artificial damping vs. air speed for the wing steady state conditions of Table 3 and nonlinear equilibrium terms up to the second order.

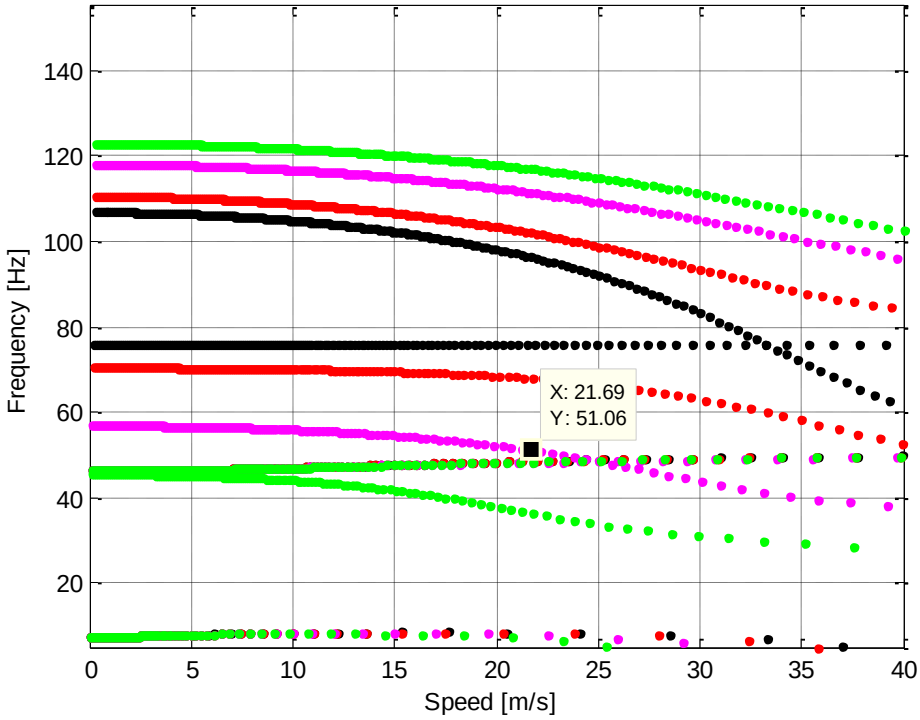

Figure 32 Frequency vs. air speed for the wing steady state conditions of Table 3 and nonlinear equilibrium terms up to the second order.

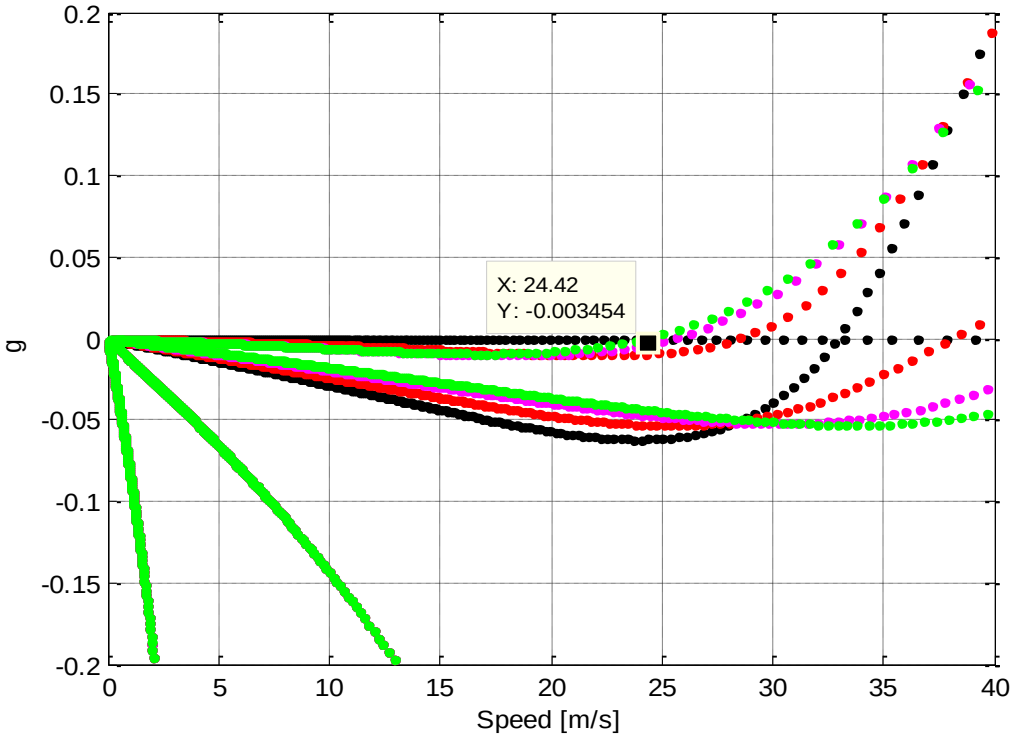

Figure 33 Artificial damping vs. air speed for the wing steady state conditions of Table 3 and nonlinear equilibrium terms up to the third order.

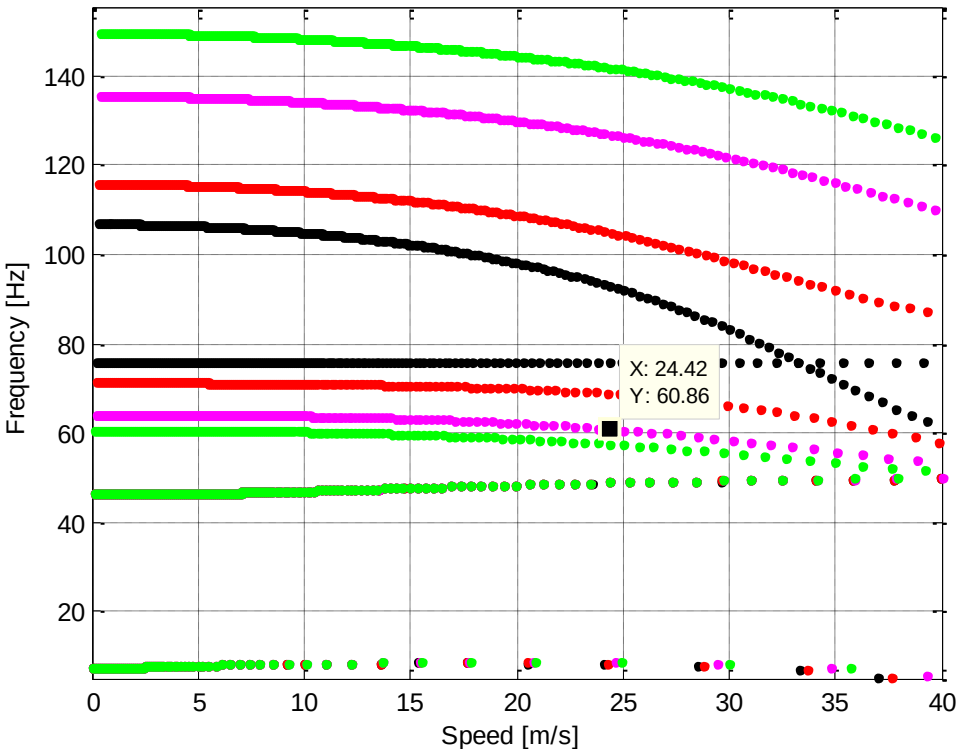

Figure 34 Frequency vs. air speed for the wing steady state conditions of Table 3 and nonlinear equilibrium terms up to the third order.

The interesting things of these results is that when we include into the numerical model the nonlinearities up to the third order the LCO condition arise at higher air speed value, moving the solution to the right side of the plots. What happen with the inclusion of the third order nonlinear terms is a stiffening effect of the model. This results is confirmed also by the time domain solution which is presented later on. The numerical results are split in four subsections: **Single-Mode analysis**, **Multi-Mode analysis**, **Effect of the main third order nonlinear terms in the flap equation** and **Experimental analysis**. The results of first subsection, **Single-Mode analysis**, refer to an analytical model which includes all the nonlinear terms up to the second order in all equations of motion of the perturbed system, and up to the third order only on the torsion equation of the equilibrium system. The simulations shown that the numerical model with nonlinear terms truncated at the second order is not always able to

guarantee a correct value of the equilibrium solution. In particular, for the assigned value of α_{trim} which gives a static vertical tip displacement of approximately 0.071 m the solution diverges. The lack of an equilibrium solution when the analytical model is limited to the second order of nonlinearity shifts the attention to the nonlinear terms of the third order. In fact, it is sufficient to introduce the third order nonlinear terms into the torsion equation, and keeping the other two governing equations to the second order, to reach a stable equilibrium solution. The higher order nonlinear terms are able to stabilize the solution since they introduce a stiffening contribution into the system.

The subsection entitled **Multi-Mode analysis** instead includes the third order nonlinear terms on both equilibrium and perturbed system but only in the torsion equation. In the subsection **Effect of the main third order nonlinear terms in the flap equation**, some third order nonlinear terms are added into the flap equation of motion. In particular, which third order terms have to included into the flap equation and which is worth to exclude is the object of the discussion of Chapter 2, where the main nonlinear terms are identified according to the asymptotic procedure. Finally, in **Experimental analysis**, the importance of the nonlinear terms is confirmed trough a set of experimental modal tests.

4.1 Single-Mode analysis

The results belonging to this subsection refer to a single mode model. The study of the multimodal response will be the content of the next subsection. M_e and L_e were set so to obtain a static wing tip vertical displacement of 0.071 m, similar to the value shown in [6] , corresponding to the incipient pre-flutter LCO. The current analysis shown a subcritical bifurcation point coherent with that identified experimentally and previously through the V-g method. At about 22m/s and with a static wing tip vertical displacement of 0.071 m, the time histories and the phase portraits of the displacement components at the wing tip are:

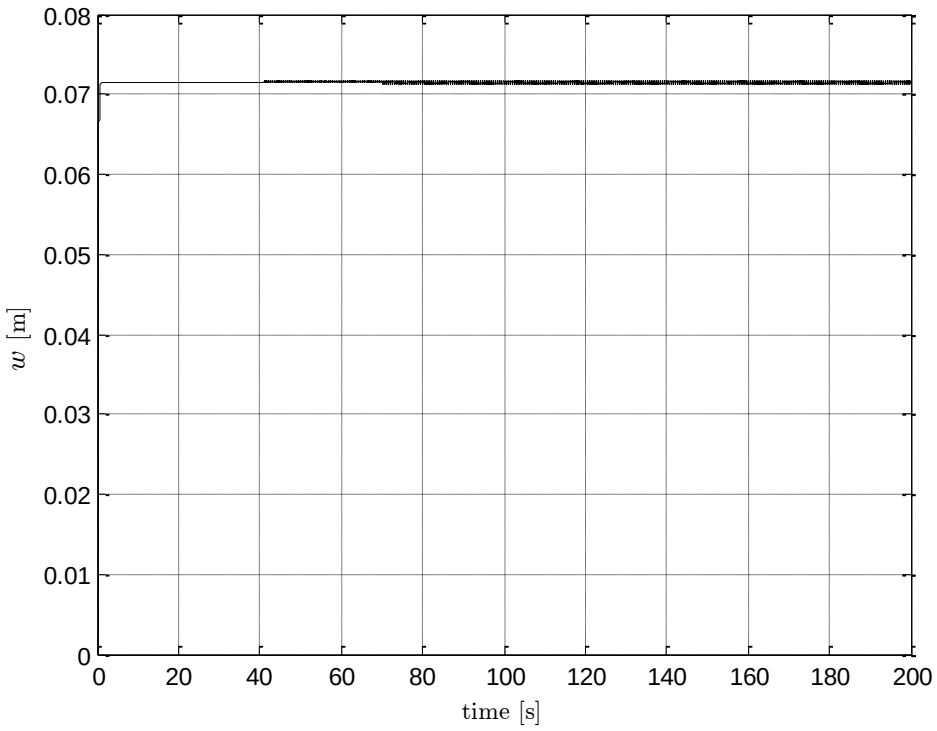

Figure 35 Time evolution of the wing tip vertical displacement [16], [17]

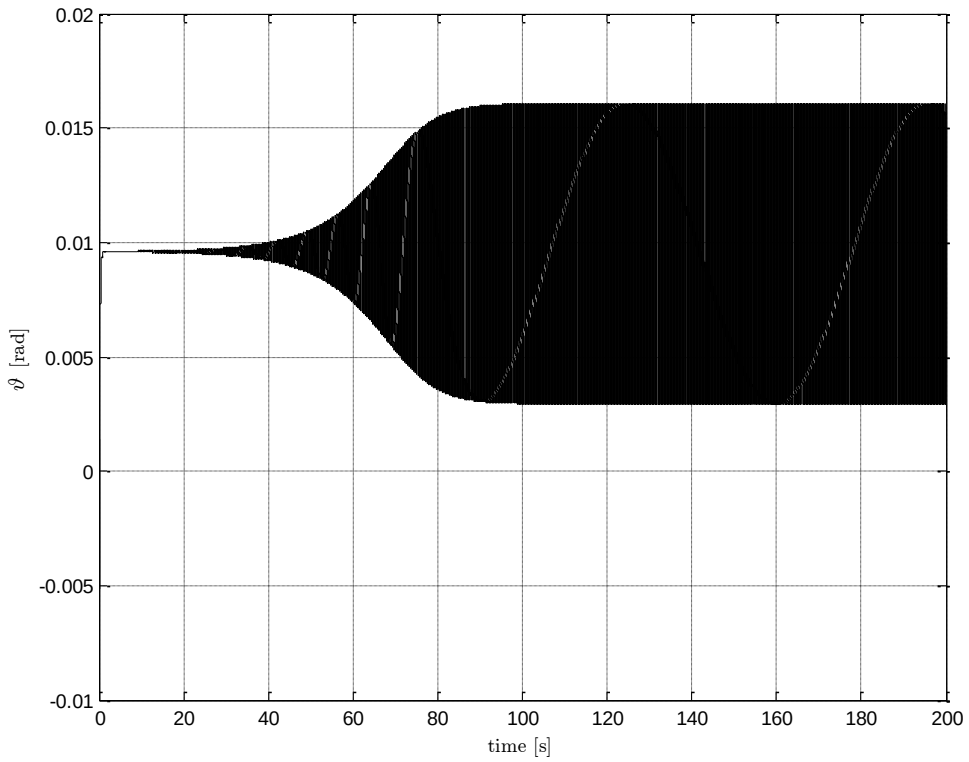

Figure 36 Time evolution of the wing tip pitch displacement [16], [17]

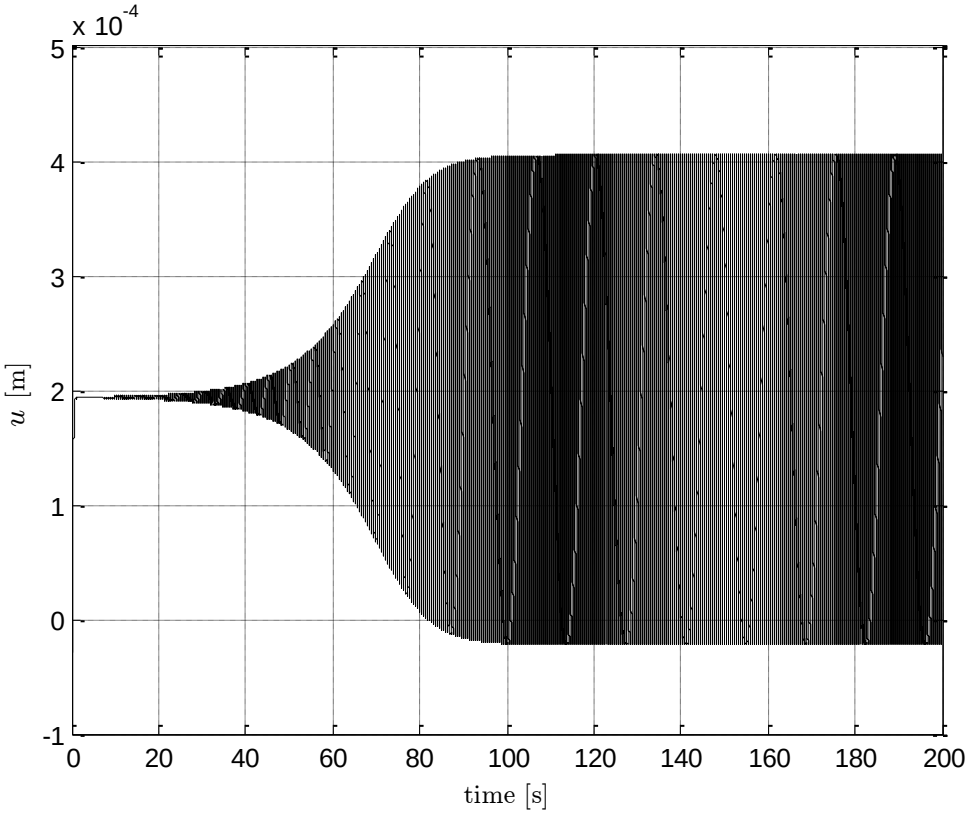

Figure 37 Time evolution of the wing tip lateral displacement [16], [17]

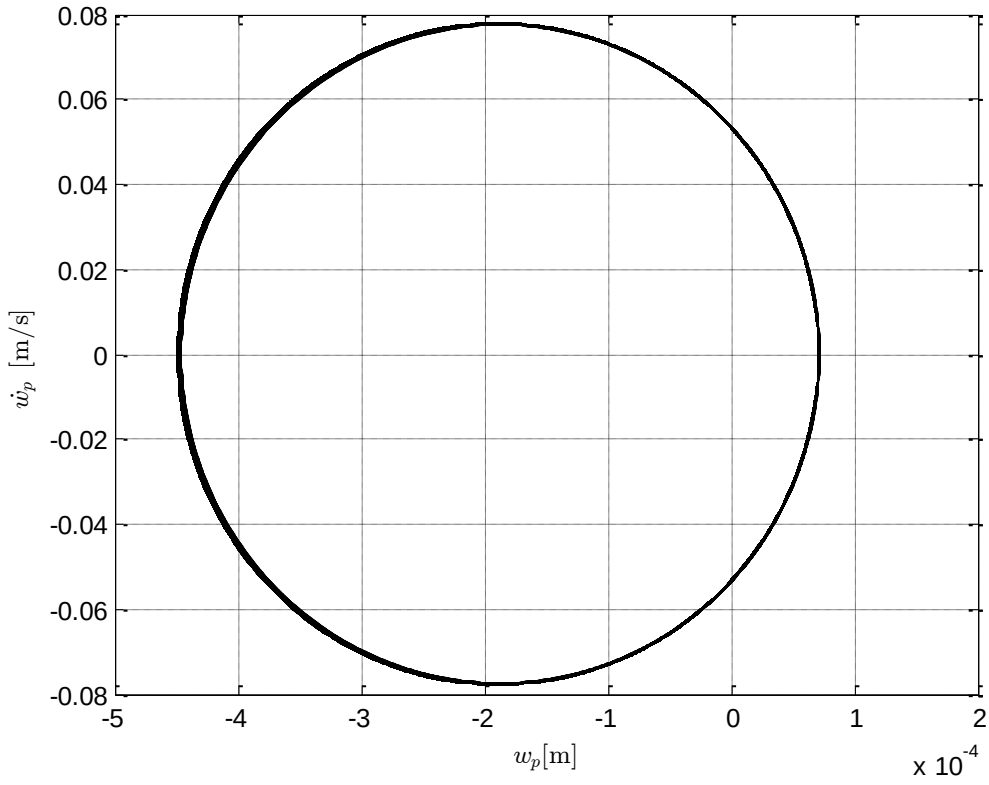

Figure 38 Phase trajectory of the last 100 seconds of Figure 36 [16], [17]

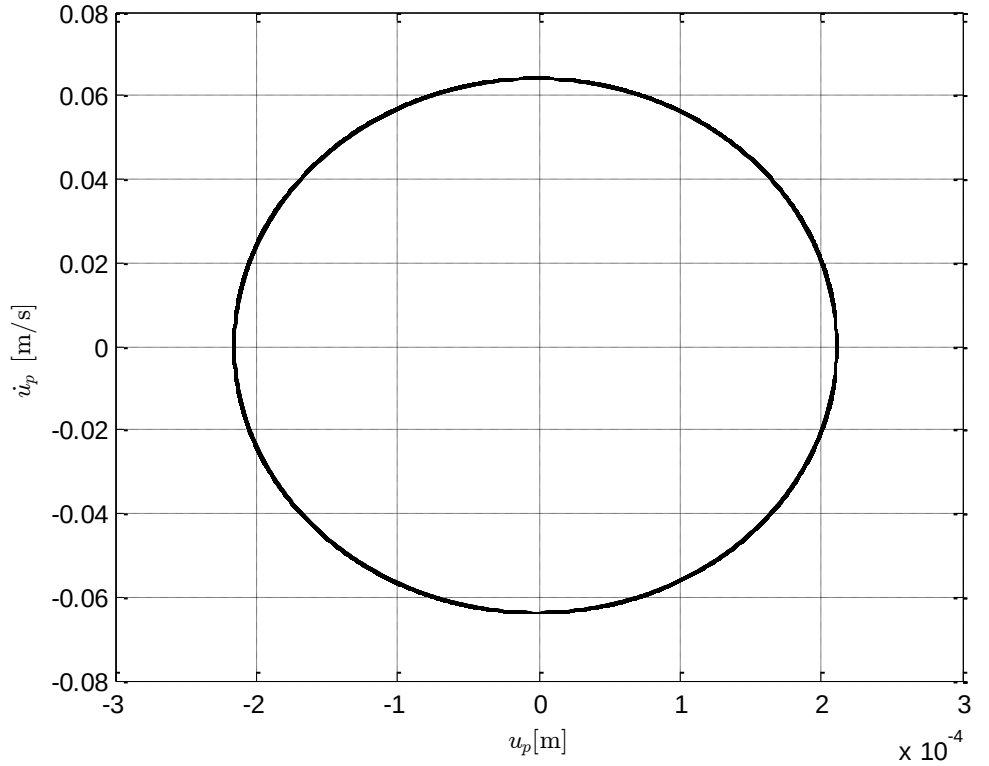

Figure 39 Phase trajectory of the last 100 seconds of Figure 37 [16], [17]

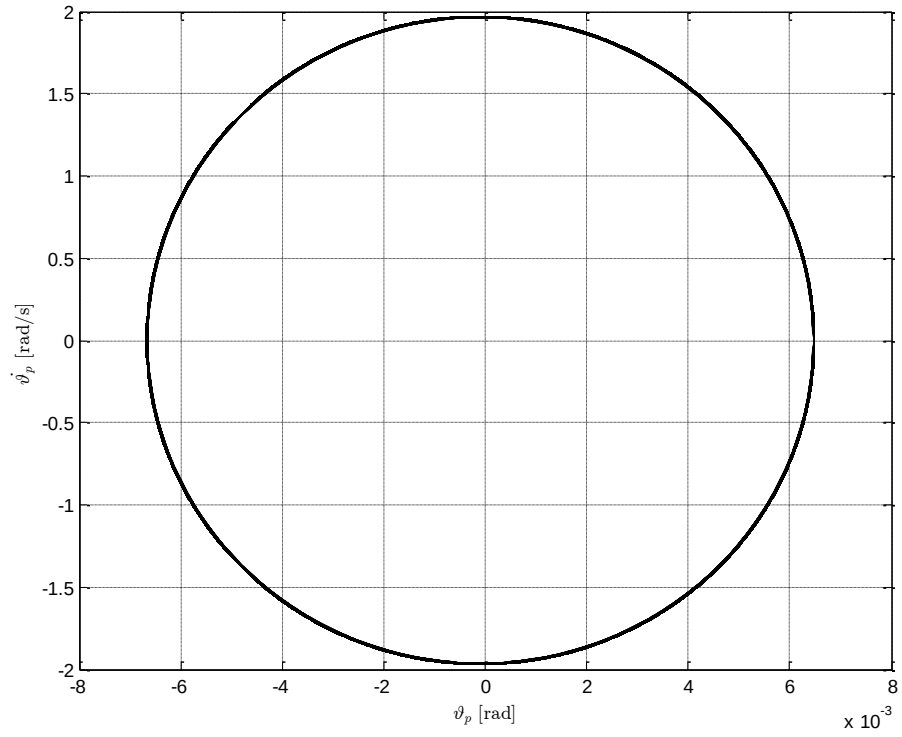

Figure 40 Phase trajectory of the last 100 seconds of Figure 38 [16], [17]

Figures from 36 to 37 show the time evolution of the global variables, obtained for superposition of the equilibrium value and of the perturbation. These time histories highlight the rise of an LCO after approximately 100 seconds, therefore the oscillations will be confined into a fixed range, how made clear by the phase trajectories in Figures 38, 39 and 40. In order to evaluate how the amplitude of the LCO varies with the air speed, the static displacement was maintained constant to the value assumed when the incipient LCO was recorded. The plunge oscillation amplitude and the plunge oscillation frequency, due to a static wing displacement, for several air speed values are reported in Figures 41 and 42. Furthermore, Figures 41 and 42 show how a static deformation of the order of 13% of the wing span, $\alpha_0 = 1.1°$, generate dynamical instabilities at a speed value which is the 35% lower than the linear flutter speed. This speed value may be further reduced, how highlighted by the early subcritical bifurcation point in Figures 41 and 42, if the assumed static load increase, $\alpha_0 = 1.3°$.

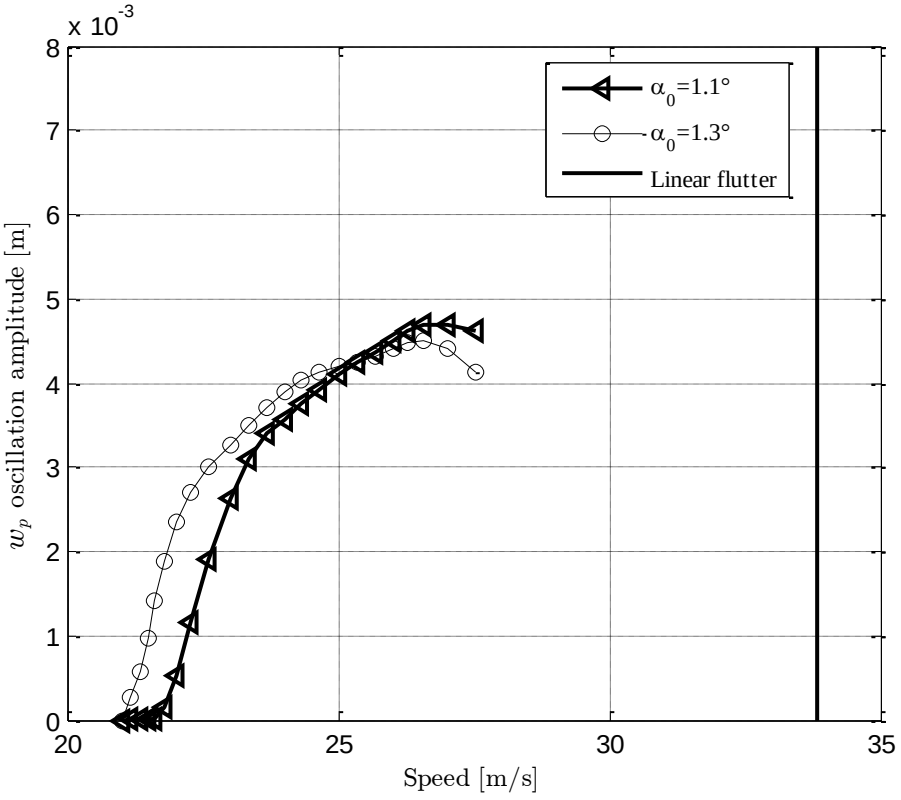

Figure 41 LCO amplitude vs. air speed [16], [17]

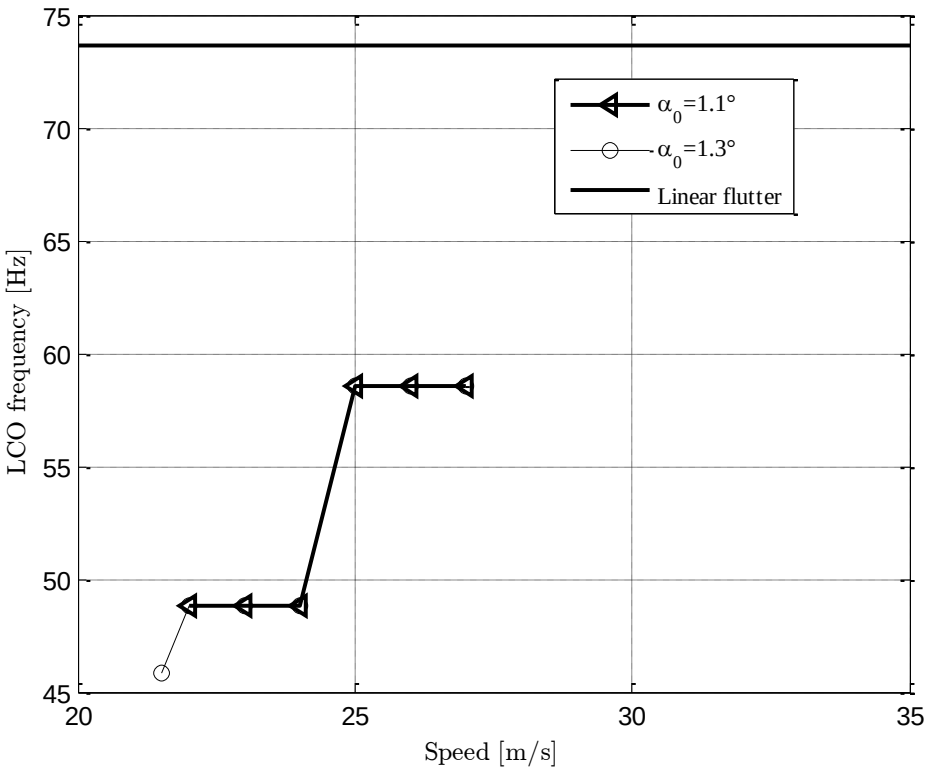

Figure 42 LCO frequency vs. Air speed [16], [17]

In order to appreciate the effect of the static load application point over the LCO response two cases were simulated and compared: the first where the static load is applied at the aerodynamic center and produce a static wing tip vertical displacement of 0.071 m, the second where the load is applied at the shear center and produce a static wing tip vertical displacement comparable to the previous case, ~0.071 m. Both cases follow the same trend, as shown in Figure 10, however the curve obtained by applying the static load at the A.C. (Aerodynamic Center) exhibits a decrease in the amplitude of the LCO for air speed higher than 27 m/s. The other case instead presents a monotonically increasing solution. One of the possible reasons of the decrease of the LCO amplitude at air speed higher than 27 m/s can be find in the work of Bunton et al. [3]. In [3] it is explained how LCO in pre-flutter might be driven more by the angle of attack associated with a maneuver than by the inertial effects. Therefore amplitudes grow in a certain range of the load factor and then diminish as the load factor continues to be increased until there is no LCO evident for higher values. However another possible reasons that lead to the evolution of the LCO, as shown in Figure 43, might be the order of nonlinearity included in the equations of the perturbed system.

Some tests, which are the contents of the next subsection, were carried out in order estimate the relevance of the order of nonlinearity on the dynamical response of the system. Besides, in order to capture other dynamical effects that the single-mode numerical simulations were not able to show, two modes per each degree of freedom are as well introduced and detailed into the next section.

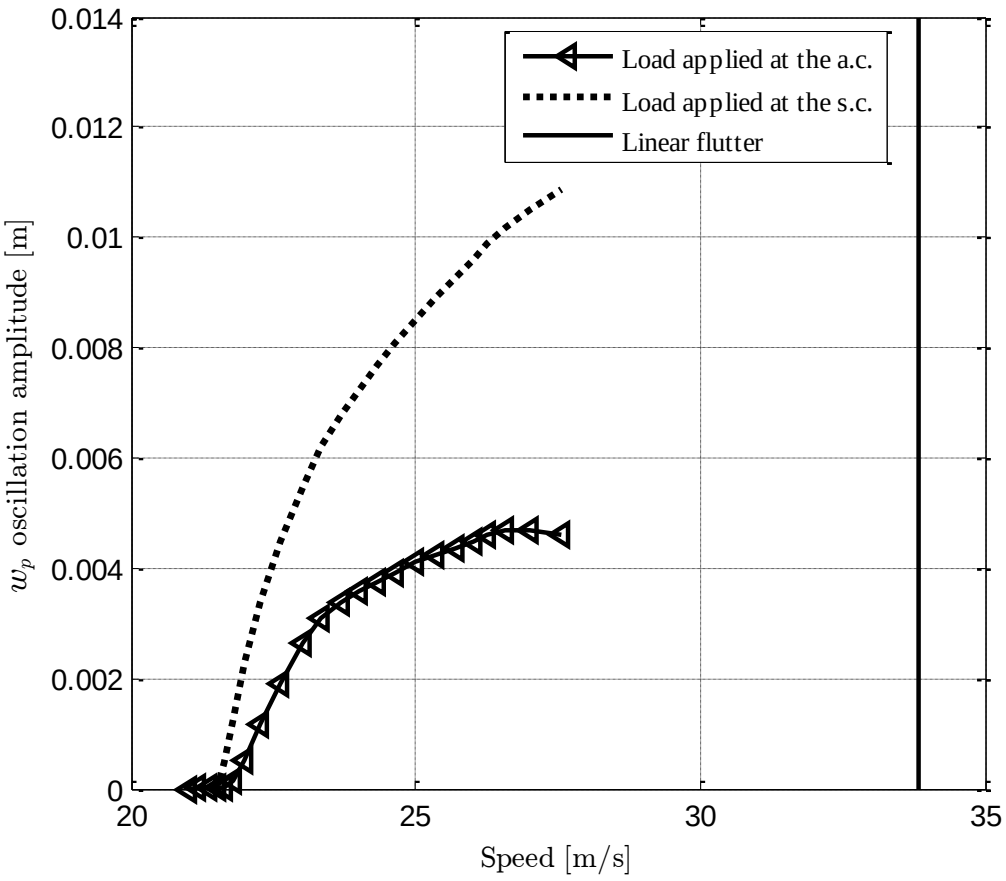

Figure 43 LCO amplitude vs. Air speed [16], [17]

4.2 Multi-Mode analysis

Two modes per each degree of freedom, six in total, were introduced into the model to analyze the evolution of the subcritical LCO, and at different loading conditions. The solutions of Figure 44 represent the LCO evolution for the multi-modes model when the static load is applied at two different chord-wise position, the A.C and the S.C. The load applied at the A.C. imply that the wing will be subjected not only to a vertical force, as in the case of the load applied at the S.C., but also to a static pitching moment. Conversely to the trend of the curves of Figure 43, where the single mode solution was represented, Figure 44 shows how the plunge amplitude which refers to model with the static load applied at the S.C. is not always the higher one. The air speed value at which the correlation between the plunge amplitudes inverts is c.a. 23 m/s. For speeds higher than 23 m/s the plunge amplitude of the LCO with static load applied at the A.C. will be higher.

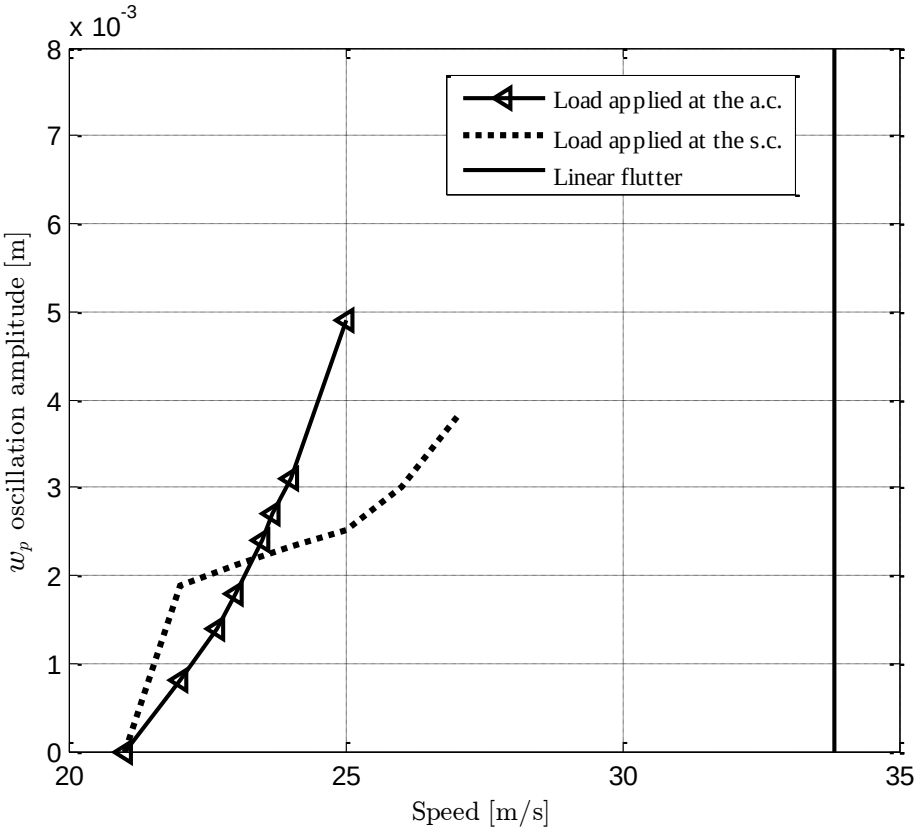

Figure 44 amplitude vs. Air speed for the multi-modes wing model [16], [17]

Another analysis which was performed in the framework of the nonlinear wing dynamic behavior concerns the inclusion of the nonlinear terms up to the third also on the perturbed torsion equation. As mentioned at the beginning of the section Numerical Results, the nonlinearities up to the third order were introduced only on the torsion equation of the equilibrium system to stabilize the steady-state solution. However introducing these terms also on the perturbed system what appears is a substantial difference in terms of oscillation amplitude with respect to the model previously analyzed, that's to say with only nonlinear terms up to the second order in the perturbed system. Figures 45 and 46 show graphically what was just mentioned.

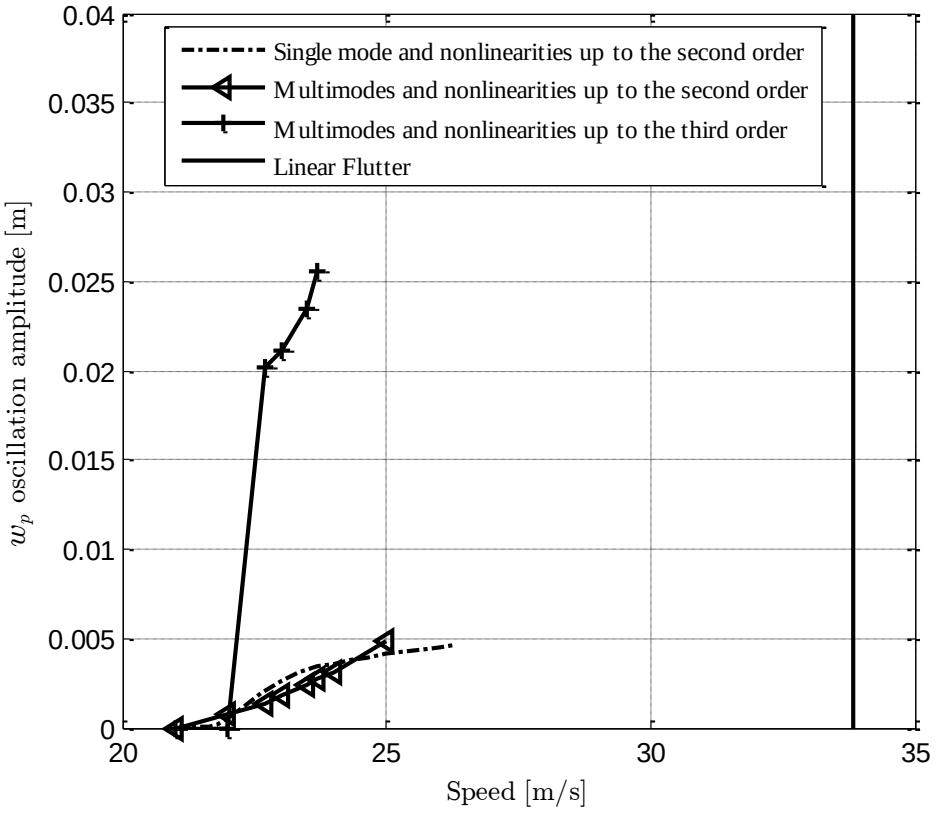

Figure 45 LCO amplitude vs. Air speed for the multi-modes wing model. The static load is applied at the A.C. (Aerodynamic Center) [16], [17]

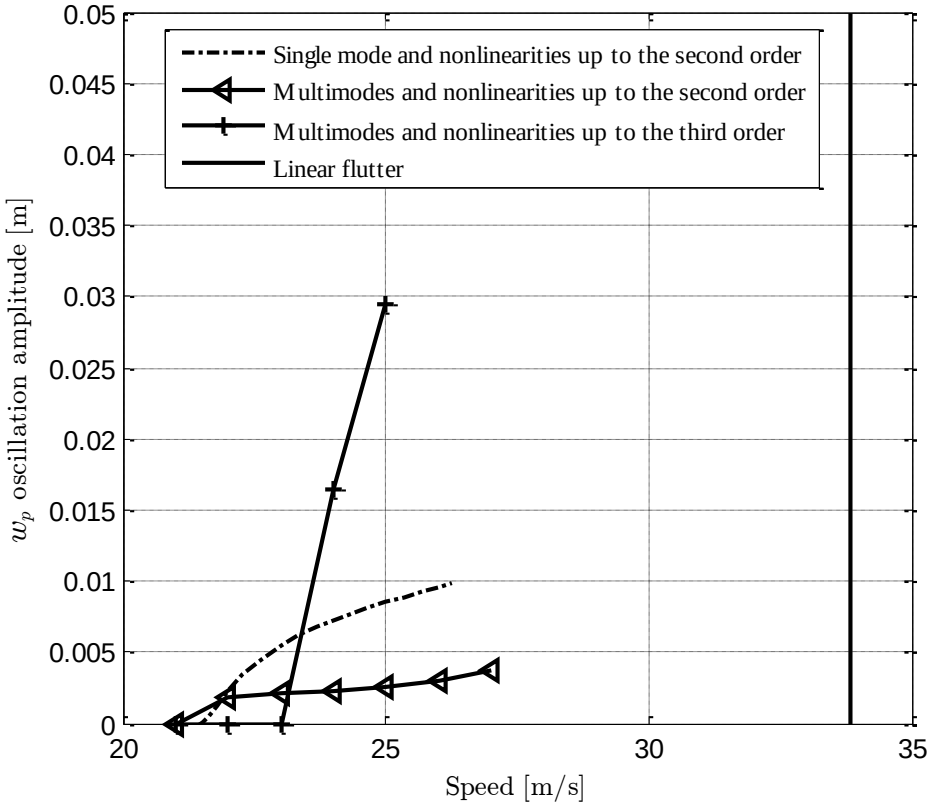

Figure 46 LCO amplitude vs. Air speed for the multi-modes wing model. The static load is applied at the S.C. (Shear Center) [16], [17]

From a direct comparison between numerical results and the experimental data available in [3] it is noticeable that the nonlinear terms up to the third order on the torsion equation of perturbed system play a primary role in the consistency of the response. In particular Figure 47 highlight how the model with static load applied at the S.C. gives a solution , for the oscillation amplitude, coherent with the experimental data within some assumptions. The importance of the third order nonlinear terms to capture the correct response of the system when the wing deflection is higher than the 7% of the wing semi-span is shown in Figure 48 through the analysis of the first two natural frequencies per each degree of freedom of the wing. The frequencies reported in Figure 48 are in the sequence from the lower to the higher the following: first flap, second flap, first lag, first torsion, second torsion and second lag.

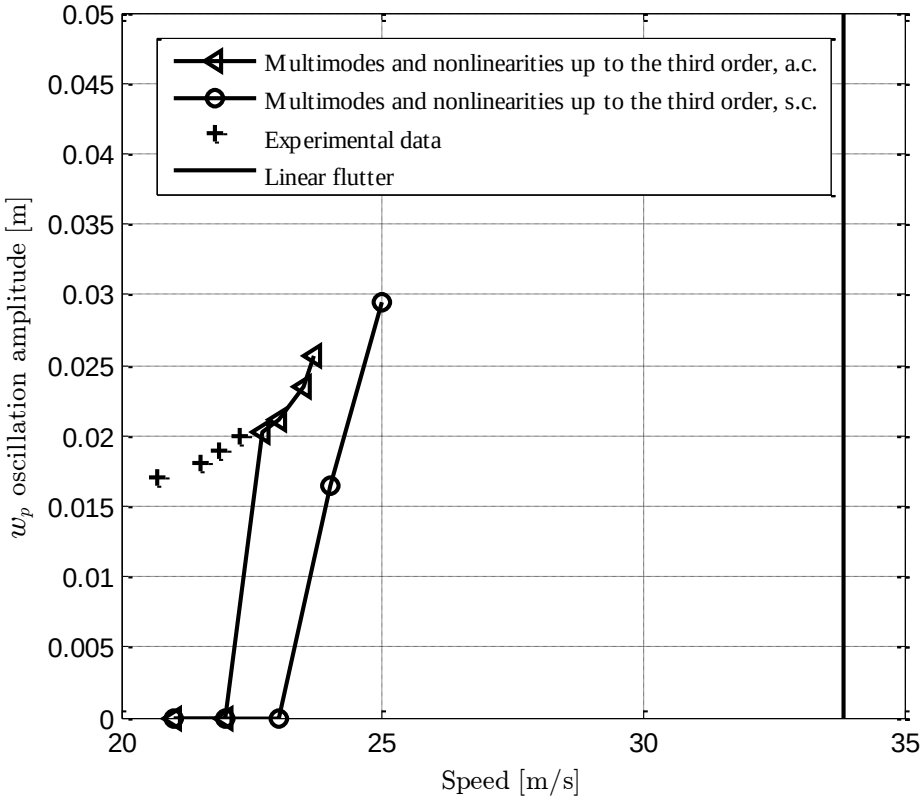

Figure 47 LCO amplitude vs. Air speed for the multi-modes wing model with experimental data [16], [17]

What appears from the frequency comparison of Figure 48 is that when the steady wing tip displacement increases the natural frequencies of the nonlinear model which includes only nonlinear terms up to the second order diverges from the value obtained from a nonlinear model with nonlinear terms up to the third order into the torsion equation and from the FEM solution. However, since the studied numerical solution is applicable to conditions which involve moderate to large static deflection, it may be possible that at in the field of high static deflections the numerical solution has to be adapted to the new condition. The time history corresponding to the first nonzero point of the curve with circles of Figure 47 is reproduced in Figure 49. This shows how after about 10 s a stable LCO arise. The value of the plunge represented on the vertical axis includes the static deformation and therefore it represent the total vertical displacement of the wing tip.

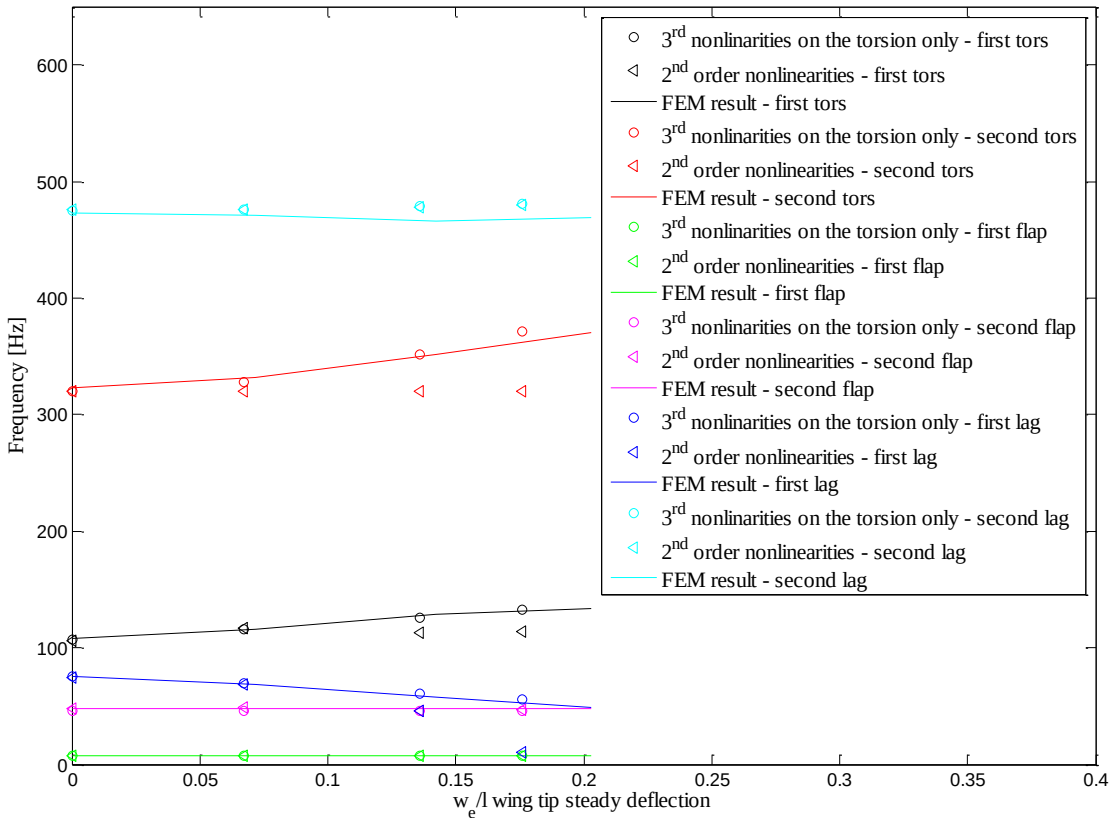

Figure 48 Natural frequencies vs. steady wing tip displacement

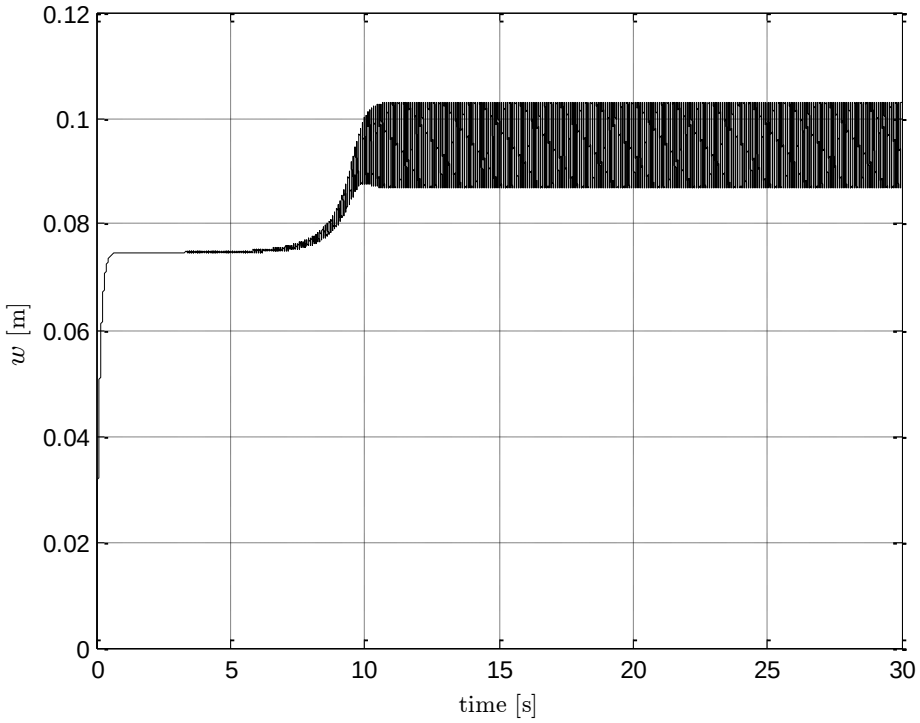

Figure 49 Time history of the plunge LCO for the multi-modes wing model and nonlinearities up to the third order in the torsion equation of the perturbed system. The load is applied at the S.C. [16] ,[17]

4.3 Effect of the main third order nonlinear terms in the flap equation

The previous subsection shows the effect of the third order nonlinear terms retained in the torsion equation only and from the results reported in Figure 47 it is possible to confirm the importance of these terms to obtain a numerical response closer as much as possible to the real one. Several differences still persist, some due to reliability of the experimental results and some due to the incompleteness of the numerical model. Very few things can be done to improve the results when the gap between the experimental and numerical solution depends of a problem of test reliability, however the second aspect, that's to say the incompleteness of the numerical model can be consistently challenged. The numerical simulations which gave the results plot in Figure 47 shown that for speed higher than 25 m/s the plunge oscillation amplitude diverge and it is not possible to estimate a reference value. This behavior of the numerical system lead to think that additional nonlinear terms have to added to the model in order to have a stable perturbed solution. The stabilizing term which was identified as the solution of the response stability problem is:

$$(D_{11} - D_{33})\theta^2 w'''' + 4(D_{11} - D_{33})\theta\theta' w''' + 2(\mathrm{D}_{11} - \mathrm{D}_{33})\theta w''\theta'' + 2(\mathrm{D}_{11} - \mathrm{D}_{33})\theta'^2 w'' \quad 4.11$$

introducing into 4.11 the same variable split of equation 2.89, the stiffness terms become:

$$K_{\theta_e} = D_{22}\theta_e'' + (-D_{11} + D_{22} + D_{33})u_e''w_e'' + D_{22}u_e'w_e''' + (-D_{11} + D_{33})\theta_e u_e''^2 + (D_{11} - D_{33})\theta_e w_e''^2 \quad 4.12$$

$$K_{\theta_p} = D_{22}\theta_p'' + (-D_{11} + D_{22} + D_{33})u_p''w_p'' + D_{22}u_p'w_p''' + (-D_{11} + D_{33})\theta_p u_p''^2 + (D_{11} - D_{33})\theta_p w_p''^2 \quad 4.13$$

$$K_{\theta_{ep}} = (-D_{11} + D_{22} + D_{33})\left(u_e'' w_p'' + u_p'' w_e''\right) + D_{22}\left(u_e' w_p''' + u_p' w_e'''\right) + (-D_{11} + D_{33})\left(\theta_e u_p''^2 + \theta_p u_e''^2 + 2\theta_e u_e'' u_p'' + 2\theta_p u_e'' u_p''\right) + (D_{11} - D_{33})\left(\theta_p w_e''^2 + \theta_e w_p''^2 + 2\theta_e w_e'' w_p'' + 2\theta_p w_e'' w_p''\right) \quad 4.14$$

$$K_{w_e} = -D_{11} w_e'''' + (-D_{11} - 2D_{22} + D_{33})\theta_e'' u_e'' + (-2D_{11} - D_{22} + 2D_{33})\theta_e' u_e''' + (-D_{11} + D_{33})\theta_e u_e'''' - D_{22}\theta_e''' u_e' - (\boldsymbol{D_{33} - D_{11}})\boldsymbol{\theta_e^2 w_e''''} - \boldsymbol{4(D_{33} - D_{11})\theta_e \theta_e' w_e''''} + \boldsymbol{2(D_{11} - D_{33})\theta_e w_e'' \theta_e''} + \boldsymbol{2(D_{11} - D_{33})\theta_e'^2 w_e''} \quad 4.15$$

$$K_{w_p} = -D_{11} w_p'''' + (-D_{11} - 2D_{22} + D_{33})\theta_p'' u_p'' + (-2D_{11} - D_{22} + 2D_{33})\theta_p' u_p''' + (-D_{11} + D_{33})\theta_p u_p'''' - D_{22}\theta_p''' u_p' - (\boldsymbol{D_{33} - D_{11}})\boldsymbol{\theta_p^2 w_p''''} - \boldsymbol{4(D_{33} - D_{11})\theta_p \theta_p' w_p''''} + \boldsymbol{2(D_{11} - D_{33})\theta_e w_e'' \theta_e''} + \boldsymbol{2(D_{11} - D_{33})\theta_e'^2 w_e''} \quad 4.16$$

$$K_{w_{ep}} = (-D_{11} - 2D_{22} + D_{33})\left(u_e'' \theta_p'' + u_p'' \theta_e''\right) + (-2D_{11} - D_{22} + 2D_{33})\left(u_p''' \theta_e' + u_e''' \theta_p'\right) + (-D_{11} + D_{33})\left(\theta_e u_p'''' + \theta_p u_e''''\right) - D_{22}\left(\theta_e''' u_p' + \theta_p''' u_e'\right) - (\boldsymbol{-D_{11} + D_{33}})\left(\boldsymbol{\theta_e^2 w_p''''} + \boldsymbol{\theta_p^2 w_e''''} + \boldsymbol{2\theta_e \theta_p w_e''''} + \boldsymbol{2\theta_e \theta_p w_p''''}\right) - \boldsymbol{4}(\boldsymbol{-D_{11} + D_{33}})\left(\boldsymbol{\theta_e' \theta_p w_e'''} + \boldsymbol{\theta_p' \theta_e w_e'''} + \boldsymbol{\theta_e' \theta_e w_p'''} + \boldsymbol{\theta_p' \theta_p w_e'''} + \boldsymbol{\theta_p' \theta_e w_p'''} + \boldsymbol{\theta_e' \theta_p w_p'''}\right) + \boldsymbol{2(D_{11} - D_{33})}\left(\boldsymbol{\theta_e w_e'' \theta_p''} + \boldsymbol{\theta_e w_p'' \theta_e''} + \boldsymbol{\theta_e w_p'' \theta_p''} + \boldsymbol{\theta_p w_e'' \theta_e''} + \boldsymbol{\theta_p w_e'' \theta_p''} + \boldsymbol{\theta_p w_p'' \theta_e''}\right) + \boldsymbol{2(D_{11} - D_{33})}\left(\boldsymbol{\theta_e'^2 w_p''} + \boldsymbol{\theta_p'^2 w_e''} + \boldsymbol{2\theta_e' \theta_p' w_e''} + \boldsymbol{2\theta_e' \theta_p' w_p''}\right) \quad 4.17$$

$$K_{u_e} = -D_{33} u_e'''' + (-D_{11} + D_{22} + D_{33}) w_e'' \theta_e'' + (-2D_{11} + D_{22} + 2D_{33}) w_e''' \theta_e' + (-D_{11} + D_{33})\theta_e w_e'''' \quad 4.18$$

$$K_{u_p} = -D_{33}u_p'''' + (-D_{11} + D_{22} + D_{33})w_p''\theta_p'' + (-2D_{11} + D_{22} + 2D_{33})w_p'''\theta_p' + (-D_{11} + D_{33})\theta_p w_p'''' \quad 4.19$$

$$K_{u_{ep}} = (-D_{11} + D_{22} + D_{33})\left(w_e''\theta_p'' + w_p''\theta_e''\right) + (-2D_{11} + D_{22} + 2D_{33})\left(w_p'''\theta_e' + w_e'''\theta_p'\right) + (-D_{11} + D_{33})\left(\theta_e w_p'''' + \theta_p w_e''''\right) \quad 4.20$$

The bold terms of equations 4.12 to 4.20 refer to equation 4.11 and derive from Eq. 2.64, where the main third order terms where identified into the out of plane equation of motion. The response of the numerical model to the introduction of the third order nonlinear terms derived from 4.11 is reported in Figure 50.

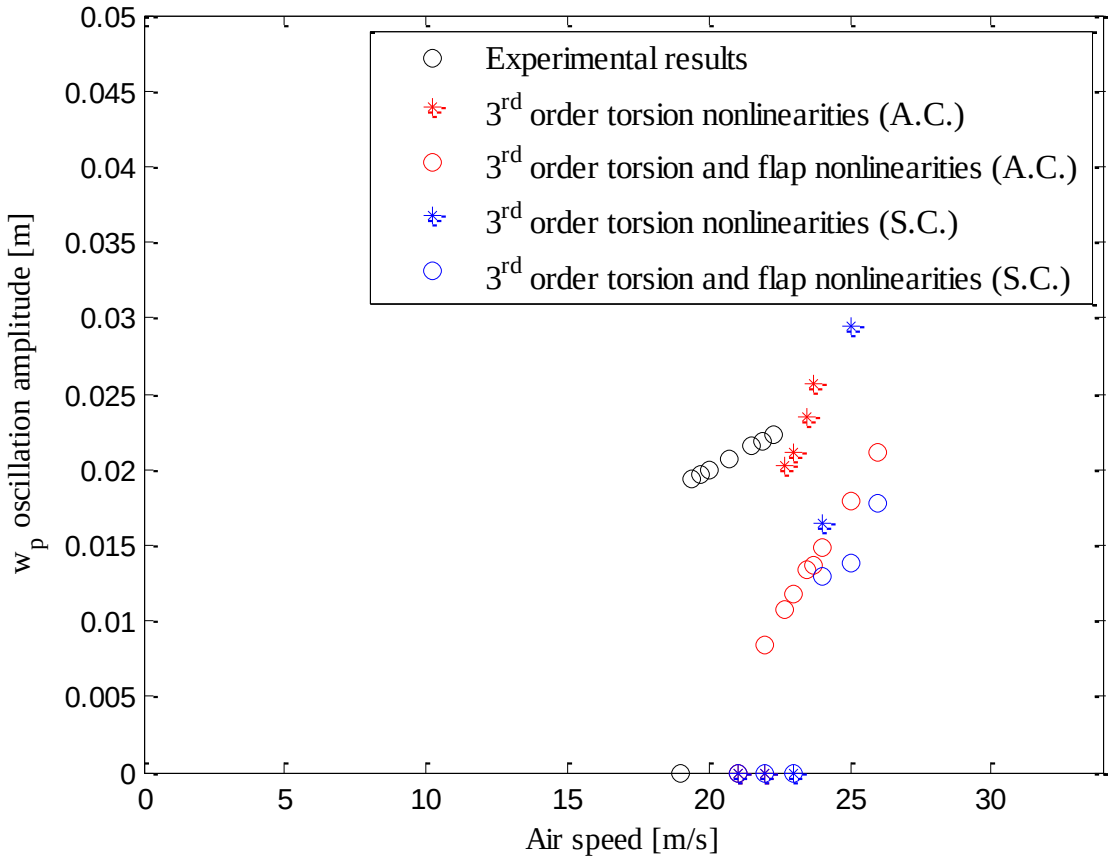

Figure 50 amplitude vs. Air speed for the multi-modes wing model with experimental data.

Figure 50 shows how now we can move to higher values of the air speed without incurring in any sort of instabilities, however for air speed values

higher than 25 m/s the dynamic stall model has to be introduced because the pitch angle exceeds $11°$. Furthermore, the oscillation amplitude appear much more comparable in a wider range of air speed to the experimental value, with the only difference to be shifted to higher values of air speed. This last might be due to a not perfect reproduction of all the experimental conditions rather than to the nonlinear terms. Another effect of the introduction of the new third order terms into the flap equation is a small shift towards lower air speed values of the hopf bifurcation point when the load is applied at the a.c. In Chapter 2 stated the importance of these additional flap terms into the equations of motion when the load is applied at the aerodynamic center, which means that the wing is subjected to static bending deflection and torsion. However Figure 50 shows how the introduction of these new flap terms have a considerable effect over the amplitude oscillation also when the load is applied at the shear center, albeit less important. The explanation might be found in the high pitch angles that wing rapidly reaches and therefore the assumption made in Chapter 2 on the order of the smallness of the pitch angle is not anymore compatible with the current situation.

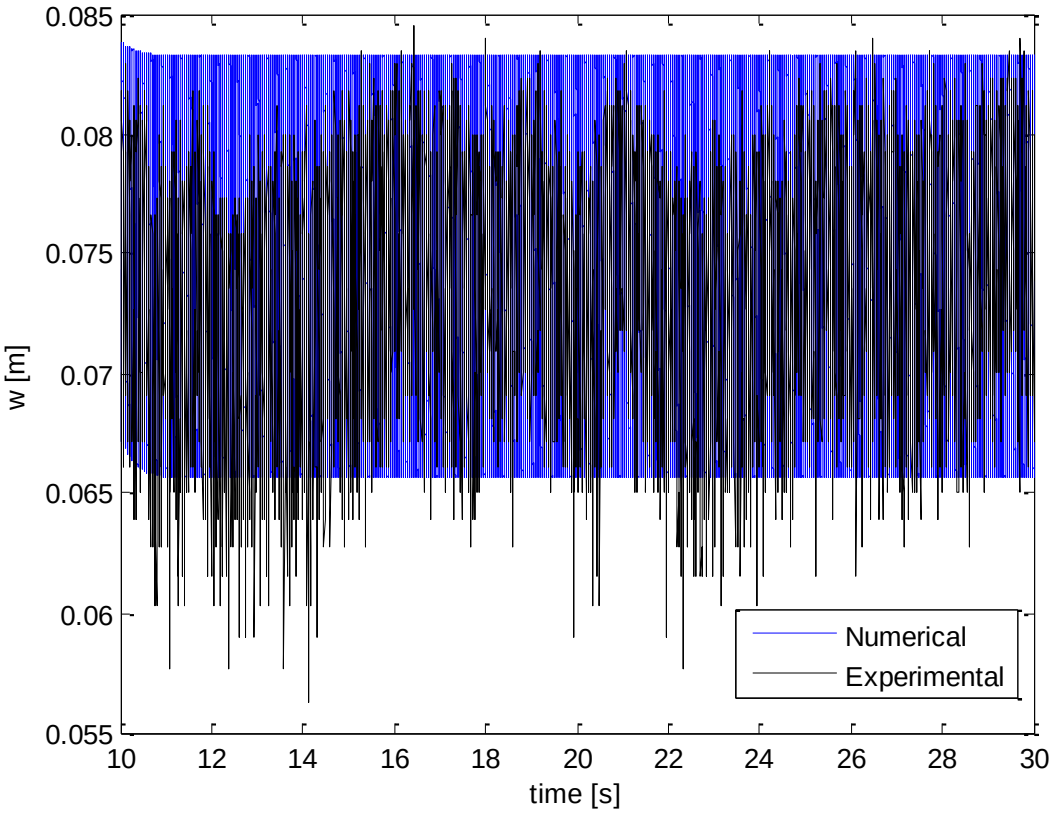

Figure 51 Comparison of the numerical and experimental time histories of the wing vertical displacement.

Figure 51 shows the comparison between the experimental and the numerical time histories of the wing total vertical displacement. The black curve represents the experimental time history at air speed of 19.92 m/s. The experimental values are obtained via a magnetic sensor pointing at the wing tip which measures linear and angular displacements together. Knowing that the experimental wing shows a hopf bifurcation at circa 18 m/s an equivalent value of air speed, suitable for the time histories comparison, might be determined for the experimental wing in the shear center load configuration; it is 26 m/s. Therefore the blue curve of Figure 51 represents the time history of the numerical wing ,when the , load is applied ate the shear center and the air speed is equal to 26 m/s. For higher values of the air speed the introduction of the stall model is required.

The study of the aeroelastic behavior of HALE aircrafts requires a model in which the nonlinearities are opportunely take into account in order to be able to reproduce some dynamical conditions which can occur during the flight. The presence of the static deformation, due to the trim condition, moves the "flutter " to lower values of speeds. The analysis performed on the single-mode nonlinear model shown an increase of the oscillation amplitude with the increase of the speed. This increase of the oscillations amplitude when the load is applied at the S.C. has a monotonic trend but different values of the oscillation amplitude when third order nonlinear terms are included in the torsion equation. In particular the third order terms lead the solution to higher values of LCO amplitude, consistent with the experimental data. It seems that the third order nonlinear terms over the torsion equation introduces a part of the model dynamical response that with the second order nonlinear terms only it was not able to capture. This last conclusion is still valid when the static load is applied at the A.C., the only difference consists in the single mode response where at air speed higher than 27 m/s the LCO decreases. The introduction of the third order nonlinear terms into the torsion equation shown to be beneficial for a more realistic representation of the wing oscillation amplitude, however it after the inclusion of some properly selected nonlinear third order terms in the flap equation of motion that the time numerical response become really comparable to the experimental one. Further investigations are required to understand the nature of this phenomenon. In particular a sensitivity study has to be performed to better understand the importance that the number of modes to include for each degree of freedom. When the value of the pitch angle involved in the numerical simulations is high the stall model cannot be neglected in the nonlinear analysis.

References

[1] Tang, D.M. and Dowell, E.H., "Effects of geometric structural nonlinearity on flutter and limit cycle oscilaltions of high-aspect-ratio wings", Journal of Fluids and Structures 19 (2004) 291-306, 2004, doi:10.1016/j.jfluidstructs.2003.10.007.

[2] Frulla, G., Cestino, E. and Marzocca, P., "Critical behavoiur of slender wing configuration", Proc. IMEchE . 224 Part G: J. Aerospace Engineering, 2009, DOI:10.1243/09544100JAERO553.

[3] Bunton, R. W., Denegri Jr.,C. M., "Limit Cycle Oscillation Characteristics of Fighter Aircraft", Journal of Aircraft, Vol. 37, No. 5, September-October 2000.

[4] Palacios, R., Cesnik, C. E.S., "Re-examined structural design procedures for very flexible aircraft", Presented at the International Forum of Aeroelasticity and Structural Dynamics 2007, Stockholm, Sweden.

[5] Tang, D., Dowell, E. H., "Limit cycle oscillations of two-dimensional panels in low subsonic flow", International Journal of Non-linear Mechanics, 2002.

[6] Dowell, E., Edwards, J., Strganac, T., "Nonlinear Aeroelasticity", Journal of Aircraft, Vol.40, No. 5, May 2003.

[7] Patil, M. J., Hodges, D. H., Cesnik, C. E. S., "Characterizing the Effects of Geometrical Nonlinearities on Aeroelastic Behavior of High-Aspect-Ration Wings", Presented at the International Forum of Aeroelasticity and Structural Dynamics , Willianmsburg, Virginia, USA, June 22-25, 1999.

[8] Bisplinghoff, R., Ashley, H., Halfman, R., *Aeroelasticity*, Dover 1996.

[9] Fung, Y.C., *An Introduction to the theory of Aeroelasticity*, Dover 0-486-67871-7.

[10] Wright, J.R., Cooper, J.E., Introduction to Aircraft Aeroelasticity and Loads, AIAA.

[11] Sedaghat, A., Cooper, J.E., Wright, J.R., Leung A.Y.T., “Prediction of non-linear aeroelastic instabilities”, ICAS Congress 2000.

[12] Cestino E., Frulla G., Perotto E.,Marzocca P. (2014) Experimental Slender Wing Model Design by the Application of Aeroelastic Scaling Laws. In: JOURNAL OF AEROSPACE ENGINEERING, vol. 27 n. 1, pp. 112-120. - ISSN 0893-1321

[13] Cestino E., Frulla G., Marzocca P. (2013). A Reduced Order Model for the Aeroelastic Analysis of Flexible Wings. In: SAE INTERNATIONAL JOURNAL OF AEROSPACE, vol. 6 n. 2. - ISSN 1946-3855

[14] Nayfeh, A. H. and Pai, P. F. Linear and non-linear structural mechanics, 2004 (Wiley Interscience, New York).

[15] Bruni C., Cestino E., Frulla G., Gibert J., Marzocca P. (2015) A Multi-objective Nonlinear Piezoaeroelastic Wing Solution for Energy Harvesting and Load Alleviation: Modeling and Simulation. In: 56th AIAA/ASCE/AHS/ASC Structures, Structural Dynamics, and Materials Conference, Florida (USA), 5-9 January 2015

[16] Romeo G, Frulla G., Cestino E., Marzocca P. Tuzcu I, " Non-linear Aerelastic Modeling and Experiments of Flexible Wings", 47th AIAA/ASME/ASCE/AHS/ASC Structures, Structural Dynamics, and Materials Confere 1 - 4 May 2006, Newport, Rhode Island.

[17] Frulla G., Cestino E., Marzocca P., " Critical behaviour of slender wing configurations", Proc. IMechE Vol. 224 Part G: J. Aerospace Engineering, DOI: 10.1243/09544100JAERO553.

5 Energy harvesting

Several are the alternative power sources in nature for micro-powering: photons, kinetic, thermal and biochemical. In this section only the power produced from vibrations will be treated. The vibrations take their origin from the ambient, from the human motion, from the atmosphere. The power extracted from all these natural processes has to be stored into temporary storage system, such as ultra capacitors or rechargeable batteries, and then delivered to power electronic devices. The forecasts assign to this new technologies a relatively consistent portion of the future energy market, corroborated by the increasing power needs for small electronics. The main applications concern environmental monitoring, structural monitoring, interactive and control, surveillance, medical remote sensing , military and aerospace. The main benefits of these energy harvesting techniques are: long last operability, no chemical disposal, cost saving safety, maintenance free, no charging points, inaccessible site operability, flexibility and applications otherwise impossible.

5.1 Introduction to the Energy harvesting Techniques from Ambient Vibrations, with a particular attention to piezoelectric materials

The most common vibration harvesters are based on electromagnetic [6], electrostatic [5] or capacitive, magnetostrictive mechanisms [4] and piezoelectric [7]. Table 6 highlight tautly some of the characteristics of each family of harvesters.

Table 6 : Description of the main characteristic of the most common harvester.

Type	Advantages	Disadvantages
Electromagnetic	- no need of smart material - no external voltage sources	- bulky size: magnets and pick-up coil - difficult to integrate with MEMS - max voltage of 0.1 V
Electrostatic	- no need of smart material - compatible with MEMS - voltage of 2-10 V	- external voltage (or charge) source - mechanical constraints needed - capacitive
Magnetostrictive	- ultra-high coupling coefficient > 0.9 - no depolarization problems - high flexibility - suited to high frequency vibration	- nonlinear effect - pick-up coil - may needed bias magnets - difficult to integrate with MEMS
Piezoelectric	- no external voltage source - high voltage of 2-10 V - compact configuration - compatible with MEMS - high coupling in single	- depolarization - brittleness in bulk piezolayer - poor coupling in piezo-film (PVDF) - charge leakage

	crystals	- high output impedance

The working principle of the electromagnetic energy harvesting from vibrations is based on Faraday's law of electromagnetic induction, stating that: “an electrical current will be induced in any closed circuit when the magnetic flux through a surface bounded by the conductor changes”. One of the most effective way of achieving this for energy harvesting is by making use of a permanent magnet and a coil . Electromagnetic harvesters are simple and rugged, do not require any smart materials or source of voltage, but are difficult to manufacture in micro scale. Output voltage is low (0,1 V).

The electrostatic devices use a viable capacitor structure to generate charges from a relative motion between two plates. Ambient vibrations induces displacement of charged plates of variable capacitors and so mechanical energy is converted into electrical energy. The advantages of electrostatic harvesting devices are their easy integration into printed circuit boards of MEMS, no need for smart materials and high output voltage (2~10 V) . The disadvantages instead are their dependence on external voltage source.

Magnetostrictive energy scavengers use the Villari effect of magnetostrictive materials. Magnetostriction is a property of ferromagnetic materials that causes them to change their shape as a result of magnetization or vice versa. Magnetostrictive harvesters offer some advantages such as high coupling coefficient and high flexibility that make them suitable for high frequency applications. Stated disadvantages are difficult integration with MEMS, non-linear effect, need of pickup coil .

Finally piezoelectric materials, which generate electric charge when a mechanical load is applied and therefore are used to convert mechanical

energy form pressure or force into electric energy. Energy harvesting device employing piezoelectric conversion mechanism typically consists of cantilever beam coated with piezoelectric material and a mass placed on the tip of a beam. Piezoelectric energy harvesters require no external voltage source, output voltage is relatively high, their compact dimensions allow for MEMS integration. Coefficient of electromechanical coupling is high. On the other side, piezoelectric materials such as PZT are often brittle and tend to change their properties through operational life.

Although the choice of piezoelectric materials highlights some disadvantages, as listed in Table 6, and in addition fact of being expensive, currently they are the major method of harvesting energy from ambient vibrations. It mainly depends on the recent advances made in low power electronics and on the increasing interest for MEMS technology. Piezoelectric materials, indeed, are fully compatible with MEMS, do not require an external power source and are particularly suitable to exploit the mechanical strains for electrical energy generation. Therefore piezoelectric energy harvesting devices, in the form of MEMS generator or nanogenerators, are a novel technology that is a reliable alternative energy source for powering wireless sensor devices.

Some of the vibration sources which unable the piezoelectric devices to work as a power generator are available in [1], and they mainly consist in: impact coupled devices, human power piezoelectric generation, cantilever-based piezoelectric generators, etc.

Cantilever-based piezoelectric generators are an interesting and widely applied configuration, included in the aeronautical field, where they find their most blatant similarity, in terms of structural constraints and dynamical behavior, with the aircraft wing and empennages . The aircraft wing in particular is the object of the study included in this thesis, however

it represents a consistent study for many others applications which reflect such a mechanical configurations. In fact one can straightforwardly assume to properly design an embedded cantilever-based piezoelectric generator which exploit the global aircraft vibrations to generate electrical energy, [3] and [1].

Before entering into the details of the energy harvesting from wing vibration, some specific information about the characteristic of piezoelectric materials are hereafter reported, in order to better appreciate the mathematical modeling and the results presented into the next chapters.

5.2 Piezoelectric Materials

The ability of piezoelectric materials to transform electrical energy into mechanical energy and vice versa depends on their crystalline structure. The piezoelectric effect depends on the absence of a centre of symmetry in the crystal, which is responsible for the charge separation between positive and negative ions and for the formation of Weiss domains, i.e. dipole groups with parallel orientation. By applying an electric field to a piezoelectric material, the Weiss domains align proportionally to the field, consequently, the material dimensions change, increasing or decreasing if the direction of Weiss domains is the same or opposite to the electric field. After the sintering stage, polycrystalline piezoceramics, consist of a huge number of randomly oriented dipoles without piezoelectric properties. In these isotropic materials the piezoelectricity is induced by a poling process, consisting in the application of a strong electric field at high temperatures, which aligns the molecular dipoles in the same direction of the applied field. The dipole moment remains unchanged after removing the electric field, and the ceramic exhibits piezo-electric properties unless an excessively high voltage or high stress is imposed upon it or unless it is heated to very high temperatures. If either of these conditions is reached, the energy input to the domains exceeds the internal binding force holding the domains in alignment and the material once again becomes unpoled. In order to provide a deeper and more quantitative knowledge on the piezoelectric properties of piezoceramics, a number of interrelated coefficients, many of which have been standardized by the IEEE will be introduced. Because of the anisotropic nature of piezoceramics, the effects are strongly dependent upon the orientation with respect to the poled axis. This latter represents the direction of polarization and is generally designated as the z-axis of an orthogonal crystallographic system. The axes

x, y and z are respectively represented as 1, 2 and 3 directions and the shear directions around these axes are represented respectively as 4, 5 and 6, Figure 52.

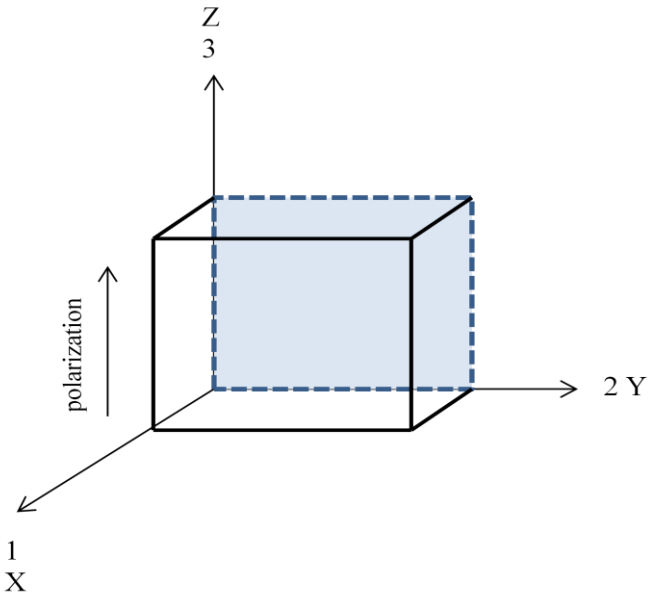

Figure 52 Conventional axis system used in describing piezoelectric properties

To link electrical and mechanical quantities, double subscripts (e.g. d_{ij}) are introduced. The first subscript gives the direction of the electrical field associated with the voltage applied or the charge produced. The second subscript gives the direction of the mechanical stress or strain. Superscripts "S, T, E, D" describe an electrical or mechanical boundary condition:

S = strain = constant (mechanically clamped)

T = stress = constant (not clamped)

E = field = constant (short circuit)

D = electrical displacement = constant (open circuit)

It should be clearly understood that the piezoelectric coefficients described here are not independent constants but vary with temperature, pressure, electric field, form factor, mechanical and electrical boundary conditions etc. The coefficients only describe material properties under small signal conditions.

5.2.1 Properties of the piezoelectric materials

The piezoelectric charge (or Strain) constant d represents the mechanical strain produced by an applied electric field:

$$d = \frac{strain\ development}{applied\ electric\ field} \qquad \left[\frac{m}{V}\right] \tag{5.1}$$

Large d_{ij} constants relate to large mechanical displacements, which are usually sought in motional transducer devices. Conversely, the coefficient may be viewed as relating the charge collected on the electrodes, to the applied mechanical stress.

$$d = \frac{short\ circuit\ charge\ density}{applied\ mechanical\ stress} \qquad \left[\frac{C/m^2}{N/m^2}\right] \tag{5.2}$$

According to the different modes with which the stress can be applied, it is possible to have different *d* constants:

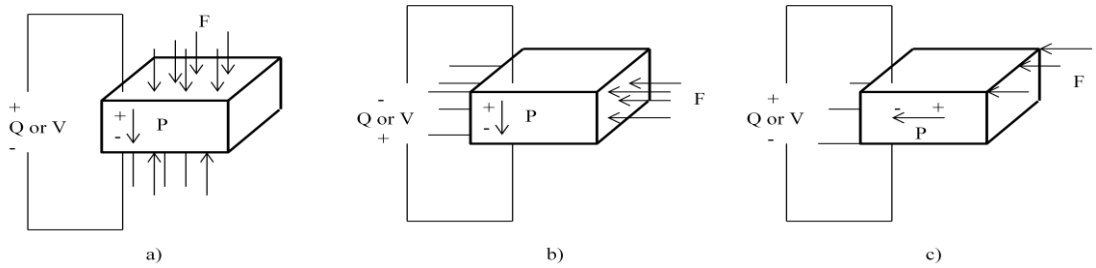

Figure 53 Relationship between force and electric charge for different vibration modes of piezoelectric crystals

- d_{33} (direct *d*) is used when the force is in the 3 direction (along the polarization axis) and is impressed on the same surface on which the charge is collected, Figure 53 a); in this case the mechanical stress is parallel to the dipole moment, producing an enhancement of the spontaneous polarization along the 3 axis; - d_{31} (transverse *d*) is used when the charge is collected on the same surface as before, but the force is applied perpendicularly to the polarization axis, Figure 53 b); - d_{15} (shear

d) is used when the charge is collected on electrodes perpendicular to the original poling electrodes and the applied mechanical stress is shear that tilts the dipoles, Figure 53 c). The three previous conditions are called respectively as d_{33}, d_{31} and d_{15} effects and they are intrinsic contributions to the piezoelectric coefficients, coming from the distortions of the crystal structure.

The piezoelectric Voltage constant g represents the electric field produced at open circuit by a mechanical stress:

$$g = \frac{open\ circuit\ electric\ field}{applied\ mechanical\ stress} \qquad \left[\frac{V/m}{N/m^2}\right] \tag{5.3}$$

The g constant is a measure of the sensitivity of a piezoelectric material, because it is proportional to the open circuit voltage. The sensitivity needs to be sufficiently high so that the generated signal can be detected above the background noise. The sensitivity is maximized when the g coefficient is maximized. Therefore, high g_{ij} constants are required for sensors. Although the g coefficients are called voltage coefficients, it is also correct to say that g_{ij} is the ratio of strain developed over the applied charge density:

$$g = \frac{strain\ developed}{applied\ charge\ density} \qquad \left[\frac{m^2}{C}\right] \tag{5.4}$$

According to the different modes with which the stress can be applied, it is possible to have different *g* constants:

- g_{33} (direct g) is used when the electric field and the mechanical stress are both along the polarization axis, Figure 53 a);
- g_{31} (transverse g) is used when the pressure is applied at right angles to the polarization axis, but the voltage appears on the poling axis 3, Figure 53 b);

- g_{15} (shear g) is used when the applied stress is shear and the resulting electric field is perpendicular to the polarization axis, Figure 53 c).

The electro-mechanic coupling coefficient k describes the conversion of energy from electrical to mechanical form or vice versa representing a sort of piezoelectric efficiency of the material. It measures how strong the coupling is between the vibration mode and the excitation. Since this coefficient is an energy ratio, it is dimensionless. Subscripts denote the relative directions of electrical and mechanical quantities and the kind of motion involved. Large k_{ij} coefficients provide a more efficient energy transfer and are required in the piezoelectric actuators. k_{ij} determines the bandwidth of filters and transducers.

$$k = \sqrt{\frac{accumulated\ electric\ energy}{supplied\ mechanical\ energy}} \quad \text{or}$$

$$k = \sqrt{\frac{accumilated\ mechanical\ energy}{supplied\ electrical\ energy}} \qquad 5.5$$

The relative dielectric constant K is the ratio of the permittivity of the material, ε, to the permittivity of free space, ε_0, in the unconstrained condition, i.e., well below the mechanical resonance of the part.

$$K = \frac{\varepsilon}{\varepsilon_0} \qquad 5.6$$

Large dielectric constants are required for sensors in order to overcome the losses associated with the cables, but an excessive value of K decreases the voltage coefficients and thus the sensitivity according this relationship between d and g coefficients:

$$g_{ij} = \frac{d_{ij}}{K\varepsilon_0} \qquad 5.7$$

The Curie temperature is the critical temperature at which the crystal structure changes from a non-symmetrical (piezoelectric) to a symmetrical

(non-piezoelectric) form in which the piezoelectric properties are lost. Upon cooling the dipoles don't realign unless they are subjected to a strong electric field. Other consequences of increasing temperature are changes in the value of electromechanical coefficients and the process called "thermally activated aging". As a practical rule, the maximum operating temperature of a piezoceramic is about half the Curie temperature.

The Young's modulus of a piezoelectric material, i.e. the ratio of stress (force per unit area) to strain (change in length per unit length), changes with the electric load. Because mechanical stressing of the ceramic produces an electrical response, which opposes the resultant strain, the effective Young's Modulus with electrodes short-circuited is lower than with the electrodes open circuited. In addition, the stiffness is different in the 3 direction from that in the 1 or 2 direction. Therefore, in expressing such quantities, both direction and electrical conditions must be specified. The Young's Modulus of a piezoceramic is about one quarter that of steel.

The dielectric dissipation factor $\tan\delta$ is the ratio of power loss to reactive power in a specimen subjected to a sine wave input at a frequency far below its self-resonant frequency.

The ceramic polarization gradually fades with time and the rate of this process, given in percent per decade of time, is known as aging rate, which is a logarithmic function of time. Therefore, the aging process is the tendency of the ceramic to change back to its original state prior to polarization and can be attributed to the relaxation of the dipoles in the material.

Each piezoceramic has a specific elastic vibration frequency, which is a function of the material and its shape. When an alternating voltage is applied to a piezoceramic with a frequency equal to its specific vibration frequency, the piezoceramic exhibits resonance. This phenomenon is exploited in many piezoelectric applications, because at the resonance the

electromechanical coupling coefficient is maximum. Piezoelectric ceramics may have various vibration modes (resonant modes), which depend on their shape, orientation of polarization and the direction of the electric field. Each of these vibration modes has unique resonant frequencies and piezoelectric characteristics.

5.2.2 Constitutive equations of piezoelectric materials

The constitutive equations of poled piezoeceramics, which are generally transversally isotropic materials, are given in matrix form as:

$$\begin{bmatrix} S \\ D \end{bmatrix} = \begin{bmatrix} s^E & d^t \\ d & \varepsilon^T \end{bmatrix} \begin{bmatrix} T \\ E \end{bmatrix} \tag{5.8}$$

where $[T]$ is the stress vector, $[S]$ is the stress vector, $[E]$ the vector of the electric field and $[D]$ of the electric displacement. The superscript E and T denote that variable are evaluated at constant electric field and constant stress, respectively [13]. When the piezoelectric behavior is to be modeled as a thin beam, as for the purpose of this work, the constitutive equations reduce to:

$$\begin{Bmatrix} T_1 \\ D_3 \end{Bmatrix} = \begin{bmatrix} \bar{c}_{11}{}^E & -\bar{e}_{31} \\ \bar{e}_{31} & \bar{\varepsilon}_{33}{}^S \end{bmatrix} \begin{Bmatrix} S_1 \\ E_3 \end{Bmatrix} \tag{5.9}$$

where $\bar{c}_{11}{}^E = \frac{1}{s_{11}{}^E}$, $\bar{e}_{31} = \frac{d_{31}}{s_{11}{}^E}$, $\bar{\varepsilon}_{33}{}^S = \varepsilon_{33}{}^T - \frac{d_{31}{}^2}{s_{11}{}^E}$ [13].

5.2.3 Typical electric circuits for energy harvesting and vibrations damping

The piezoelectric components in order to work as energy harvesters or structural dampers need to be connected to an electric circuit. While the structural damping can be achieved by both passive and active shunting solutions, the energy harvesting is a peculiarity only of the passive piezo shunting. The explanation why passive shunting is the only solution for energy harvesting lies behind the meaning of active shunting, which actively, from outside, provide an electric load to the piezoelectric elements in order they can deform in such a way to contrast or limit the global structure displacement. Therefore some energy has to be provided to control the deformation of the main structure, by implying a negative energy balance. The same damping effect is obtained through a passive shunting of the piezoelectric elements, which connected to a passive electric circuit are able to extract kinetic energy from the system and to remove it via the electrical dissipation. This last solution foresees less energy consumption but under some conditions it is less effective in terms of structural damping, that's why the active damping is widely used despite the non-negligible piezo brittleness concerns. The energy extracted via the passive shunting may be simply dissipated or collected for other purposes, and here comes the energy harvesting application. In fact, the energy collected is useful to power some on board electronic devices or it can also used to drive the same piezo-element if it was thought to work in both passive and active ways. However this multipurpose solution is rarely deployed because it requires big optimization efforts and most of the time the design, which guarantee a good structural damping, does not coincide with that which guarantee the best energy harvesting. All the possible configurations have to be investigated based on the system geometry,

dynamic response and working conditions. Figure 54 shows all the possible electrical circuits that can be connected to a piezo-patch. In particular for the purpose of this study a simple passive resistive shunt solution was used, which allows to better understand the characteristics of the energy harvesting process but also the limitations. In fact, in Chapter 6 is it shown how the purely resistive solution imply several limitations for energy harvesting from multimodal response. A better choice could be the a resonant electric circuit, as shown in Figure 54, where the optimum modal condition may be acquired on a wider frequencies spectrum [17], [18]. Hagood et al. [18] showed that the resonant shunting of piezoelectric elements exhibit a very similar behavior to the mechanical tuned vibration absorber. Furthermore they showed that the resonant shunting can have larger effects on the mode to which it is tuned while the resistor shunting have a larger bandwidth. Hollkamp et al. [19] propose a resonant shunt design to autonomously tune to the desired mode frequency. In order to have an effect on a wider range of frequency simultaneously the shunt circuit has to be built with a reactance neutralizing circuit, as shown by Wu in [20]. Devis et al. [21] propose a capacitive shunting circuit by improving the frequency tunability of the device. A recent alternative to the most standard technique of passive and active control using piezoelectric material can be found in the semi-passive and semi-active techniques. Passive control systems, which use R-L shunting, are simple, but their control performances is sensitive to the variations of the system parameters. Moreover, the passive control system usually need large inductance in the low frequency domain, which is difficult to achieve. Active control systems, instead, require high-performance digital signal processors and bulky power amplifiers to drive actuators, which are not suitable for many applications. To overcome all these disadvantages, several semi-passive/active approaches have been proposed. These circuits implement

switches to change the dynamics of the shunt in such a way that the vibration damping can be improved. The works of Guyomar et al. [22], of Lallart et al. [23] and many others show such advantages.

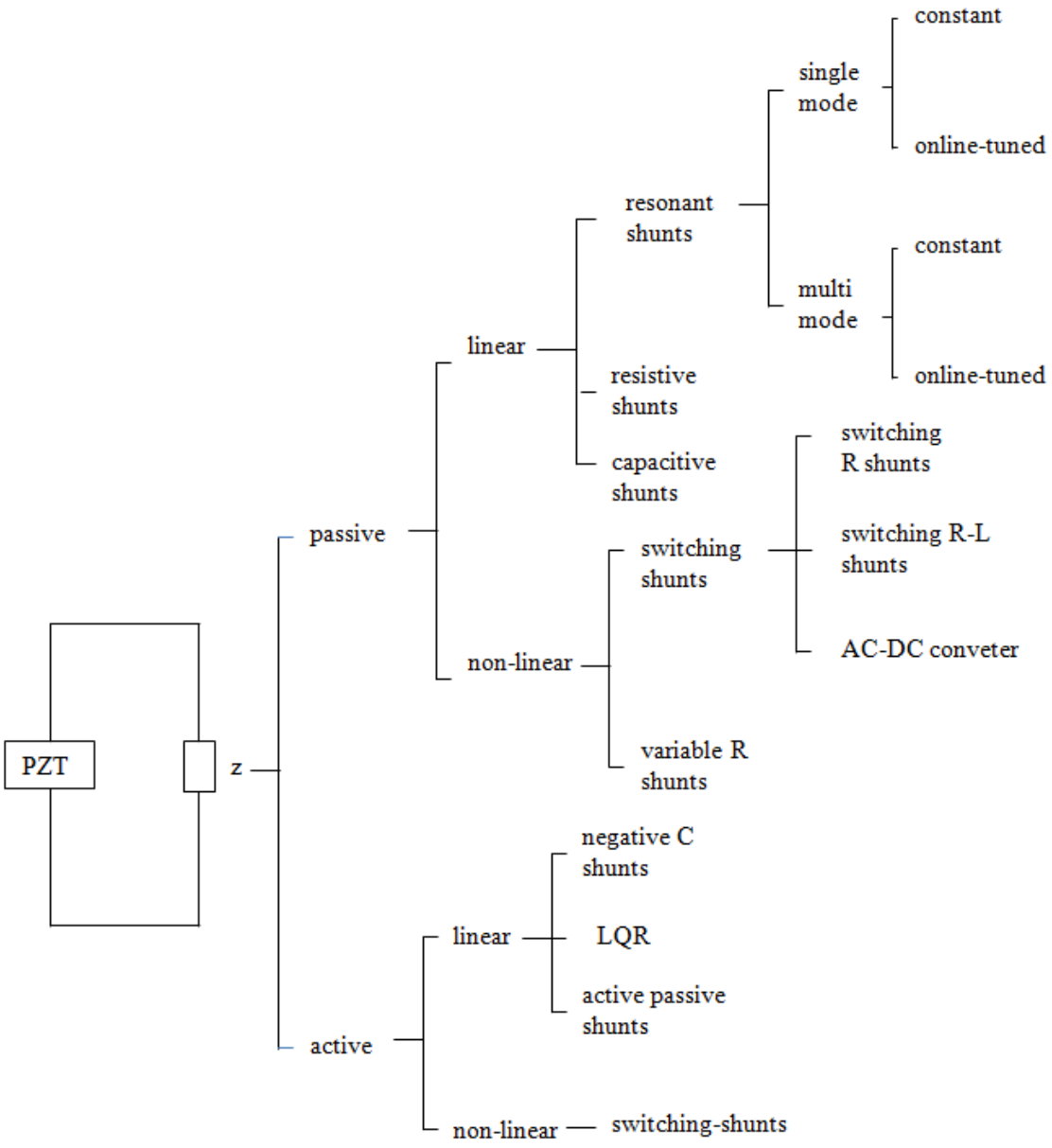

Figure 54 Piezo shunting methods. Based on [16].

5.3 Energy Harvesting from Aeroelastic Phenomena

Chapter 4 introduces to a wide number of accessible solutions to extract reusable energy from vibrations, and one of them is represented by the piezoelectric harvesters. The sources of vibrations in aeronautic are many: the vibration of the nacelles, of the landing gear doors, of the flight control surfaces, of the empennages, of the wing and so on. In this section are the wing vibration phenomena to be treated for the purposes of the energy harvesting, in particular all dynamic conditions already treated in Chapter 3: Flutter, LCO and Gust disturbances. The piezoelectric wing studied in the frame of energy harvesting from aeroelastic phenomena is characterized by two PZT layers, assumed perfectly bonded on the upper and lower longitudinal faces of the wing box, on the proximity of the wing root, see Figure 55, and fully coated by electrodes connected in parallel to a purely restive electric load.

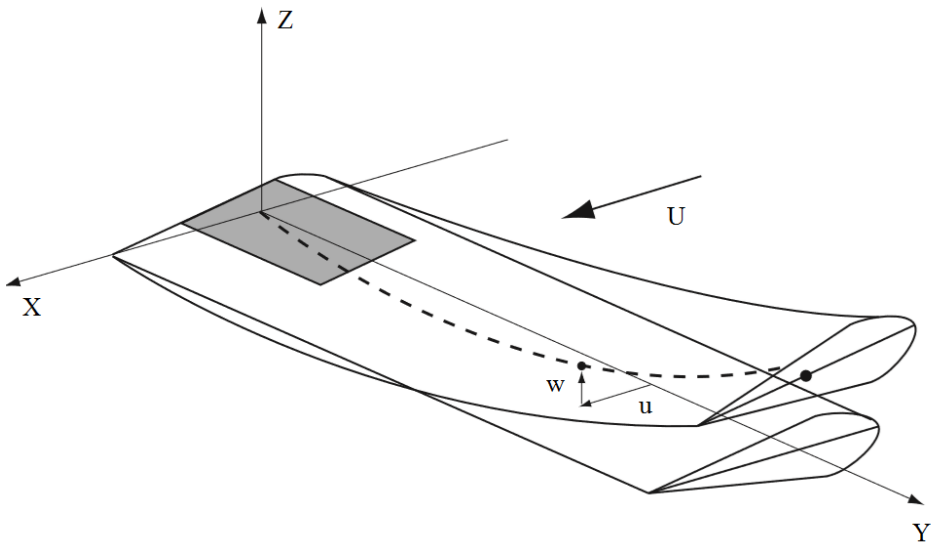

Figure 55 Piezoelectric wing configuration. [24]

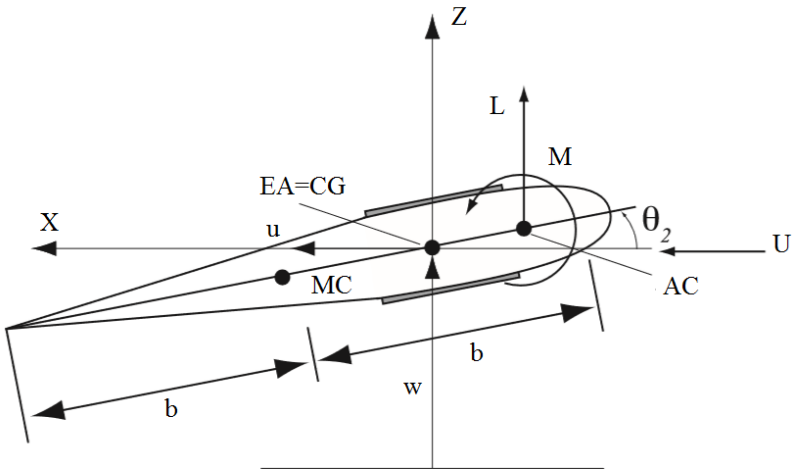

Figure 56 Piezoelectric wing configuration [2].

The wing and piezo data used for this part of the numerical investigations are reported in Table 7. The wing of Table 7 is the same of that analyzed in the previous chapters, the only difference is in the piezoelectric contribution that now appears.

Table 7 Wing and PZT data

WING		
Name	**Value**	**Definition**
l	1.2	Wing length $[m]$
b	0.135	Wing semi-chord $[m]$
h	0.0324	Wing-box thickness $[m]$
m_w	1.973	Wing mass $[Kg/m]$
EI_1	476.9	Wing out of plane stiffness $[N \cdot m^2]$
EI_3	20980	Wing in plane stiffness $[N \cdot m^2]$
GJ	3.988	Wing torsion stiffness $[N \cdot m^2]$
PZT		
Name	**Value**	**Definition**

l_p	0.04	PZT length $[m]$
s_p	0,02	PZT width $[m]$
t_p	0,0005	PZT thickness $[m]$
m_p	0,077	PZT mass $[Kg/m]$
E_p	6,30E+010	PZT elastic modulus $[N \cdot m^2]$
d_{31}	-1,79E-010	PZT strain coefficient $[m/V]$
k_3	1800	PZT dielectric constant

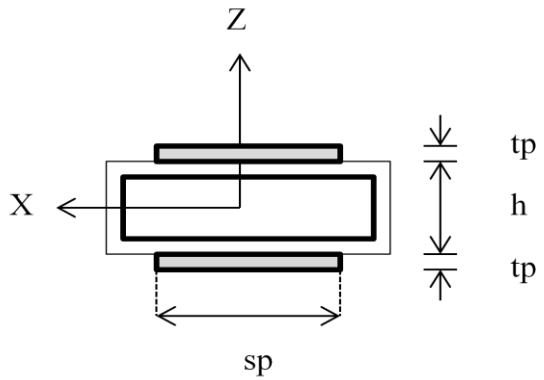

Figure 57 win box cross section.

The position of the piezoelectric elements with respect to the wing reference frame is shown in Figure 547

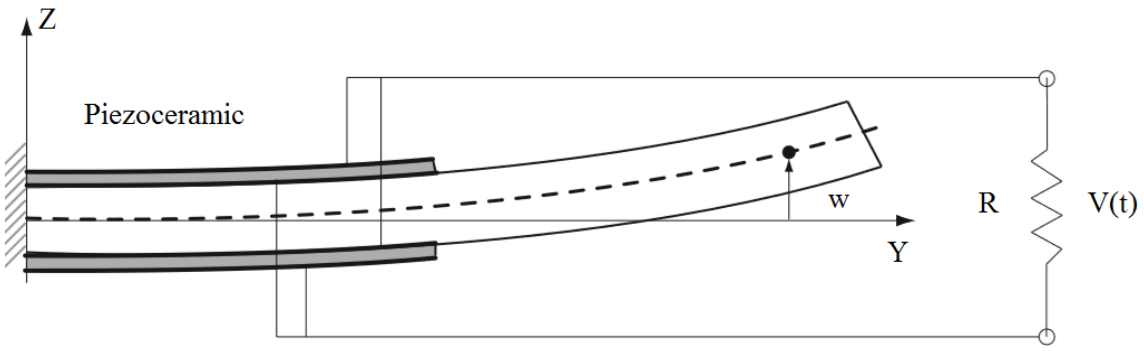

Figure 58 Representation of the PTZs and electric circuit connection [24].

Figure 58, Indeed, proposes the type of electric connection of the piezoelectric elements used for the study on energy harvesting. Ref [8] provides a comparative study between the parallel and the series connections of a pair of piezoelectric elements, bonded on the longitudinal surfaces of a cantilever beam. In particular it shows how the typical piezoelectric parameters are influenced by the specific connection we choose.

The mathematical model and the results discussed in this section of Chapter 5 refer to a parallel connection of the electrodes. This type of connection cause the electric field E_3, in i_3 direction, to be dependent of the voltage V and of $\chi(\zeta)$, which is a function of the ζ coordinate, but remains constant across the PZT thickness, such as [11], [14]:

$$E_3 = \chi(\zeta)V = \begin{cases} \frac{-V}{t_p} & \frac{h}{2} < \zeta < \frac{h}{2} + t_p \\ 0 & -\frac{h}{2} < \zeta < \frac{h}{2} \\ \frac{V}{t_p} & -\frac{h}{2} - t_p < \zeta < -\frac{h}{2} \end{cases} \quad 5.8$$

The purely elastic components of the wing are assumed to deform as a nonlinear 3-D Euler-Bernoulli. However , as a first approximation it will be assumed that the piezoelectric elements deform linearly. The wing model is maintained exactly as in Chapter 2, therefore all the assumptions previously made and the equations derived are still valid. What changes here is the introduction into the model of two piezoelectric layers, whose mathematical representations is derived according to the same procedure explained in Chapter 2, that's to say trough the extended Hamilton energy approach, as shown from equation 5.12. As previously mentioned, for the sake of simplicity, the piezos are assumed to behave linearly, contrary to the wing whose dynamical behavior is influenced by the nonlinear terms

assumed into the equations of motion. This simplification which affects the piezoelectric elements do not represent a concrete obstacle for the correct analysis of the results. The assumed piezos are two very short elements and are located into an area of the wing surface where the introduction of the nonlinearities is not justified dynamical response of the same piezos. Numerical evidence to this will be given later on.

The constitutive equations of the PTZs layers above are derived according to [9].

$$\begin{Bmatrix} M_1 \\ M_2 \\ M_3 \\ B_3 \end{Bmatrix}_P = \begin{bmatrix} C_{11}H & 0 & 0 & N_{14}H \\ 0 & C_{22}H & 0 & 0 \\ 0 & 0 & C_{33}H & 0 \\ N_{41}H & 0 & 0 & N_{44}H \end{bmatrix} \begin{Bmatrix} \rho_1 \\ \rho_2 \\ \rho_3 \\ V \end{Bmatrix} \tag{5.9}$$

The subscript P identify the PZT related measures, while V is the voltage across the electrodes. M_1, M_2, M_3 are the moments with respect to $\xi\eta\zeta$ and B_3 is the integral of the electric displacement over the PZT electrodes. Consequently, the elements of the PZT constitutive matrix which characterize the coupled electromechanical behavior are defined as:

$$\begin{aligned} N_{14} &= -\frac{e_{31}\, s_p}{t_p}\left({t_p}^2 + h * t_p\right) \\ N_{41} &= \frac{e_{31}\, s_p}{t_p}\left({t_p}^2 + h * t_p\right) \\ N_{44} &= 2 s_p \frac{{\varepsilon_{33}}^S}{t_p} \end{aligned} \tag{5.10}$$

where e_{31} and ${\varepsilon_{33}}^S$ are the piezoelectric coupling coefficient and the electric permittivity, respectively, both evaluated at constant strain and s_p the piezo width. The nomenclature of the piezoelectric constants is in agreement with the IEEE Standard of Piezoelectricity but their value is properly adapted to the wing configuration. H appearing in Eq. 5.9 is a combination of two Heaviside functions, introduced into the model, as in

[10] , to take into account the difference in the PZTs length with respect to the wing length, since the PZT patches cover only a portion of the wing. It is defined as:

$$H = H_1(y) - H_2(y - l_p) \tag{5.11}$$

where l_p is the piezos length. The extended Hamilton principle is used to derive the equations of motion:

$$\int_{t_1}^{t_2} (\delta T - \delta \Pi)\, dt = 0 \tag{5.12}$$

where T and Π are the kinetic and potential energy functions, respectively. Π, contains the sum of two additional energy terms, the strain energy U and the potential energy due to the external and damping forces W_c. The energy terms referring to the PZT layers are accounted in Eq. 5.12 as explained in [11]. By substituting the wing and piezos energy contributions into Eq. 5.12 and equating to zero all the expressions depending on the partial derivatives of each time dependent function, the following four equations of motion are obtained:

Torsion:

$$\begin{aligned} &-I_y\ddot{\theta} - c_5\dot{\theta} - D_{11}\theta u'^2 + D_{33}\theta u'^2 - D_{11}u'w'' + D_{22}u'w'' + D_{33}u'w'' + \\ &D_{11}\theta w''^2 - D_{33}\theta w''^2 + D_{22}\theta'' + D_{22}u'w'' - \mathrm{I}_{\mathrm{y_p}}H\theta'' + \mathrm{C}_{22}H\theta'' + \\ &\mathrm{C}_{22}H'\theta' + \mathrm{C}_{33}H\theta u''^2 + \mathrm{C}_{33}Hu''w'' - \mathrm{C}_{33}H\theta w^{(2,0)^2} = -q_\theta \end{aligned} \tag{5.13}$$

Out of plane bending:

$$\begin{aligned} &-m_w\ddot{w} + I_X\ddot{w}'' - c_3\dot{w} - D_{11}w'''' - D_{11}u''\theta'' - 2D_{22}u''\theta'' + D_{33}u''\theta'' - \\ &2D_{11}\theta'u''' - D_{22}\theta'u''' + 2D_{33}\theta'u''' - D_{11}\theta u'''' + D_{33}\theta u'''' - D_{22}u'\theta''' + \\ &2D_{11}\theta'^2w'' - 2D_{33}\theta'^2w'' + 4D_{11}\theta\theta'w''' - 4D_{33}\theta\theta'w''' + D_{11}\theta^2w'''' - \\ &D_{33}\theta^2w'''' - m_pH\ddot{w} + I_{X_p}H\ddot{w}'' - C_{11}Hw'''' + I_{X_p}H'\ddot{w}' - C_{11}Hw'''' - \end{aligned}$$

$$C_{11}H''w'' - 2C_{11}H'w''' + C_{33}\theta H''u'' + 2C_{33}H'\theta'u'' - C_{33}\theta^2H''w'' - 4C_{33}\theta H'\theta'w'' - 2C_{33}H\theta'^2w'' - 2C_{33}H\theta w''\theta'' + 2C_{33}\theta H'u''' + 2C_{33}H\theta'u''' - 2C_{33}\theta^2H'w''' - 4C_{33}H\theta\theta'w''' + C_{33}H\theta u'''' - C_{33}H\theta^2w'''' - N_{14}H''V = -q_w \quad 5.14$$

In plane bending:

$$-m_w\ddot{u} + I_Z\ddot{u}'' - c_1\dot{u} - D_{33}u'''' - D_{11}w''\theta'' + D_{22}w''\theta'' + D_{33}w''\theta'' - 2D_{11}\theta'w''' + D_{22}\theta'w''' + 2D_{33}\theta'w''' - D_{11}\theta w'''' + D_{33}\theta w'''' - m_pH\ddot{u} + I_{Z_p}H\ddot{u}'' - C_{33}Hu'''' + I_{Z_p}H'\ddot{u}' - C_{33}H''u'' - 2C_{33}H'u''' + C_{33}\theta H''w'' + 2C_{33}H'\theta'w'' + C_{33}Hw''\theta'' + 2C_{33}H'\theta w''' + 2C_{33}H\theta'w''' + C_{33}H\theta w'''' = 0$$

5.15

In some cases the piezo contribution might be assumed purely linear. This happen, as in all chapter 5, when the length of the piezo patch is very small compared to the wing semi span and so the displacement filed which in the region where the piezo patch is applied. Chapter 6 instead shows that when the length of the piezo element is not negligible with respect to the wing semi-span the nonlinear terms of the piezo contribution have to be considered. Eqs. 5.13, 5.14 and 5.15 include only the main nonlinear terms, obtained in agreement with the asymptotic reduction procedure of Chapter 2. The full representation of the nonlinear piezoelectric equations of motion is reported in Appendix. q_w, q_θ are the external aerodynamic loads in the out-of-plane bending and torsion directions.

Piezoelectric circuit:

$$-Q + N_{44}H\,V + N_{41}Hw'' = 0 \quad 5.16$$

Where V is the voltage across the electrodes and Q is the total charge gathered over these. It can be rewritten in terms of the resistive load R of the electrical circuit connected to PZT layers as:

$$\dot{Q} = -\frac{V}{R} \tag{5.17}$$

It has to be noted that the piezo contributions appear linearly in Eqs. 5.13 through 5.16. This simplifying assumption is justified by the small displacements field which involves the piezo elements, numerically evaluated, in terms of its relative value with respect to the displacement, which at 1.2 m circa from the wing tip is in the order of $10^{-8}m$.

Once the equations of motion of the piezoelectric wing are defined, they can be used to estimate the amount of energy that can be extracted from some aeroelastic phenomena, such as Flutter, LCO and atmospheric instabilities. Flutter is the easiest condition to analyze because it requires the linear terms only of equations 5.13, 5.14 and 5.15, therefore they become:

Torsion:

$$-I_y\ddot{\theta} - c_5\dot{\theta} + D_{22}\theta'' - I_{y_p}H\ddot{\theta} + C_{22}H\theta'' + C_{22}H\theta' = -q_\theta \tag{5.18}$$

Out of plane bending:

$$-m_w\ddot{w} + I_X\ddot{w}'' - c_3\dot{w} - D_{11}w'''' - m_pH\ddot{w} + I_{X_p}H\ddot{w}'' - C_{11}Hw'''' + I_{X_p}H'\ddot{w}' - C_{11}H''w'' - 2C_{11}H'w''' - N_{14}H''V = -q_w \tag{5.19}$$

In plane bending:

$$-m_w\ddot{u} + I_Z\ddot{u}'' - c_1\dot{u} - D_{33}u'''' - m_pH\ddot{u} + I_{Z_p}H\ddot{u}'' - C_{33}Hu'''' + I_{Z_p}H'\ddot{u}' - C_{33}H''u'' - 2C_{33}H'u''' = 0 \tag{5.20}$$

Equation 5.16 doesn't change, it is already linear. The approximation of the dynamical behaviour of the structure is achieved by introducing the modal representation of the displacements field by the Galerkin approach. The displacements are therefore represented by the product of a time function variable and a set of truncated modes to approximate the solution:

$$\begin{Bmatrix}\theta\\ w\\ u\end{Bmatrix} = [\Phi(y)]\{r(t)\} =$$

$$\begin{bmatrix}\phi_{\theta_1} & \cdots & \phi_{\theta_n} & 0 & \cdots & 0 & 0 & \cdots & 0\\ 0 & \cdots & 0 & \phi_{w_1} & \cdots & \phi_{w_n} & 0 & \cdots & 0\\ 0 & \cdots & 0 & 0 & \cdots & 0 & \phi_{u_1} & \cdots & \phi_{u_n}\end{bmatrix} \begin{Bmatrix} r_{\theta_1}\\ \vdots\\ r_{\theta_n}\\ r_{w_1}\\ \vdots\\ r_{w_n}\\ r_{u_1}\\ \vdots\\ r_{u_n}\end{Bmatrix} \quad 5.21$$

All the components of the displacement vector are discretized with the first decoupled bending-torsion modes of the clamped beam :

$$\phi_{\theta_i} = \sqrt{2}\sin(\gamma_i y) \quad 5.22$$

$$\phi_{w_i,u_i} = \cosh(\alpha_i y) - \cos(\alpha_i y) - \beta_i(\sinh(\alpha_i y) - \sin(\alpha_i y)) \quad 5.23$$

with $\gamma_i = \frac{\pi\left(i-\frac{1}{2}\right)}{1}$, α_i and β_i chosen coherently with the assumed number of modes. The values used here for the flutter analysis, and corresponding to the first modes, are:

$$\alpha_1 = \frac{1.87510}{l}, \beta_1 = 0.734096, \gamma_1 = \frac{\pi\left(1-\frac{1}{2}\right)}{1} \quad 5.24$$

In Chapter 3 the typical flutter response was presented. It consist of a simple harmonic motion where the time dependent coordinate, the generalized coordinate can be written as the product of a constant value and

an exponential function: $\{r(t)\} = \{\bar{r}e^{i\omega t}\}$. Therefore the system degrees of freedom become:

$$\begin{Bmatrix} \theta_2 \\ w \\ u \end{Bmatrix} = \begin{bmatrix} \phi_{\theta_1} & 0 & 0 \\ 0 & \phi_{w_1} & 0 \\ 0 & 0 & \phi_{u_1} \end{bmatrix} \begin{Bmatrix} \bar{r}_{\theta_1} e^{i\omega t} \\ \bar{r}_{w_1} e^{i\omega t} \\ \bar{r}_{u_1} e^{i\omega t} \end{Bmatrix} \quad 5.25$$

substituting Eq. 5.25 into Eqs. 4.18, 5.19, 5.20 and 5.16 we obtain:

Torsion:

$$\omega^2 I_y \phi_{\theta_1} \bar{r}_{\theta_1} - i\omega\, c_5 \phi_{\theta_1} \bar{r}_{\theta_1} + D_{22} \phi_{\theta_1}{}'' \bar{r}_{\theta_1} + \omega^2 I_{y_p} H \phi_{\theta_1} \bar{r}_{\theta_1} + C_{22} H \phi_{\theta_1}{}'' \bar{r}_{\theta_1} + C_{22} H \phi_{\theta_1}{}' \bar{r}_{\theta_1} = -q_\theta \quad 5.26$$

Out of plane bending:

$$\omega^2 m_w \phi_{w_1} \bar{r}_{w_1} - i\omega\, c_3 \phi_{w_1} \bar{r}_{w_1} - D_{11} \phi_{w_1}{}'''' \bar{r}_{w_1} + \omega^2 m_p H \phi_{w_1} \bar{r}_{w_1} - C_{11} H \phi_{w_1}{}'''' \bar{r}_{w_1} - C_{11} H'' \phi_{w_1}{}'' \bar{r}_{w_1} - 2C_{11} H' \phi_{w_1}{}''' \bar{r}_{w_1} - N_{14} H''\, \bar{r}_V = -q_w \quad 5.27$$

In plane bending:

$$\omega^2 m_w \phi_{u_1} \bar{r}_{u_1} - i\omega\, c_1 \phi_{u_1} \bar{r}_{u_1} - D_{33} \phi_{u_1}{}'''' \bar{r}_{u_1} + \omega^2 m_p H \phi_{u_1} \bar{r}_{u_1} - C_{33} H \phi_{u_1}{}'''' \bar{r}_{u_1} - C_{33} H'' \phi_{u_1}{}'' \bar{r}_{u_1} - 2C_{33} H' \phi_{u_1}{}''' \bar{r}_{u_1} = 0 \quad 5.28$$

Electric circuit

$$\frac{1}{R} \bar{r}_V + i\omega\, N_{44} H\, \bar{r}_V + i\omega\, N_{41} H \phi_{w_1}{}'' \bar{r}_{w_1} = 0 \quad 5.29$$

q_θ and q_w are those of equations 3.3 and 3.4.

5.3.1 Energy harvesting from Flutter oscillations

As in Chapter 3 the flutter condition is estimated by applying the V-g method. Figures 59 and 60 show the V-g plot for two values of the resistive load, $R = 1\ [\Omega]$ and , $R = 10^7[\Omega]$.

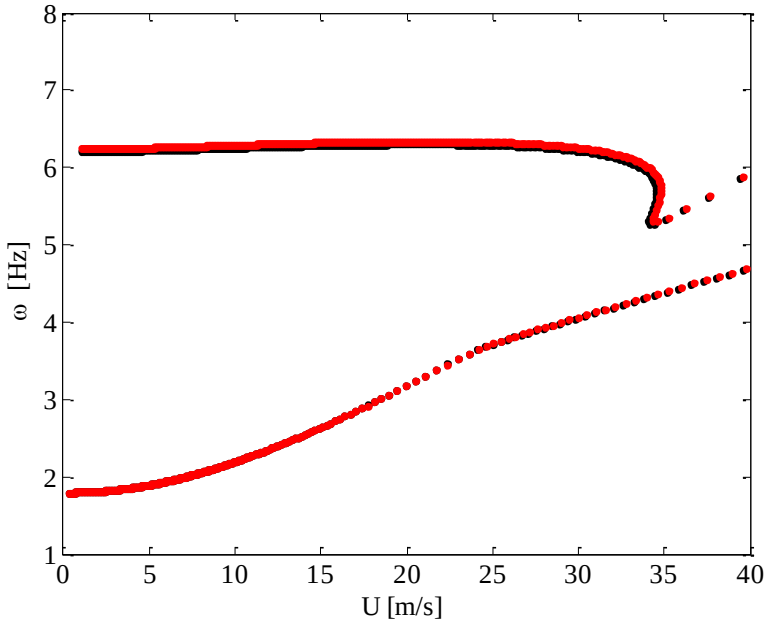

Figure 59 Frequencies Vs. Air speed for $R = 1[\Omega]$ (black dots) and $R = 10^7[\Omega]$ (red dots)

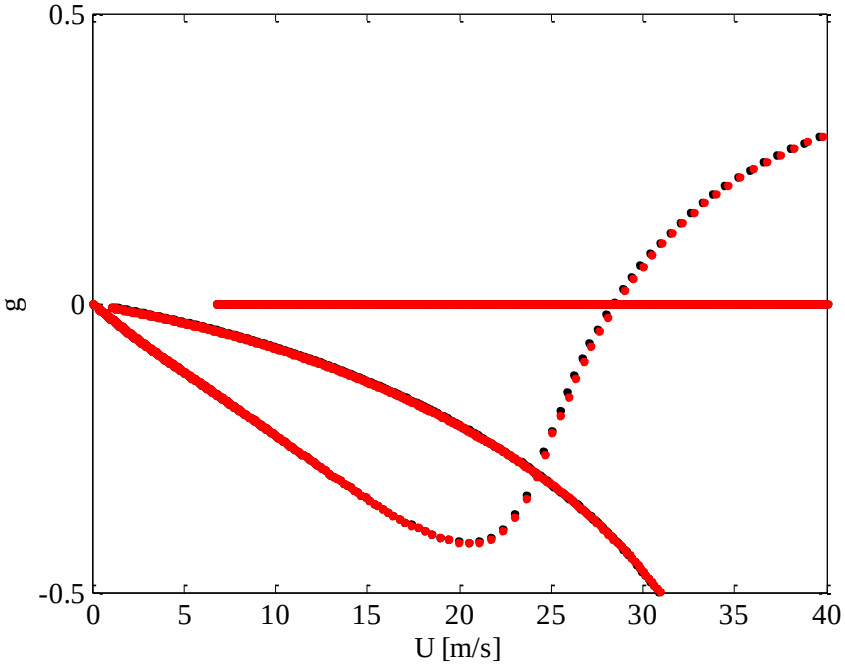

Figure 60 Artificial damping Vs. Air speed for $R = 1[\Omega]$ (black dots) and $R = 10^7[\Omega]$ (red dots)

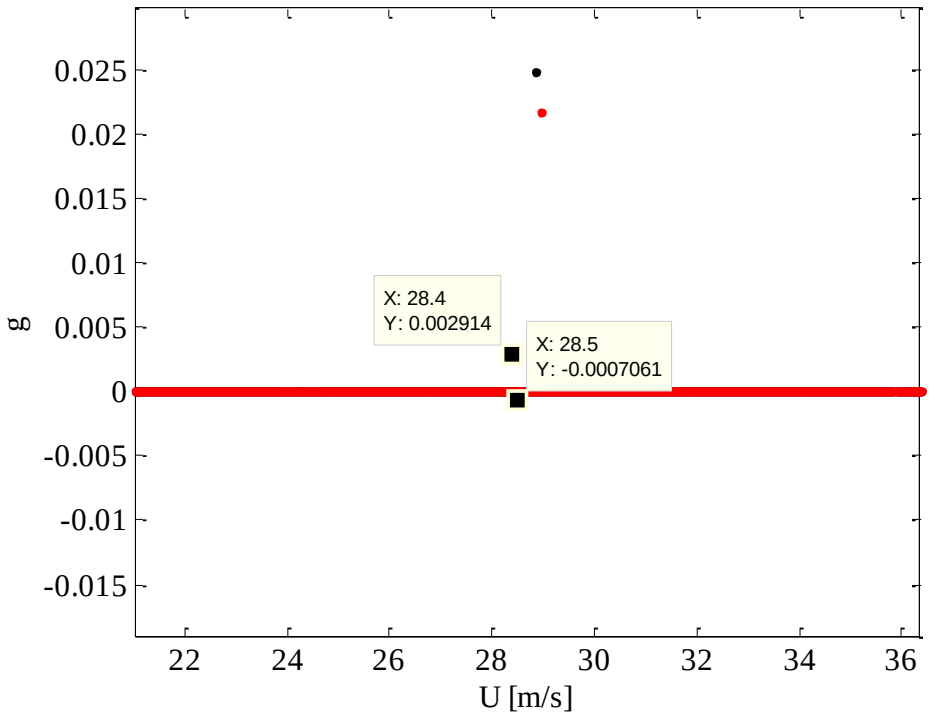

Figure 61 Detail of Figure 60

The flutter condition is identified by the g=0 axis crossing point. The domain of the reduced frequency is explored by using a discretization interval of 0.001 which do not guarantee the exact zero artificial damping condition. Therefore it is assumed by taking the closest point to this condition. The black dots refer to the $R = 1\ [\Omega]$ configuration, while the reds to the $R = 10^7\ [\Omega]$ one. The higher value of the electric load moves the zero damping condition to higher speed values, which imply a postponement of the flutter phenomena. The increase of the flutter speed for this piezoelectric wing configuration is not so relevant and its maximum percentage increase, circa 1.7%, is achieved for a value of the resistive load around $10^6\ [\Omega]$, as reported in Figure 62. Although the results are not promising in the frame of the flutter postponement we cannot exclude that a different configuration of the piezoelectric wing is going to be more effective in terms of flutter postponement.

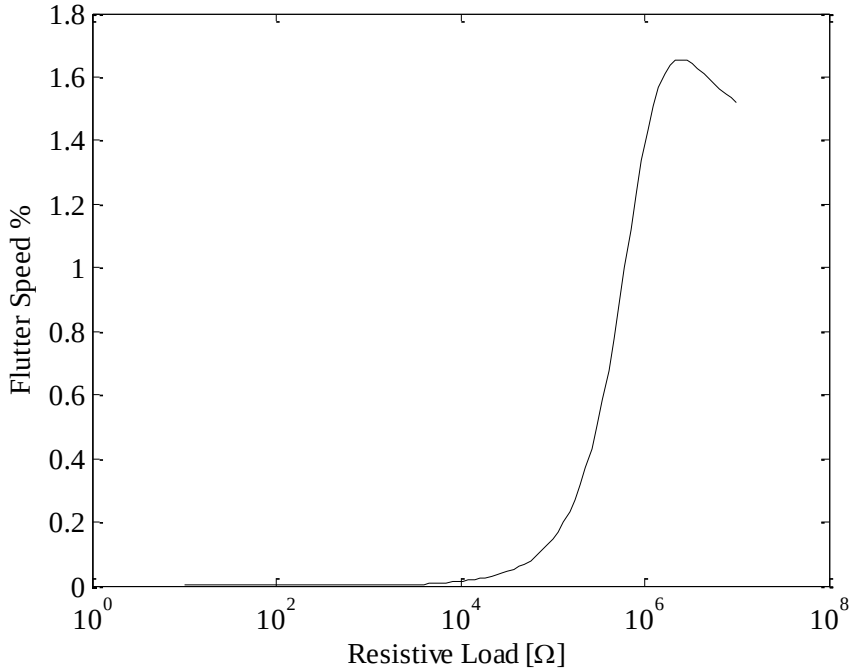

Figure 62 % increase of the flutter speed Vs. electric resistive loads

The amount of energy harvested from the flutter condition is derived from equation 5.30 as proposed in [12], [14] .

$$Power/_{wing\ tip\ plunge\ amplitude} = \frac{1}{R}\left(\frac{\bar{r}_V}{\phi_{w_1}(l)*\bar{r}_{w_1}}\right)^2 = \frac{1}{R*\phi_{w_1}(l)}\left(\frac{i\omega_{flutter}\, N_{41} H \phi_{w_1}{}''}{\frac{1}{R}+i\omega_{flutter}\, N_{44} H}\right)^2 \qquad 5.30$$

The flutter condition is characterized by a simple harmonic oscillation but its amplitude is undetermined since it depends on the initial condition set in the numerical simulations. However, albeit the oscillation amplitude assume an arbitrary value, the ratio of the power generated from the flutter oscillation and win tip amplitude maintains constant and is vary with the electric resistance as in Figure 63. The curve representing the power normalized with respect to the wing tip displacement vs. the resistive load shows a maximum for at $R = 10^5$ [Ω], which do not coincide with the maximum of Figure 62.

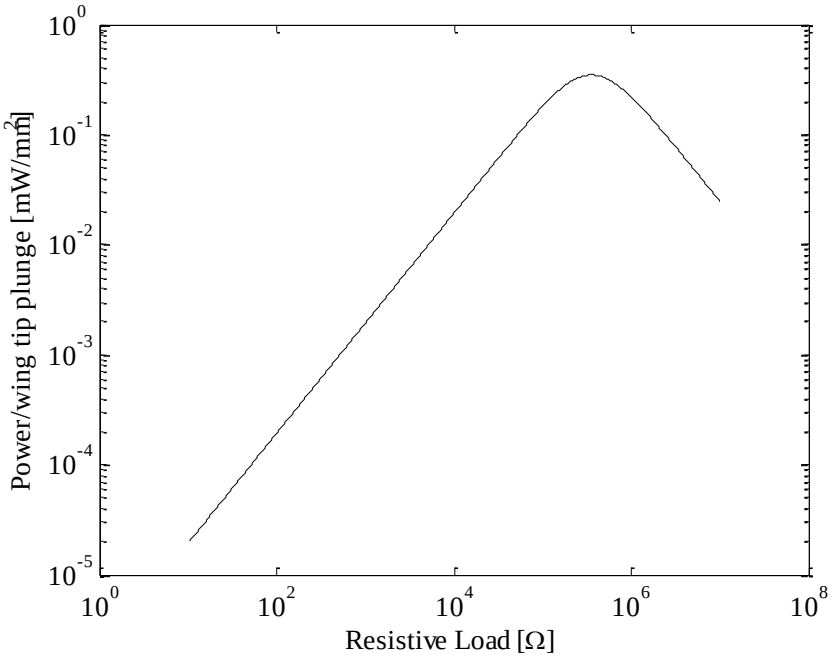

Figure 63 Normalized power vs. electrical resistive load

5.3.2 Energy harvesting from LCOs

As previously stated the amount of energy extracted from the flutter condition cannot be easily estimated since it depends strictly from the initial conditions of the system. It is different when the dynamic behavior of the structure is driven by nonlinearities, therefore during LCOs motion. In the LCOs condition the oscillation amplitude is independent from the initial disturbance which initiates the motion in the numerical simulations. This unable a more accurate analysis on the amount of energy extractable from pre and post flutter LCO, which is not limited to the purely critical flutter condition but to a wider air speed range. To achieve such a flexibility in the study of the model response, the equations of motion, Eqs. from 5.13 to 5.16, have to be solved in the time domain and not in the frequency domain as for the identification of the critical flutter condition. The discretization approach, consisting in the application of the modal

approximation and of the Galerkin method, is the same as for the flutter solution, with the differences that for the LCO solution the nonlinear terms are retained. The unsteady aerodynamic forces are modeled as in Chapter 2, according to the Wagner model.

The four equations of motion, to which the Galerkin method has been applied, can be rewritten according to the state-space formulation,. This allows compact and convenient way to reorganize the ordinary differential equations for numerical simulations by collecting all the terms according to the state vector $\{z\} = \{\dot{r} \quad r \quad V \quad w_1 \quad \cdots \quad w_4\}^T$, with $\{r\} = \{r_\theta \quad r_w \quad r_u\}^T$

$$\{\dot{z}\} = [S]\{z\} + [N]\{z(0)\} \tag{5.31}$$

$$[S] = \begin{bmatrix} -[M]^{-1}[D] & -[M]^{-1}[K] & [M]^{-1}[\Xi] & -[M]^{-1}[W] \\ I & 0 & 0 & 0 \\ -[\Xi]^T {C_p}^{-1} & 0 & -\left(R \cdot C_p\right)^{-1} & 0 \\ 0 & & [W_0] & \end{bmatrix} \tag{5.32}$$

where $[M], [K], [D]$ represent the modal mass matrix, the modal stiffness matrix and the modal damping matrix, respectively. Each of them contains both linear and nonlinear terms:

$$\begin{aligned} [M] &= [M]_L + [M]_{NL} \\ [K] &= [K]_L + [K]_{NL} \\ [D] &= [D]_L + [D]_{NL} \end{aligned} \tag{5.33}$$

In addition, $[\Xi] = \begin{bmatrix} 0 \\ N_{14} \int_0^l \phi_w \frac{d^2 H}{{d_y}^2} dy \\ 0 \end{bmatrix}$ is the electromechanical coupling vector, C_p is the piezoelectric capacitance while $[W]$ and $[W_0]$ are two linear matrix depending of the constant terms of the Wagner function. $[N]$ is a linear matrix containing the first time derivative of the Wagner's

function. Moreover the state-space formulation is very convenient because allows to introduce any required control scheme into the model without particular modeling efforts. Assuming $R = 10^5$ [Ω] as initial value of the resistive load, which contrary to the flutter condition it doesn't necessarily represent the optimum value for the purpose of the extraction of energy. The post-flutter LCO condition has a frequency value which is higher than the critical flutter one and it increase with the speed, therefore the optimum value of the resistive load might change with the speed (as shown later on). From the V-g solution we know the flutter speed therefore by including into the model the geometrical nonlinearities up to the third order and setting the external air speed to a value higher than the flutter one, the system will experience the LCO. Figures 64 and 65 show the time histories of the wing tip plunge displacement and of the wing tip pitch at the air speed equal to 29 m/s. Figures 66 and 67 are the phase plots of these same degrees of freedom.

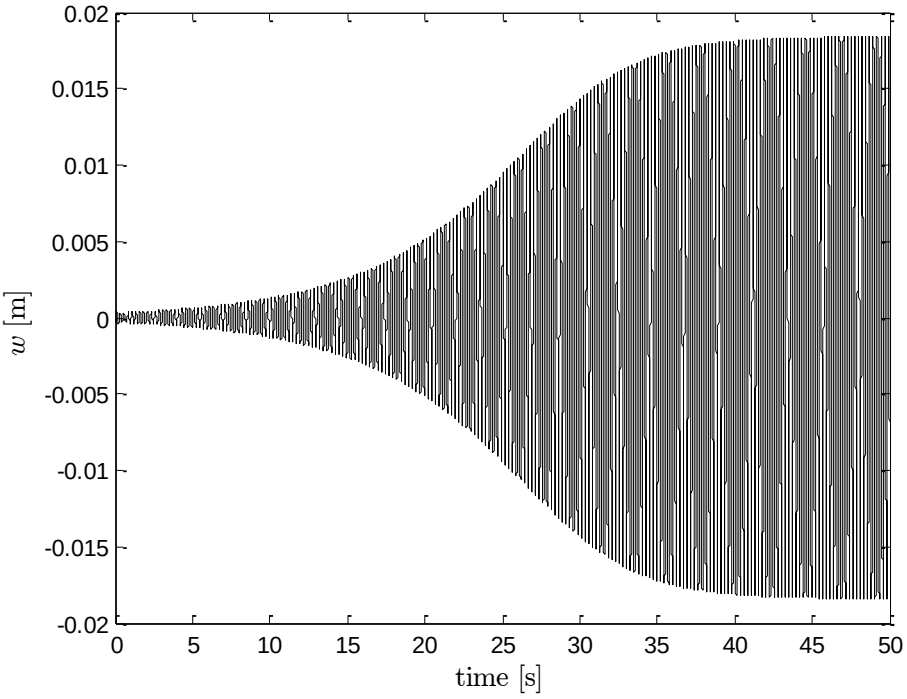

Figure 64 Wing tip plunge time history at 29 m/s [15].

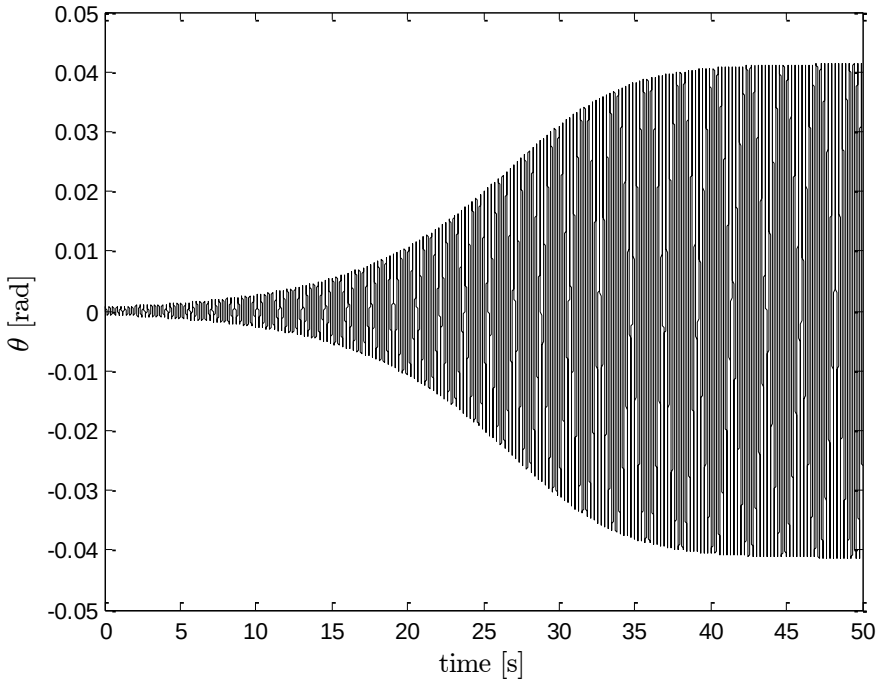

Figure 65 Wing tip pitch tome history at 29 m/s [15].

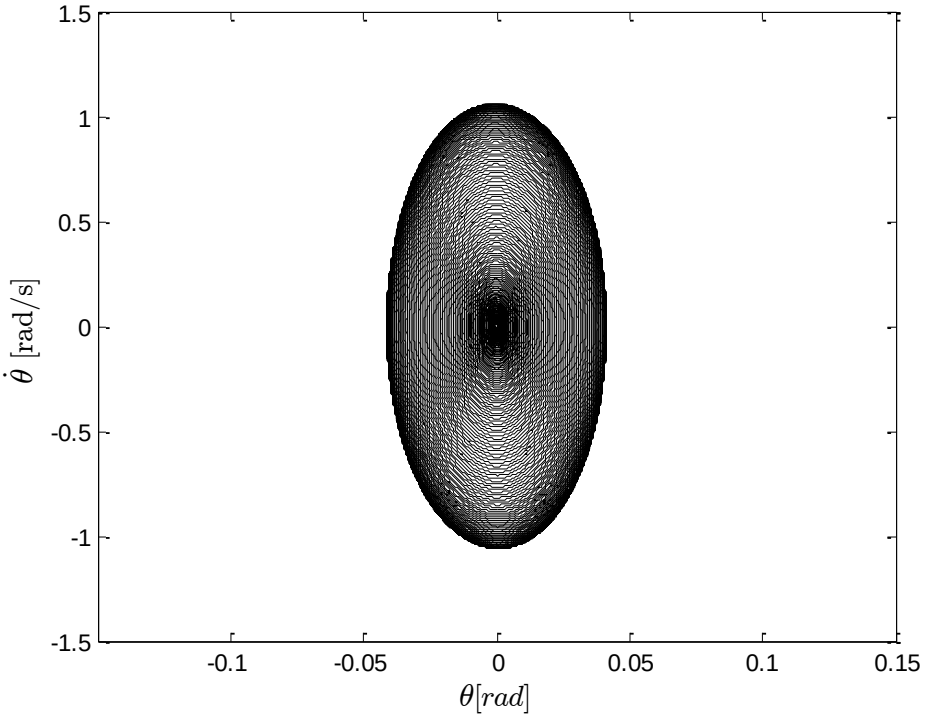

Figure 66 Phase diagram of the wing pitch at 29 m/s. [15].

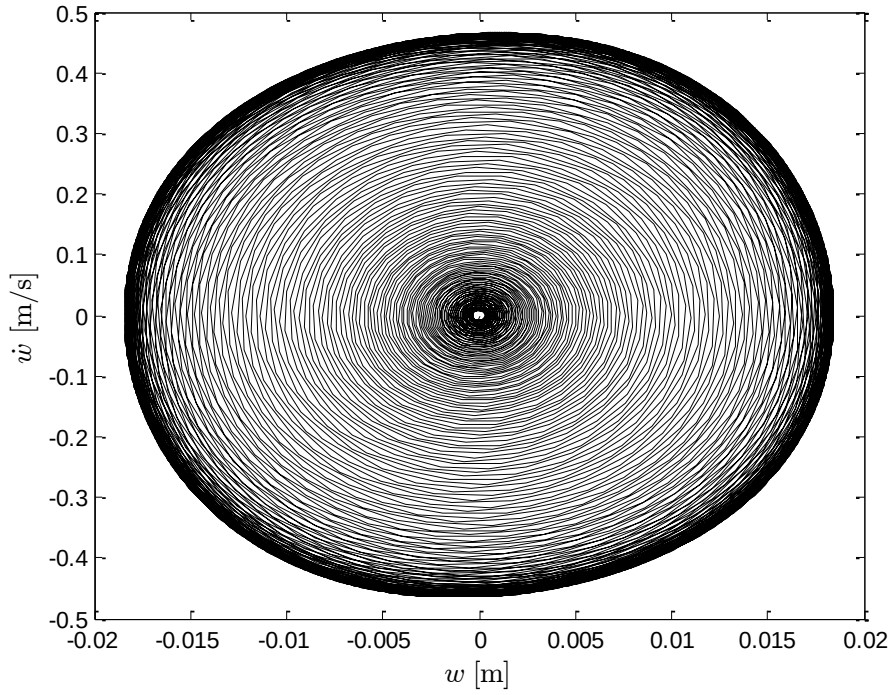

Figure 67 Phase diagram of the wing plunge at 29 m/s [15].

Particularly Figures 66 and 67 show how at a certain point the amplitude of the oscillation remain constant, which is what identify the establishment of the LCO. Increasing the air speed, as we can see from Figures from 68 to 71, the transitory is reduced and the LCO oscillation amplitude amplified with respect to the previous condition at lower air speed.

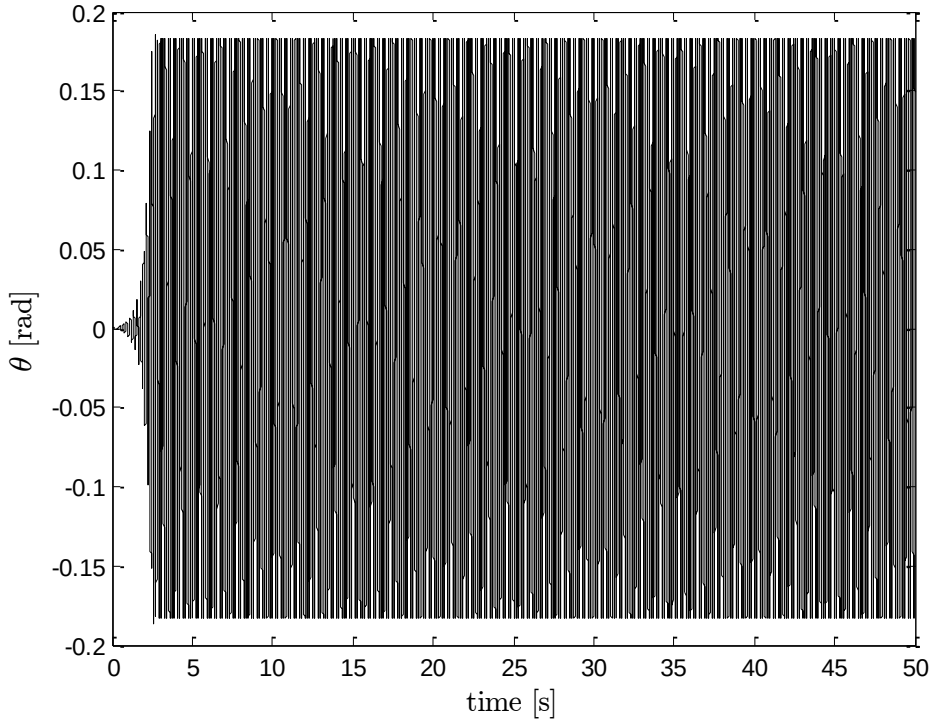

Figure 68 Wing tip pitch time history at 40 m/s [15].

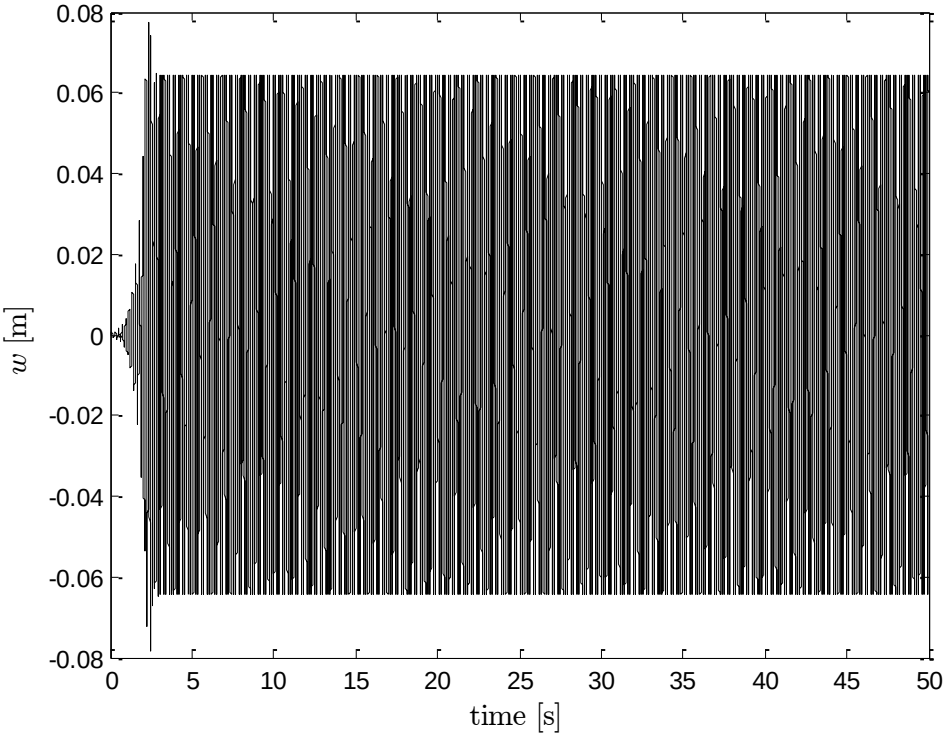

Figure 69 Wing tip plunge time history at 40 m/s [15].

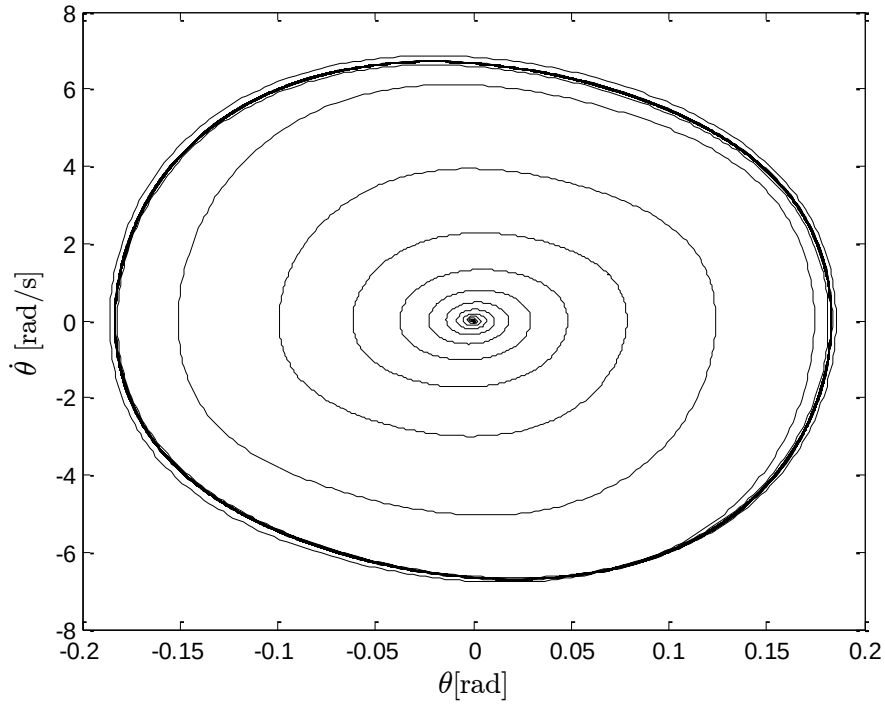

Figure 70 Phase diagram of the wing pitch at 40 m/s [15].

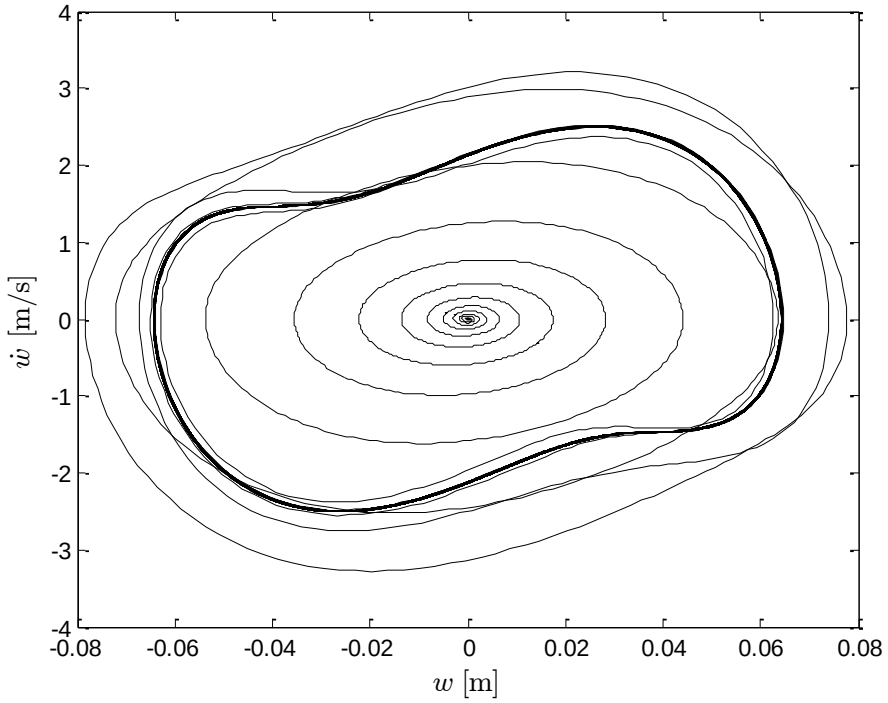

Figure 71 Phase diagram of the wing plunge at 40 m/s[15].

The instantaneous power extracted from these two LCOs is obtained from the instantaneous voltage as:

$$P(t) = \frac{(V(t))^2}{R} \qquad 5.34$$

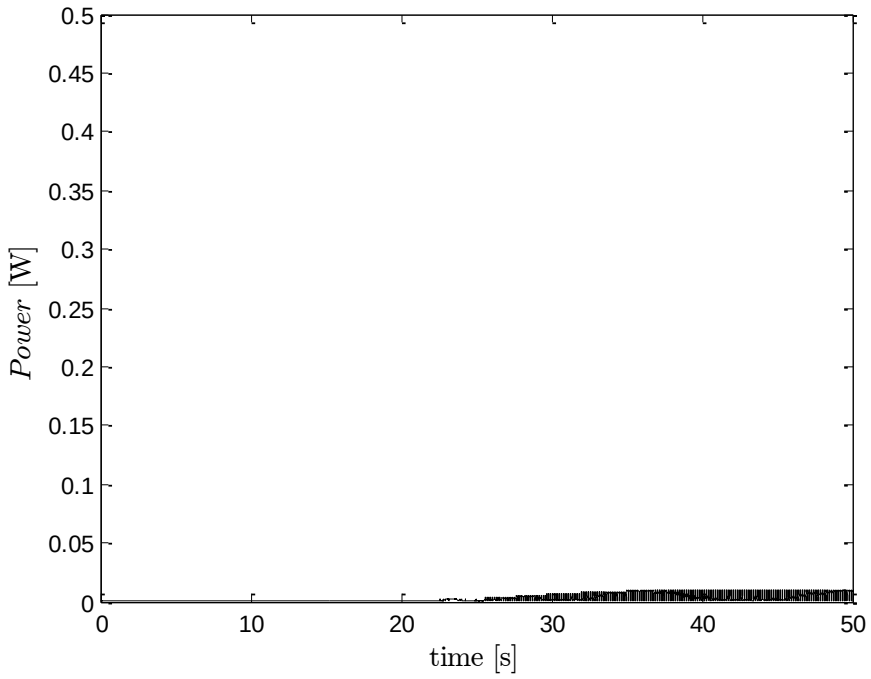

Figure 72 Instantaneous power at 29 m/s .

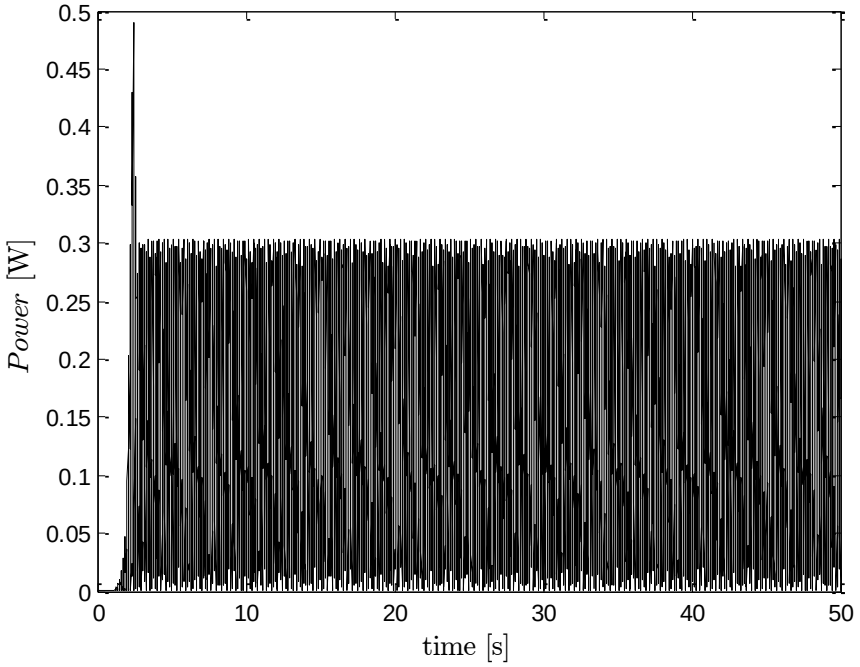

Figure 73 Instantaneous power at 40 m/s.

The effect of the resistive load over the maximum instantaneous power amplitude and over the maximum wing tip plunge oscillation amplitude at 29 m/s is reported in Figure 74.

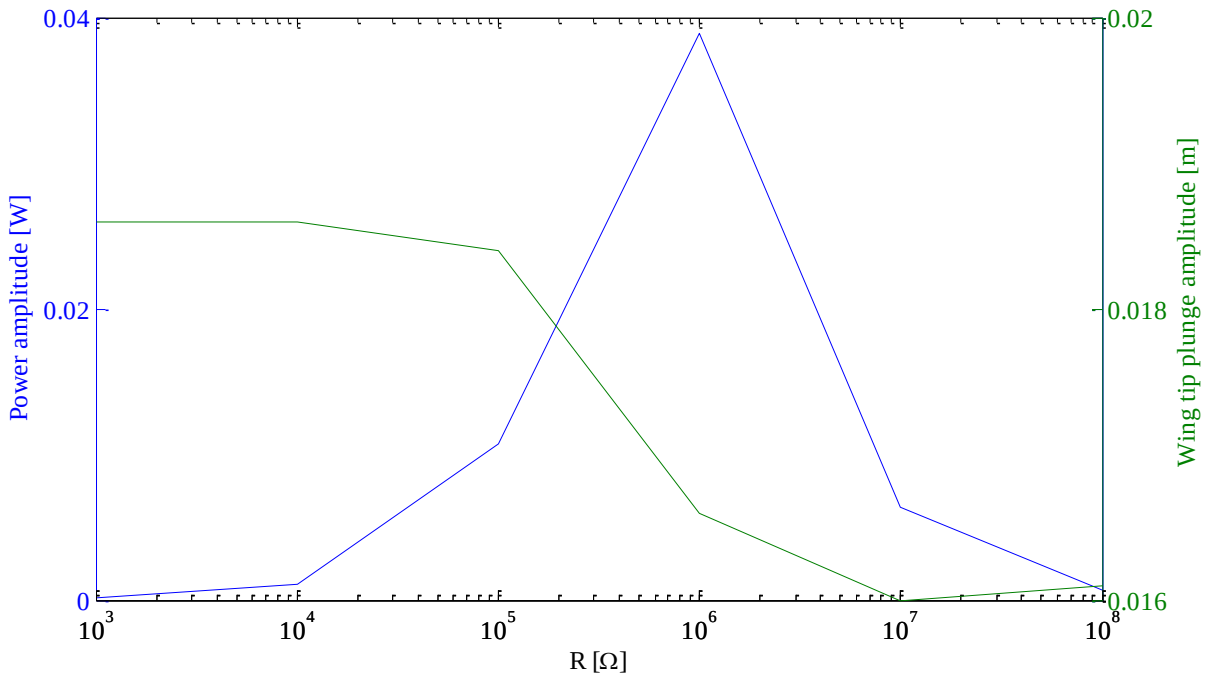

Figure 74 Power amplitude and wing tip plunge amplitude vs. electric resistive load.

At 29 m/s the maximum power amplitude is obtained for a resistive electric load equal to 10^6 [Ω] while the lowest value of the wing tip plunge amplitude is achieved at $R = 10^7$ [Ω]. Two distinct values of R were already highlighted during the analysis of flutter response for various values of the electric resistive load. Besides the energy extracted from the system can be further increased by properly designing the piezo element. As shown in Figure 75, if the length of the two piezo layers, which covers a portion of the upper and lower longitudinal surfaces of the wing, is increased, the flutter boundary can be expanded and more energy can be favorably harvested.

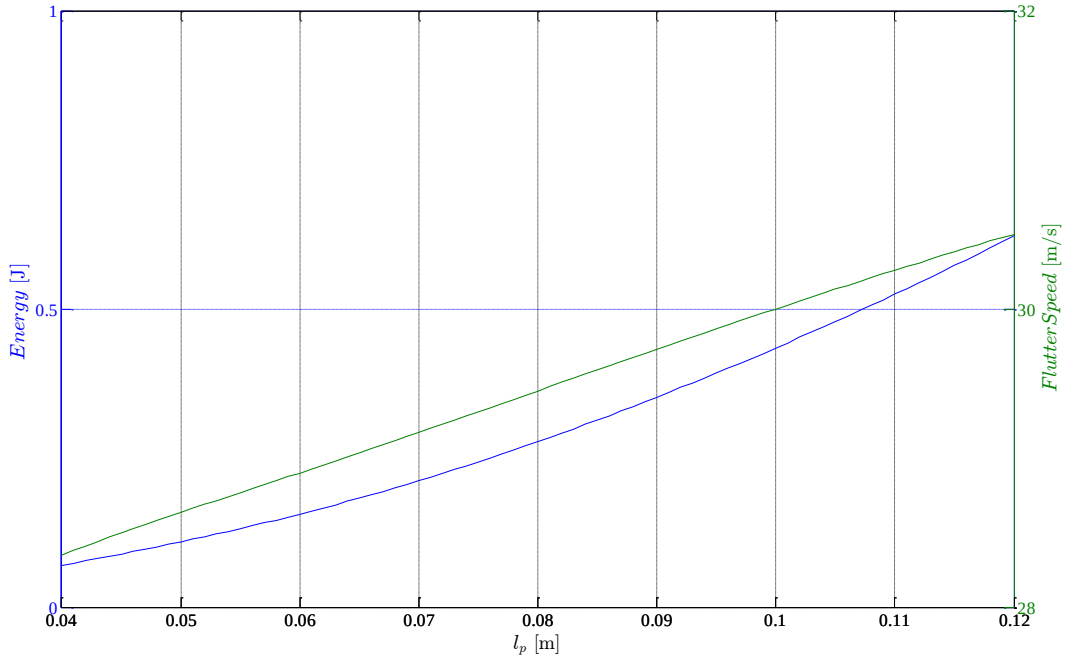

Figure 75 Energy harvested and flutter speed increase over the length of the piezo elements [15].

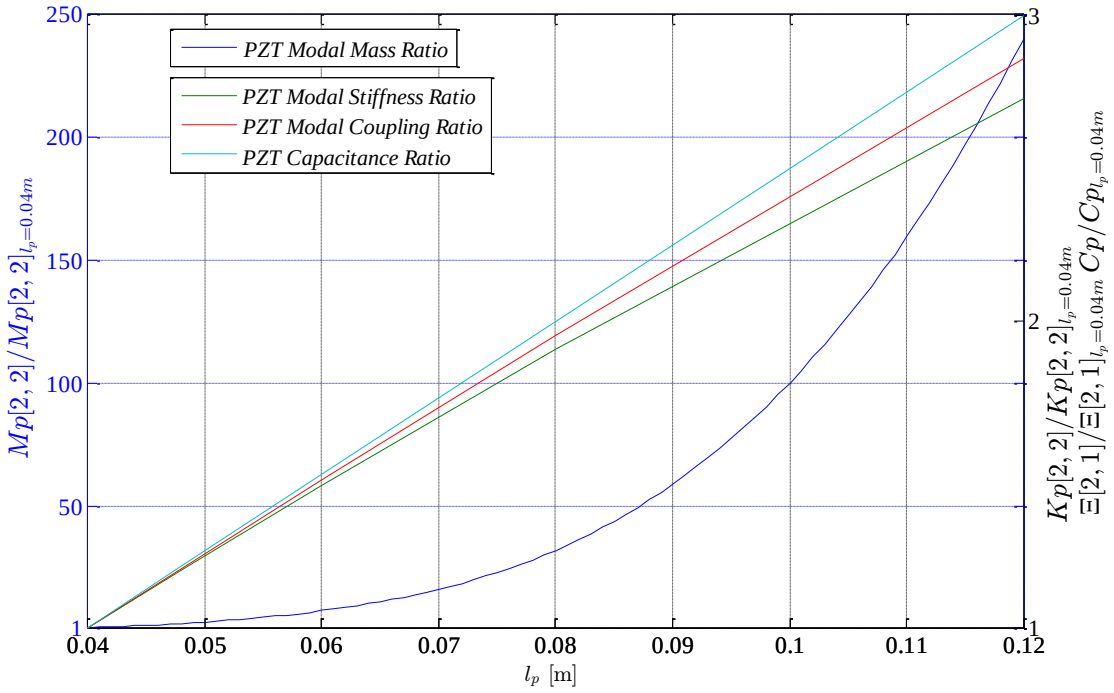

Figure 76 Modal matrices variation over the piezo length [15].

Figure 75 highlights how increasing the piezos' length increases linearly the flutter speed and the amount of energy harvested during the LCO

increases according to a quadratic dependence. The amount of energy harvested has been estimated by integrating the power time history, obtained by increasing by the same increment the flutter speed identified for each specific piezos' length,over a time interval equal to 10 seconds. The increase of the amount of energy harvested and of the flutter speed are the consequences of the variation of the PZT's inertia and stiffness which are influenced by the choice of piezos' length. Figure 77 shows the variation of the modal mass, $M_p[2,2]$, of the modal bending stiffness $K_p[2,2]$, of the electromechanical coupling, $\Xi[2,2]$, and of the electric capacitance, C_p, of the PZT in respect to their value at a piezo whose length is equal to 0.04m, Increasing the length causes large changes in the modal mass of piezoceramic; however, the mass still remains small, on the order of the order of $10^6\, g$ for a piezo length equal to 0.12 m. Furthermore, examining Figs. 76 and 77 together indicate the harvesters' behavior is not sensitive to changes in the piezoelectric mass and that the stiffness of the combined wing and PZT plays the dominant role the onset of flutter and increases the energy able to be extracted from the flow field. It must be noted the even though the effects from choosing a larger piezo element seem to be beneficial in all counts, it is not always practical. The material is brittle nature and therefore larger PZT's are susceptible to a higher risk of crack and fracture. From Figure 76 one can deduce that the piezoceramics introduce a delay effect into the flutter rise and this is due to the fact, as shown in Figure 77, that the piezo patches stiffen the original wing structure and at the same time removes kinetic energy from the system.

5.3.3 Harvesting from the gust response

Gusts are typically characterized by their profiles in space. A rigorous analytical treatment of atmospheric disturbances encountered by an aircraft requires the use of a continuous turbulence model. However, these profiles can be viewed as consisting of isolated pulses and can be approximated with a discrete description. The 2-D representation of the load and moment induced by the gust on the wing can be written, as already seen in Chapter 3, as:

$$L_g = -2\pi\rho bU \int_0^t U_g(\sigma)\dot{\Psi}(t-\sigma)d\sigma \qquad 5.35$$

$$M_g = L_g ec \qquad 5.36$$

where $\Psi(t-\sigma) = 1 - A_3 e^{-\frac{b_3 U}{b}(t-\sigma)} - A_4 e^{-\frac{b_4 U}{b}(t-\sigma)}$ is the Küssner's function, while $U(\sigma)$ is the amplitude of the chosen gust profile. The constants A_3, and A_4 are both equal to 0.5, while $b_3 = 0.13$, and $b_4 = 1.00$. Two deterministic gust profiles are the 1-COSINE gusts and the squared gusts. The function which defines the velocity profile for the 1-COSINE gust in space domain is written as:

$$U_g(s) = \frac{U_{ds}}{2} H(s)\left(1 - \cos\frac{\pi s}{S}\right) - \frac{U_{ds}}{2} H(s-2S)\left(1 - \cos\frac{\pi s}{S}\right) \qquad 5.37$$

where H is the Heaviside step function, S is the gust gradient, and the distance traveled by the wing in the gust is $s = Ut$ The 1-COSINE gust function [25], [26], [27] is modified to be consistent with Federal Aviation (FAR) Regulations (1993). U_{ds} is the design gust velocity, i.e., the maximum amplitude of the 1-COSINE gust shape and is defined by:

$$U_{ds} = U_{ref} F_g \left(\frac{S}{R_g}\right)^{\frac{1}{6}} \qquad 5.38$$

where U_{ref} is the reference velocity, F_g, is the flight alleviation factor, R_g specify the maximum range of the gust, 350 ft, for which the maximum amplitude is considered valid.

Figure 77 a) shows four 1-COSINE gust profiles used for the numerical simulations. Each of them is characterized by a distinct value of the gust gradient, S, chosen to cover a part of the parameter's range prescribed by the FARs. Figure 77 b) presents squared gusts, [25], [26], [27], which are also commonly used in the research community.

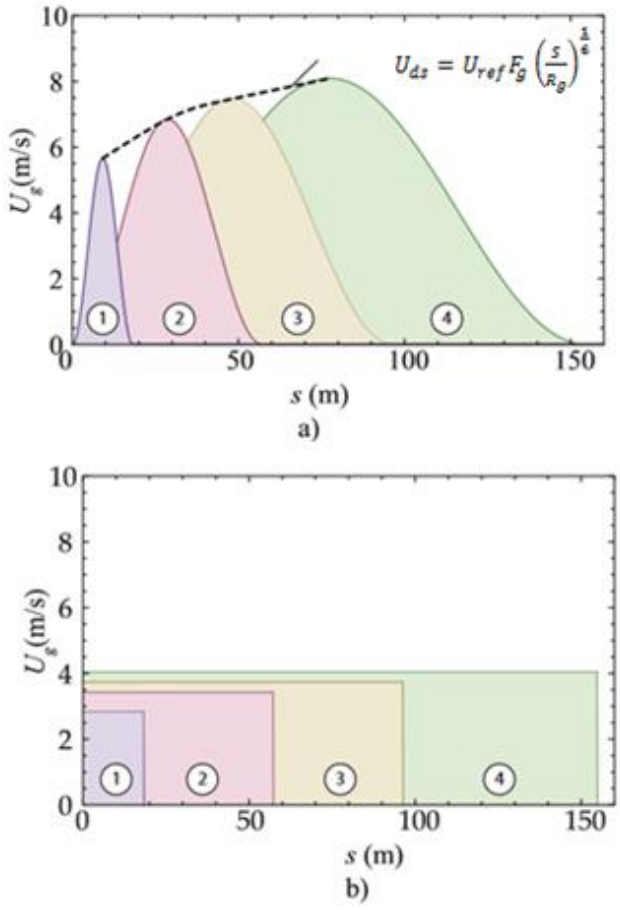

Figure 77 1-Cosine and squared gust profiles [24].

The form presented here is slightly modified to be represented by two Heaviside step functions. This allows the simulation of the response of the harvester after the gust abruptly subsides. The squared gust can be written as:

$$U_g(s) = \bar{U}_g H(s) - \bar{U}_g H(s - 2S) \quad 5.39$$

where $\bar{U}_g$ is the amplitude of the gust vertical velocity, properly chosen to guarantee the same value of the area under the 1-COSINE and squared gust profiles. In comparing the two deterministic gusts, we assume they are comparable if they have the same effective area, i.e., they provide the same energy. The numerical values of the parameters used in all simulations which follow are listed in Table 7. The gust loads are incorporated into the equations of motion as:

$$F = \begin{Bmatrix} q_{\theta_2} \\ q_w \\ 0 \end{Bmatrix} + \begin{Bmatrix} M_g \\ L_g \\ 0 \end{Bmatrix} \quad 5.40$$

The primary purpose of this research is to examine the effect of changes in gust parameters on the energy extracted by an aeroelastic energy harvester. However, the aeroelastic behavior is sensitive to the assumed free stream velocity, U. Significant variation of both the oscillation frequency and damping can occur, which influence both the mechanical and electrical response of the harvester. Not that for the given geometry and material parameters the flutter velocity is approximately 27m/s. The investigation here is arbitrarily chosen at a free stream velocity of 25 m/s. Examining the wing's response and the power harvested from the two afore defined deterministic gust models. Note that while the model is capable of predicting an in-plane bending response, the excitation considered here only affects the out of plane bending and rotational displacement of the wing. Each gust acts for a predetermined gust gradient S and therefore has a specified time evolution. Recall, that gusts with the same S are defined as having the same effective area, i.e., the area under the gust curve are the same for both the 1-COSINE and the squared gust. Figures 78 and 79 a), b), c), and d) illustrate the pitch response of the wing to both a square and

1-COSINE gusts for gust gradients, S, equal to 9.14 m, 28.56 m, 48.16 m, and 77.42 m, respectively. In all cases the free stream velocity is 25m/s.

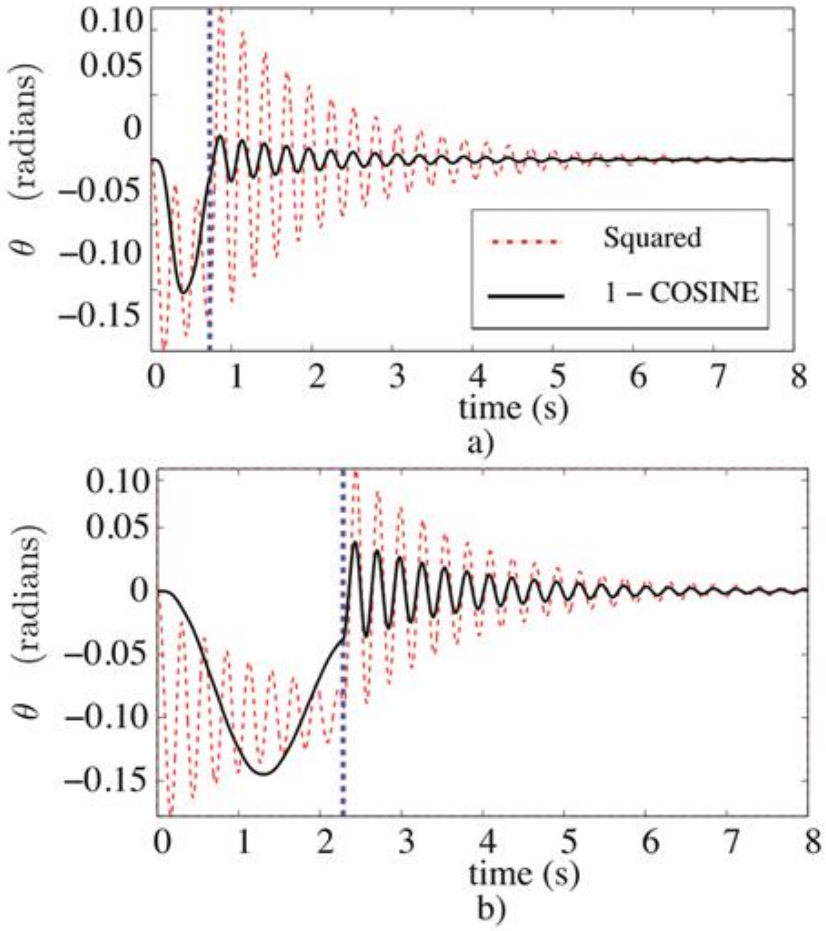

Figure 78 Pitch response to the 1-Cosine and the squared gust profiles, 9.14 m and 28.56 m. [24]

The dotted line indicates when the gust ends. The square gusts acts similar to a step input to the system. The response is transient both during and after the gust. Conversely, during the 1-COSINE gust the harvester's response is forced; seen by the wing's pitch having the same cosine profile but slightly lagging the excitation. Once the gust is removed the wing vibrates freely, the magnitude of this vibration is dependent on the value of the pitch right before the gust terminates.

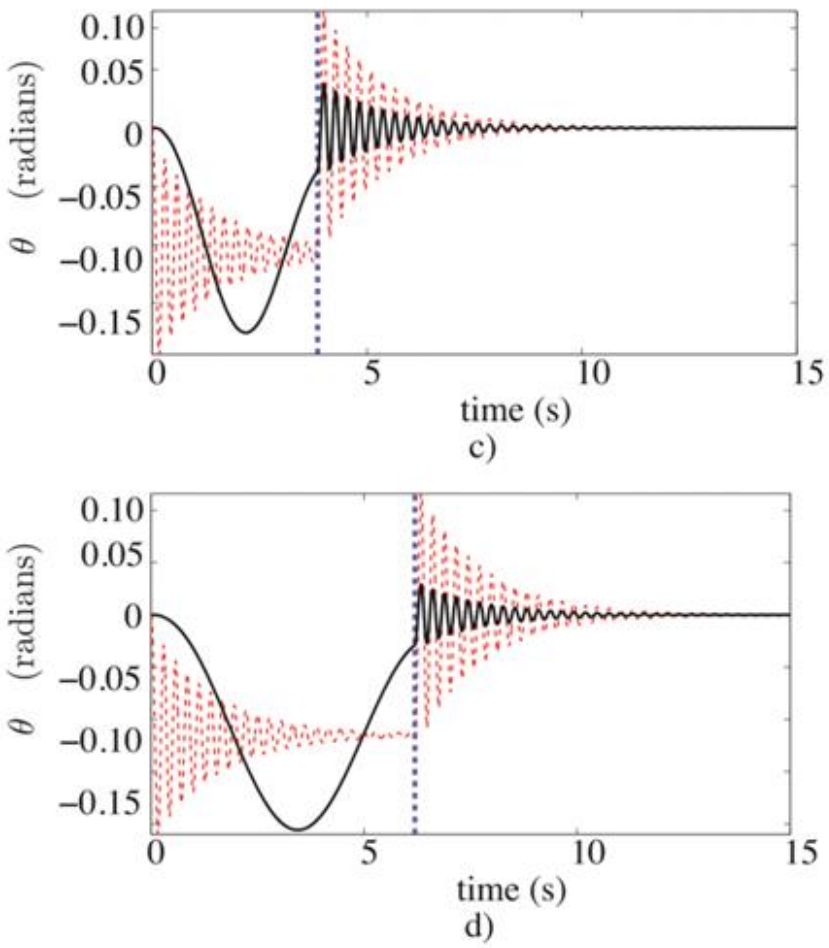

Figure 79 Pitch response to the 1-Cosine and the squared gust profiles, 48.16 m and 77.42 m. [24]

Similar trends are seen in the bending deformation of the wing, Figures 80 a), c), e), and g).

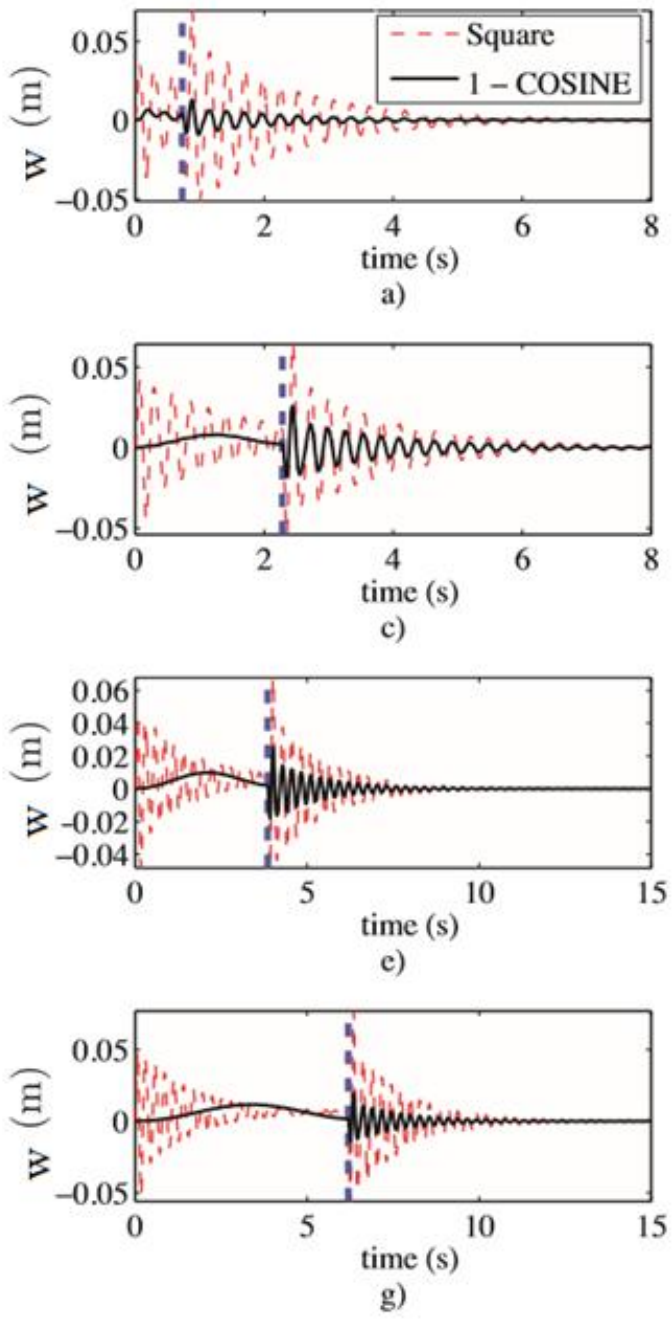

Figure 80 Instantaneous plunge response to different gust profiles. [24]

Figures 81 b), d), g), and h) present the instantaneous power extracted from gusts with gradients S, equal to 9.14 m, 28.56 m, 48.16 m, and 77.42 m.

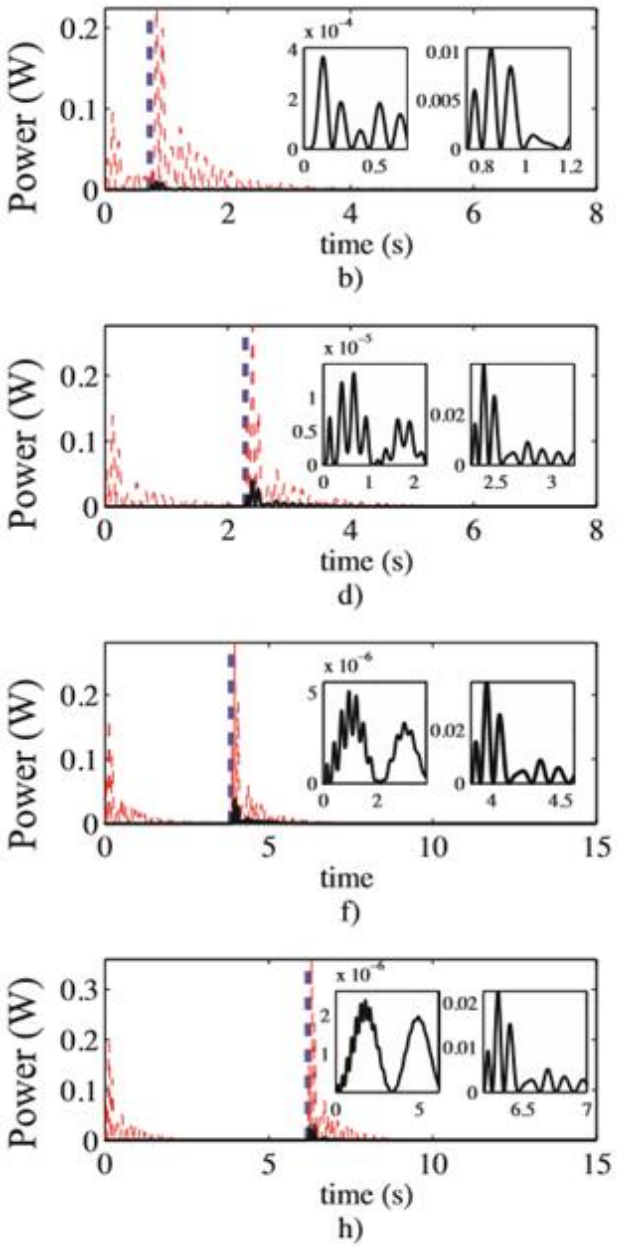

Figure 81 Instantaneous power response to different gust profiles. [24]

The power harvested from the 1-COSINE gust is less than that harvested from the square gust. Furthermore, the power generated when the 1-COSINE gust is active is less than the power produced when the gust is inactive. Conversely, the square gust generated power of similar magnitudes at the start and end of the gusts. The peak power extracted for both the 1-COSINE gust increases with an increase in gust gradient. This increase is present both when the gust is active and after it subsides. Note

that both gust profiles regardless of the value of the gradient produce more power after the gust terminates. Due to transient nature of the response it is worth noting the conditions that yield maximums and minimums in the power response over time. Defining the curvature of the beam as $k = \frac{\partial^2 w}{\partial Y^2}$, when the capacitance of the harvester is small then the voltage and power generated by the harvester is proportional to integral of the rate of curvature over the harvester's electrodes area, i.e., $V \propto \int_0^{l_p} \frac{\partial k}{\partial t} dY$, and $P \propto \left(\int_0^{l_p} \frac{\partial k}{\partial t} dY \right)^2$, as shown by [13] Under these conditions, zero instantaneous power occurs at points in time when the rate of curvature $\frac{\partial k}{\partial t} = \frac{\partial^3 w}{\partial Y^2 \partial t}$ is zero or equivalently when the rate of the bending deformation, $\frac{\partial w}{\partial t}$, equals zero. This behavior is clearly evident when examining the power harvested during the 1-COSINE gust, where at the maximum bending deformation in time the power harvested is zero. Similarly, maximum instantaneous power is harvested when $\frac{\partial^2 k}{\partial t^2}$ or equivalently $\frac{\partial^2 w}{\partial t^2}$ equals zero, i.e., at the inflection points of the bending deformation curve in time. In the case of the 1-COSINE gust there are at least two inflection points and one global maximum in the gust profile. During the gust the bending deformation mirror this 1-COSINE profile. This yields at least two peaks in power and one point of zero power. Figures 82 a) and b) clearly shows this influence of the bending response on the instantaneous power. Any distortion in the bending deformation from 1-COSINE profile due to transient harmonics causes local peaks and minimums in the instantaneous power, Figs. 80 b), d), g), and h). In the case of the gust of shorter gradients, i.e., S, equal to 9.14 m, 28.56 m, the transient harmonics reduce the peak power harvested.

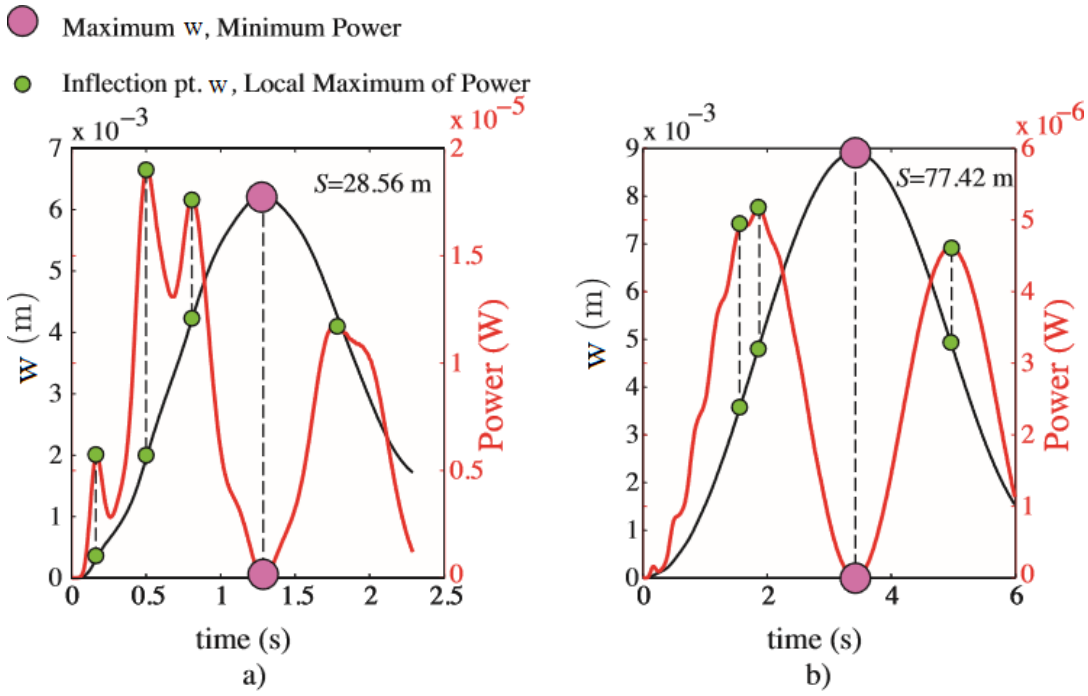

Figure 82 Influence of the bending response on the instantaneous power [24]

Figures 83 a) and b) shows peak instantaneous power harvested for the both the square and 1-COSINE profiles during and after the gust, respectively. More power is extracted from the squared gust. Additionally, for the squared profile during the gust, the power harvested increases with increasing gust gradient. Conversely, a wing disturbed by 1-COSINE profile the amount of power scavenged decreases with gust gradient when the gust is active. Examining the power harvested after the gust subsides the following holds. The peak instantaneous power from squared profile oscillates with gust gradient. However, the effects are lessened as the gradient increases. Overall for the squared profile, the average power harvested increases when the gust gradient increases. Consequently,atlargervaluesofgustgradientthebendingdeformationdecays to a set point before the gust terminates for larger values of gradient this lessens the oscillation in the power. In the power extracted from the 1-COSINE profile, the transient oscillations cause local peaks in the power extracted versus gust gradient for lower values of gradient, Fig. 83 b).

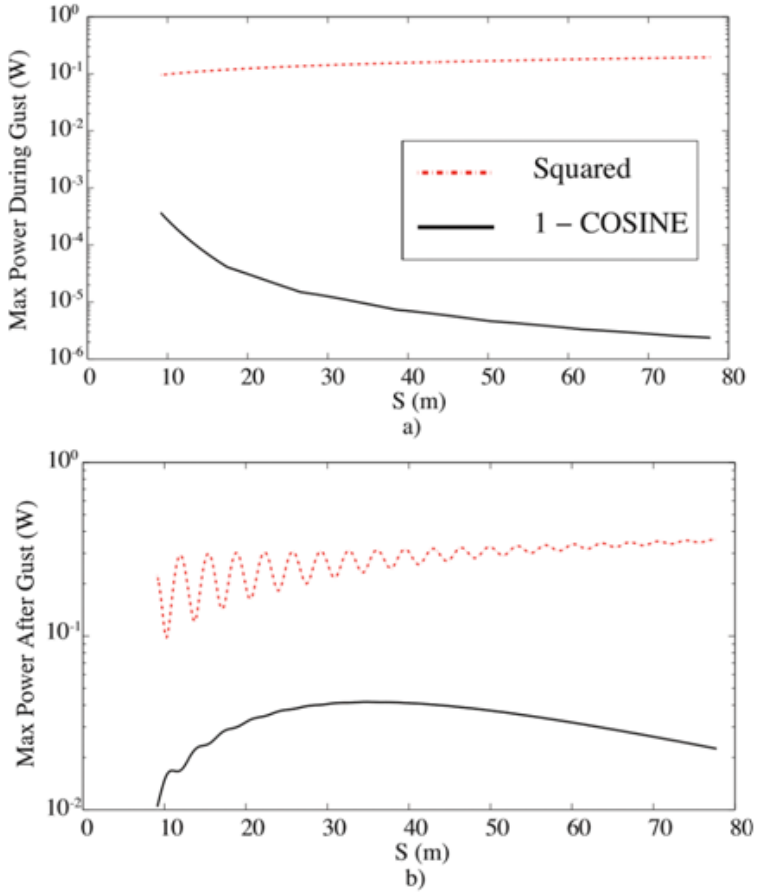

Figure 83 Peak of the instantaneous power collected during and after the gust action. [24]

However, as the gradient increases these oscillation are annihilated and the peak instantaneous power reaches a maximum at a gust gradient of approximately 35m. Similar trends can be seen in the energy harvested per cycle, Figs. 85 c) and d). Absent in this study is the role of the sharp edged gust. However, the oscillations caused by the squared gust decays before the gust terminates, then the squared gust effectively captures the response of the sharp gusts. This behaviors occurs for squared gust with large values of the gust gradient S. The results in the previous analysis was obtained using a resistance value of 105 Ohms. However, each gust profile the optimal peak power is a function of both the gust gradient and equivalent resistance.

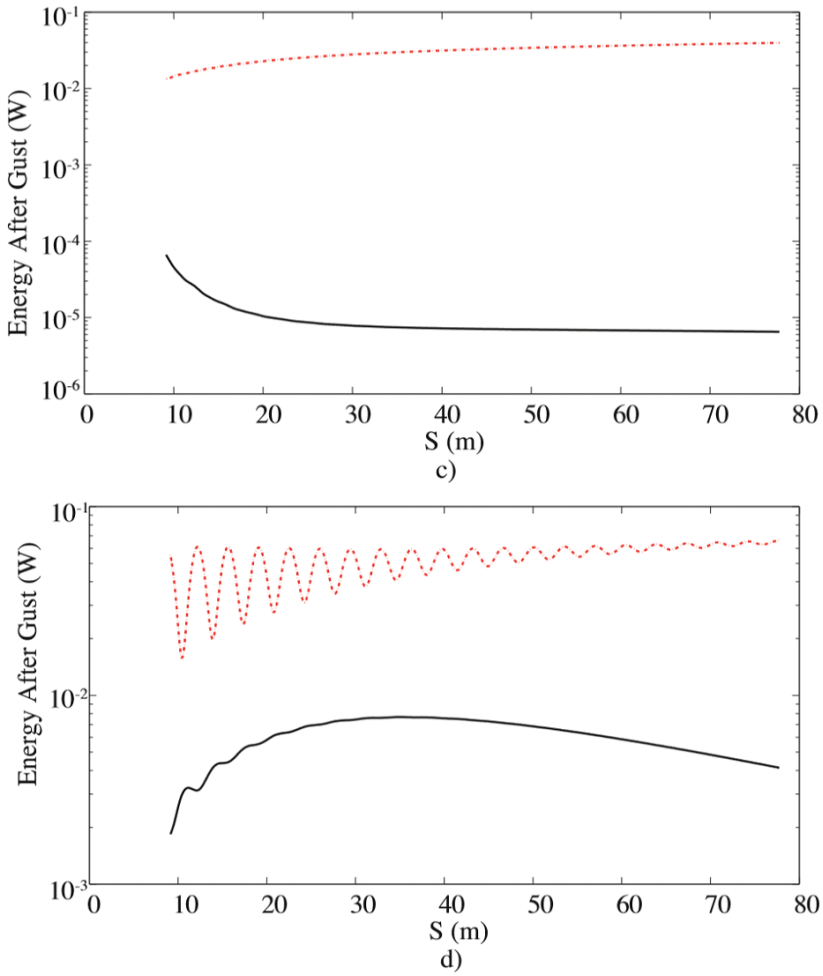

Figure 84 Energy harvested during and after the gust action. [24]

Figure 83 a) shows that the peak power the 1-COSINE is a unimodal. Furthermore, the squared gust profiles shows the aforementioned oscillation with gust gradient, Fig. 83 b). The power overall increases with gust gradient and there does exist a global optimum for the gradients and resistance considered. The preceding results are from a model with unsteady aerodynamic loads and gusts. The angle of attack on the entire wing does not change instantaneously this allows for lag in the development of lift on the wing. This behavior is captured by an unsteady representation of the aerodynamic loads and gusts and neglected by quasi-steady approximations. In comparing the differences in response from an unsteady approximation to quasi steady approximation the free stream velocity is reduced from 25 m/s to 18 m/s to avoid a divergent response.

Figures 85 illustrate the effects of this lag on the wing's bending deformation and pitch by comparing the responses at due quasi steady aerodynamic loading and gust loading caused by a 1-COSINE profile.

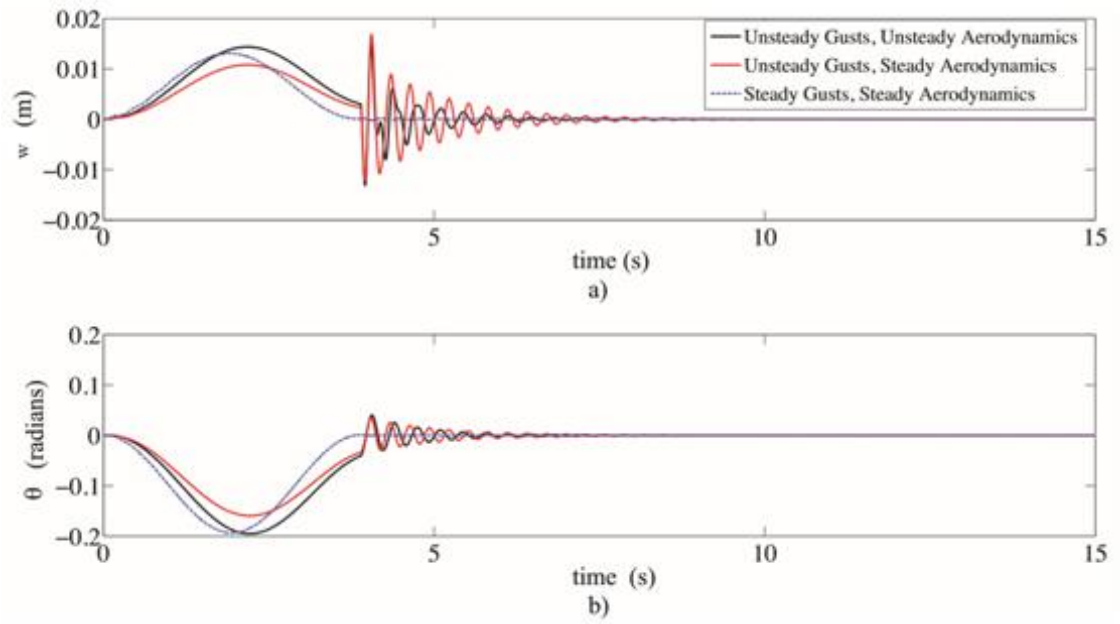

Figure 85 Wing plunge and pitch response for different aerodynamic models. [24]

Specifically, Fig. 86 a) compares pitch deformations and Fig. 86 b) shows the pitch displacement for a gust gradient of S equal to 35m, and three different aerodynamic models: 1) both the aerodynamic and the gust loads are assumed unsteady, 2) the aerodynamic lift and moment are quasi steady but the gust loads unsteady, and 3) both the aerodynamic and the gust loads are quasi steady. Heretofore, the loadings will be referred to as 1), 2), and 3) respectively. During the gust, both the pitch and bending response due to quasi steady loads and gusts, i.e. 3), leads the responses of loads 1) and 2). During the gust the peak amplitude of 3) is almost the same as the unsteady model of 1). However once the gust subsides, the full quasi steady model, 3), predicts minimal oscillations in both bending and pitch. While the oscillations of the unsteady models have the same order of magnitude. This behavior has several consequences on the power. When the gust is active the models with unsteady gusts, i.e., 1) and 2), predict larger values of

instantaneous power. After the gust the power harvested from the fully quasi-steady model, 3), is minuscule, Fig. 86.

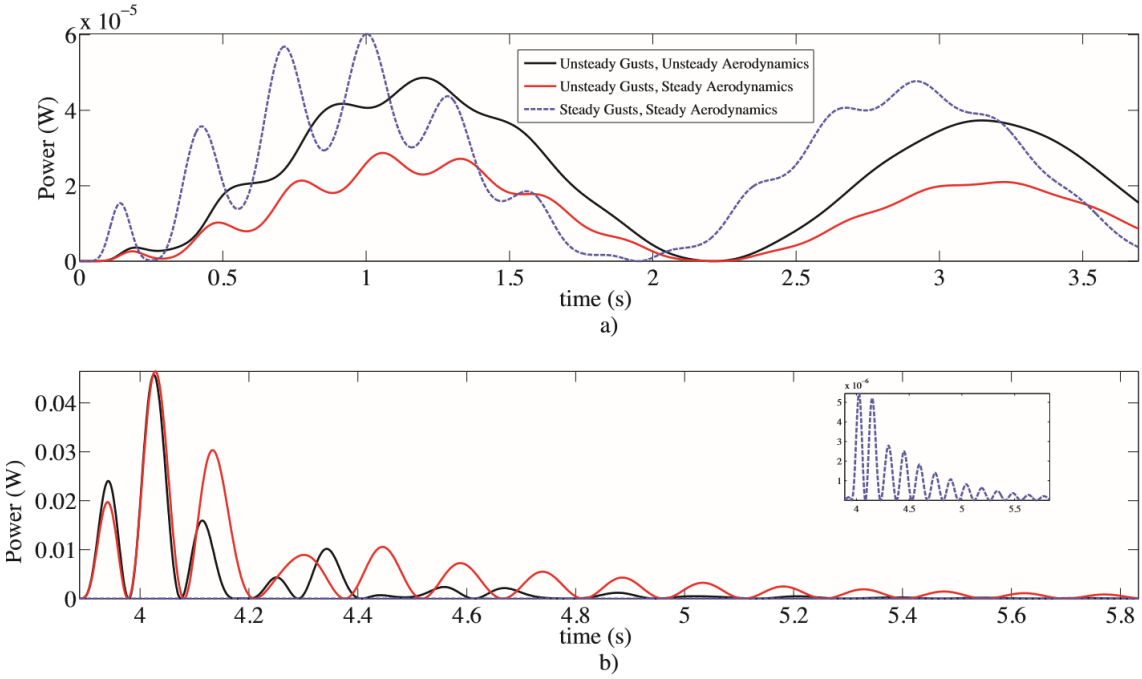

Figure 86 Instantaneous power extracted from different aerodynamic models. [24]

The amplitude of power harvested is dependent on the value of gust gradient. Consequently, when the gust is active the quasi steady model, 1), overestimates the power harvested when compare to a model with both unsteady gust and aerodynamic loads, 3), and the model with quasi steady aerodynamics but unsteady gust, 3), Fig. 87 a). Increasing the gust gradient causes the fully quasi-steady model to predict nearly the same peak values of instantaneous power but the waveforms differ, Fig. 87 b). However, during the gust, the loads in 2) predict instantaneous power amplitudes are consistently less than those of the fully unsteady model 3) regardless of the gradient. These results highlight the importance of using unsteady aerodynamics in designing this type of aeroelastic harvesters.

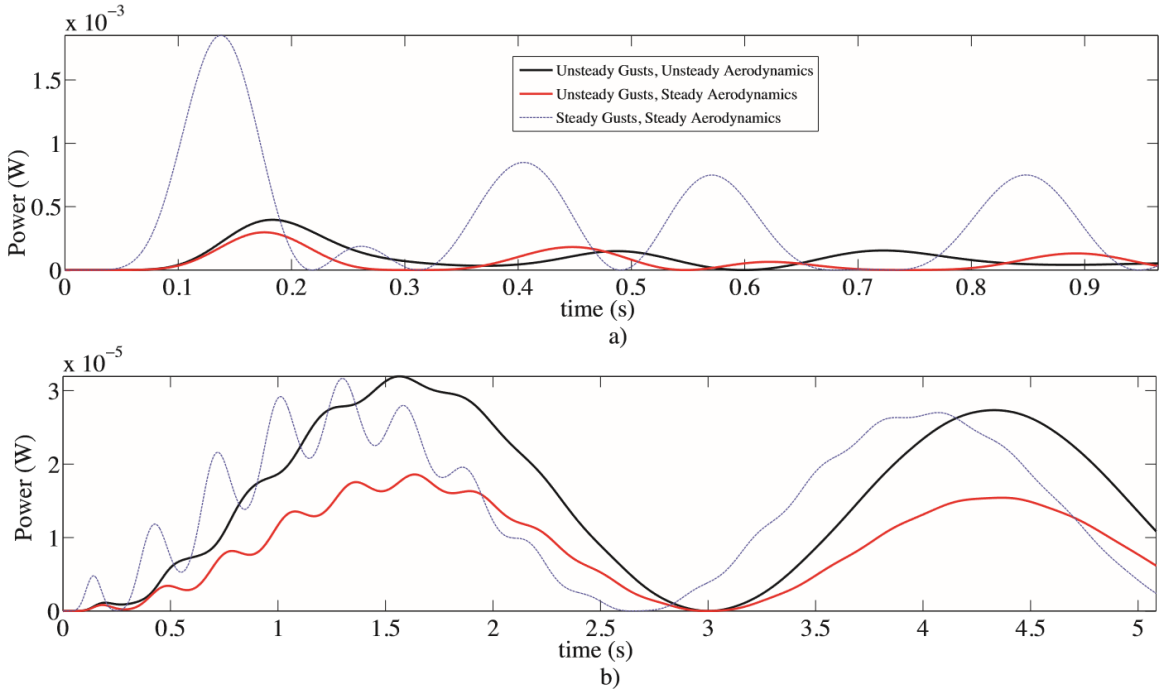

Figure 87 Detail of Figure 81. [24]

References

[1] Beeby, S. P.,Tudor, M. J., White, N. M., "Energy harvesting vibration sources for microsystems applications", Meas. Sci. Technol. 17, 2006, doi:10.1088/0957-0233/17/12/R01.

[2] IEEE Stantard on Piezoelectricity, American National Standard Institute, 1987.

[3] Erturk, A., Inman, D. J., "An experimentally validated bimorph cantilever model from piezoelectric energy harvesting from base excitations", Smart Materials and Structures, 2009, doi:10.1088/0964-1726/18/2/025009.

[4] Wang, L., Yuan, F. G., "Vibration energy harvesting by magnetostrictive materials", Smart Materials and Structures, 2008, doi:10.1088/0964-1726/17/4/045009.

[5] Boisseau, S., Despesse, G., Seddik, B. A., " Electrostatic conversion for vibration energy harvesting", Small-Scale Energy Harvesting, Intech, 2012 , : http://dx.doi.org/10.5772/51360.

[6] Yang, B., Lee, C., Xiang, W., Xie, J., He, J. H., Kotlanka, R. K., Low, S. P., Feng, H.," Electromagnetic energy harvesting from vibrations of multiple frequencies", Journal of Micromechanics and Microengineering, 2009, doi:10.1088/0960-1317/19/3/035001.

[7] Bowen, C. R., Kim, H. A., Weaver, P. M., Dunn, S., "Piezoelectric and ferroelectric materials and structures for energy harvesting applications", Royal Society of Chemistry, 2014, DOI: 10.1039/c3ee42454.

[8] Erturk, A., Inman, J., "An experimentally validated bimorph cantilever model for piezoelectric energy harvesting from base exitations", Smart Materials and Structures, 2009, doi:10.1088/0964-1726/18/2/025009.

[9] Jang, J., An introduction to the theory of piezoelectricity, Springer Science + Business Media, Inc, 2010

[10] Gibert, J. M.,"Demonstration of the effect of piezoelectric polarization vector on the performance of a vibration energy harvester." SPIE Smart Structures and Materials.Nondestructive Evaluation and Health Monitoring. International Society for Optics and Photonics, 2014.

[11] Sodano, H. A., Park, G., Inman, D. J.,"Estimation of Electric Charge Output for Piezoelectric Energy Harvesting" Blackwell Publishing Ltd, 2004

[12] Erturk, A., Vieria, V. G. R., De Marqui, C. Jr., Inman, D. J., "On the energy harvesting potential of piezoaeroelastic systems", 2010 American Institute of Physics. doi:10.1063/1.3427405.

[13] Erturk, A., Inman, D. J., *Piezoelectric energy harvesting*, Published 2011 by John Wiley & Sons, Ltd. ISBN: 978-0-470-68254-8.

[14] Bruni, C., Cestino, E., Frulla, G., "Parametric analysis of a fluttering piezoelectric wing", Aircraft Engineering and Aerospace Technology, 2016,Vol. 88, Iss. 3, DOI: 10.1108/AEAT-02-2014-0024.R2

[15] Bruni, C., Frulla, G., Cestino, E., Gibert, J., Marzocca, P., " A Multi-Objective Nonlinear Piezoaeroelastic Wing Solution for Energy Harvesting and Load Alleviation: Modeling and Simulation ", 56th AIAA/ASCE/AHS/ASC Structures, Structural Dynamics, and Materials Conference, 5-9 January 2015, Kissimmee, Florida.

[16] Niederberg, D., Smart Damping Materials using Shunt Control, Dissertation thesis submitted to the Swiss Federal Institute of Technology (ETH), Zurich, 2005.

[17] Ha, S. K., Keilers, C., & Chang, F. K. (1992). Finite element analysis of composite structures containing distributed piezoceramic sensors and actuators. *AIAA journal*, *30*(3), 772-780.

[18] Hagood, N. W., & von Flotow, A. (1991). Damping of structural vibrations with piezoelectric materials and passive electrical networks. *Journal of Sound and Vibration*, *146*(2), 243-268.

[19] Hollkamp, J. J., & Starchville, T. F. (1994). A self-tuning piezoelectric vibration absorber. *Journal of Intelligent Material Systems and Structures*, *5*(4), 559-566.

[20] Wu, S. Y. (2001, July). Broadband piezoelectric shunts for passive structural vibration control. In *SPIE's 8th Annual International Symposium on Smart Structures and Materials* (pp. 251-261). International Society for Optics and Photonics.

[21] Davis, C. L., Lesieutre, G. A., & Dosch, J. J. (1997, May). Tunable electrically shunted piezoceramic vibration absorber. In *Smart Structures and Materials' 97*(pp. 51-59). International Society for Optics and Photonics.

[22] Guyomar, D., Jayet, Y., Petit, L., Lefeuvre, E., Monnier, T., Richard, C., & Lallart, M. (2007). Synchronized switch harvesting applied to selfpowered smart systems: Piezoactive microgenerators for autonomous wireless transmitters.*Sensors and Actuators A: Physical*, *138*(1), 151-160.

[23] Lallart, M., & Guyomar, D. (2008). An optimized self-powered switching circuit for non-linear energy harvesting with low voltage output. *Smart Materials and Structures*, *17*(3), 035030.

[24] Bruni, C., Gibert, J. Frulla. G., Cestino, E., Marzocca, P., "Energy Harvesting from Aeroelastic Vibrations induced by Discrete Gust Loads", Journal of Intelligent Materials Systems and Structures, 2016.

[25] F. Hoblit (1988). Gust Loads on Aircraft: Concepts and Applications. American Institute of Aeronautics & Astronautics. D. L. Jinwu Xiang, Yining Wu (2015). ‘Energy harvesting from the discrete gust response of a piezoaeroelastic wing: Modeling and performance evaluation’. Journal of Sounds and Vibration 343:176–193.

[26] P.Marzocca, et al.(2001). ‘Aeroelastic response of 2-D lifting surfaces to gust and arbitrary explosive loading signatures’. International Journal of Impact Engineering 25(1):41–65.

[27] Z. Qin (2001). Vibration and Aeroelasticity of Advanced Aircraft Wings Modeled as Thin-Walled Beams âŁ“Dynamics, Stability and Control. Ph.D. thesis, Virginia Polytechnic Institute and State University.

6 Design of a piezoelectric wing for energy harvesting based on a wing test configuration.

Chapter 6 contains all the assumptions, the parametric analysis and the simulations carried out to design a wing with embedded piezoelectric actuators based on the results of a forced vibration test and wind tunnel (WT) test campaign. The experimental tests were performed at Clarkson University (USA) in the framework of the EU funded Marie-Curie A2-NET TEAM program. The project involved several universities, BUTE (Hungary), AAS (Armenia), POLITO (Italy), CU (USA) and UL (Slovenia), and was based on the development of advanced aircraft network for theoretical and experimental aero-servoelastic models. Part of the activity presented in the following and in some of the previous chapters, such as the experimental test, was accomplished in the contest of the just mentioned research program during a six month secondment at Clarkson University. A brief overview of the test facilities, of the procedures and of the testing devices is included in Section 6.1, while Sections 6.2 through 6.6 propose a new wing design based on results of the experimental tests. It is worth noticing here that the final objective is not to reproduce exactly the experimental test conditions since some differences exist between the experimental and the numerical wing model, which cannot be physically removed nor numerically represented, but to use the results as the base for a validation of the amount of extractable energy, for a parametric study and for the future development of an optimized energy harvester.

6.1 Design of the experimental wing

The design of the wing with embedded piezoelectric actuators tested at Clarkson University was mainly influenced by two aspects: 1) the maximum speed recordable in the wind tunnel test section and 2) the choice of an efficient set of piezoelectric patches, which could guarantee an high value of the output voltage across the electrodes. The first aspect is strongly dependent of the geometry and the manufacturing materials of the wing while the second it is not straightforwardly achievable. In particular this last aspect will be shown by performing a parametric study of the wing configurations revealing that the amount of extractable power via the piezo-patches is strictly related to the wing dynamical response of the structure, which unless the system is forced to work at a predefined condition, it is quite difficult to predict. The constrain of the limited flutter speed was achieved by a special wing design, also reported by Bisplinghoff [1], which consist in a two spars torque-tubes structure, Figure 88 (a). The two spars are responsible for the bending stiffness of the structure while the torque tubes, here represented by 34 slices shaped as the NACA 0012 airfoil, are primarily responsible for the torsional stiffness, Figure 88 (b).

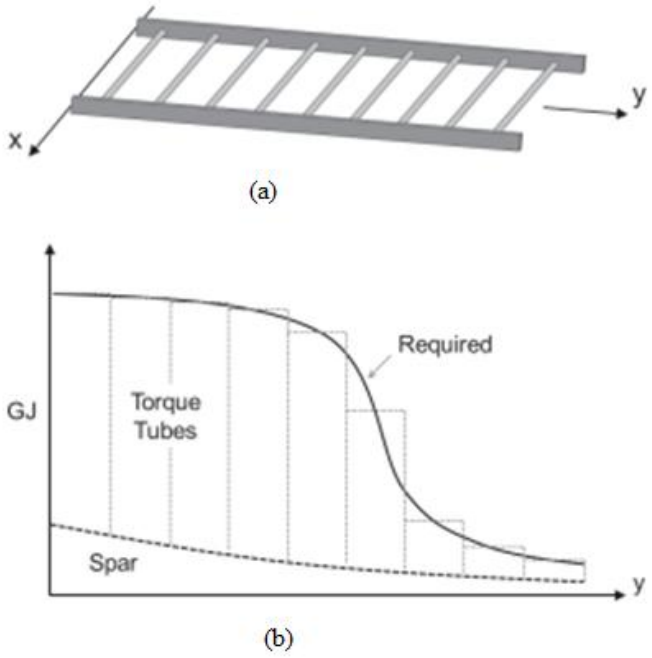

Figure 88 Two spars torque-tubes structure from [1].

Albeit the major contribution to the torsional stiffness comes from the torque tubes, there will be also a moderate participation of the spars, as shown in Figure 88 (b). Thanks to the just mentioned design solution and by knowing the structural constraints coming from the characteristics of the piezo-patches, in terms of geometry and performances, it is possible to identify the most suitable piezo-wing configuration that matches the wind tunnel requirements. The final geometry of the wing is reported in Figure 89. The use of 34 slices of 10 mm thick each instead of a unique body is crucial to reduce the global torsional stiffness of the wing and therefore guarantee the desired dynamic characteristics. Furthermore, being the slices airfoil shaped, they provides together structural and aerodynamic capacities. Figure 90 shows the internal geometry of the slices.

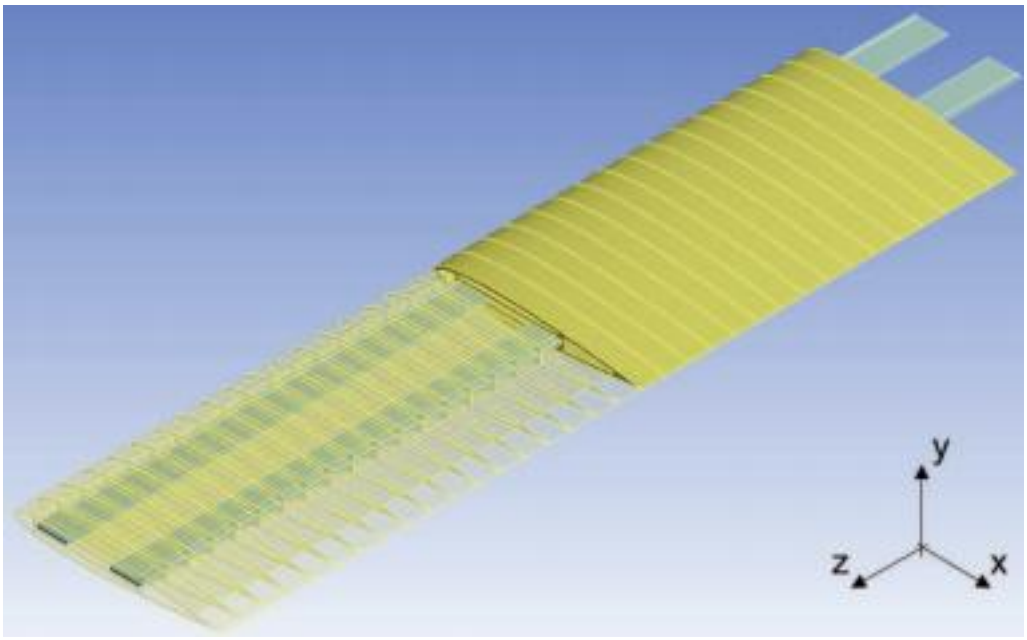

Figure 89 Test wing layout [2]

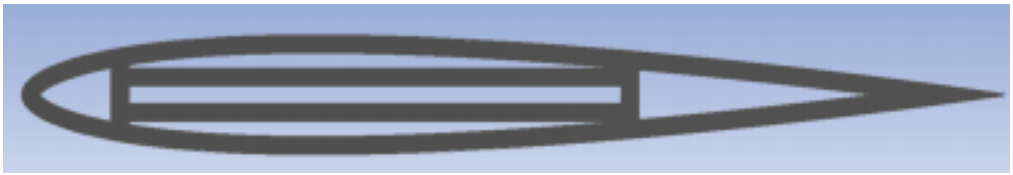

Figure 90 Wing slice cross section [2].

The rectangular hole, located at the airfoil symmetry axis, as shown in Figure 90, was introduced for each slice to host the two spars. Over the upper spars' surfaces, in the longitudinal directions, are bonded two Micro Fiber Composites (MFC) piezo-patches from Smart Material Corporation, Figure 91.

Figure 91 Piezo-patches bonded over the wing spars [2].

The MFC were chosen for their high flexibility and high length of the patches. MFC technology, invented by NASA in 1996, consists of rectangular piezoelectric rods sandwiched between layers of adhesive, electrodes and polyimide film. Piezo ceramic rods are made of PZT (Lead Zirconate Titanate), and immersed is an epoxy resin. The patches are half of the wing semi-span and their geometry, structural and electrical characteristics, such as those of the wing, are reported in Table 8. The PZTs are placed in the concave region of the spars, created and shaped specifically to host the PZTs, Figure 92.

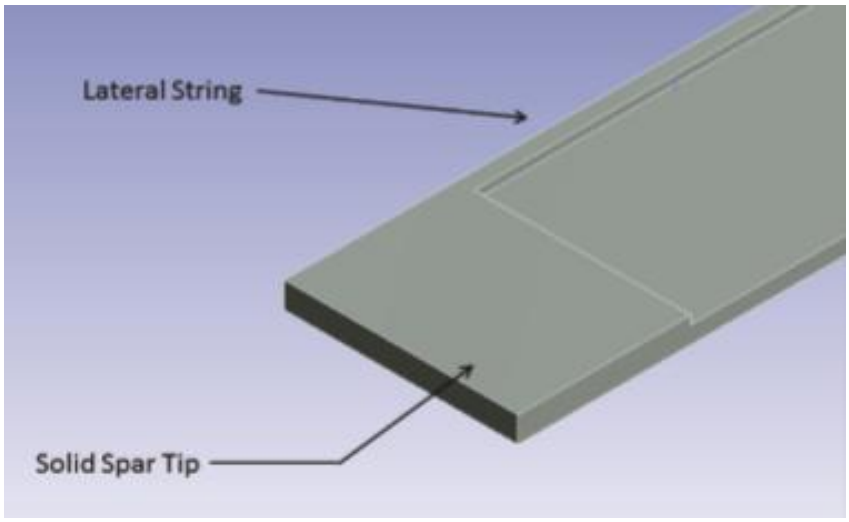

Figure 92 Detail of spar tip [2].

A thicker lateral string, as shows Figure 92, is preserved all over the spars with the function of avoiding the contact between the piezoelectric elements end the slices. The solid cross section at the tip of the spars, together with the last slice which is bonded on it, work as a locker for all the remaining slices which run freely through the spars, Figures 94 and 95. The spars are made of a standard aluminum alloy, to guarantee a good flexibility, a low transverse thickness and a good surface for the bonding of the piezoelectric elements. The slices are instead made of Poly-Lactic Acid (PLA) plastic, manufactured via a 3-D printer. Since the wing had to endure the forced vibration shaker test and the wind tunnel test campaign, it had to be conceived in such a way that both tests were feasible by a unique piece.

The shaker applies the load on the wing through a stringer, which consists of a thin flexible rod. To apply the load symmetrically it was necessary to introduce a small solid plane section at the root of the wing where the stringer could act symmetrically with respect to the wing chord. Therefore, the two spars were elongated and jointed at the root in order to accomplish the shaker loading requirements, Figure 93.

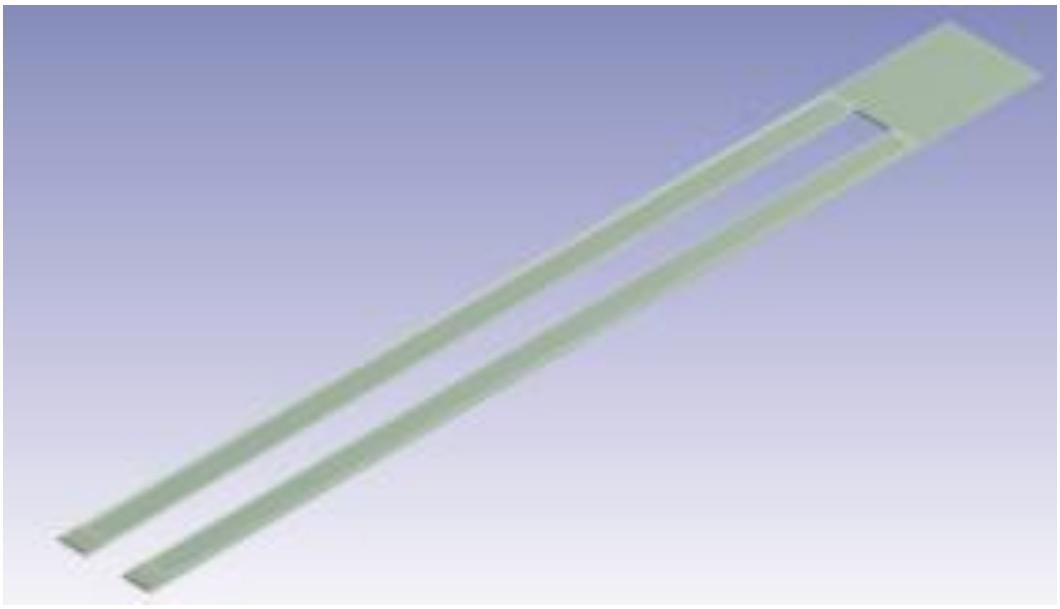

Figure 93 Spars design.

This spars solution is also very practical for the wind tunnel test, since it become easier to vertically anchor the wing to the wooden support. The fact of having jointed spars guaranteed a good grip between the spars and the wooden support to not move during the test.

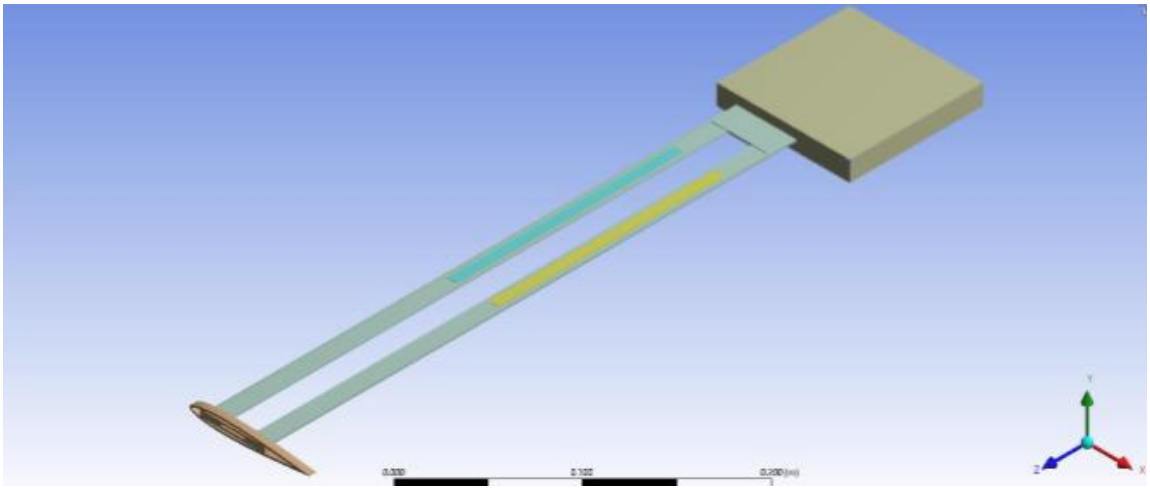

Figure 94 Shaker configuration.

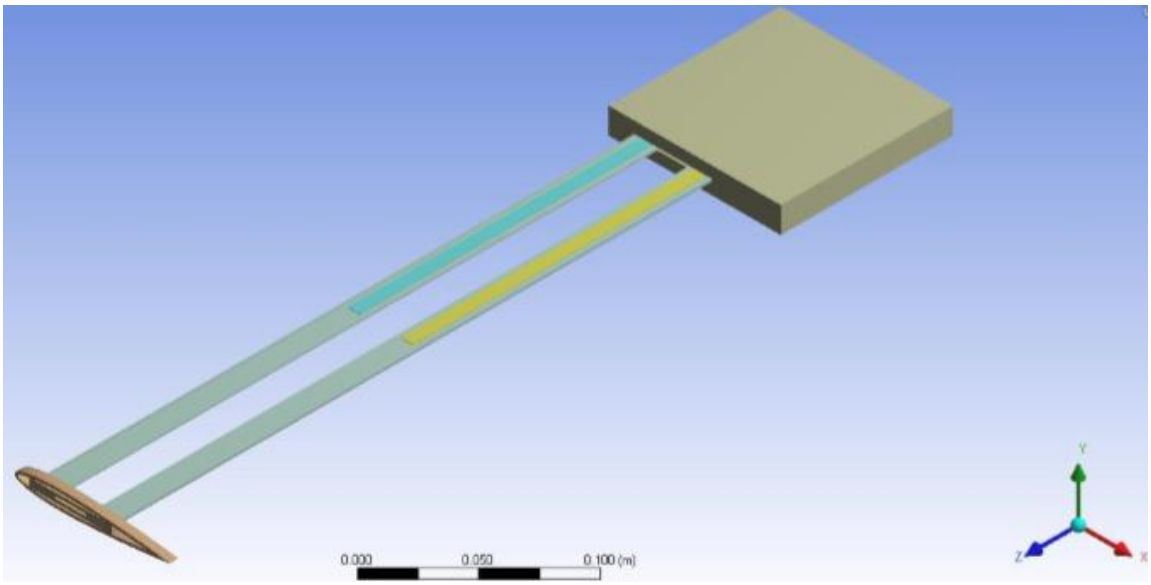

Figure 95 WT configuration.

Therefore two different wing configurations, shaker, Figure 94, and wing tunnel (WT), Figure 95, are tested. Due to the two different clamping strategy of the spars, between shaker and WT tests, there will be two sets of wing equivalent parameters, Table 8, which has to be considered in the numerical modeling of the wing. These parameters are obtained from the finite element model presented in the next Section, as close as possible the geometrical and mechanical characteristic of the experimental wing.

6.2 Finite element model of the piezoelectric wing

A finite element model was built prior to the experimental one, by the means of Patran/Nastran ®, to predict the dynamical behavior of the wing and so to extract the equivalent parameters used in the numerical model based on equations 5.14, 5.15 and 5.16. The geometry and the materials used for the finite element model of the wing are chosen coherently to those selected for the experimental wing, however some differences, such as machining errors, the high variability of the PLA mechanical characteristics, friction between the slices, imperfections in the piezo bonding and so on, cannot be avoided. The global FEM layout is reported in Figure 96 and it includes all the elements which identify the experimental wing: 1) the spars, 2) the slices and 3) the MFCs, which are hidden by the slices in Figure 96 but are well recognizable in Figure 97.

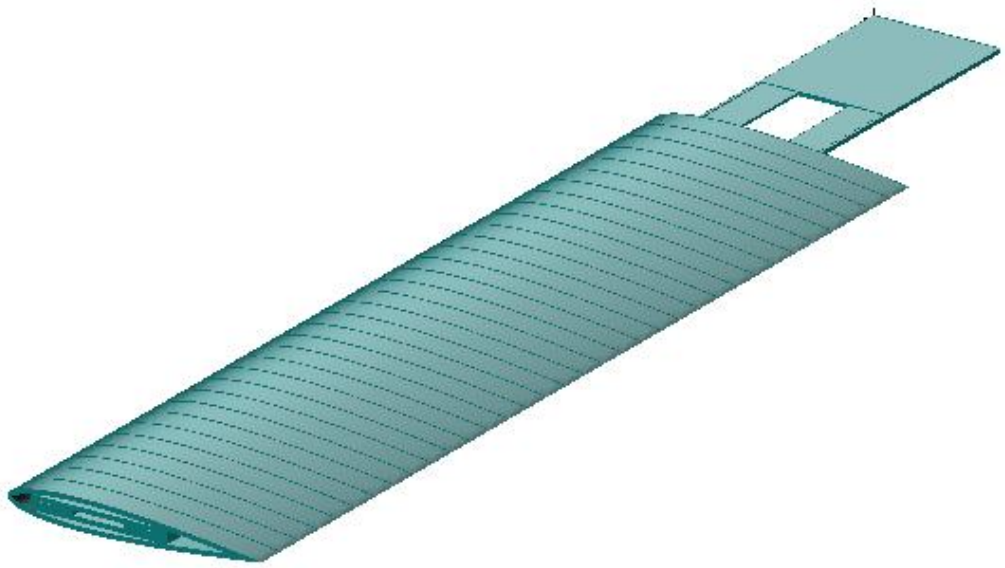

Figure 96 Full wing represenatation.

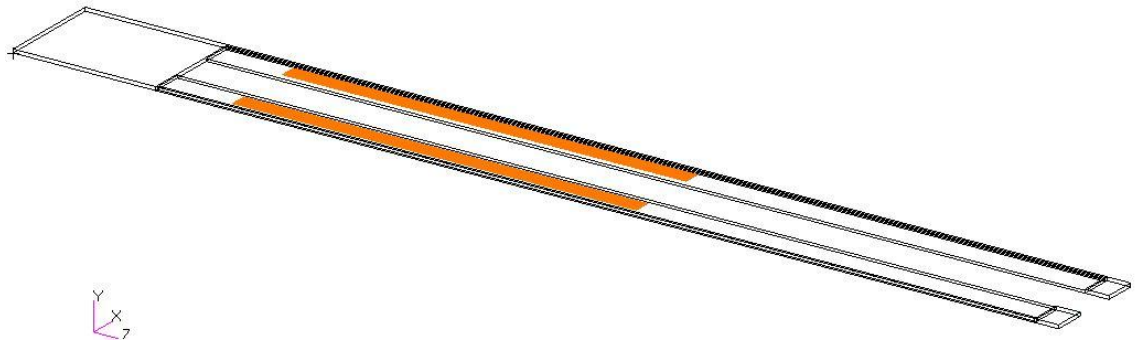

Figure 97 Spars and MFCs.

For each component was used a different type of mesh, according to the geometry and the function of the components. For the spars it was used the solid element HEXA 8, for the MFCs components the QUAD 4 elements, while for the slices the TETRA 10. Figure 98 reports some details of the spars and of the tip slice.

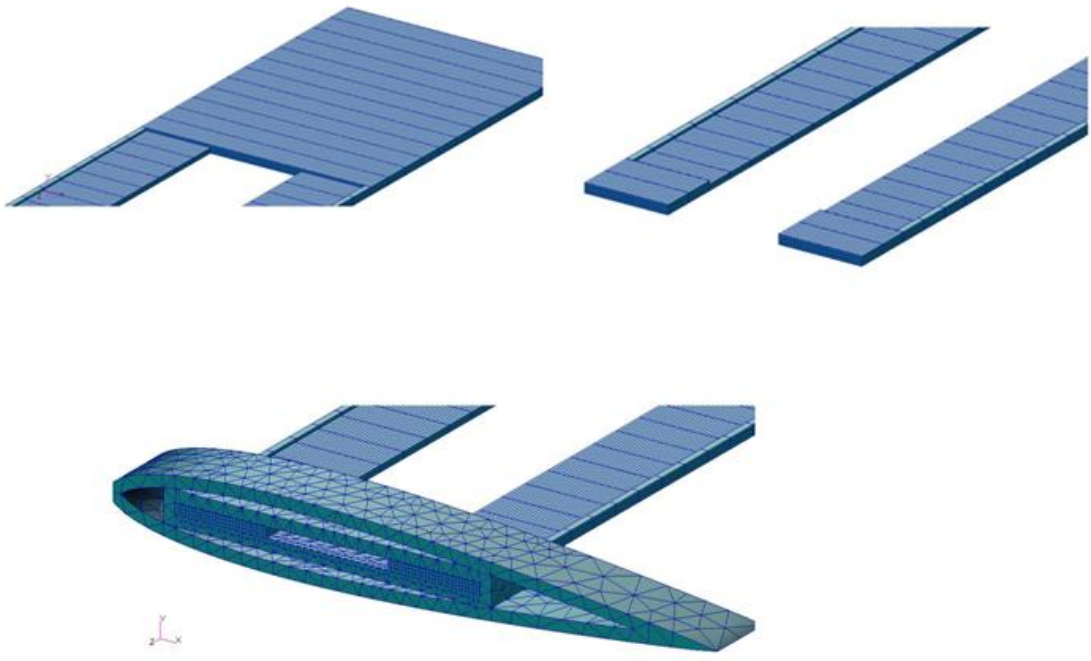

Figure 98 Details of the different mesh over the main components.

Once defined the solid model of the piezoelectric wing a linear modal analysis was launched in order to determine its natural frequencies. Figure

99 shows the modal response of the wing for the first three natural frequencies: the first out of plane bending, the second out of plane bending and finally the torsion.

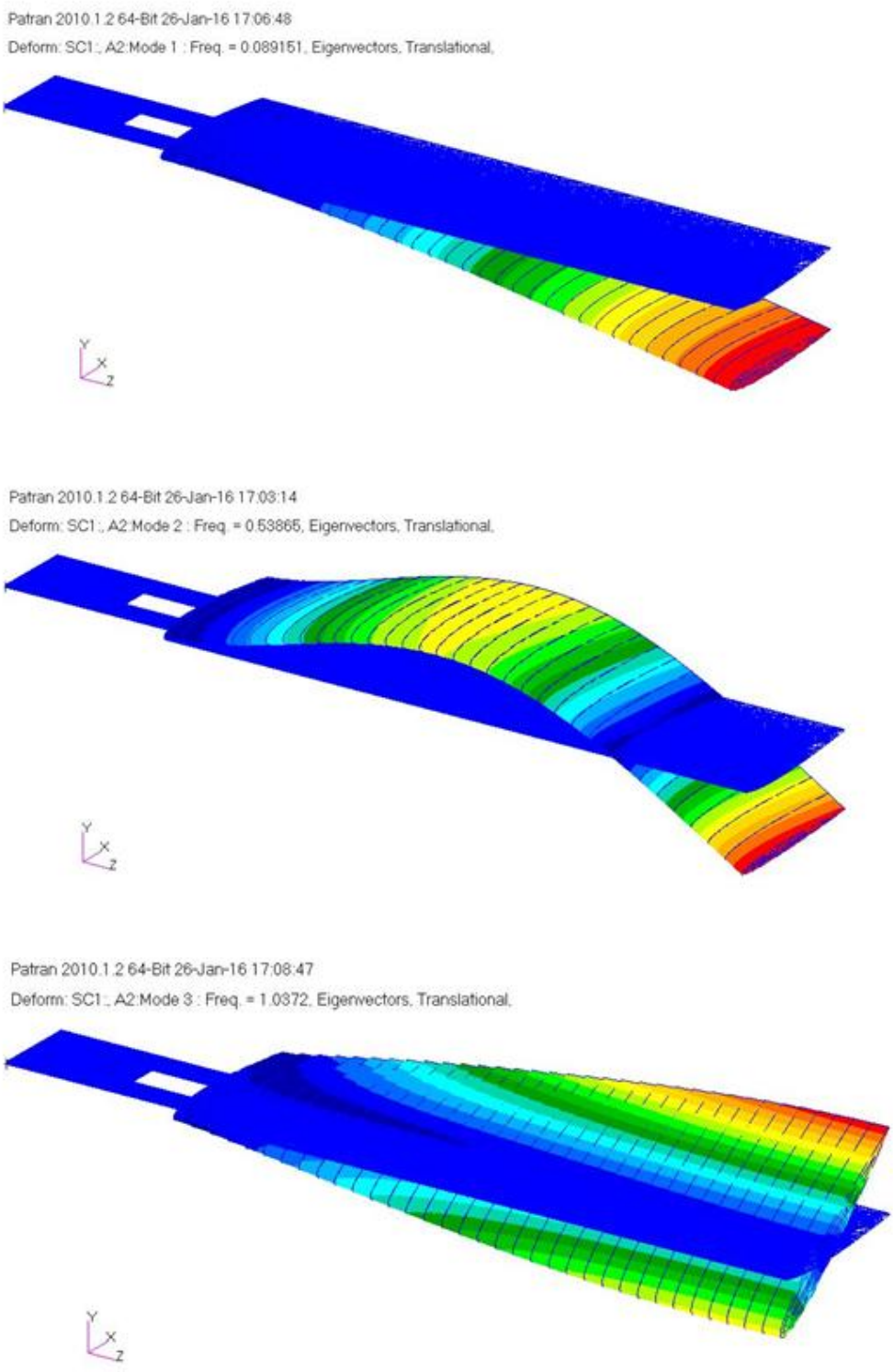

Figure 99 Patran/Nastran modal solution for the first three natural frequencies of the wing model.

All the parameters useful to the definition of an equivalent numerical wing model are obtained for the wing finite element model and summarized in Table 8.

Table 8 Wing data and piezoelectric constants .

Piezoelectric Wing		
Length - shaker configuration	L_s	$0.40\ m$
Length - WT configuration	L	$0.35\ m$
Chord	c	$0.09\ m$
Wing total mass - shaker configuration	m_s	$217.9 * 10^{-3}\ Kg$
Wing total mass - WT configuration	m	$212 * 10^{-3}\ Kg$
Polar moment of inertia - shaker configuration	I_s	$1.044 * 10^{-4}\ Kg * m^2$
Polar moment of inertia - WT configuration	I	$1.032 * 10^{-4}\ Kg * m^2$
Position of the gravity center in X direction - shaker configuration	X_{cg_S}	$5.13 * 10^{-3}\ m$
Position of the gravity center in Y direction - shaker configuration	Y_{cg_S}	$-0.024 * 10^{-3}\ m$
Position of the gravity center in Z direction - shaker configuration	Z_{cg_S}	$172.2 * 10^{-3}\ m$
Position of the gravity center in X direction - WT configuration	X_{cg}	$5.27 * 10^{-3}\ m$
Position of the gravity center in Y direction - WT configuration	Y_{cg}	$-0.022 * 10^{-3}\ m$
Position of the gravity center in Z direction - WT configuration	Z_{cg}	$177.9 * 10^{-3}\ m$
Elastic modulus aluminum	E_A	$71\ GPa$
Poisson ratio aluminum	ν_A	0.33
Elastic modulus PLA	E_{PLA}	$1.4\ GPa$
Poisson ratio PLA	ν_{PLA}	0.35
Piezoelectric constant [3]	d_{31}	$-2.1 * 10^2\ pC/N$
Elastic modulus of the MFC [3]	E_p	$30.336\ GPa$
Capacitance [3]	$\mathrm{C_p}$	$91\ nF$
MFC active length [3]	$\mathrm{l_p}$	$0.17\ m$

MFC active width [3]	s_p	$0.007\ m$
MFC thickness [3]	t_p	$0.0003\ m$
MFC total mass	m_p	$0.00388\ Kg$

The characteristics of the piezoelectric elements are extracted from the MFC catalog [3]. The data obtained from the finite element model provide a good agreement between the FEM, the analytical/numerical and experimental wings, as shown by the frequency comparison in Paragraph 6.4, however some differences still exist and the possible root causes will be discussed more in details in the next paragraphs.

6.3 Equivalent Numerical Wing Model

In order to investigate the aeroelastic response of the wing, and so to verify if the selected experimental design solution is able to accomplish to the initial requirement of having a flutter speed well behind the maximum wind tunnel speed, a numerical piezoelectric wing model, in line with the analytical solution of the previous chapters and based on the equivalent parameters extracted from the FEM, is here presented. The choice of a two spars experimental wing was independently made from the definition of the analytical/numerical model therefore some design choices about the experimental wing are not exactly captured by the numerical design. One of this is the solid tip surface, shown in Figure 92, or the lateral string, from the same figure. A simplified geometrical model was considered, therefore it was assumed an equivalent wing cross section, constant in the longitudinal direction, whose stiffness per unitary length is obtained from the modal frequencies of the FEM model. The position and the geometry of the PTZs, instead, are kept in the numerical model exactly the same as in the experimental configuration, since the piezoelectric coupling and therefore the voltage output are related to the position of the piezo-patches with respect to the bonding surface. Figure 100 shows the detail of the PZTs location with respect to the wing inertial reference frame.

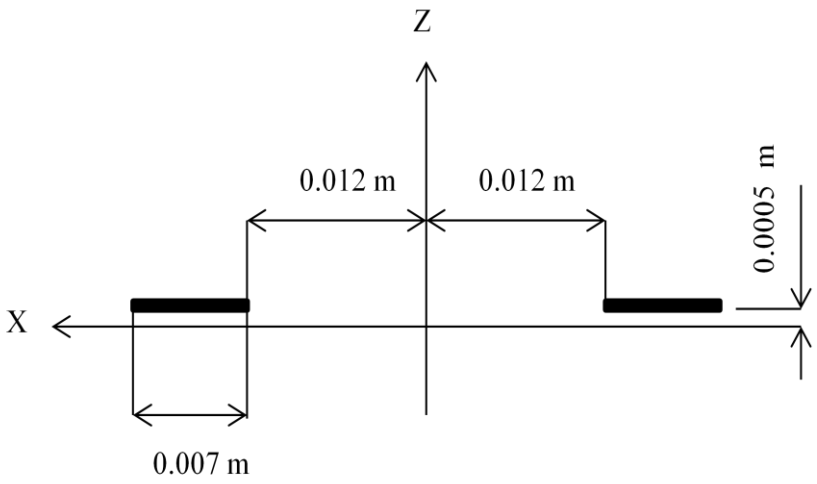

Figure 100 Frontal view of the PZTs bonded on the spars.

The equations of motion used to study the response of the current piezoelectric wing are Eqs. 5.13, 5.14, 5.15 and 5.16. The two piezoelectric elements are separately connected, in the experimental wing, to two equivalent resistive loads. It corresponds to a parallel connection of the piezos, as studied in Chapter 5, where the resistive load to which both piezo-patches are connected is equal to $R_{eq} = 2 \cdot R$, as in Figure 101.

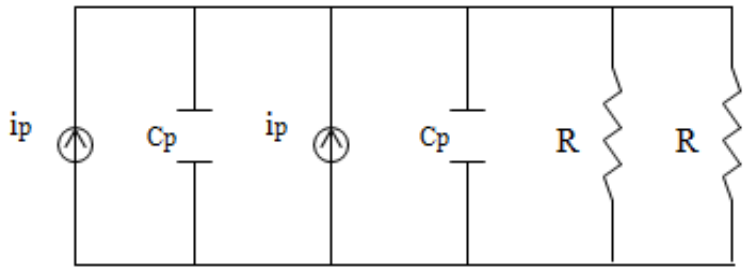

Figure 101 Equivalent electric circuit

The electromechanical coupling parameters, Eq. 5.10, even if the piezos are placed differently with respect to the hosting structure, preserve the same mathematical form. The only difference is in Eq. 5.17, where the resistive load has to be assumed twice:

$$\dot{Q} = -\frac{V}{2 \cdot R} \qquad 6.1$$

The description of the numerical model clarifies the fact that the experimental and the numerical wings are not perfectly equivalent but there are parameters which can be tuned in order to make the behavior of the two wings similar under certain conditions. The next Section shows the equivalence between the models through the frequencies comparison.

6.4 Frequencies comparison and parametric study.

As explained in Section 6.3 the cross sectional characteristics of the equivalent numerical wing, without MFCs, are derived from the FEM of the wing, for its WT configuration, by assuming the global values, such as the mass, the polar inertia or the stiffness, constant throughout the wing. The characteristics of PTZs, instead, are obtained from data available in the MFC catalog [3]. The cross sectional parameters of the equivalent numerical wing model are assumed the same in both WT and shaker configurations, for the sake of simplicity, but this is not the case for the finite element model or for the experimental wing where the parameters are different because of the change of geometry across the wing longitudinal direction. The data set which pertains to the equivalent numerical wing model are reported in Table 9. Herein the parameters which refer to the wing do not take into account of the PTZs contribution, while the PTZs data are reported in the last rows of Table 9.

Table 9 Wing and PZT data used for the following numerical simulations.

WING		
Wing length - shaker configuration	l_s	$0.40\ m$
Wing length - WT configuration	l	$0.35\ m$
Wing Chord	c	$0.09\ m$
Wing mass - no MFC	m_w	$208 * 10^{-3}\ Kg$
Wing polar moment of inertia - WT configuration	I	$1.032 * 10^{-4}\ Kg * m^2$
Position of the center of gravity in X direction - WT configuration	X_{cg}	$5.27 * 10^{-3}\ m$

Position of the center of gravity in Y direction - WT configuration	Y_{cg}	$-0.022 * 10^{-3}\ m$
Position of the center of gravity in Z direction - WT configuration	Z_{cg}	$177.9 * 10^{-3}\ m$
Wing torsional stiffness	D_{22}	$0.45\ N\ m^2$
Wing out of plane bending stiffness	D_{11}	$0.235\ N\ m^2$
Wing in plane bending stiffness	D_{33}	$235\ N\ m^2$
Elastic axis position, normalized by the wing half chord, w.r.t. the mid-chord.	a	-0.28
PZT		
MFC length [3]	l_p	$0.170\ m$
MFC active width [3]	s_p	$0.007\ m$
MFC thickness [3]	t_p	$0.0003\ m$
MFC density [3]	ρ_p	$5440\ Kg/m^3$
Piezoelectric constant [3]	d_{31}	$-2.1 * 10^2\ pC/N$
Elastic modulus of the MFC [3]	E_p	$30.336\ GPa$
Capacitance [3]	C_p	$91\ nF$

Tables 10 and 11 show the frequencies associated to the first three modes of the piezoelectric wing according the three distinct analysis: FEM, experimental and numerical. Table 10 refers to the shaker wing layout, which means a 5mm longer wing with respect to the WT layout, Table 11, for the numerical model, while a 5 mm longer and with a variation of the cross section at the clamped end for the FEM and the experimental wing, as shown in Figure 94.

Table 10 Natural frequencies for different wing models in their shaker test configuration.

Shaker configuration			
	First bending	**Second bending**	**First torsion**
FEM	2.2596 Hz	13.801 Hz	27.566 Hz
Experimental	2.563 Hz	14.72 Hz	21.44 Hz
Numerical	2.518 Hz	15.11 Hz	26.7 Hz

Table 11 Natural frequencies for different wing models in their WT test configuration.

WT configuration			
	First bending	**Second bending**	**First torsion**
FEM	2.815 Hz	17.019 Hz	32.867 Hz
Experimental	3.063 Hz	18.13 Hz	29.25 Hz
Numerical	3.128 Hz	18.77 Hz	28.61 Hz

By comparing the frequencies of Tables 10 and 11, the three models, FEM, experimental and numerical, appear quite comparable, however the critical flutter solution obtained through the equivalent numerical model is very different from what experienced experimentally. Table 12 shows these differences.

Table 12 Flutter speed and flutter frequency according to the experimental and numerical results.

WT configuration		
	Flutter speed	**Flutter frequency**
Experimental	~27,5 m/s	~17.53 Hz
Numerical	40.4 m/s	13.43 Hz

The differences shown in Tables 10, 11 and 12 may have several explanations. What may lead to a mismatch between the experimental and the FEM results are: 1) the mechanical properties of the PLA used by the 3-D printing, which may not be exactly the same of that used by the FEM, 2) the friction between the slices which is not reproduced by the FEM, 3) the machining errors, which may appear only in the experimental model, 4) the electric circuit, which is missing in the FEM analysis, and 5) the gravity center position. In particular, concerning the gravity center position, it was verified, through additional experimental measurements, performed on a single slice, that the position of the gravity center provided by the FEM is not exactly coincident with the experimental value, an error of 31% circa for the gravity center position was measured in the chord-direction. Therefore knowing all the possible sources of discrepancies a parametric study was performed in order to better understand, whenever it possible, which has to be assumed as the real cause of the mismatch between the numerical and the experimental results. The relevant parameters for the purpose of the parametric study are: 1) x_a, the position of the center of gravity along the wing chord with respect to the elastic axis, 2) D_{22}, the torsional stiffness of the wing cross section, this was selected in particular because of the uncertainties shown in its experimental determination and because of the mechanical properties of the PLA, 3) a, the location of the elastic axis, normalized by the half of the wing chord, with respect to the mid-chord position. Figures 102, 103 and 104 highlight the effects of the variation of the previous mentioned parameters over the critical flutter speed, while Figures 105, 106 and 107 provide the frequencies variations.

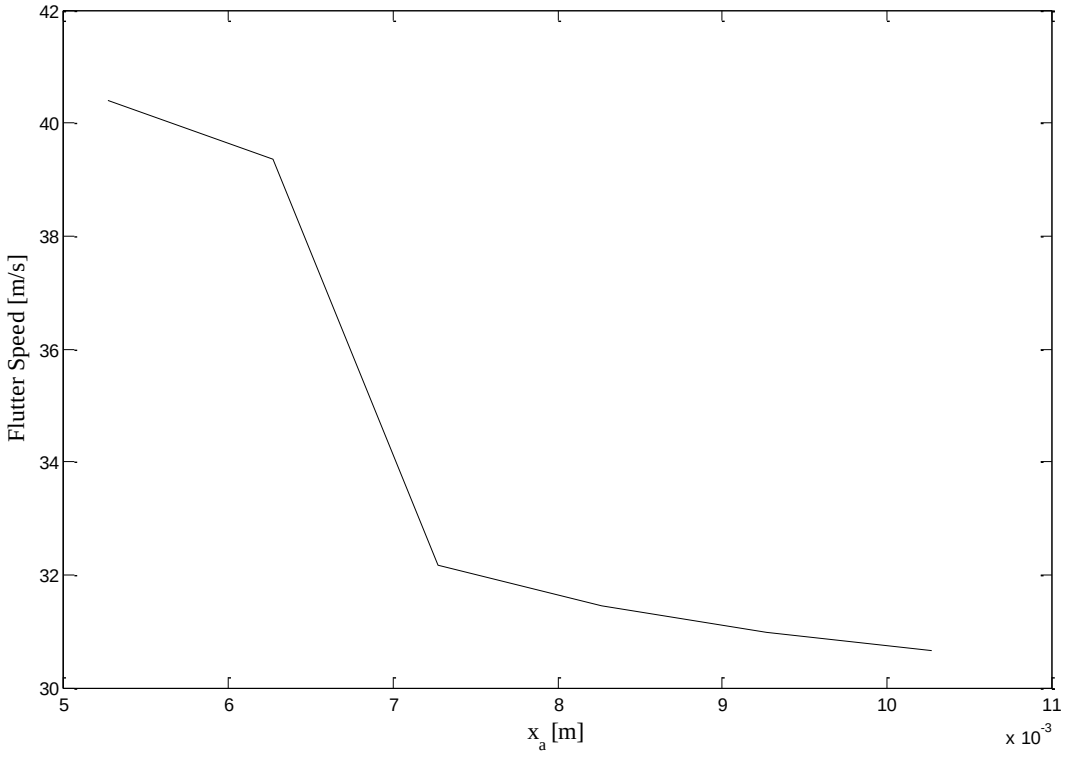

Figure 102 Flutter speed vs. center of gravity position w.r.t. the elastic axis in the chord direction. $D_{22} = 0.45\ N\ m^2, a = -0.28$.

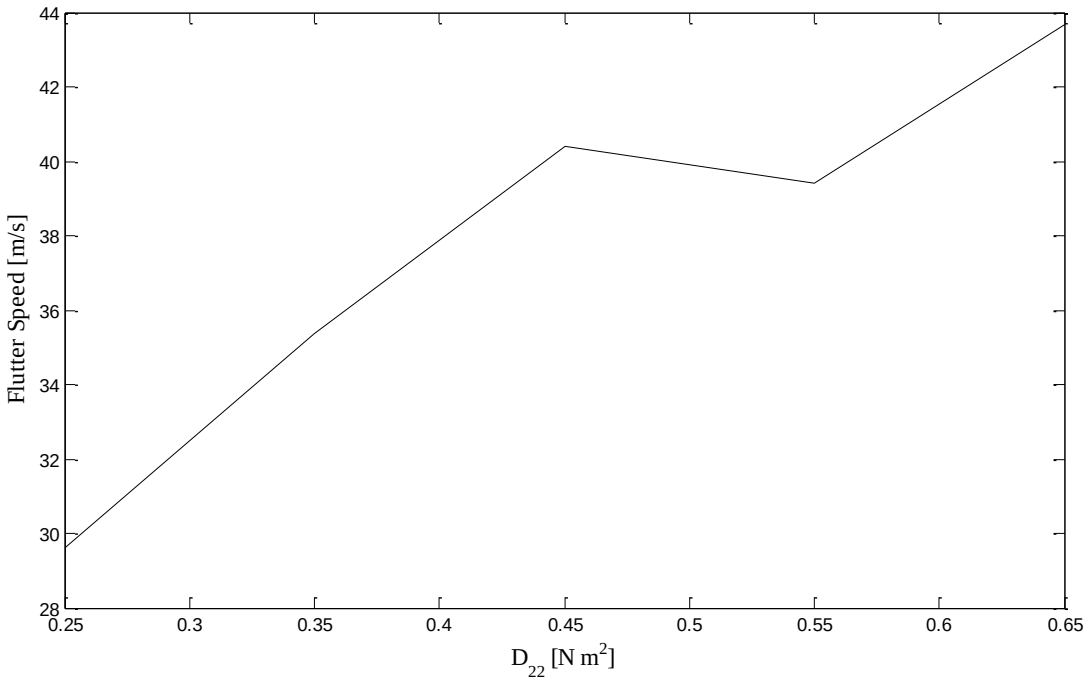

Figure 103 Flutter speed vs. Torsional stiffness per unitary length. $x_a = 0.00527\ m,\ a = -0.28$.

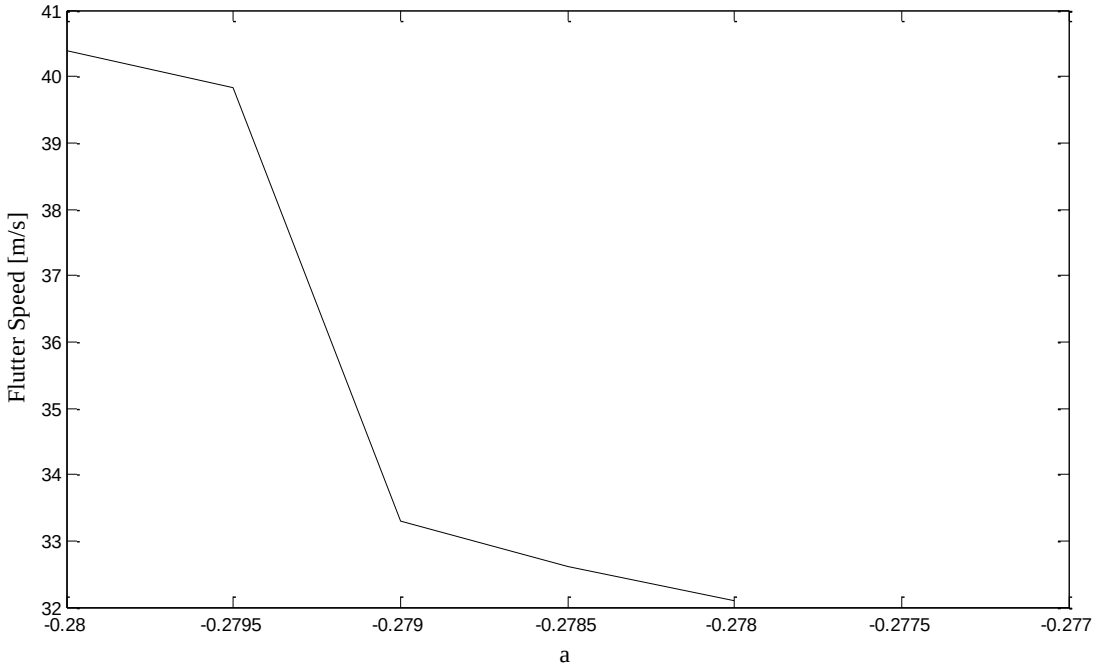

Figure 104 Flutter speed vs. shear center position, normalized by the half chord, w.r.t. the mid-chord. $D_{22} = 0.45\ N\ m^2, x_a = 0.00527\ m$.

By increasing the parameters x_a and a the reduction of the flutter speed follows a similar trend, while the torsional stiffness D_{22} has to be reduced in order to get a lower flutter speed. The natural frequencies are barely influenced by the variations of x_a and a while D_{22} , as expected, influences considerably the frequency of the first torsional mode. The red curve on the plots of Figures 105, 106 and 107 represents the evolution of the flutter frequency with respect to the parameters x_a, a and D_{22}. Figure 106 shows that to increase the value of the flutter frequency the torsional stiffness has to be increased. However, the increase of the torsional stiffness won't produce any beneficial effect on the flutter speed which will continue to be high, or even higher, with respect to the experimental results, as shown in Figure 103. In order to get a reduction of the flutter speed and an increase of the flutter frequency at the same time the position of the gravity center or of the elastic axis have to be slightly moved. Figures 102, 104, 105 and 107 show how moving towards the trailing edge the center of gravity or the

shear center induces an increase of the flutter frequency and a decrease of the flutter speed. In particular, from the just mentioned plots, it is possible to identify a range of values, for both parameters, in which the variation over the flutter frequency and speed is more significant. This range is between $6.27 * 10^{-3}\ m$ and $7.27 * 10^{-3}\ m$ for the position of the center of gravity, and between 0.2795 and 0.279 for the elastic axis position. The variation of the gravity center position is a likely circumstance since, as previously stated, subsequent measurements on one of the slices used for the experimental model showed such a discrepancy.

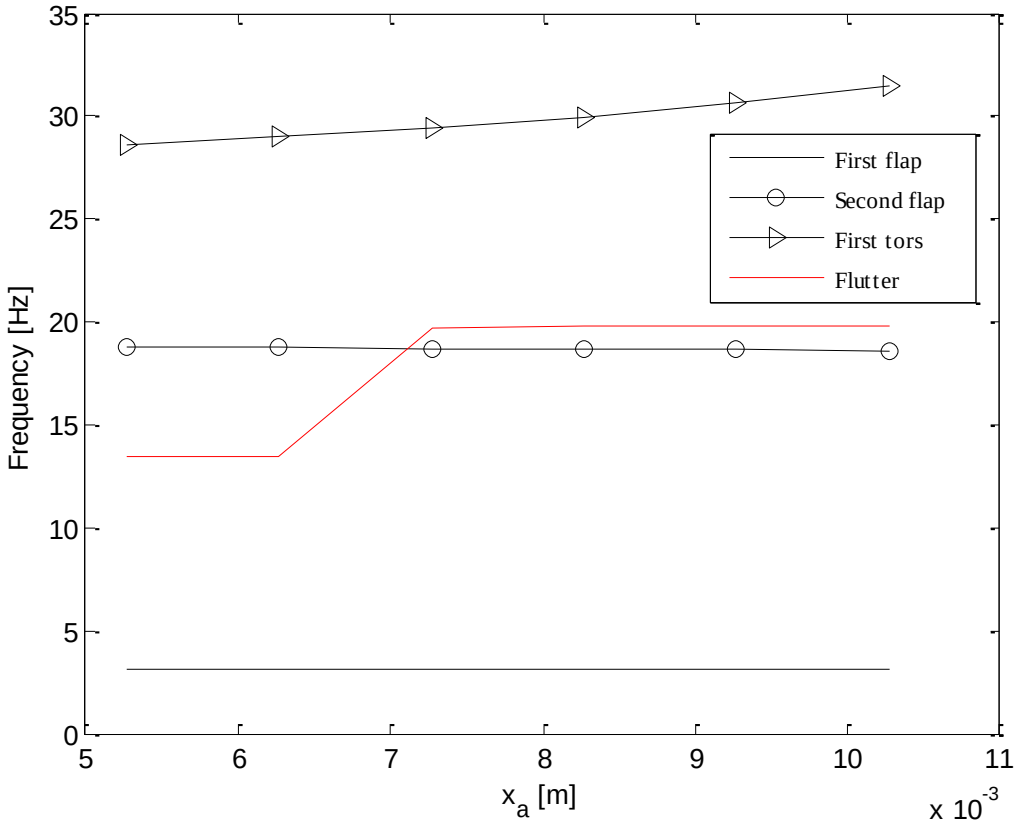

Figure 105 Flutter frequency vs. center of gravity position w.r.t. the elastic axis in the chord direction. $D_{22} = 0.45\ N\ m^2,\ a = -0.28$.

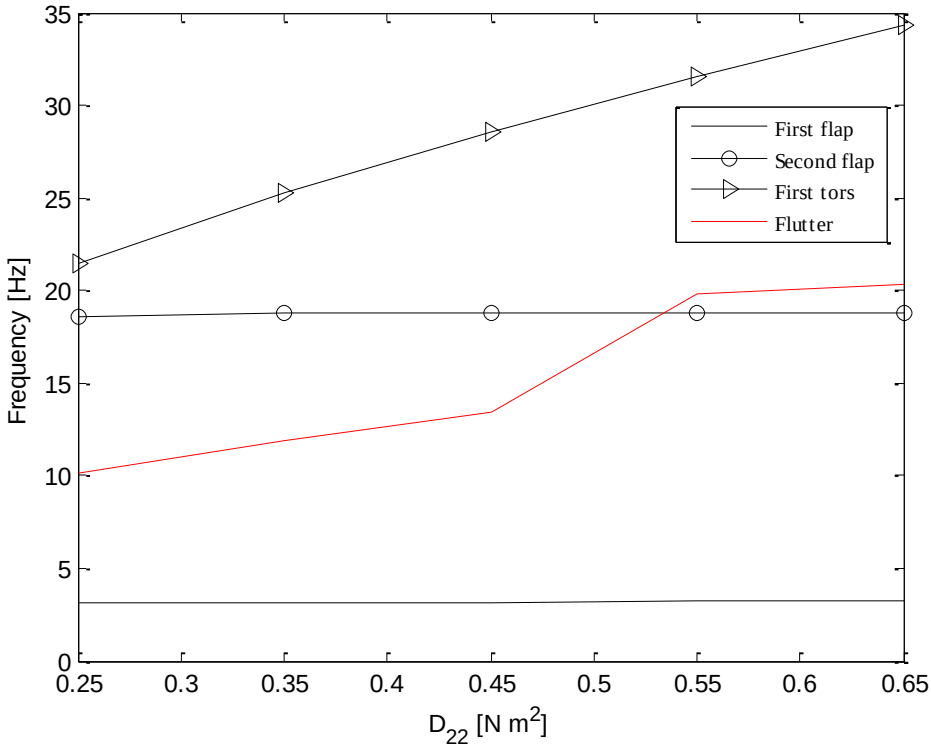

Figure 106 Frequency vs. Torsional stiffness per unitary length. $x_a = 0.00527\ m$, $a = -0.28$.

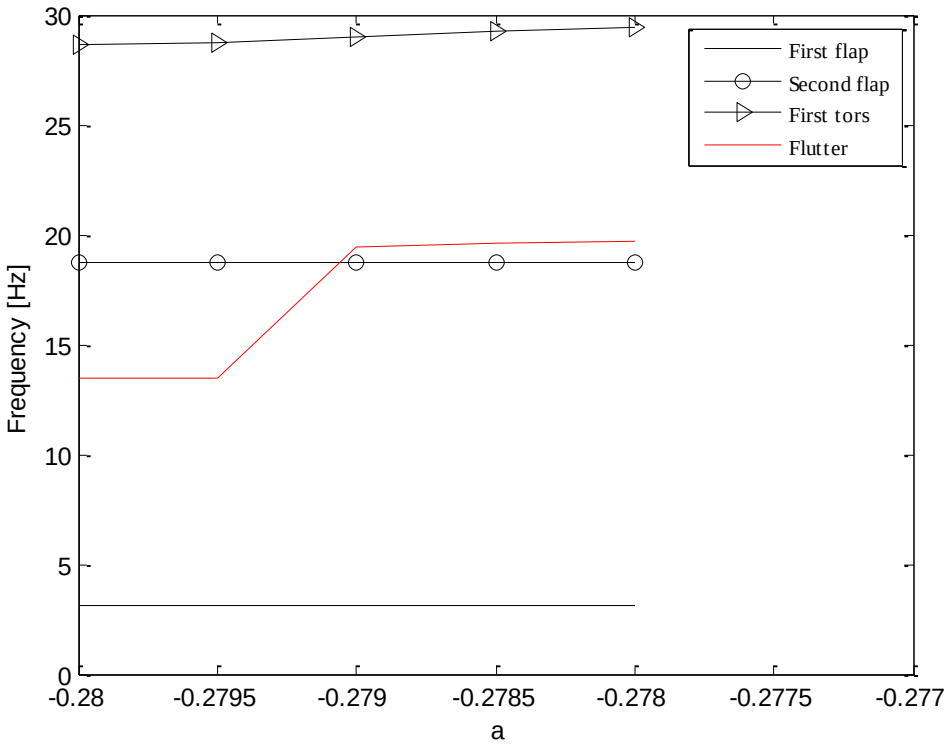

Figure 107 Frequency vs. shear center position, normalized by the half chord, w.r.t. the mid-chord. $D_{22} = 0.45\ N\ m^2, x_a = 0.00527\ m$

To better appreciate the effect of a parameter change, the evolution with the air speed of the piezoelectric wing frequencies, for three representative values of each parameter, are reported in Figures 108, 109 and 110. The piezoelectric elements are in the open circuit condition, therefore the frequencies are not influenced by any specific resistive load. The aerodynamic loads implemented in the numerical model follow Eqs. 3.3 and 3.4. Figure 108 shows how the first three frequencies of the piezo-wing evolve with the air speed when the center of gravity is moved towards the wing trailing edge. When the center of gravity is in the original configuration, that's to say $5.27 * 10^{-3}m$, in the chord direction from the elastic axis, the coalescence of the bending torsion frequencies occurs at speed higher than 40 m/s. By moving slightly the center of gravity to a new position equal to $7.27 * 10^{-3}m$ the coalescence occurs before, at lower speed, and for higher frequencies. If the center of gravity is pushed further aft, the flutter speed is reduced but the first torsional frequency at zero speed decreases. In each plot of Figures 108, 109 and 110 are reported the experimental values. The comparison between the experimental results and the other numerical solution of Figure 108 shows that the piezoelectric wing with the center of gravity located at $7.27 * 10^{-3}m$ from the shear center gives the better approximation of the experimental model. Figure 109 instead shows that an enhancement of the torsional stiffness, to have an higher value of the flutter frequency, leads to an increase of the flutter speed and of the natural frequency of the first torsional mode. This result make this solution less preferable with respect to the others.

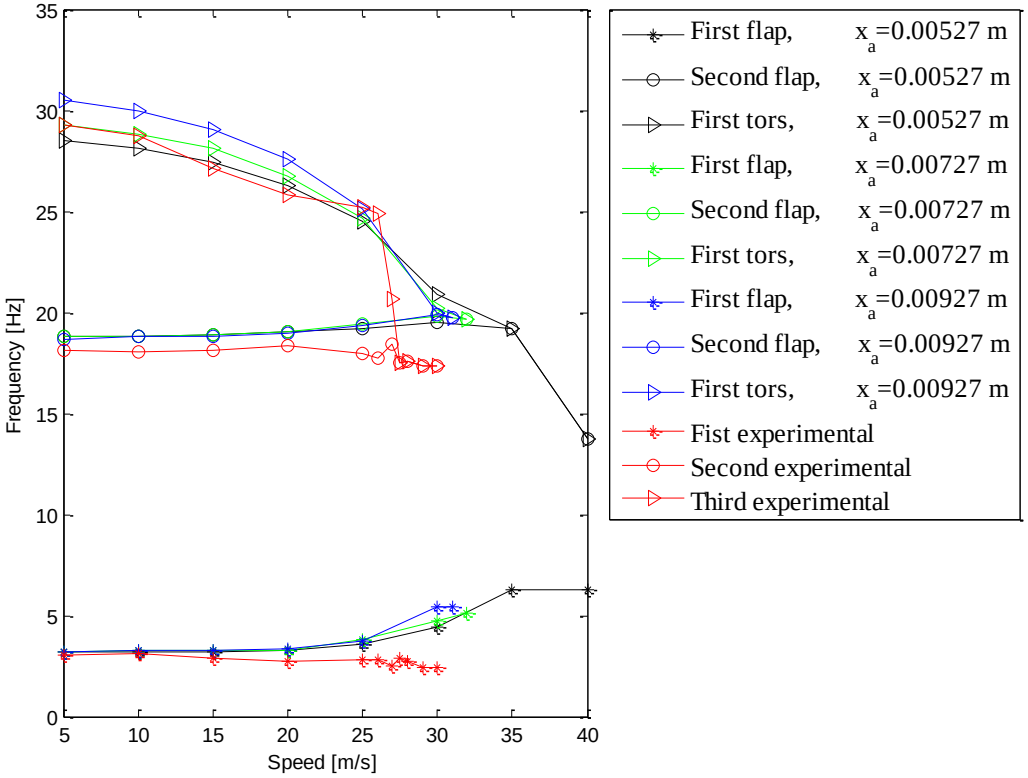

Figure 108 Frequency evolution vs. Air speed for three position of the center of gravity: $x_a = 0.00527\ m$, $x_a = 0.00727\ m$, $x_a = 0.00927\ m$.

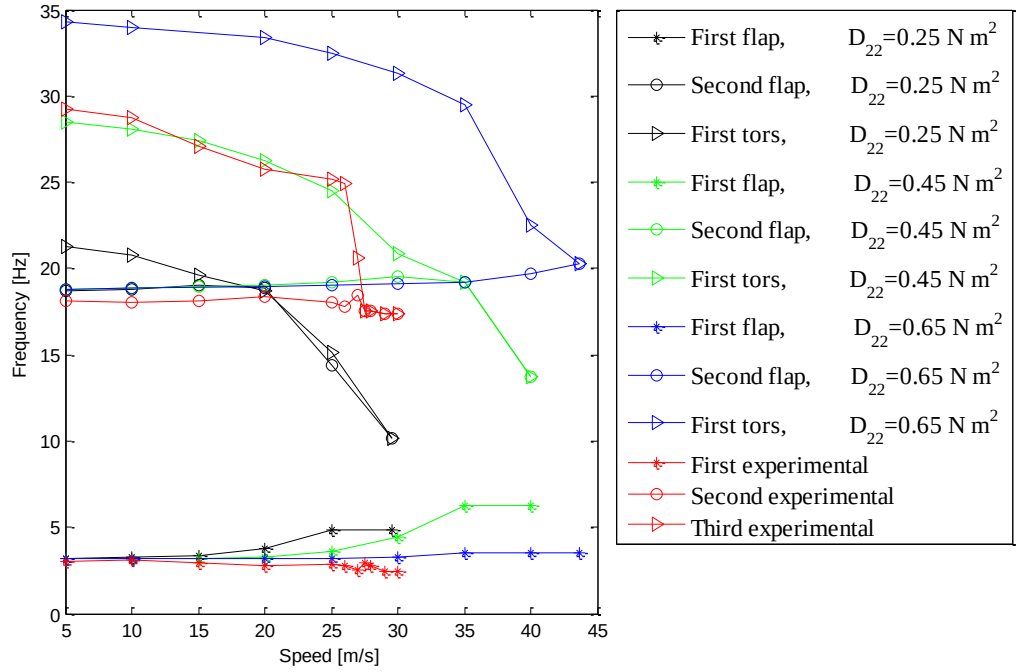

Figure 109 Frequency vs. Air speed for three distinct values of the wing cross section torsional stiffness: $D_{22} = 0.25\ N\ m^2$, $D_{22} = 0.45\ N\ m^2$, $D_{22} = 0.65\ N\ m^2$.

A trend similar to what seen in Figure 108 is reported in Figure 110, where the frequency variation versus the air speed is presented for three different positions of the elastic axis. By moving the elastic axis toward de trailing edge, keeping unchanged the distance between shear center and center of gravity, increase the flutter speed and decrease the flutter frequency as for the cases analyzed in Figure 108. However, by assuming all the parameters variations, as shown in Figures from 102 through 110, and the level of confidence for each data extracted from the experimental model and from the FEM, a small variation in the position of the gravity center is the most reasonable adjustment that can be introduced into the numerical model. The new position of the center of gravity of gravity with respect to the elastic axis is $X_{cg} = 7.27 * 10^{-3} m$ instead of $X_{cg} = 5.27 * 10^{-3} m$. All the other data are unchanged with respect to Table 9.

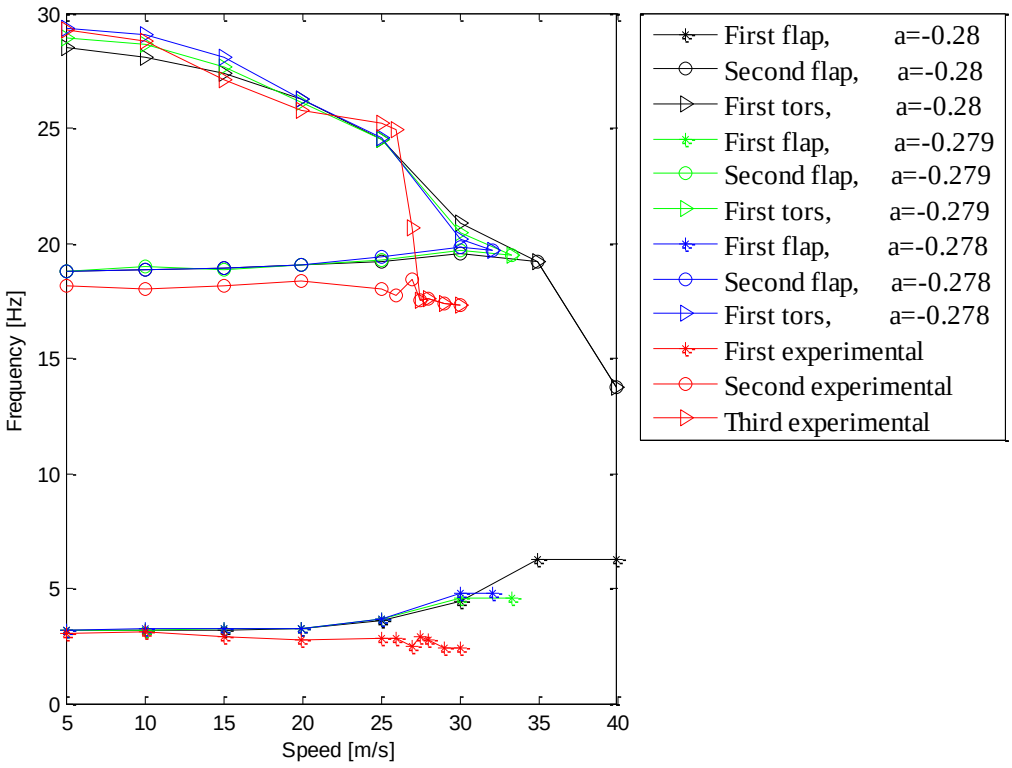

Figure 110 Frequency vs. air speed for three position of the shear center, normalized by the half chord, w.r.t. the mid-chord position: $a = -0.28, a = -0.279, a = -0.278$.

The center of gravity positioned at $X_{cg} = 7.27 * 10^{-3} m$ reduces the flutter speed from $40.4\, m/s$ to $32.18\, m/s$ and the flutter frequency from $13.43\, Hz$ to $19.78\, Hz$. These values are still not those obtained experimentally but much comparable than before. Another possible cause of the flutter speed reduction is the static deflection of the wing due to the aerodynamic loads. The static deflection, when of the order of the 10% of the wing length, may cause an anticipation of the flutter event. To investigate the effects of the static deformation over the natural frequencies of the piezoelectric wing, the nonlinear equations of motion 5.13, 5.14 and 5.15 have to be implemented. In particular it is worth at this point to highlight the importance of the correctness of the initial assumptions. In Chapter 5 the piezoelectric wing was always represented by a slender wing and short piezo patches placed in the proximity of the wing root. Due to the small dimensions of the piezos and the low displacements field involving the region where the patches were located, the piezo structural contribution, in Chapter 5, was assumed linear. Based on that, the linearity of the piezo patches cannot be acceptable for a wing model with the structural and geometrical characteristic of Table 9. The piezos length is half of the wing length which makes the condition of low displacement field to decay. Figure 111 shows the comparison between a wing model with piezo patched that behaves linearly while the hosting structure model include nonlinear terms up to the third order and a wing model with piezo patched that behaves linearly while the hosting structure model include nonlinear terms up to the second order.

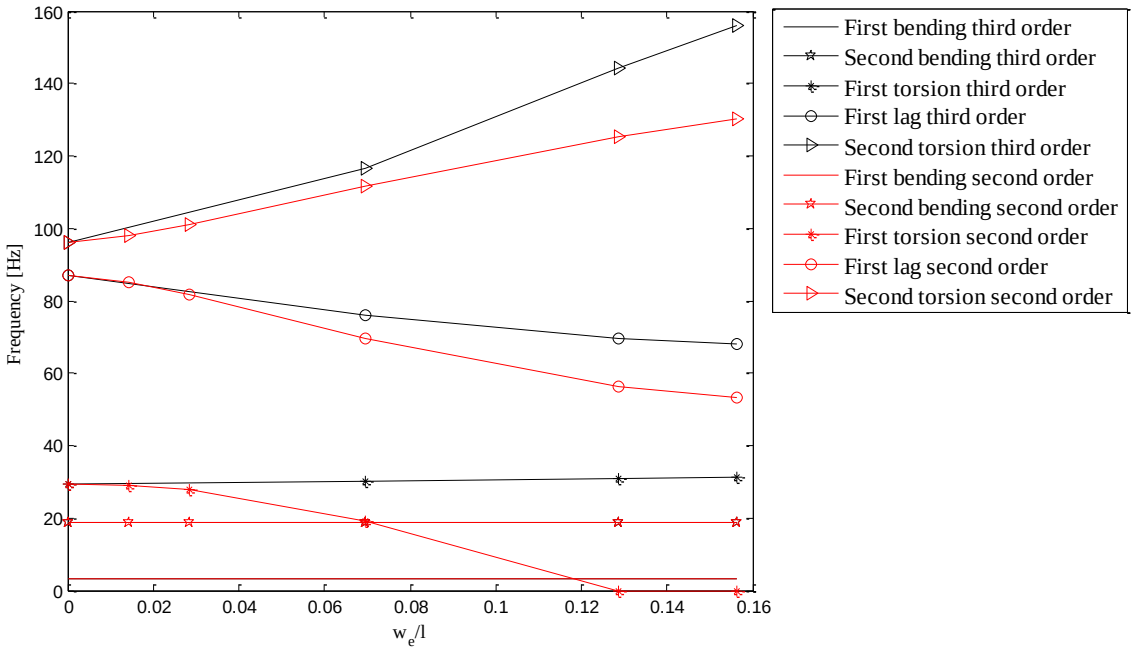

Figure 111 Frequency vs. relative static deflection for two different nonlinear model.

What clearly comes out from Figure 111 confirm that the assumption of linear PZT is not acceptable in this case. In fact, when the nonlinear terms which refer to the hosting structure are retained up to the second order the first three frequencies of the piezoelectric wing remain unvaried with the static deformation. It is due to the fact that it is missing the nonlinear contribution of the piezo patches which create an imbalance between the linear and nonlinear stiffness of the overall structure. By reducing the nonlinear contribution of the hosting structure through a truncation of the nonlinear terms to the second order it is possible to observe, directly from Figure 111, that the natural frequencies changes in some way with the increase of the piezoelectric wing static deformation, as expected. However as showed in Chapter 4, when the static deformation become important the second order nonlinear terms are not any more sufficient, higher order terms are requested. Figures 112 and 113 report the comparison between two third order nonlinear wing model where in one case the piezo elements

behaves linearly and in the other nonlinearly, with the same order of nonlinearity as the hosting structure.

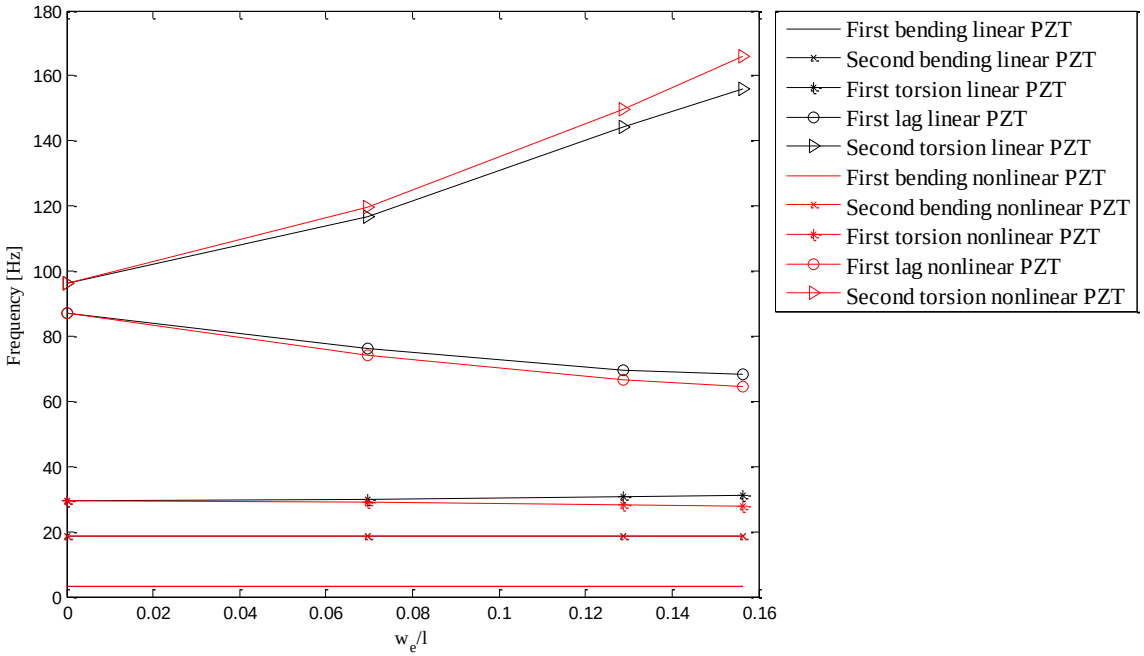

Figure 112 Frequency vs. relative static deflection for a nonlinear wing model with learn PZT and a full nonlinear piezoelectric wing model.

The full non linear model, that's to say nonlinear wing and nonlinear piezo patches, introduce a variation of the frequencies with respect to the wing static deformation which was not present before and, as better highlighted in Figure 113, and much more reasonable than that reported in Figure 111. Figure 113 display that in order to have an effect over the natural frequencies of the piezoelectric wing and so experiencing a sub-critical LCO, the static deformation has to be high. This results make quite improbable the occurrence of subcritical LCO during the experimental tests since the static displacement experienced before the rise of the flutter event is of the order of $0.5\,mm$, which means the 0.15% of the wing length. Figure 114 provide such a evidence.

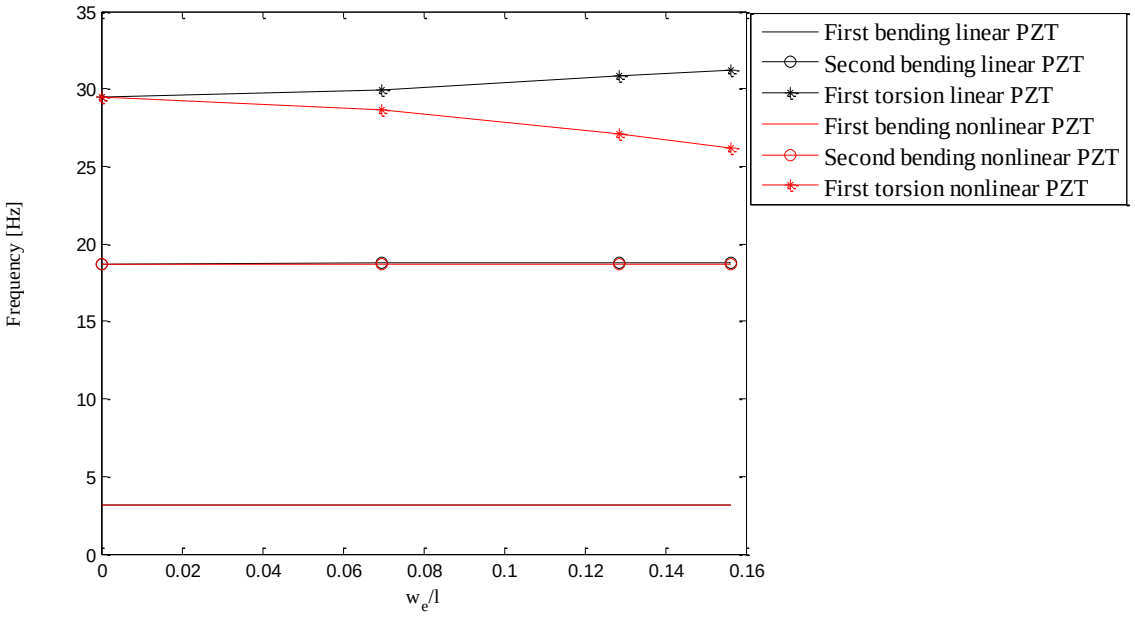

Figure 113 Detail of Figure 112.

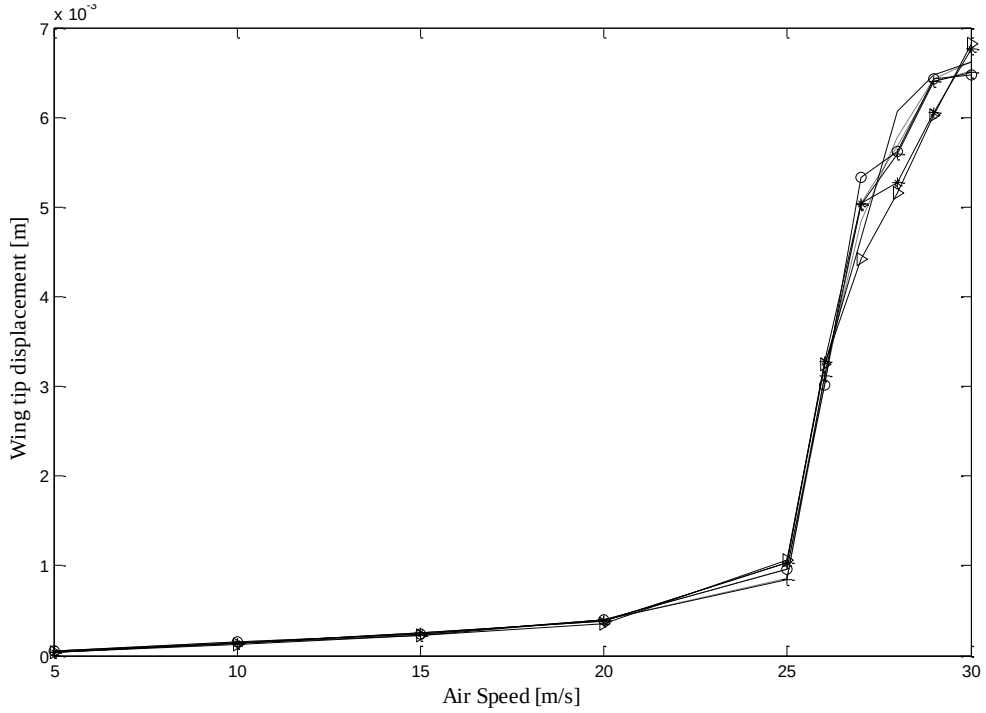

Figure 114 Experimental results of the wing tip displacement vs. the air speed [2].

6.5 FEM reduced model

The uncertainties between the FEM and the experimental model, highlighted in the previous paragraph, lead to perform further experimental checks over the physical experimental slice, and specifically that based on the evaluation of the weight and of the gravity center. The just mentioned test revealed a difference between the physical PLA slice and the solid numerical slice obtained through the FEM; a gap of about 1.63 mm, as shown in Figure 11, was measured.

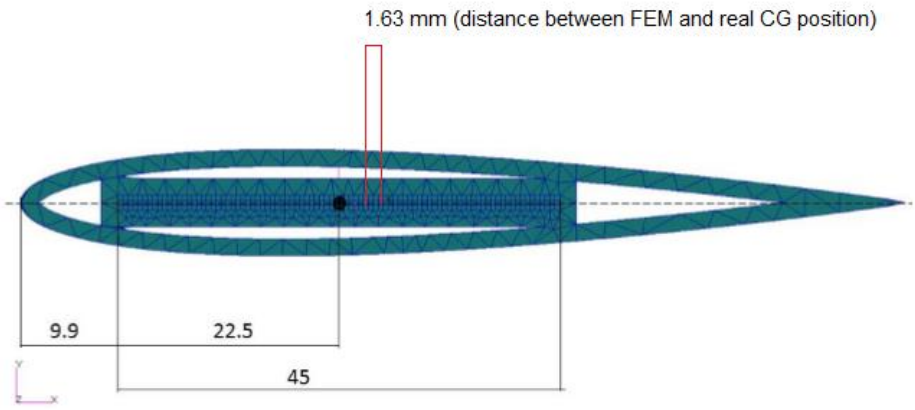

Figure 115 Difference between the FEM CG position of a single slice and the physical measured one.

Based on the verified shift of the gravity center of each slice it was built a simplified FEM model, comparable with the analytical/numerical model in order to take into account of the last changing in the gravity center position. Furthermore, the reduced model is much more practical to perform the nonlinear analysis since the solid model is extremely heavy and require a very long computation time. The characteristics of the simplified FEM piezoelectric wing are: 1) the distributed stiffness, which includes the spars, the slices and the piezo patches, 2) the mass of the spars and of the piezo elements is distributed over shear center, while the mass of the slices and their proper moment of inertia are represented by a set of concentrated

properties, uniformly distributed to a distance from the shear center of 7.27 mm in the chord direction and -0.022 mm in the plunge direction, which correspond to the new overall position of the gravity center. Figure 116 shows the layout of the just described FEM simplified model.

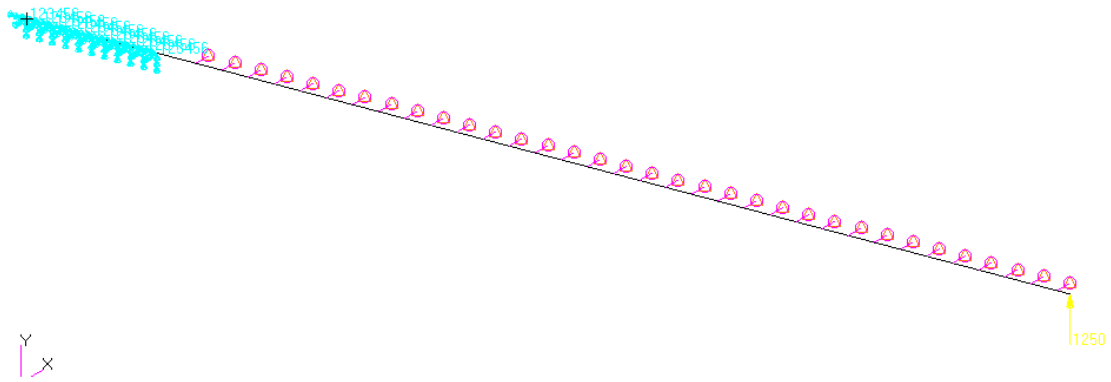

Figure 116 FEM simplified wing

The value of the first three natural frequencies are reported in Table 13. The comparison between the reduced FEM and the analytical/numerical results of Table 13 shows the similarity between the two models.

Table 13 Comparison between reduced FEM, numerical and experimental models.

WT configuration			
	First bending	**Second bending**	**First torsion**
FEM reduced	2.97 Hz	18.61 Hz	28.85 Hz
Numerical	3.14 Hz	18.72 Hz	29.46 Hz
Experimental	3.063 Hz	18.13 Hz	29.25 Hz

The simplified FEM of the piezoelectric wing guarantees a fast nonlinear analysis and therefore the possibility to validate the behavior of the analytical/numerical model. Figures 117, 118 and 119 represent the nonlinear response of the first three modes of the piezoelectric wing, when

subjected to a tip load of 0.5 N and a wig tip displacement of about 27.1 mm.

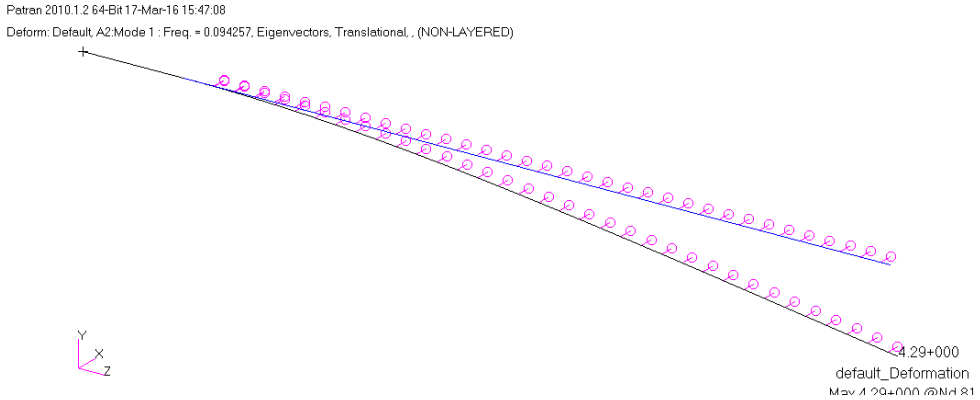

Figure 117 Nonlinear wing response to the first out of plane bending mode.

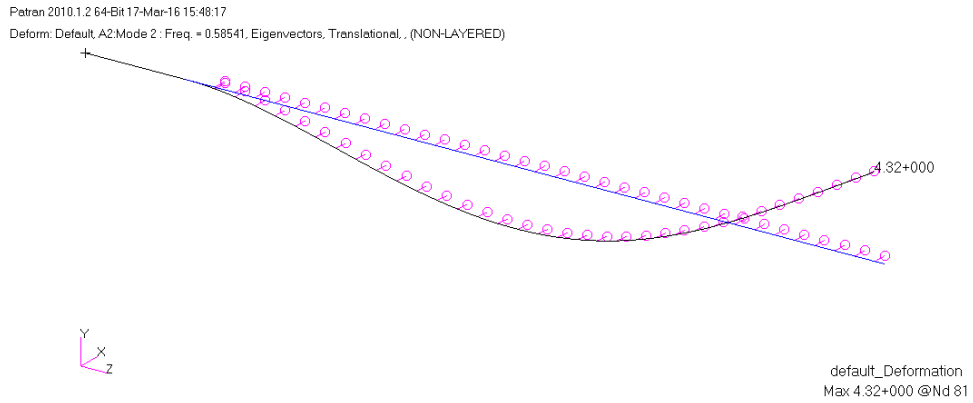

Figure 118 Nonlinear wing response to the second out of plane bending mode.

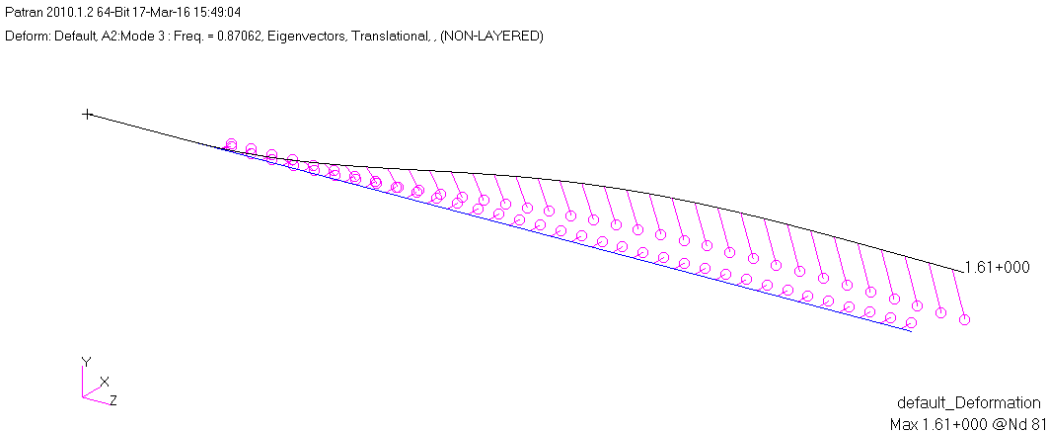

Figure 119 Nonlinear wing response to the first torsion mode.

The effect of the nonlinear analysis when the wing is subjected to a static deformation in the vertical direction emerge from the comparison between Figure 119 and Figure 120.

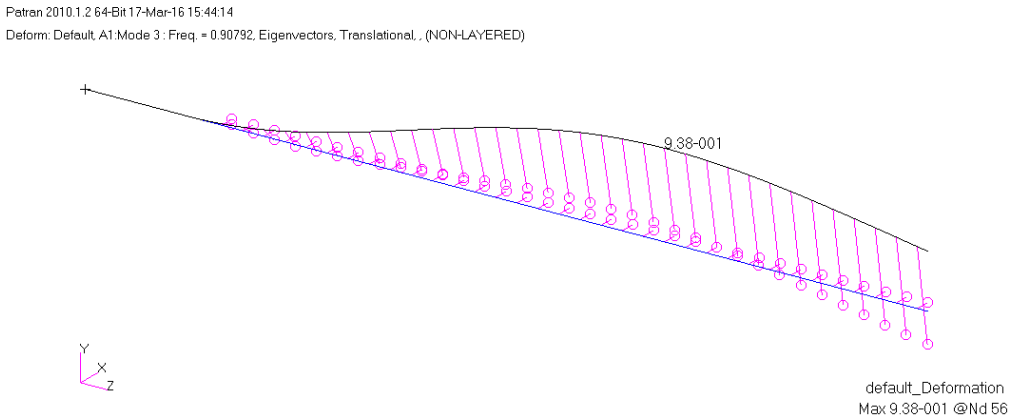

Figure 120 Linear wing response to the first torsion mode.

When the nonlinearities are assumed into the FEM analysis the modal response of a deflected wing, in the out of plane direction, is not that of a simple torsion as shown in Figure 120 for the linear case, it is therefore a coupled torsion-lag response, as in Figure 119. Figure 121 offers a comparison between the frequency response of the reduced FEM and of the numerical model, for various static wing tip deflection from 0 mm to 35 mm. This last plot confirms the correctness of the numerical solution thanks to the good agreement between the first three modal FEM and numerical frequencies, ω_1, ω_2 and ω_3.

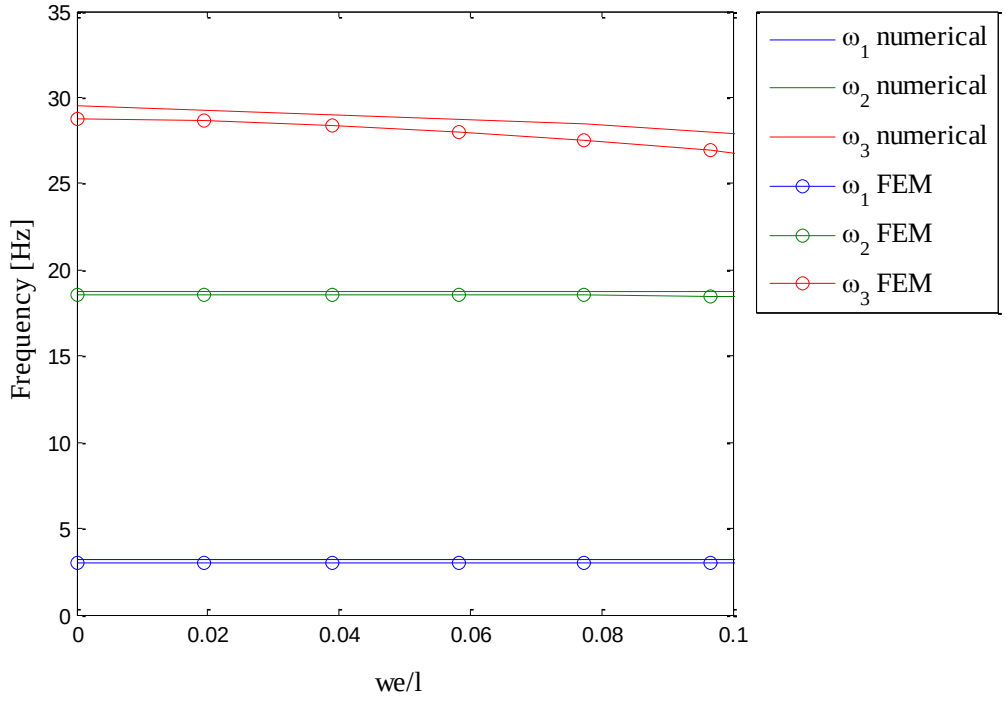

Figure 121 Frequency response of the out of plane deflected piezoelectric wing.

6.6 Study of the best piezoelectric wing configuration for energy harvesting. Shaker test.

The test campaign carried out at Clarkson university started from the modal excitation tests performed on the piezoelectric wing in its shaker configuration, Figure 94, with the aim of analyzing the modal response and evaluating the amount of energy that can be extracted from each mode. The piezoelectric wing is vertically mounted in order to avoid any initial static deflection induced by the wing weight. Figure 115 provides an overview of the test configuration layout.

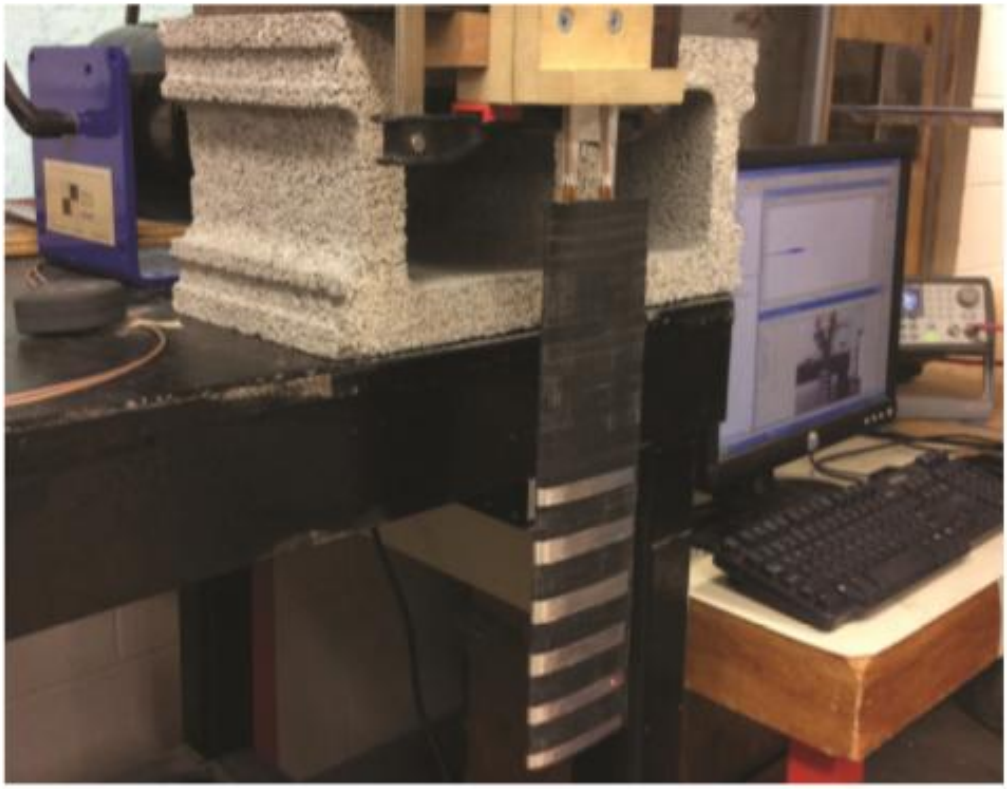

Figure 122 Modal test wing setting [2]

The instruments used for the modal testing are reported in Figure 115. The signal generator is shown in Figure 116 (a), followed by the signal amplifier, Figure 116 (b), the shaking machine, Figure 115 (c) and the laser scanning head, Figure 116 (d)

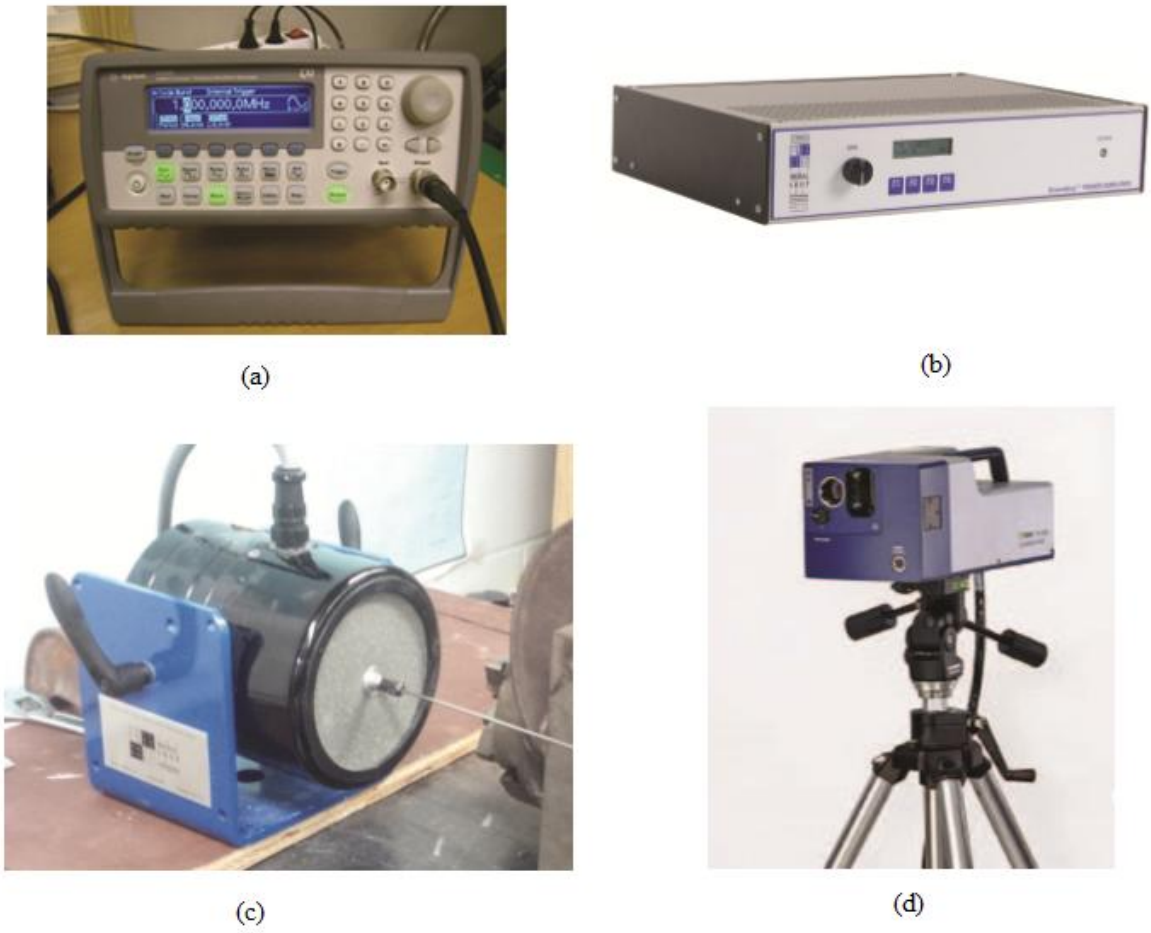

Figure 123 Modal test instruments [2]

The signal produced by the signal generator and subsequently amplified is transferred by the shaker head to the wing via the stringer, a metallic road glued on the wing surface to ensure a stable contact. The load is applied in the proximity of the wing root, where the displacements field is very small, so the continuous contact between the wing surface and the stringer is always guaranteed, and far from the first beam vibration nodes . Five stripes of silver adhesive tape are placed over the wing outer surface, near

the laser scanning points, to have an higher reflectance of the laser light, Figure 117 (b). The laser Scanning Points, over the wing, are scanned one by one in sequence by the laser light, obtaining from that the data velocity of each scanned points. The experimental instruments interact as in Figure 117 (a), starting from the signal generator to the data acquisition system.

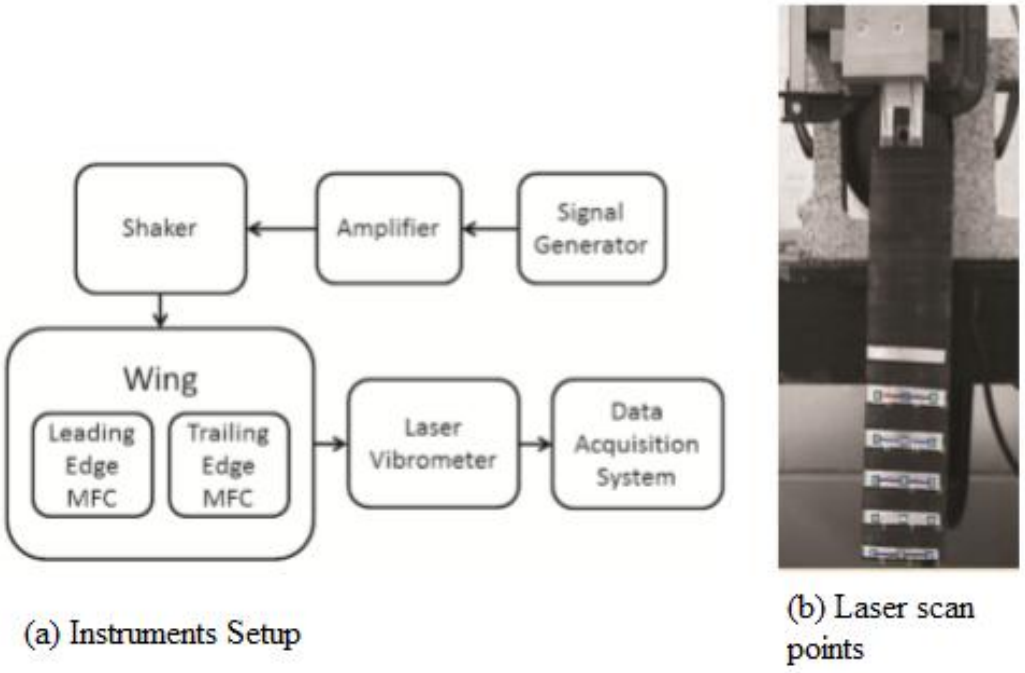

Figure 124 (a) Signal generation and propagation scheme, (b) Laser scan points over the wing [2].

The electrodes of each piezoelectric patch are connected to a variable electric resistance, set on the breadboard, Figure 118 (a), and the voltage across the resistance is measured through an oscilloscope, Figure 118 (b). Figure 118 (c) illustrate schematically the just mentioned process. The modal shaker test is based on the knowledge of the natural frequencies of the structure in order to be excited with a sinusoidal load which has a proper frequency as close as possible to the structure resonant frequency in order to reduce the applied load amplitude.

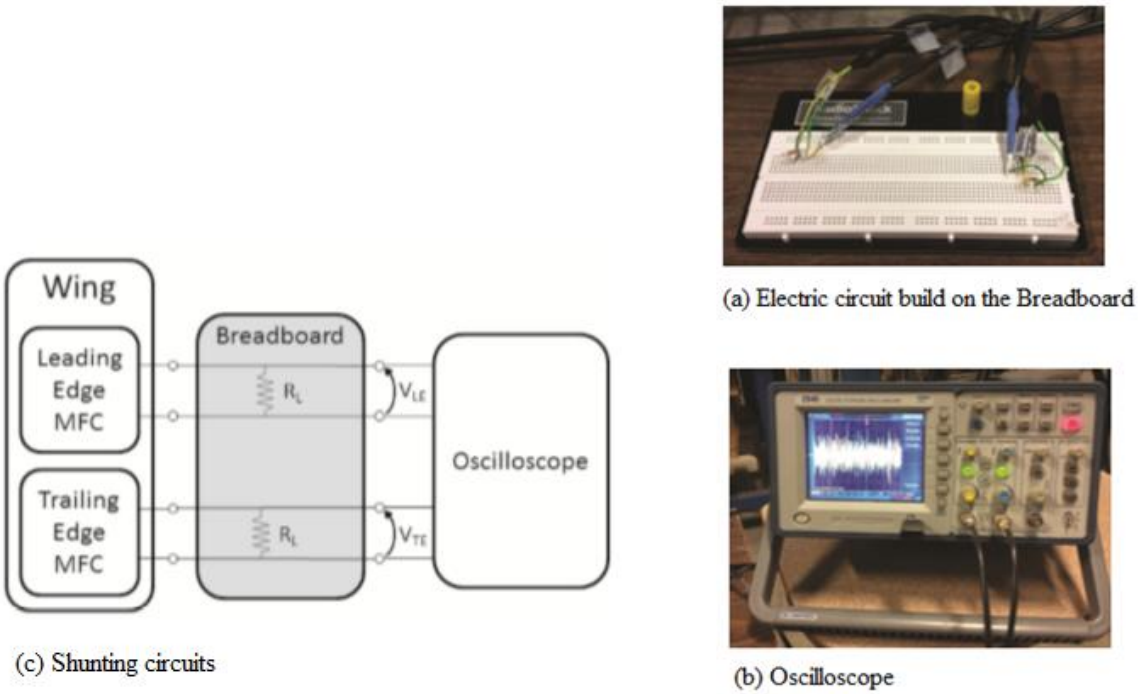

Figure 125 Piezos shunting circuits [2].

The natural frequencies of the piezoelectric wing, where the electrodes, which cover the entire surface of the piezo patches, are connected to a resistive load equal to 10^8 Ω, experimentally assumed as the open circuit condition, are obtained by an impulse excitation and reported in Table 13, which reports to the first two bending modes. Table 13 provides the same data referring to the numerical model.

Table 14 Comparison between experimental and numerical natural frequencies for a restive load equal to 10^8 Ω.

Modal shaker test configuration		
	First bending $R = 10^8$ Ω	**Second bending $R = 10^8$ Ω**
Experimental	2.563 Hz	14.72 Hz
Numerical	2.48 Hz	15.09 Hz

Once identified the natural frequencies the experimental test consisted in slightly and manually vary the frequency of the sinusoidal signal in order to

get close to the resonant condition, which correspond to the natural frequency of the vibration mode. Starting with an electric resistance of $10^8\,\Omega$, which is close to the open circuit condition, the resonance frequencies, of the first two bending modes, was identified at 2.6 Hz and 14.7 Hz. These two frequencies are assumed during the experimental test, together with the load amplitude, a fixed input data-set for the whole modal test campaign. Unfortunately during the experimental test the amplitude of the applied load was not recorded therefore the only data that can be used as reference value for the numerical representation of the modal test is the wing tip displacement due to the sinusoidal excitation. Therefore the modal shaker test consisted in exciting the piezoelectric wing with a constant amplitude sinusoidal load at 2.6 Hz and 14.7 Hz, alternatively, in order to record the electric voltage across the electric load, for each modal excitation. While the characteristics of the external load were always kept constant at each modal excitation, the restive load was changed, allowing to evaluate the power extraction as a function of connected resistive load. The numerical reproduction of such experimental modal test was quite a challenge since some information related to the experimental tests were not available, such as the applied load amplitude and the exact position of the stringer over the wing. In order to set the numerical wing model as close as possible to the experimental testing conditions, the external load application point was assumed at 0.02 m from the wing root and the load amplitude and frequencies tuned to have a wing tip displacement comparable to the one obtained during the experimental test for a resistive load equal to $10^8\,\Omega$. The two frequencies assumed for the numerical simulation of the modal shaker test are 2.48 Hz and 15.083 Hz, very close to those reported in Table 13. The analytical representation of the shaker loading condition is reported in Eq. 6.2, which differs from Eq. 5.13 for the presence of the shaker load.

$$\{\dot{z}\} = [S]\{z\} + [N]\{z(0)\} + \{F_{shaker}\} \quad 6.2$$

The load applied by the stringer to the wing is analytically represented by equation 6.3, where A is the amplitude of the sinusoidal load and $\delta(y - 0.02)$ is the Dirac function which define the external load application point.

$$\{F_{shaker}\} = \begin{Bmatrix} 0 \\ 0 \\ \int_0^l \phi_{w1}(y)\delta(y-0.02) * A\sin(\omega_i t)\, dy \\ \int_0^l \phi_{w2}(y)\delta(y-0.02) * A\sin(\omega_i t)\, dy \\ 0 \\ 0 \end{Bmatrix} \quad 6.3$$

Figures 119 and 120 show the comparison between the results obtained experimentally and those obtained numerically from the piezoelectric wing model. The power in both experimental than numerical is calculated according to Eq. 6.4:

$$Power = \frac{{V_{RMS}}^2}{R} \quad 6.4$$

where for a sinusoidal signal $V_{RMS} = \frac{V_{peak}}{\sqrt{2}}$.

The results obtained from the numerical simulations are quite satisfactory if compared with the experimental results. The peak of power is coherently displayed at $10^6\,\Omega$ for the first mode and $10^5\,\Omega$ for the second, highlighting the importance of a tunable shunting circuit when the wing is excited in a wide range of frequencies. The amplitude of the extracted power is of the order of $10^{-1}\,mW$ when the wing is excited at a frequency close to its second bending mode natural frequency, while it is of the order of $10^{-3}\,mW$when the excitation frequency approach the first bending mode natural frequency.

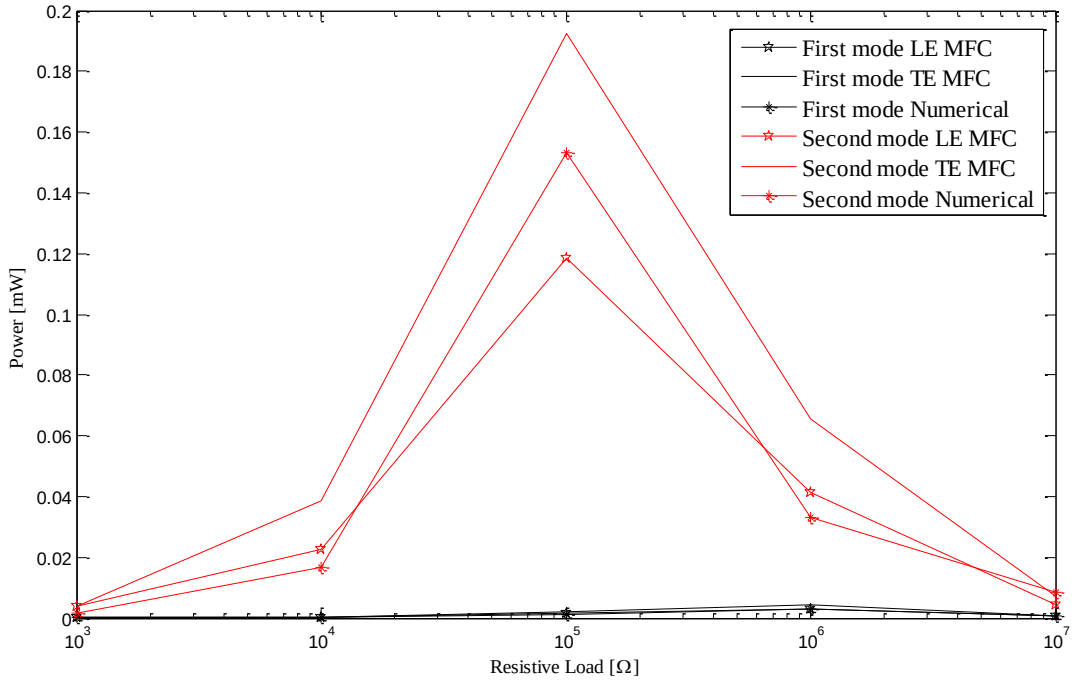

Figure 126 Power extracted from the wing modal excitation. Experimental and numerical comparison.

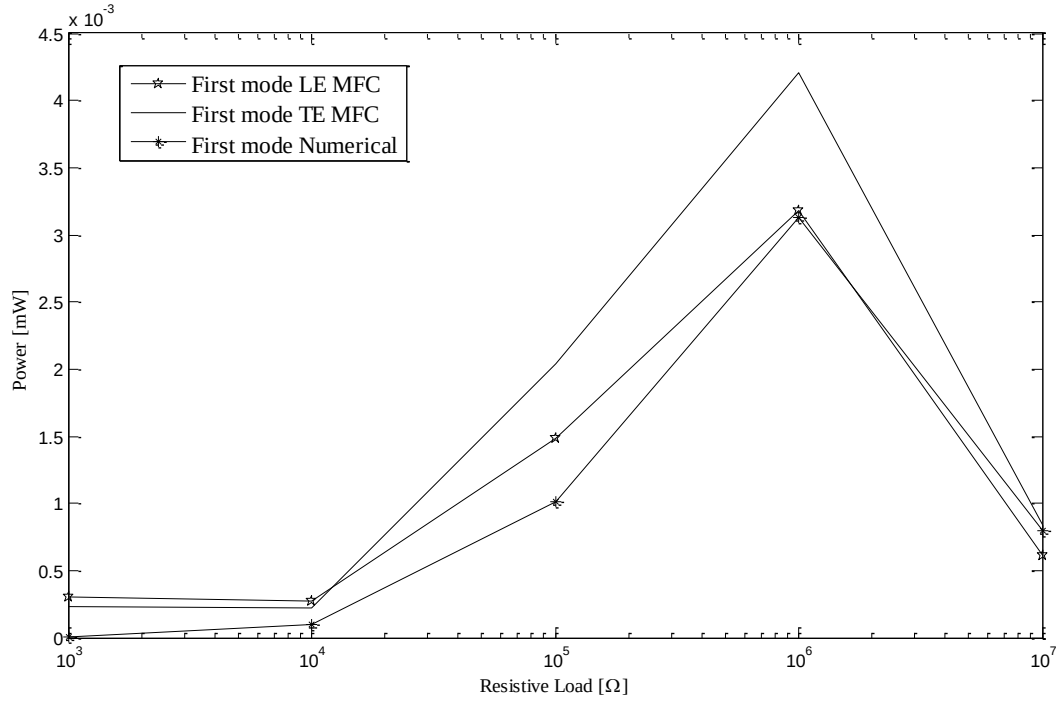

Figure 127 Detail of Figure 119. Experimental and numerical comparison.

Figure 119 shows that the extracted numerical power lays between the value obtained from the Leading Edge (LE) piezoelectric circuit and the

Trailing Edge (TE) piezoelectric circuit. It is a reasonable result since the numerical model doesn't consider two separate electric circuit but only one where the piezos are connected in parallel to two equal electric resistances, as explained in Paragraph 6.3. This means that the fact that the numerical output voltage stay in the middle between LE and TE voltage is not a surprising outcome. However, looking at Figure 120 the results for the first bending mode seem not being exactly in line with what previously stated, since the power extracted from the numerical simulation is slightly behind the expected value. The explanation for such mismatch, whether it is reasonable to define it as a mismatch, can be find in several factors and one over all the sensitiveness of the model to the excitation frequency and therefore the difficulty to reply exactly the same displacement obtained during the experimental tests. Nevertheless looking at both Figures 119 and 120 it can be affirmed that the modeled harvester work properly, in good agreement with the experimental results. Another important effect which is worth to consider when the results of the extracted power are analyzed is the dependence of the power extracted from the position of the piezo patches with respect to the wing length. In fact, as shown in Figure 121 by simply moving of a few millimeters the piezo towards the clamped end, or the wing root, the amount of power extracted from each mode may change with a certain relevance.

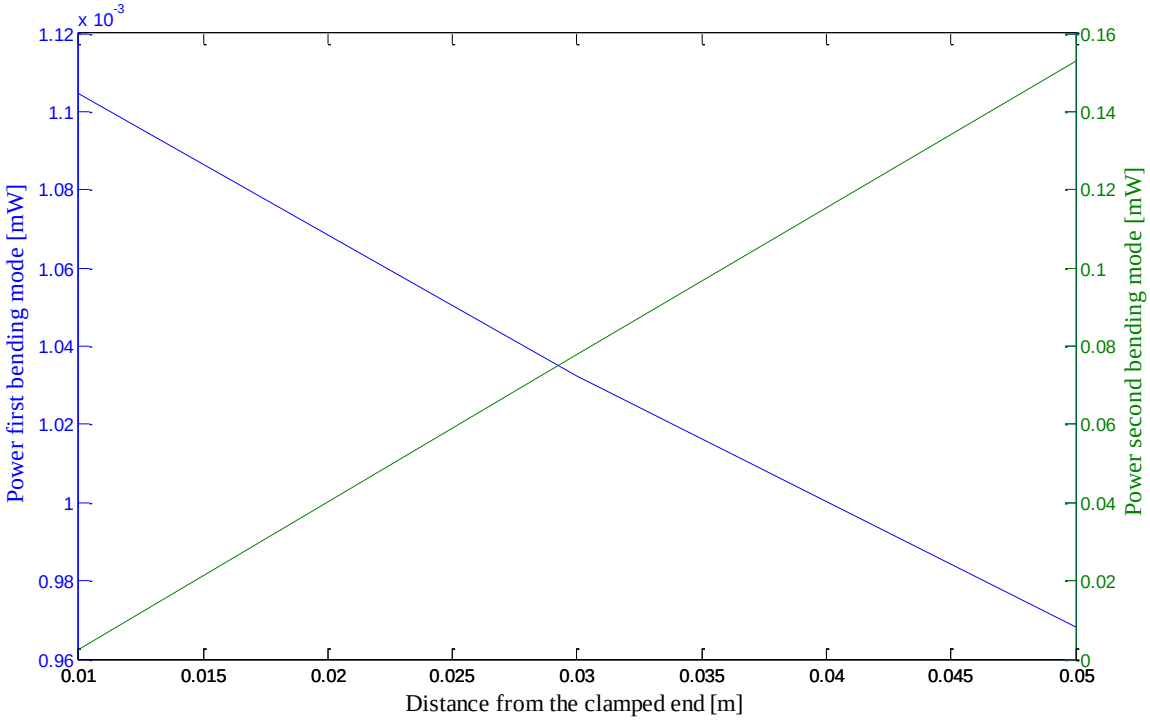

Figure 128 Power extracted from the first two bending mode at $R = 10^5\ \Omega$ vs. the piezo patches position with respect to the wing root.

When the piezo patches are moved towards the wing root the power extracted from the first mode slightly increase, while the power extracted from the second mode decrease in a quite consistent way. This last results highlight the importance of a preliminary optimization study which involve several parameters such as the position of the piezoelectric patches based on the expected dynamic response.

6.7 Energy harvesting from flutter and LCO: Wind tunnel test.

The wind tunnel tests were possible thanks to the facilities and the instrumentations available at Clarkson University. The high speed wind tunnel, in which the experimental test were performed, may reach in the test chamber a maximum speed of 70 m/s. A proper calibration test of the wind tunnel was performed before the experimental test over the wing in order to avoid any undesired result. The maximum speed variation in the testing chamber is lower than 0.5 m/s and the turbulence level quite negligible. The flow speed in the testing chamber is measured through a classical Pitot tube, installed upstream, and connected to a digital pressure transducer. Figure 122 shows the high speed wind tunnel used to the test the piezoelectric wing at air speed above the critical flutter speed. The wing is mounted vertically thanks to a wooden support which allow to anchor the piezoelectric wing to the roof of the testing chamber. The typical Reynolds numbers in the WT are reported in Table 14.

Table 15 Reynolds numbers vs. Air speed

Air Speed	Reynolds Number
5 m/s	$30.4 * 10^3$
10 m/s	$60.8 * 10^3$
20 m/s	$1.22 * 10^5$
30 m/s	$1.82 * 10^5$

(a) High speed wind tunnel

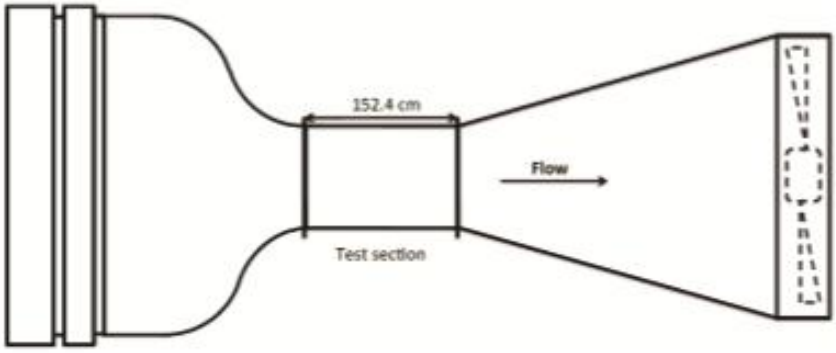

(b) representation of the winf tunnel

Figure 129 High speed wind tunnel [32]

The wing used for the WT tests, as mentioned in Section 6.1, differs from that used in the modal testing for its length, which is in now 0.35 m and without the solid clamping section, and for the piezo patches location, which start from the clamped end of the wing. For the sake of scrupulosity the fact that the piezo patches are exactly placed from the clamped and onward can only be affirmed for the numerical model, the experimental model may be effected by some small shifting of the piezo position. As for the modal testing the piezoelectric patches are connected to two equivalent resistive circuits and the output voltage is read by an oscilloscope as in Figure 123.

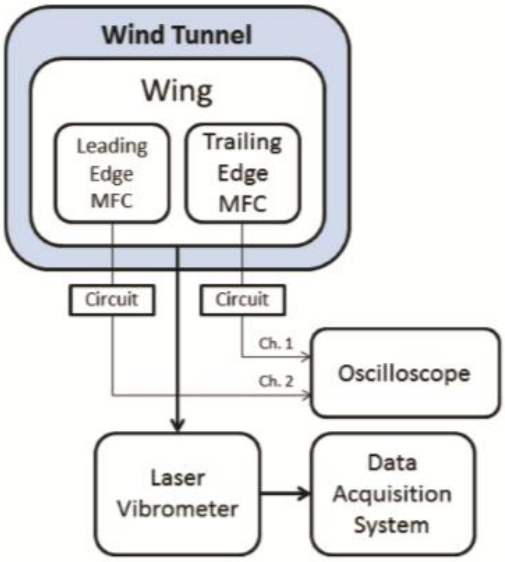

Figure 130 Shunting scheme of the piezoelectric wing.

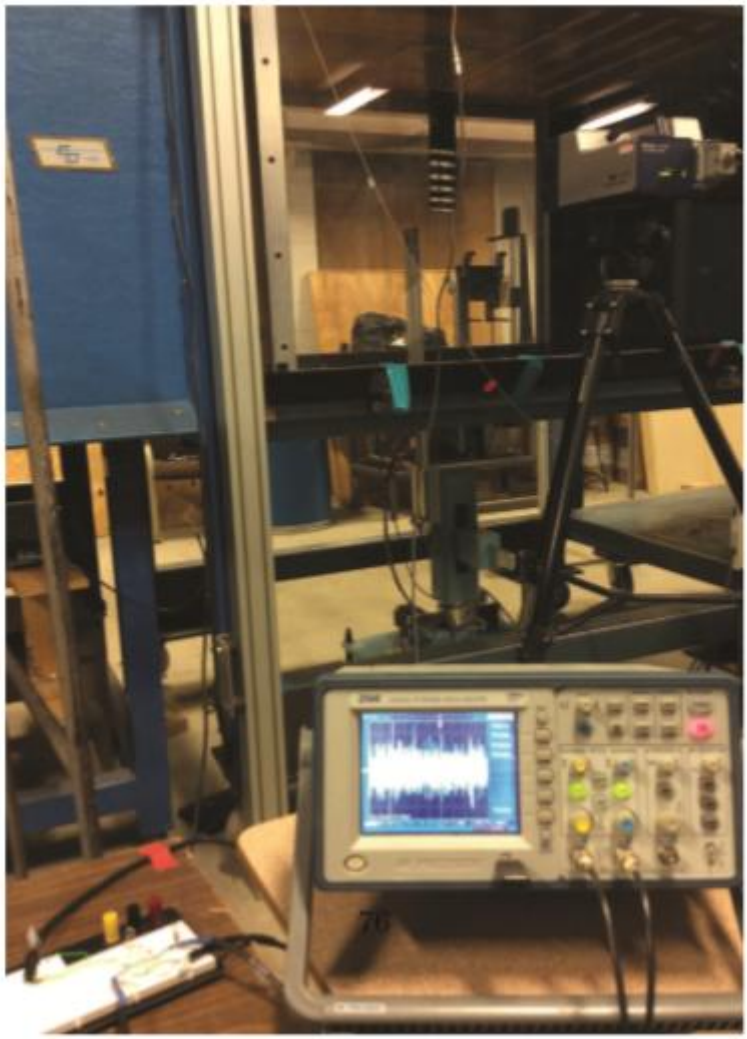

Figure 131 WT setup.

Figure 124 shows the wind tunnel setup. As for the previous tests the displacements of the wing tip are measured through a laser vibrometer but the number of scan points over the silver stripe are now increased to better capture the wing displacement at higher air speed values. The experimental tests were performed by progressively increase the flow speed in the testing chamber from 5 m/s to 30 m/s. The tests shown that when the piezo patches are not connected to any electric circuit the flutter speed is found at about 27m/s, experiencing an abrupt jump of the oscillation amplitude. However when the patches are connected to a resistive electric circuit the oscillation amplitude increase more gradually and it is slightly attenuated. Figure 125 shows the root mean square of the wing tip oscillation amplitude vs. the air speed. The red curves refer to the numerical results while the black curves to the experimental results.

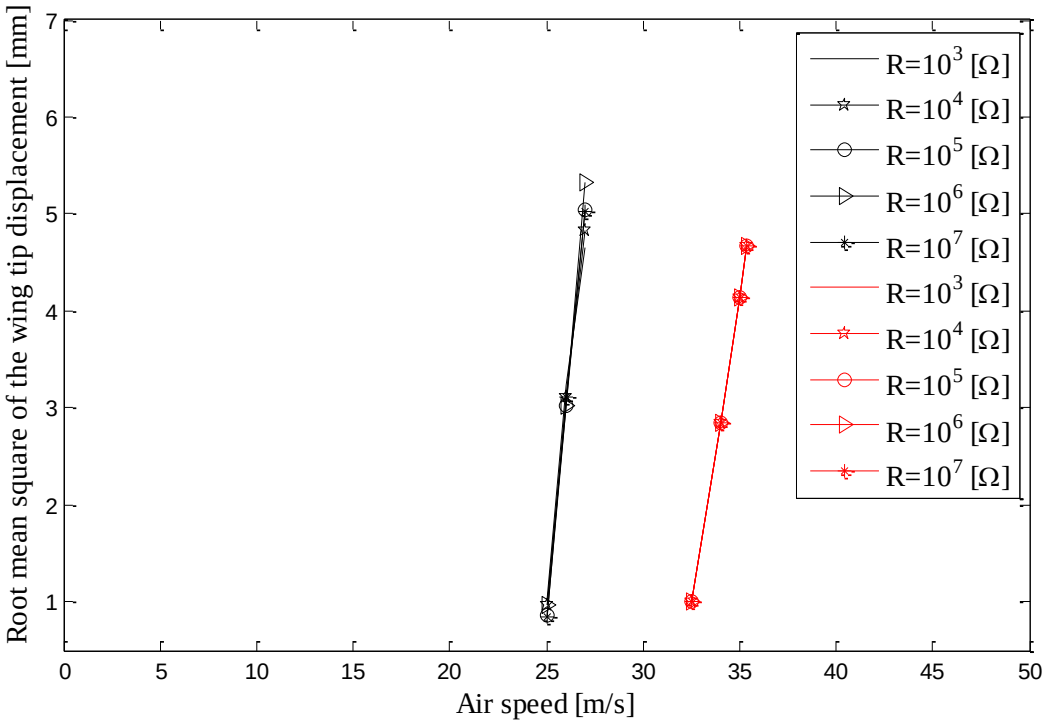

Figure 132 Wing tip displacement comparison between the experimental and the numerical wing.

As largely analyzed in Paragraph 6.4 the numerical wing have an open circuit critical flutter speed which is higher than the experimental one, it is 32.18 m/s circa, but the LCO response is pretty comparable. The rate of growth of the numerical oscillation amplitude is little bit lower than that of the experimental one and for speed higher than 35.35 m/s the amplitude start to decrease instead of increasing. It is the same situation experienced in Chapter 4 and this may be due to the fact that when the oscillation amplitude gets high the nonlinear model needs to expand to higher order nonlinear terms or has to include the dynamic stall model. The numerical results presented in this section consider an nonlinear model up to the third order, obtained through the asymptotic reduction procedure, presented in Chapter 2, which include nonlinear terms on both wing and piezo elements, according to the analytical representation of EQs. 5.13, 5.14 and 5.15. The results displayed in Figure 125 suggest another consideration which relate to the effect of the electric resistance over wing tip amplitude. The experimental results show that the electric resistance, albeit in a very inappreciable way, may affect the oscillation amplitude, while the numerical results seems not being sensitive to such effect of the resistive load. The LCO amplitude in terms of wing tip displacement and voltage obtained by the numerical simulations at 35.35 m/s and with a resistive load equal to $10^5\,\Omega$ is reported in Figures 126 and 127. The power extracted from the LCOs is computed through equation 6.4 and a comparison between experimental and numerical results is offered in Figure 128. The experimental data reported in Figure 128 refer to the LE electric circuit; the power obtained from the TE output is globally higher.

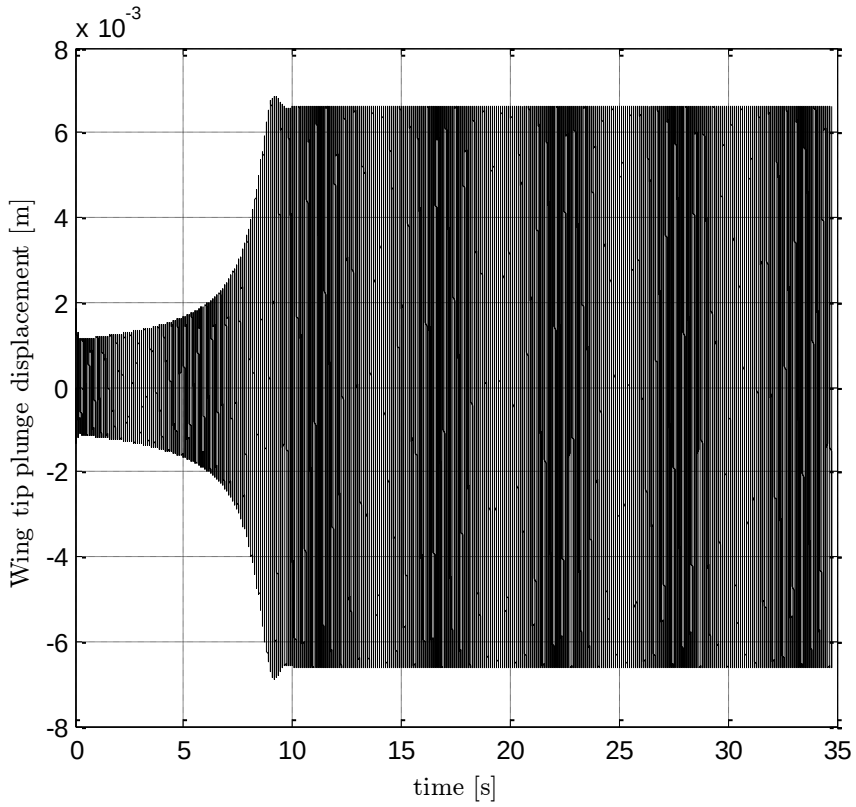

Figure 133 Time history of the wing tip oscillation at U=32.35 m/s and $R = 10^5\ \Omega$

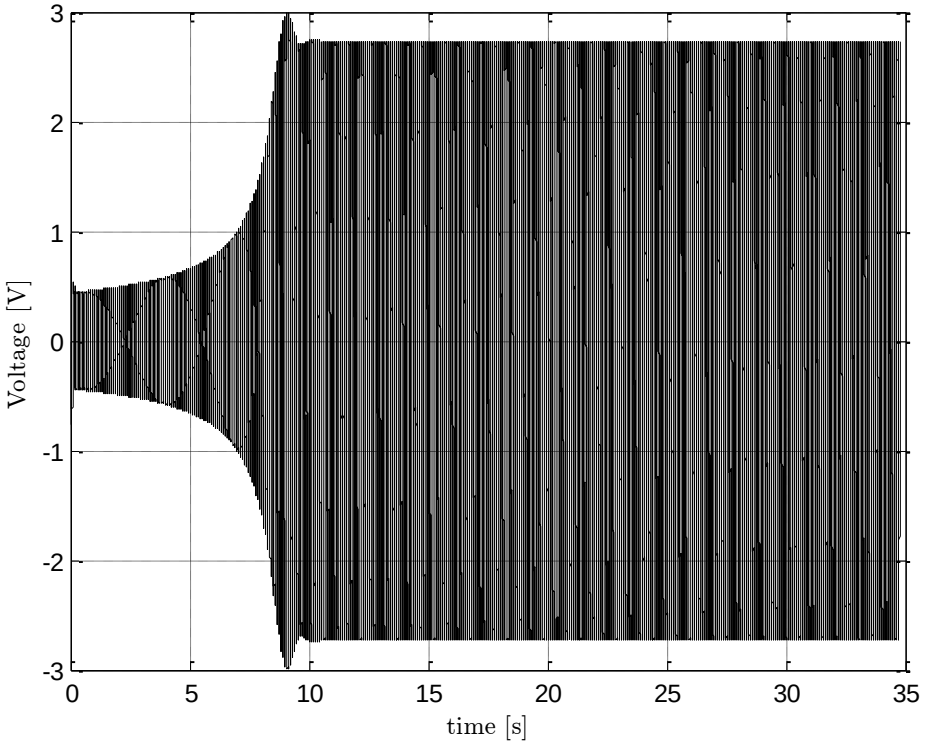

Figure 134 Time history of the voltage oscillation at U=32.35 m/s and $R = 10^5\ \Omega$

What shows figure 128 is that the power numerically estimated has the same order of magnitude of that obtained experimentally but with some differences. It may be due to multiple reasons which are: the correct positioning of the piezo patches over the wing, the not huge but still existing difference in the oscillation amplitude between experimental and numerical, or the initial approximations made to develop the analytical model. It is very important to consider the fact that the numerical model is not the exact representation of the experimental model and that the purpose of the investigation was not only to validate the numerical representation of the harvester but also to exploit the experimental results in order to performs some dedicated studies on the driving parameters and configurations in a piezoelectric harvesting process.

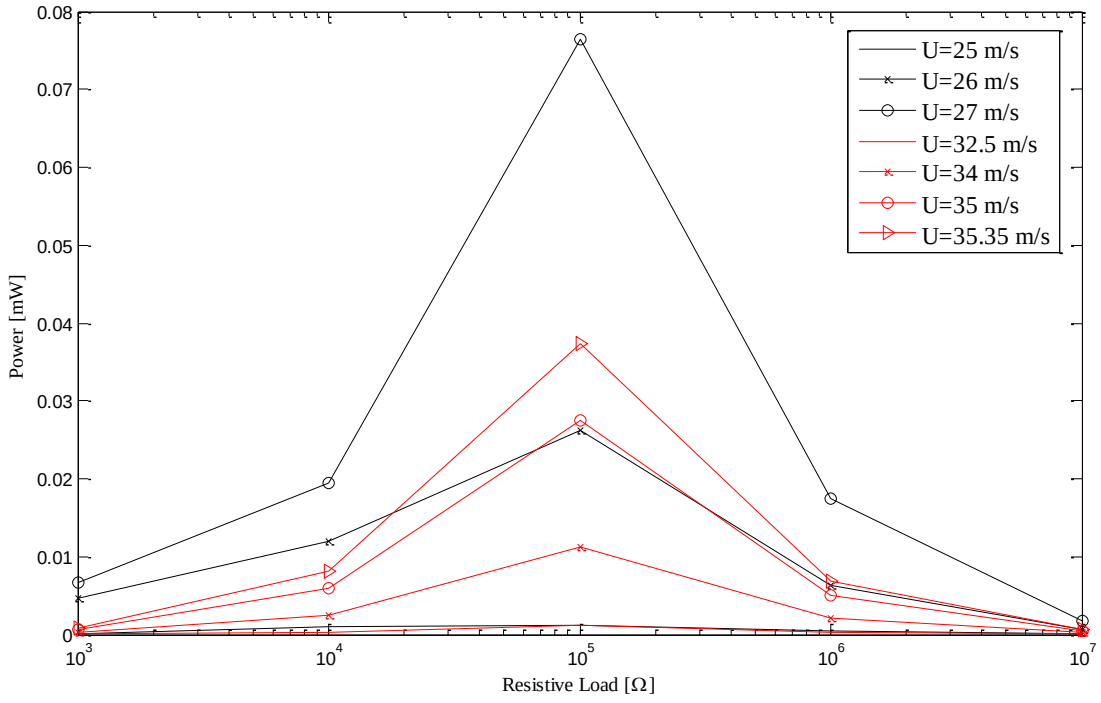

Figure 135 Comparison of the power output obtained from the LE electric circuit and the numerical results.

The amount of power showed in Figure 128 refers to a single piezo patch; the LE patch for the experimental wing, while any of the two patches for

the numerical wing. This means that the real power which this piezoelectric wing is able to provide to the global energy system , for the way it is designed, is the double of the value displayed in Figure 128. A power amount of the order of 1 mW is even more than the energy demand of MEMS technology and therefore it is worth, with a large margin of improvements, to be considered as an option for additional power onboard of the HALE aircrafts.

References

[1] Bisplinghoff, R., Ashley, H., Halfman, R., Aeroelasticity, Dover 1996.

[2] D'onghia, N., " Numerical and Experimental Analysis of an Aeroelastic Model for Energy Harvesting", Master's thesis, 2015, Politecnico di Torino.

[3] Micro Fiber Composites - MFC. www.smart-materilas.com

[4] Ewins, D.J., Modal Testing: Theory and Practice, JOHN WILELY& SONS INC, 1984.

[5]Fundamental of modal testing, Agilent Technologies, Application note 243-3.

7 Conclusions

The diffused interest in developing new autonomous aircrafts which may perform very long missions, of the order of the months, acted as a driver for many dedicated studies on the design optimization, as the results of a global compromise between reduced weight and high in flight autonomy. In order to guarantee high autonomy, although HALE are supposed to linger for a great part of their flight mission at very high altitudes, were the consumption is reduced, the weight increase is an unavoidable effect. Higher autonomy means, higher energy stocks on board, which means higher overall weight. The current market offers several solution which provides high energy contents without enormous penalties in terms of weight with respect to the more conventional systems, such as ordinary batteries. Fuel cells or solar panels for example if properly optimized may not be tremendous issue in terms of weight and bring the advantage of being potentially an infinite source of energy since conversely to the conventional batteries they don't have to be substituted, which an incredible goal for the accomplishment of the mission demanded to HALE UAV. However, although the efforts made up to now, some of the long range missions envisaged for these aircrafts is still unachievable for a matter of onboard available energy. Therefore the solution as to come from autonomous systems which are able to recharge onboard in a similar way as solar panels. The NASA Helios aircraft is an example or the Facebook Aquila drone. Several studies, thanks to the recent advances in MEMS and wireless technologies in terms of reduced power consumptions, made possible to think to new energy sources such as vibrations. Energy extraction from vibrations is not a very recent concept and it is already used in urban infrastructure as a structural damper, but what changed in recent year is the development of very flexible and light piezoelectric composites

which enlarged the spectrum of the possible applications. Energy harvesting from aeroelastic disturbances is one of those, and it doesn't occupy anymore only a place among the academic interests, it is already under the consideration of big industrial companies. The advantages of piezoelectric harvesting, especially of micro fiber composites (MFC), is primarily the fact of being able to provide energy from any vibration source which otherwise would be lost, they don't need to be substituted, and globally they don't introduce big weight penalties.

Vibrations are a constant on aircrafts, from the ground phases to the flight phases the structure is subjected to different types of vibrations. Turbulence is one of the cause of the high vibration level experienced by the wing during the flight phases but also aeroelastic instabilities may induce an high level of oscillation at operational speed, especially when high aspect ratio wings are considered, as HALE aircraft or gliders. The purpose of the research activity presented in this dissertation thesis was to investigate the possibility to extract energy from the most commons aeroelastic phenomena and from the gust response, through the application of two piezo-patches over surface of high aspect ratio wings. A nonlinear analytical aeroelastic piezoelectric wing model, which includes geometrical nonlinearities up to the third order, was derived with the purpose of investigating aeroelastic phenomena such as supercritical and subcritical LCOs. The equations of motion were obtained via the extended Hamilton principle and under the assumptions of the 3D Euler-Bernoulli beam theory and of unsteady aerodynamic, according to the Wagner model. The equations of motion were then simplified, according to an asymptotic reduction procedure, in order to retain only the very important terms into the equations for the wings type here analyzed. The importance of higher order nonlinear terms is furthermore investigated via a comparison with

FEM and experimental results. The effect of the high static deformation, which affect high aspect ratio wing during the flight, over the dynamic response of the wing is experienced by the previously mentioned analytical model, numerically implemented into a Matlab ® code, through the rise of subcritical LCOs. The numerical results, in agreement with the experimental results, shown that when the wing undergoes to high static deformations a state of dynamical instabilities may settle at speed even 50% lower than the critical flutter speed. Furthermore the studies shown that when the oscillation amplitude become high the nonlinear analytical model has to include higher order terms to correctly capture the real oscillation amplitude. Once a reliable and exhaustive nonlinear model has been determined it was used to study some of the classical aeroelastic phenomena, including the gust response, and to estimate the amount of power generated by the aeroelastic instabilities. In particular the energy extraction was possible thanks to a purely resistive electric circuit connected to the electrodes which covers the piezo patches. Albeit energy harvesting from flutter is a subject sufficiently treated in literature, energy harvesting from LCOs is barely represented and when, most of the time by the means of a simplified model which consist in a 2-DOF aeroelastic airfoil where the nonlinearities are represented via a nonlinear restoring force. The aerodynamic nonlinearities, such as the dynamic stall model, are often responsible of the establishment of post critical LCOs but this normally happens when the pitch angle is of the order of 10°. At low values of the pitch angle the geometrical nonlinearities are the drivers for the LCOs settlement. Therefore the model in the current work is able to capture those instabilities that as we just mentioned with a similar level of intensity may appear also at low speed. Two types of discrete gust profiles are assumed to study the wing response to an atmospheric disturbance: 1) Squared gust, a combination of two sharp edge gusts, and 2) 1-Cosine gust.

The Squared gust seemed to be more effective for energy harvesting purposes than the 1-Cosine if compared, as it was done in Chapter 5, on the base of the energy content subtended by each curve of the gust profiles. Although the 1-Cosine appeared less effective in terms of the amount of power that it can provide to the wing for energy harvesting, it was identified an optimal value of gust penetration gradient at which the assumed piezoelectric wing was able to extract the maximum amount of energy. LCOs and ideally flutter, are clearly the most favorable conditions for energy harvesting since they provide a constant oscillation in time and amplitude, at a give air speed, therefore they may be seen as a constant source of energy but as how it is easily understandable for reasons of structural safety it is not possible to rely in them as the only sources of vibration energy on board, that's way all the possible phenomena that may induced vibrations, such as turbulence, need to be investigated. It is true that an extended exposition to harmonic vibrations may cause fatigue issues therefore it has to be avoided, at least for the primary structure, but other solution are not missing in the literatures. In fact some researchers propose the connection of optimized piezoelectric surfaces to the wing in such a way that they may undergo to aeroelastic instabilities, driven by the wing induced loads, at low speed and without any detrimental effects for the primary structure.

Finally, thanks to the modal shaker and wind tunnel tests campaign performed in the frame of the A2-NET team at Clarkson University (USA) it was possible to investigate, starting from the experimental results of a piezoelectric wing, the importance of the location of the piezoelectric patches over the wing with respect to its dynamical response. What was seen is that the amount of energy extractable from the second bending mode of the wing is higher than that extractable from the first bending

mode and in it increase if the piezo patches are slightly moved towards the wing center. This results suggest the necessity to develop a piezoelectric wing with multiple piezoelectric patches properly located in order to extract energy from the higher number of modes, or simply to the most excited mode, according to the good knowledge of the operational wing dynamic behavior. The WT the order of magnitude of the energy extractable from LCOs which is of the order of 10 mW, a good result if compared to power demand many modern electronic devices.

8 Research gaps and suggestions

The piezo-aroelastic wing model used to study some of most common aeroelastic disturbances was properly defined to capture the desired conditions. However for the purpose of a wider application it has to enriched by adding more higher order nonlinear terms and the dynamic stall model.

The shunting circuit and nonlinear effect over piezoelectric properties may be subjected to improvements. Several studies available in literature showed the limits of a purely restive shunting circuit, that's to say the restriction to work at only one resonant frequency while by the addition of an electric inductance it is possible to extended the range of maximum energy extraction. A more sophisticated piezoelectric model would include nonlinearities also on the electrical parameters. The choice of considering only geometrical nonlinearities was made since the beginning to avoid misinterpretations in the results. Another important thing that has to be included is the structural damping that in the current study was assumed always negligible, often due to the lack of the data, but in some cases this may not be acceptable.

The suggestions for future works based on the results obtained by the numerical analysis are to investigate on the potential of such piezoelectric configuration for load alleviation purposes. The numerical results were not able display any relevant effect in this direction however the experimental tests highlighted some variations, even very small, of the oscillations amplitude when the piezo was connected to an electric resistance that may lead to believe that the piezoelectric patches if properly located are effective also as wing load alleviators.

Appendix

The full set of equations of the piezoelectric elements is reported hereafter.

Torsion PZT

$$-\mathbf{IyP}\boldsymbol{H\theta}^{(\mathbf{0,2})} + \mathbf{C22}\boldsymbol{H\theta}^{(\mathbf{2,0})} + \mathbf{C22}\boldsymbol{H}^{(\mathbf{1,0})}\boldsymbol{\theta}^{(\mathbf{1,0})} - \mathrm{C11}H\theta u^{(2,0)^2} + \mathrm{C33}H\theta u^{(2,0)^2} + \mathrm{C22}H^{(1,0)}u^{(1,0)}w^{(2,0)} - \mathrm{C11}Hu^{(2,0)}w^{(2,0)} + \mathrm{C22}Hu^{(2,0)}w^{(2,0)} + \mathrm{C33}Hu^{(2,0)}w^{(2,0)} + \mathrm{C11}H\theta w^{(2,0)^2} - \mathrm{C33}H\theta w^{(2,0)^2} + \mathrm{C22}Hu^{(1,0)}w^{(3,0)}$$

Out of plane bending PZT

$$\boldsymbol{Hm_P w}^{(\mathbf{0,2})} + \mathbf{Ix}\boldsymbol{Hw}^{(\mathbf{2,2})} + \mathbf{Ix}\boldsymbol{H}^{(\mathbf{1,0})}\boldsymbol{w}^{(\mathbf{1,2})} - \mathbf{C11}\boldsymbol{Hw}^{(\mathbf{4,0})} - \mathbf{C11}\boldsymbol{H}^{(\mathbf{2,0})}\boldsymbol{w}^{(\mathbf{2,0})} - \mathbf{2C11}\boldsymbol{H}^{(\mathbf{1,0})}\boldsymbol{w}^{(\mathbf{3,0})} - \mathbf{N14}\boldsymbol{H}^{(\mathbf{2,0})}V - \mathrm{C11}\theta H^{(2,0)}u^{(2,0)} + \mathbf{C33}\boldsymbol{\theta H}^{(\mathbf{2,0})}\boldsymbol{u}^{(\mathbf{2,0})} - \mathrm{C11}H^{(2,0)}u^{(1,0)}w^{(1,0)}u^{(2,0)} - 2\mathrm{C11}H^{(1,0)}\theta^{(1,0)}u^{(2,0)} - \mathrm{C22}H^{(1,0)}\theta^{(1,0)}u^{(2,0)} + \mathbf{2C33}\boldsymbol{H}^{(\mathbf{1,0})}\boldsymbol{\theta}^{(\mathbf{1,0})}\boldsymbol{u}^{(\mathbf{2,0})} - 2\mathrm{C11}H^{(1,0)}w^{(1,0)}u^{(2,0)^2} + \mathrm{C11}\theta^2 H^{(2,0)}w^{(2,0)} - \mathbf{C33}\boldsymbol{\theta}^{\mathbf{2}}\boldsymbol{H}^{(\mathbf{2,0})}\boldsymbol{w}^{(\mathbf{2,0})} - \mathrm{C11}H^{(2,0)}w^{(1,0)^2}w^{(2,0)} + 4\mathrm{C11}\theta H^{(1,0)}\theta^{(1,0)}w^{(2,0)} - \mathbf{4C33}\boldsymbol{\theta H}^{(\mathbf{1,0})}\boldsymbol{\theta}^{(\mathbf{1,0})}\boldsymbol{w}^{(\mathbf{2,0})} + 2\mathrm{C11}H\theta^{(1,0)^2}w^{(2,0)} - \mathbf{2C33}\boldsymbol{H\theta}^{(\mathbf{1,0})^2}\boldsymbol{w}^{(\mathbf{2,0})} - 2\mathrm{C11}H^{(1,0)}u^{(1,0)}u^{(2,0)}w^{(2,0)} - \mathrm{C22}H^{(1,0)}u^{(1,0)}u^{(2,0)}w^{(2,0)} + \mathrm{C33}H^{(1,0)}u^{(1,0)}u^{(2,0)}w^{(2,0)} - 2\mathrm{C11}Hu^{(2,0)^2}w^{(2,0)} - \mathrm{C22}Hu^{(2,0)^2}w^{(2,0)} + \mathrm{C33}Hu^{(2,0)^2}w^{(2,0)} - 3\mathrm{C11}H^{(1,0)}w^{(1,0)}w^{(2,0)^2} - \mathrm{C11}Hw^{(2,0)^3} - \mathrm{C11}Hu^{(2,0)}\theta^{(2,0)} - \mathrm{C22}Hu^{(2,0)}\theta^{(2,0)} + \mathrm{C33}Hu^{(2,0)}\theta^{(2,0)} + 2\mathrm{C11}H\theta w^{(2,0)}\theta^{(2,0)} - \mathbf{2C33}\boldsymbol{H\theta}\boldsymbol{w}^{(\mathbf{2,0})}\boldsymbol{\theta}^{(\mathbf{2,0})} - 2\mathrm{C11}\theta H^{(1,0)}u^{(3,0)} + \mathbf{2C33}\boldsymbol{\theta H}^{(\mathbf{1,0})}\boldsymbol{u}^{(\mathbf{3,0})} - 2\mathrm{C11}H^{(1,0)}u^{(1,0)}w^{(1,0)}u^{(3,0)} - 2\mathrm{C11}H\theta^{(1,0)}u^{(3,0)} - \mathrm{C22}H\theta^{(1,0)}u^{(3,0)} + \mathbf{2C33}\boldsymbol{H\theta}^{(\mathbf{1,0})}\boldsymbol{u}^{(\mathbf{3,0})} - 3\mathrm{C11}Hw^{(1,0)}u^{(2,0)}u^{(3,0)}$$

$$-2\mathrm{C11}Hu^{(1,0)}w^{(2,0)}u^{(3,0)} - \mathrm{C22}Hu^{(1,0)}w^{(2,0)}u^{(3,0)} + \mathrm{C33}Hu^{(1,0)}w^{(2,0)}u^{(3,0)} + 2\mathrm{C11}\theta^2 H^{(1,0)}w^{(3,0)} - \mathbf{2C33}\boldsymbol{\theta}^{\mathbf{2}}\boldsymbol{H}^{(\mathbf{1,0})}\boldsymbol{w}^{(\mathbf{3,0})} - 2\mathrm{C11}H^{(1,0)}w^{(1,0)^2}w^{(3,0)} + 4\mathrm{C11}H\theta\theta^{(1,0)}w^{(3,0)} - \mathbf{4C33}\boldsymbol{H\theta\theta}^{(\mathbf{1,0})}\boldsymbol{w}^{(\mathbf{3,0})} - \mathrm{C11}Hu^{(1,0)}u^{(2,0)}w^{(3,0)} - \mathrm{C22}Hu^{(1,0)}u^{(2,0)}w^{(3,0)} + \mathrm{C33}Hu^{(1,0)}u^{(2,0)}w^{(3,0)} - 4\mathrm{C11}Hw^{(1,0)}w^{(2,0)}w^{(3,0)} - \mathrm{C11}H\theta u^{(4,0)} + \mathbf{C33}\boldsymbol{H\theta u}^{(\mathbf{4,0})} - \mathrm{C11}Hu^{(1,0)}w^{(1,0)}u^{(4,0)} + \mathrm{C11}H\theta^2 w^{(4,0)} -$$

$$\mathbf{C33}H\theta^2 w^{(4,0)} - \mathrm{C11}Hw^{(1,0)^2}w^{(4,0)} + \mathrm{C22}H^{(2,0)}u^{(1,0)}\theta^{(1,0)} + \mathrm{C22}H^{(1,0)}\theta^{(1,0)}u^{(2,0)} + \mathrm{C22}H^{(2,0)}u^{(1,0)^2}w^{(2,0)} - \mathrm{C11}H^{(1,0)}u^{(1,0)}u^{(2,0)}w^{(2,0)} + 3\mathrm{C22}H^{(1,0)}u^{(1,0)}u^{(2,0)}w^{(2,0)} + \mathrm{C33}H^{(1,0)}u^{(1,0)}u^{(2,0)}w^{(2,0)} - \mathrm{C11}Hu^{(2,0)^2}w^{(2,0)} + \mathrm{C22}Hu^{(2,0)^2}w^{(2,0)} + \mathrm{C33}Hu^{(2,0)^2}w^{(2,0)} + 2\mathrm{C22}H^{(1,0)}u^{(1,0)}\theta^{(2,0)} + \mathrm{C22}Hu^{(2,0)}\theta^{(2,0)} - \mathrm{C11}Hu^{(1,0)}w^{(2,0)}u^{(3,0)} + \mathrm{C22}Hu^{(1,0)}w^{(2,0)}u^{(3,0)} + \mathrm{C33}Hu^{(1,0)}w^{(2,0)}u^{(3,0)} + 2\mathrm{C22}H^{(1,0)}u^{(1,0)^2}w^{(3,0)} - \mathrm{C11}Hu^{(1,0)}u^{(2,0)}w^{(3,0)} + 3\mathrm{C22}Hu^{(1,0)}u^{(2,0)}w^{(3,0)} + \mathrm{C33}Hu^{(1,0)}u^{(2,0)}w^{(3,0)} + \mathrm{C22}Hu^{(1,0)}\theta^{(3,0)} + \mathrm{C22}Hu^{(1,0)^2}w^{(4,0)}$$

In plane bending PZT

$$-\boldsymbol{Hm_P u^{(0,2)}} + \mathbf{Iz}\boldsymbol{H^{(1,0)}u^{(1,2)}} + \mathbf{Iz}\boldsymbol{Hu^{(2,2)}} - \mathbf{C33}\boldsymbol{Hu^{(4,0)}} - \mathbf{C33}\boldsymbol{H^{(2,0)}u^{(2,0)}} - \mathbf{2C33}\boldsymbol{H^{(1,0)}u^{(3,0)}} - \mathrm{C11}\theta^2 H^{(2,0)}u^{(2,0)} + \mathrm{C33}\theta^2 H^{(2,0)}u^{(2,0)} - \mathrm{C33}H^{(2,0)}u^{(1,0)^2}u^{(2,0)} - 4\mathrm{C11}\theta H^{(1,0)}\theta^{(1,0)}u^{(2,0)} + 4\mathrm{C33}\theta H^{(1,0)}\theta^{(1,0)}u^{(2,0)} - 2\mathrm{C11}H\theta^{(1,0)^2}u^{(2,0)} + 2\mathrm{C33}H\theta^{(1,0)^2}u^{(2,0)} - 3\mathrm{C33}H^{(1,0)}u^{(1,0)}u^{(2,0)^2} - \mathrm{C33}Hu^{(2,0)^3} - \mathrm{C11}\theta H^{(2,0)}w^{(2,0)} + \mathrm{C33}\theta H^{(2,0)}w^{(2,0)} - \mathrm{C11}H''u^{(1,0)}w^{(1,0)}w^{(2,0)} - 2\mathrm{C11}H^{(1,0)}\theta^{(1,0)}w^{(2,0)} + \mathrm{C22}H^{(1,0)}\theta^{(1,0)}w^{(2,0)} + 2\mathrm{C33}H^{(1,0)}\theta^{(1,0)}w^{(2,0)} - \mathrm{C11}H^{(1,0)}w^{(1,0)}u^{(2,0)}w^{(2,0)} - 2\mathrm{C11}H^{(1,0)}u^{(1,0)}w^{(2,0)^2} + \mathrm{C22}H^{(1,0)}u^{(1,0)}w^{(2,0)^2} - \mathrm{C11}Hu^{(2,0)}w^{(2,0)^2} + \mathrm{C22}Hu^{(2,0)}w^{(2,0)^2} - 2\mathrm{C11}H\theta u^{(2,0)}\theta^{(2,0)} + 2\mathrm{C33}H\theta u^{(2,0)}\theta^{(2,0)} - \mathrm{C11}Hw^{(2,0)}\theta^{(2,0)} + \mathrm{C22}Hw^{(2,0)}\theta^{(2,0)} + \mathrm{C33}Hw^{(2,0)}\theta^{(2,0)} - 2\mathrm{C11}\theta^2 H^{(1,0)}u^{(3,0)} + 2\mathrm{C33}\theta^2 H^{(1,0)}u^{(3,0)} - 2\mathrm{C33}H^{(1,0)}u^{(1,0)^2}u^{(3,0)} - 4\mathrm{C11}H\theta\theta^{(1,0)}u^{(3,0)} + 4\mathrm{C33}H\theta\theta^{(1,0)}u^{(3,0)} - 4\mathrm{C33}Hu^{(1,0)}u^{(2,0)}u^{(3,0)} - 2\mathrm{C11}\theta H^{(1,0)}w^{(3,0)} + 2\mathrm{C33}\theta H^{(1,0)}w^{(3,0)} - 2\mathrm{C11}H^{(1,0)}u^{(1,0)}w^{(1,0)}w^{(3,0)} - 2\mathrm{C11}H\theta^{(1,0)}w^{(3,0)} + \mathrm{C22}H\theta^{(1,0)}w^{(3,0)} + 2\mathrm{C33}H\theta^{(1,0)}w^{(3,0)} - \mathrm{C11}Hw^{(1,0)}u^{(2,0)}w^{(3,0)} - 3\mathrm{C11}Hu^{(1,0)}w^{(2,0)}w^{(3,0)} + 2\mathrm{C22}Hu^{(1,0)}w^{(2,0)}w^{(3,0)} - \mathrm{C11}H\theta^2 u^{(4,0)} + \mathrm{C33}H\theta^2 u^{(4,0)} - \mathrm{C33}Hu^{(1,0)^2}u^{(4,0)} - \mathrm{C11}H\theta w^{(4,0)} + \mathrm{C33}H\theta w^{(4,0)} - \mathrm{C11}Hu^{(1,0)}w^{(1,0)}w^{(4,0)}$$